A novel all-solid-state laser source for lithium atoms and three-body recombination in the unitary Bose gas

Ulrich Eismann

DÉPARTEMENT DE PHYSIQUE
DE L'ÉCOLE NORMALE SUPÉRIEURE

LABORATOIRE KASTLER-BROSSEL

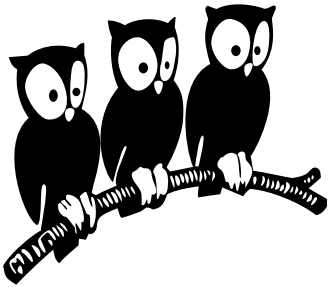

THÈSE DE DOCTORAT DE L'UNIVERSITÉ PARIS VI

Spécialité : Physique Quantique

présentée par

Ulrich Eismann

Pour obtenir le grade de
Docteur de l'Université Pierre et Marie Curie (Paris VI)

A novel all-solid-state laser source for lithium atoms and three-body recombination in the unitary Bose gas

---

Soutenue le 3 Avril 2012
devant le jury composé de :

Isabelle Bouchoule	Rapporteuse
Frédéric Chevy	Directeur de Thèse
Francesca Ferlaino	Examinatrice
Anders Kastberg	Rapporteur
Arnaud Landragin	Examinateur
Christophe Salomon	Membre invité
Jacques Vigué	Examinateur

Contents

Abstract

In this thesis we present novel techniques for the study of ultracold gases of lithium atoms.

In the first part of this thesis, we present the development of a narrow-linewidth laser source emitting 840 mW of output power in the vicinity of the lithium D-line resonances at 671 nm. The source is based on a diode-end-pumped unidirectional ring laser operating on the 1342-nm transition in Nd:YVO_4, capable of producing 1.3 W of single-mode light delivered in a diffraction-limited beam. The output beam is subsequently frequency-doubled using periodically-poled potassium titanyl phosphate (ppKTP) in an external buildup cavity. We obtain doubling efficiencies of up to 86%. Tunability of the output frequency over more than 400 GHz and frequency-locking of the cavity ensemble with respect to the lithium D-line transitions are accomplished. We measure the linewidth to be 200^{+400}_{-200} kHz.

In the second part of this thesis, we employ the source in an experimental setup to produce to cool and trap lithium atoms. We realize samples of finite-temperature unitary Bose gases around the center of a Fano-Feshbach resonance, where interactions between the atoms are maximized. We present temperature-dependent measurements of the unitarity-limited three-body loss rate. The measured losses attain the limiting value imposed by quantum mechanics without adjustable parameters. This measurement allows for the introduction of a criterion for quasi-equilibrium. In this regime, by using technique based on in-situ imaging developed in our group, we provide a first measurement of the equation of state of the unitary Bose gas at low fugacities.

Résumé

Dans cette thèse, nous présentons des nouvelles techniques et leur application dans l'étude des gaz d'atomes de lithium ultrafroids.

Dans la première partie de cette thèse, nous présentons le développement d'une nouvelle source laser de faible largeur spectrale, capable d'émettre 840 mW de puissance dans la gamme des longeurs d'ondes des raies D du lithium atomique à 671 nm. La source est basée sur un laser en anneau pompé par diode, fonctionnant sur la transition à 1342 nm dans le Nd:YVO_4, capable de produire 1.3 W de lumière monomode dans un faisceau limité par la diffraction. Le faisceau de sortie est ensuite doublé en fréquence dans un cristal de phosphate de potassium titanyl (ppKTP) périodiquement polarisé dans une cavité externe. Nous obtenons un rendement du doublage de 86%. Une accordabilité de la fréquence de sortie sur plus de 400 GHz et le verrouillage de l'ensemble des cavités par rapport aux raies D du lithium sont accomplis. Nous avons mesuré la largeur de raie d'émission à 200^{+400}_{-200} kHz.

Dans la deuxième partie de cette thèse, nous employons la source sur un dispositif expérimental pour refroidir et piéger des atomes de lithium. Nous réalisons des echantillons du gaz de Bose unitaire à température finie au voisinage d'une résonance de Fano-Feshbach, où les interactions entre les atomes sont maximales. Nous présentons des mesures du taux de pertes à trois corps en fonction de la température. Les pertes mésurées atteignent la valeur limite imposée par la mécanique quantique sans aucun paramètre ajustable. Cette mesure permet l'introduction d'un critère de quasi-équilibre. Dans ce régime, en utilisant une technique basée sur l'imagerie in-situ développée dans notre groupe, nous fournissons une première mesure de l'équation d'état du gaz de Bose unitaire à basse fugacité.

Zusammenfassung

In dieser Arbeit werden neue Techniken für die Untersuchung von ultrakalten Gasen bestehend aus Lithiumatomen vorgestellt.

Im ersten Teil dieser Arbeit präsentieren wir die Entwicklung einer schmalbandigen Lichtquelle, welche 840 mW Ausgangsleistung im Bereich der Lithium-D-Linien bei 671 nm liefert. Die Quelle beruht auf einem diodenendgepumpten unidirektionalen Ringlaser, der unter Benutzung des 1342-nm-Überganges in Nd:YVO_4 1.3 W monofrequentes Licht in einem beugungsbegrenzten Strahl emittiert. Die Laserstrahlung wird anschließend unter Benutzung von periodisch gepoltem Kaliumtitanylphosphat (ppKTP) in einem externen Resonator frequenzverdoppelt. Der maximale Wirkungsgrad dieser Frequenzkonversion beträgt 86%. Eine Abstimmbarkeit der Ausgangsfrequenz über mehr als 400 GHz und eine Frequenzstabilisierung des Resonatorensembles in Bezug auf die Lithium-D-Linien werden erreicht. Wir bestimmen die Linienbreite des emittierten Lichts zu 200^{+400}_{-200} kHz.

Im zweiten Teil dieser Arbeit benutzen wir die Lichtquelle zum magnetooptischen Fangen von Lithiumatomen. Mit diesen präparieren wir unitäre Bose-Gase bei endlicher Temperatur in unmittelbarer Umgebung einer Fano-Feshbach-Resonanz, wo die Wechselwirkung zwischen den Atomen ihren maximalen Wert annimmt. Wir präsentieren temperaturabhängige Messungen der Dreikörperverlustrate. Die gemessenen Verluste erreichen das durch die Quantenmechanik auferlegte unitäre Limit, wodurch die Einführung eines Quasi-Gleichgewichtskriteriums ermöglicht wird. Innerhalb dieses Regimes präsentieren wir mithilfe einer in-situ-Bildgebungstechnik, welche in unserer Gruppe entwickelt wurde, eine erste Messung der thermodynamischen Zustandsgleichung des unitären Bose-Gas bei niedrigen Fugazitäten.

Remerciements

Je tiens à remercier ici les personnes qui ont contribué à la réalisation de ma thèse. J'aimerais commencer en adressant mes remerciements à Isabelle Bouchoule, Francesca Ferlaino, Anders Kastberg, Arnaud Landragin et Jacques Vigué pour avoir fait partie de mon comité de thèse. Je considère que c'est un immense honneur d'avoir été évalué par ces éminents chercheurs, dont les travaux ont été une source de grande inspiration pour mon travail et dont j'ai apprecié les commentaires sur ce manuscrit. Je suis également profondément reconnaissant à mon directeur de Diplomarbeit Achim Peters et à Richard Stein, camarade berlinois et parisien, de m'avoir conseillé de réaliser mon doctorat à Paris.

Je tiens à remercier mon directeur de thèse Frédéric Chevy de m'avoir accueilli dans son groupe. Ses dons d'enseignant sont rares. J'ai été très impressionné par ses connaissances extrêmement étendues dans des domaines scientifiques très variés. Son intérêt constant et les nombreuses discussions que nous avons eues dans notre bureau commun ont été une source formidable d'informations pour moi. Il aura certainement toujours une longueur d'avance dans ses réflexions sur notre travail. En outre, avec son sens de l'humour, il a su créer une atmosphère trés productive au sein du groupe. Je tiens à remercier mon « conseiller en second », Christophe Salomon, pour son accueil chaleureux. A chacune de nos rencontres, j'ai été impressionné par son expérience exceptionnelle en physique, de même que par son éternel optimisme qui lui a permis de m'encourager même dans les moments un peu difficiles. La liberté qu'il nous a laissé dans le travail de tous les jours est admirable. J'ai apprécié les longues discussions fructueuses que nous avons partagées sur une grande variété de sujets.

Je suis profondément reconnaissant à Fabrice Gerbier, qui a collaboré avec notre groupe dans le cadre du projet laser lithium. Son travail s'est caractérisé par une grande perfection puisque nous avons pu, en très peu de temps, convertir la conception de la cavité de génération de somme de fréquence, qu'il avait initialement développée pour l'expérience sodium au LKB, dans une cavité de doublage de fréquence. Ses créations de circuits électroniques de verrouillage de fréquence ont été une excellente base pour contrôler le système de 671 nm. Son aide la plus précieuse a sans doute été sa grande disponibilité pour partager des dicussions, ainsi que pour fournir des conseils, des réponses et des commentaires supplémentaires sur une vaste palette de questions (non-)linéaires.

Je tiens à saluer les « Toulousains », Jacques Vigué et Gérard Trénec, pour l'excellent travail qu'ils ont effectué sur le développement de leur première génération de source laser infrarouge. Sans leurs conseils et l'échange très important de composants optiques, le projet n'aurait pas pris la forme qu'il a prise. Le développement de l'aimant permanent puissant utilisé pour la rotation de Faraday est une condition préalable fonda-

mentale pour le fonctionnement unidirectionnel efficace du laser. Cela concerne l'essai des cristaux ppKTP de Stockholm, à un moment où aucune source de lumière capable d'émettre une puissance de sortie au niveau du Watt n'était disponible dans notre laboratoire. J'attends avec impatience les résultats concernant le développement de leur dernier laser à 1342 nm de la classe de 10 Watt « à la Kaiserslautern ». Je tiens également à remercier Florian Lenhard de Photonikzentrum Kaiserslautern d'avoir partagé avec moi ses vastes connaissances au sujet de sa source laser particulière [1], ainsi que Carlota Canalias, de la KTH à Stockholm, pour avoir fourni le ppKTP. Je suis profondément reconnaissant à Peter Zimmermann, de Layertec GmbH, de m'avoir fait profiter de ses vastes connaissances au sujet de la fabrication des composants optiques, et pour toute l'intelligence qu'il a mise dans les dessins des traitements des composants (en nous le faisant ou non savoir ...).

J'ai rejoint le LKB en tant que membre de l'équipe FerMix. J'ai passé d'agréables moments au sein du laboratoire avec les physiciens de la « première génération » : David Wilkowski, Saptharishi Chaudhuri, Armin Ridinger et Tomas Salez. J'ai apprécié les discussions sur la façon dont il est important de donner des noms d'animaux aux lasers, et bien sûr sur le fait de rester cohérent compte tenu des questions géographiques... Je tiens également à féliciter les étudiants de la « deuxième génération », Diogo Fernandez, Norman Kretzschmar et Franz Sievers, pour leurs nouvelles idées et l'énergie qu'ils ont fournie pour l'expérience FerMix. Je n'oublie pas de remercier Franzl pour toutes les expériences d'escalade que nous avons partagées ensemble, ainsi que pour sa participation dans le cadre du projet de deuxième génération du laser lithium.

La seconde partie de ma thèse, je l'ai passée au sein du groupe de lithium du LKB, pour lequel nous avons utilisé le laser lithium comme source de lumière. J'ai passé de très bons moments au début de cette période avec Kenneth Günter, Nir Navon et Trong Canh Nguyen. Je leur dois beaucoup. Puis cela a été un grand plaisir de travailler avec la nouvelle « équipe de rêve » composée d'Andrew Grier, de Benno Rem et d'Igor Ferrier-Barbut. Le nombre de câbles, « dudes » et chansons de Jacques Brel que nous avons trouvés dans la salle de manip est tout absolument « incroyable » ! Nous avons passé de bons moments avec notre visiteur, Tim Langen, et avec Marion Delahaye, qui a rejoint récemment notre groupe en tant que stagiaire. Je dois beaucoup à Andrea Bergschneider, qui s'est retrouvée presque seule à réaliser la source laser de deuxième génération pendant que je me consacrais à la rédaction de ce manuscrit.

Le LKB est un endroit idéal pour travailler, notamment grâce aux gens qui s'y trouvent. Il est difficile de les nommer tous, une liste ne pourrait être qu'incomplète. Il se trouve parmi ces gens des amis : Yves Candela, Roman Schmeißner, Fabien Souris et Jonas Mlynek. Je tiens à remercier Félix Werner pour les discussions approfondies que nous avons eues au sujet de la physique théorique et, en particulier, du problème des trois corps bosoniques. Je tiens à remercier tous les groupes du LKB avec qui nous avons échangé toutes sortes de matériel qui, généralement, n'a jamais trouvé le chemin du retour ... Tout aussi importantes à mes yeux sont les personnes en charge de l'organisation. Je tiens à remercier le personnel du secrétariat, qui a toujours eu une oreille attentive et l'esprit ouvert pour les problèmes d'organisation qui se sont parfois présentés : Emmanuelle André, Dominique Giafferi, Monique Granon, Thierry Tardieu, Françoise Tarquis et surtout Christophe Bernard. Je suis profondément re-

connaissant aux gens de l'atelier mécanique, plus particulièrement à Jean-Michel Isac, pour la réalisation d'une grande partie des composants « sur mesure » nécessaires pour la physique expérimentale. Je tiens également à remercier les personnes de l'atelier d'électronique ainsi que les gens de l'informatique Francis Hulin-Hubard, Christophe Bonnet et Frédéric Ayrault. J'adresse également mes remerciements aux hommes et aux femmes qui oeuvrent dans les lieux où ce manuscrit a été rédigé : Schnittchen à Berlin, Omnibus, La Brioche dorée, Au rendez-vous des artistes à Pigalle, l'université d'Erfurt, Peckham's, la Deutsche Bahn, la SNCF ...

Enfin, je tiens à remercier les personnes qui ont corrigé ce manuscrit et l'ont ainsi rendu beaucoup plus lisible et agréable à lire : Andrea, Andrew, Armin, Benno, Christophe, Fred, Igor et bien sûr Léa et Sandrine ! Et merci à vous, mes chers parents, pour tout !

Introduction

The realization of the first Bose-Einstein condensate in dilute alkali atom vapors in 1995 marks the starting point of a revolution in physics, allowing one to experimentally create new exotic states of matter.

The indispensable requirement for obtaining these ultracold dilute gases was the development of experimental techniques allowing to increase the phase-space densities of atomic vapors by magneto-optical cooling and evaporative cooling in conservative traps. Light forces on particles are known at least since Kepler's times from the shape of the tails of comets. In 1929, Pringsheim proposed to use light fields for acting mechanically on atoms [2], however, sufficiently brilliant light sources were not available at that time. The invention of the laser [3] allowed trapping of dielectric particles by Ashkin in 1970 [4], and in 1975, Hänsch and Schawlow proposed to use light to act dissipatively on atomic ensembles [5]. The most important experimental breakthroughs appeared one decade after the proposals with the ground-state cooling of the motion of a simple trapped ion [6] and the observation of optical molasses and sub-Doppler cooling and the explanation of its mechanisms [7, 8]. This earned the field the 1997 Nobel prize in physics to Steven Chu, Claude Cohen-Tannoudji and William D. Phillips "for development of methods to cool and trap atoms with laser light". This was soon after followed in 2001 by the Nobel prize to Eric A. Cornell, Wolfgang Ketterle and Carl E. Wieman "for the achievement of Bose-Einstein condensation in dilute gases of alkali atoms, and for early fundamental studies of the properties of the condensates".

The imprint of the lasers as a tool for mechanical action on atoms can thus hardly be overestimated. Apart from changing the atomic phase-space density by more than ten orders of magnitude [9], lasers have countless applications in cold-atom experiments, for instance the creation of almost arbitrarily shaped potentials, phase imprinting, coherent separation, to only name a few. These techniques allow for the realization of model Hamiltonians from almost all domains in physics, be it condensed matter-, statistical- or even particle physics. The possibility to realize many-body quantum systems in an extremely clean environment at nanokelvin-scale temperatures resulted in an explosion of works in the subject, making it one of the most active research fields in contemporary physics.

Outline of this thesis

According to the different but related subjects the thesis work was devoted to, this thesis is separated in two parts:

- In **Part I**, we present an all solid-state laser source emitting 840-mW output power of narrowband 671-nm light frequency-locked to the Lithium D-line transitions. We demonstrate the suitability of this stable, robust, spectrally narrow and frequency-stabilized light source for laser cooling of Lithium atoms.
- In **Part II**, we present work on the finite-temperature unitary Bose gas. We discuss temperature-dependent measurements of the unitarity- limited, three-body loss rate. Moreover, we measure the equation of state of the finite-temperature unitary Bose gas.

Part I

High power 671-nm laser system

Chapter 1

Introduction to Part I

The theoretical description of stimulated emission dates back to Albert Einstein. In 1916, he introduced this process to balance the rate equations of light absorption and emission of molecules in radiation fields [10]. Under the condition of inversion of the excited-state molecular population, stimulated emission can lead to gain of intensity of an incident radiation. Radar technology advanced rapidly in World War II, and it was on the quest to develop low-noise microwave amplifiers that Nicolay Gennadiyevich Basov and Aleksandr Mikhailovich Prokhorov theoretically proposed an amplifier using stimulated emission in 1952. It was put in practice in 1954 by Charles Hard Townes and the group of Basov and Prokhorov [11, 12] in the form of the MASER (microwave amplification by stimulated emission of radiation), winning them the 1964 Nobel prize in physics. In 1960 Maiman applied the same principle to visible wavelengths [3]. He realized the first MASER in the visible spectrum called LASER (light amplification by stimulated emission of radiation) using flashlamp-pumped ruby as a gain medium, and aluminum coatings on the end faces forming a cavity.

The impact of the development of the laser on our society, and on various domains of science is hard to be overestimated. In fact, the laser has become a part of our every-day life. Its particular impact on science is remarkable, and many fields would nowadays be unimaginable without the use of lasers. In high-resolution spectroscopy, light frequencies and thus spectroscopic features can be measured on an absolute scale with sub-Hertz precision. Laser pulse durations and thus timescales of dynamic processes measured using this radiation can be in the attosecond regime. With the help of lasers, one can address single atoms or ions and create exotic states of matter by cooling dilute atomic gases to quantum degeneracy, where the de-Broglie wavelength reaches the order of the inter-particle distance.

The electro-magnetic fields provided by laser radiation can even reach the order of magnitude of intra-atomic fields. Thus, intense laser fields can cause nonlinear responses when interacting with matter. These effects can be exploited to create light waves of frequencies different from the incident ones. Since laser sources are generally limited in their output frequency spectrum, the spectral coverage of laser-like sources can largely be augmented by applying nonlinear conversion processes. Only one year after the invention of the laser, second-harmonic generation was demonstrated by P. A. Franken et al. in 1961 [13]. The later demonstration of the optical parametric oscillator [14] paved the way for the creation of radiation of any frequency below that

of a given pump source. Further nonlinear frequency conversion methods are sum- and difference-frequency generation. An overview of these techniques is given in [15]. Using this rich toolbox of frequency-conversion technologies, available in both the continuous-wave and pulsed regimes, frequency limitations for laser-like light are only due to the occurrence of absorption in the nonlinear media employed. Specific media have been devised to cover the visible and near infrared region, and beyond.

The first laser employed a solid-state gain medium. Gaseous and liquid-gain-medium laser sources were developed thereafter, as well as different solid-state gain media. Crystals and glasses doped with neodymium ions (Nd^{3+}) are a prime example, featuring a strong transition around 1064 nm. Lasers using this material class are among the most powerful and widespread laser sources. In the following, we will motivate the development of a similar all-solid-state, frequency-doubled laser source emitting at 671 nm for cooling and trapping of lithium atoms.

This chapter is organized as follows: In Section 1.1 we will present the most prominent applications for laser sources emitting at 671 nm. In Section 1.2, currently available 671-nm light sources are discussed, whereas in Section 1.3 suitable alternatives for generating frequency-doubled light at the lithium resonances are presented. We conclude in Section 1.4 with the presentation of the overall design of the 671-nm laser source developed at Laboratoire Kastler Brossel.

1.1 Applications of 671-nm light sources

Ultracold atom experiments

The domain of ultra-cold atoms is a mature research field in today's physics. The 1997 and 2001 Nobel prizes in physics were given for laser cooling of atoms and the achievement of the atomic Bose–Einstein condensate in dilute atomic gases. Laser systems for theses experiments need to fulfill several requirements:

- To be able to produce large samples of quantum degenerate gases, one needs large numbers of pre-laser-cooled atoms in a magneto-optical trap (MOT). This first step is mandatory before proceeding to the evaporative cooling phase that leads to quantum degeneracy by reducing the atom number in favor of phase-space density. To optimize the MOT capture process, one usually fixes the laser intensity around one atomic saturation intensity

$$I_{\mathrm{sat}} = \frac{\pi h c}{3\lambda^3 \tau}\,, \tag{1.1}$$

  where h is Planck's constant, c the speed of light in vacuum, λ the transition wavelength, and $\tau = 1/\Gamma$ the upper-state lifetime. I_{sat} equals $2.5\,\mathrm{mW.cm^{-2}}$ in the case of atomic lithium. The dependence of the atom capture rate R of a vapor-cell MOT as a function of laser power and geometry can be estimated to be [16]

$$R \propto w^4 \left(\frac{I/I_{\mathrm{sat}}}{1 + I/I_{\mathrm{sat}}} \right)\,, \tag{1.2}$$

where w is the laser beam power radius, and I is its intensity. It is clear from (1.2) that rising the intensity above the saturation intensity is of minor interest. The available output power is thus best used to maximize the beam diameter. Thus, more laser power leads to a better capture efficiency and larger atom numbers. In practice, several tens of milliwatts of laser power per MOT beam are necessary for operating a large MOT.

- For stable operation, it is favorable to acoustically and electronically decouple the laser system from the MOT region, and to spatially mode-clean the laser light. In practice, this is realized by coupling the generated light to polarization-maintaining, single-mode fibers. One thus requires high transversal mode quality to establish an efficient fiber transport process. This also requires a stable polarization of the output.

- The requirement on the laser linewidth for operating an ultracold atom experiment is to not exceed a small fraction of the natural linewidth Γ of the atomic transition. For stabilized single-mode lasers, this is fulfilled easily. This condition is even more relaxed for MOT operation only. Moreover, several light beams of different frequencies need to be generated.

- The relative intensity noise requirements are relatively modest as well, and fulfilled by all common sources.

To fulfill all of these requirements, a certain degree of complexity arises in the practical realization of such systems. Two typical approaches exist to create all necessary output beams:

1. The master-oscillator-power-amplifier (MOPA) principle: Low-power frequency-stabilized light is derived from a master laser, typically an external-cavity diode laser. Beams of the necessary frequencies are derived from the master output by modulators. The resulting low-power output beams need to be amplified in power, which is typically established using either tapered amplifiers ore injection-locked diode lasers. A typical example is the setup currently used at ENS, see Figure 1.1.

2. The one-source principle: All the power is derived from a single frequency-stabilized source. Beams of different frequencies are, as above, generated using modulators.

The advantage of the second approach is obvious: The use of a single laser source significantly reduces the maintenance necessary to keep the system operational. However, to take into account the power requirements of the MOT, and the losses occuring when generating the required beams, Watt-level output power is needed for the single source.

The lithium atomic species is of great interest for ultra-cold-atom experiments and the study of quantum degenerate gases. As a member of the alkali group it offers strong coupling to electromagnetic fields and a simple level structure including cycling transitions, thus making it suitable for laser cooling. The significant natural abundance of fermionic (^{6}Li) as well as bosonic (^{7}Li) isotopes allows exploration of both sorts of

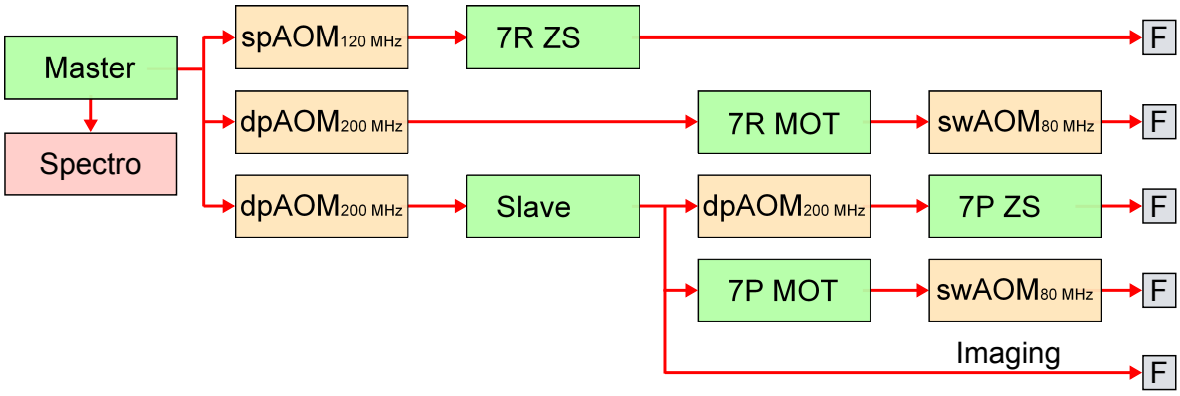

FIGURE 1.1: The current ^{7}Li laser system at ENS. Diode lasers are symbolized by green boxes, frequency modulators [acousto-optical modulators (AOMs), where sp(dp) stands for single (double passage) and the indicated frequencies are the nominal values of the respective modulator] by orange boxes and optical fibers by grey boxes. The master laser light is frequency-locked to the ^{7}Li $D2$ transition. The remaining output is frequency-shifted and amplified by an injection-locked slave laser for each of the Zeeman- and MOT output beams. The slave lasers carry a name according to their function [7 is for ^{7}Li, P(R) is for principle (repumper) beam and ZS (MOT) stands for Zeeman slower (magneto-optical trap)]. Each MOT beam is sent through a switch AOM (swAOM) to allow for fast switch-off, and all the beams are finally sent to the experimental table through single-mode optical fibers. For reasons of clarity, we do not show the mode-cleaning fiber placed before every slave laser. The lowest (non-amplified) beam is sent to the imaging setup, where further frequency-shifters are used to create imaging light resonant to different transitions at various magnetic fields. In the course of this work, we replaced the Zeeman slower beams as well as the MOT beams by the newly-developed laser source. A similar, slightly more different setup is used for cooling, trapping and manipulating ^{6}Li.

quantum statistics. Moreover, the interaction parameter at ultracold temperatures, the s-wave scattering length, is easily tunable for both species by applying a DC magnetic field in the vicinity of a Feshbach resonance [17]. The large width of these resonances, in addition to the light mass, adds up to the favourable properties of lithium for ultracold-atom experiments. However, the only Watt-level source for addressing the lithium D-line resonances at 671 nm are dye lasers, which are notoriously difficult to operate.

Atom interferometry

Atom interferometry allows experimental tests of the foundations of modern physics. It is direct evidence of the wave-particle duality in quantum mechanics [18–21]. The field takes advantage of the ultra-high degree of control achieved in atomic physics. Precise measurements of physical constants such as the gravitational constant G [22, 23] and the fine structure constant α [24, 25] stem from atom interferometers. Atom gravimeters have equaled classical falling corner-cube interferometers in terms of measurement precision of the local gravitational acceleration g [26, 27] and its gradient ∇g [28]. Refractive indices of gases for atomic wave packets were measured, as well as atomic

polarizabilities [29–31].

Atom interferometry relies on coherent splitting of atomic wave packets in either a Raman- or a Bragg scattering process by counter-propagating light waves. This yields a spatial splitting $\Delta\mathbf{r}$ due to the momentum distributed by the stimulated process of

$$\Delta\mathbf{r} = \frac{2\hbar\mathbf{k}}{m}t, \tag{1.3}$$

where $\mathbf{k}$ is the wave vector of the light used to drive the stimulated transition, m is the atomic mass, and t the waiting time after the coherent separation. When using Bragg scattering, transfer of the n-fold of the two photon momenta in Equation 1.3 to the atoms increases the spatial splitting and the sensitivity of the interferometer accordingly [32]. Transfer of 24 photon momenta was demonstrated in [32], requiring large laser power*. Since the absolute values of $\mathbf{k}$ and thus the D-line transition wavelengths of the alkalis are relatively similar, it is mostly the atomic mass which determines the spatial splitting.

Since lithium is the lightest of the alkali atoms, the large spatial splitting is particularly favorable, allowing the introduction of a septum electrode between the atomic beam paths in [33]. The laser source presented here was developed in collaboration with the lithium atom interferometry group of Jacques Vigué at the University of Toulouse [33–36]. A stable, continuous-wave, Watt-class laser is needed to achieve sufficient scattering amplitudes [36], thus an all-solid state laser would be a convenient replacement for the dye lasers currently used in the experiment, see Table 1.1.

Lithium isotope separation

Enrichment of the lighter lithium isotope ^{6}Li is of great importance for nuclear fission processes, see [37] for a review. Gaseous ^{6}Li in the chemical form of LiH is an efficient thermal neutron-getter, thus used to control the explosive power of fission bombs. Tritium, one of the constituents in the deuterium-tritium process, is bred from ^{6}Li under neutron bombardment. Tritium has a radioactive lifetime of 12.3 years and decays to ^{3}He, which can be collected from fission warheads. This is currently the only way to produce ^{3}He in significant amounts, a refrigerant necessary in scientific and security applications. It is planned to use the Deuterium-Tritium process in future fusion power plants.

The isotope separation method, initially intended for Uranium isotope separation using dye lasers, has been developed in the 1980s at Lawrence Livermore National Laboratory [38]. The diffusion isotope enrichment of ^{235}U (natural abundance: 0.7%) to plant-grade concentrations ($\sim$ 3%) or higher ($\sim$ 100% for nuclear fission bombs) normally requires many iterations because of the low selectivity. This can be overcome by applying a highly selective method, making the process less cost-extensive. The 6-eV ionization energy required for ionization of Uranium can be transferred in a three-step photo-ionization process using two intermediate atomic levels. The transition wavelengths are situated around 600 nm. The isotopic splitting of the transitions (larger than the Doppler width in an atomic jet) is sufficient to individually address

*In [32], an injection-locked Ti:Sa laser delivered 6 W of total output power at 852 nm for a cesium interferometer.

the isotopes. The ions can than be collected on a cathode inserted in the vacuum apparatus.

For isotope separation of lithium, a similar two-step photo-ionization method via the 2P state of atomic lithium has been presented in [39–41]. One first selectively excites ^{6}Li to the 2P state via the D-line transitions, from where it can be ionized using a UV laser, typically a frequency-quadrupled Nd:YAG laser [41]. The $D2$ transitions of ^{6}Li and $D1$ of ^{7}Li are almost frequency degenerate, and thus fall in the same Doppler peak at room temperature. The $D1$ line of ^{6}Li is well separated from the $D2$ line of ^{7}Li, see Figure 7.1, with a fine structure splitting of $\simeq 10\,\mathrm{GHz}$. Once ionized, the $^6\mathrm{Li}^+$ ions can covinently be separated from the atoms using electric fields, forming pure metallic ^{6}Li on the cathode. The maximum production rate $\dot{N}_{\mathrm{Li}-6}$ is identical to the D-line absorption rate and thus the laser photon flux φ_{ph} incident on the atoms, yielding

$$\dot{N}_{\mathrm{Li}-6} = \varphi_{\mathrm{ph}} = \frac{P}{\hbar\omega} \simeq 3.4 \times 10^{18}\mathrm{s}^{-1}\,, \tag{1.4}$$

or $39\,\mu\mathrm{g.s}^{-1}$, if the laser power $P = 1\,\mathrm{W}$. Thus, the production of 1 g of pure ^{6}Li takes $\simeq 8\,\mathrm{h}$ of continuous operation. A further important technical limitation comes from the need of a UV (laser) light source capable of delivering the same photon flux to ionize the excited lithium atoms.

Pump source for Cr:LiSAF lasers

Lasers based on the chromium-doped lithium strontium aluminum fluoride (Cr:LiSAF) gain material have raised as an inexpensive replacement of the common Ti:Sapphire lasers in both cw and pulsed operation [42]. The material offers emission from 780–990 nm, and 12-fs pulses have been be generated by the Kerr-lens mode-locking technique.

The main interest of this gain medium is the prominent absorption feature at 670 nm, allowing it to be pumped by inexpensive semiconductor lasers, as those presented in Section 1.2. Many of the frequency-doubled Nd:YVO_4 laser sources presented there were developed for that purpose. In contrast to these, the laser source developed in our work features the important advantages of transversal and longitudinal single-mode emission and high output power, which will yield better mode quality and stability of Cr:LiSAF laser emission.

1.2 Currently available 671-nm laser sources

The wavelength of the lithium D-line resonances (670.8 nm in air) currently restricts the choice of continuous-wave light sources to three different kinds of lasers: dye lasers, diode lasers and amplifiers and frequency-doubled solid-state lasers.

Dye lasers

Dye lasers have been a standard light source for atomic physics for several decades. They typically deliver Watt-level output power of monochromatic light in a diffraction-limited beam. The output power at a given wavelength depends on the combination

of pump source, dye and solvent, see for instance [43]. The emission spectrum is generally broadband, allowing it to easily reach the lithium D-line resonance frequencies. Although technologically well-mastered, dye lasers remain notoriously cumbersome to operate. The dyes are aging and need to be replaced frequently. Frequency stabilization is difficult because of the usage of the instable liquid dye solution in the form of a jet inside the laser cavity, and the occasional occurence of bubbles in it. The need for an expensive pump laser is a further drawback of this technology.

Table 1.1 gives an overview of current sources at 671 nm. The state-of-the-art pumping by a frequency doubled Nd:YAG laser emitting at a wavelength of 532 nm is not ideally suited for DCM [44], so the short-wave alternatives at 515 nm (frequency-doubled Ytterbium fiber laser) or 488 nm (Argon-ion laser) are preferable.

Source	**Pump**	**Dye (solvent)**[†]	**Output power**
Johnston *et al.* [43]	Ar-ion, 20 W @ 488 nm	DCM (AMX, BZ(5:1), COT)	3 W
Thomas group [45]	Ar-ion, 6-7 W @ 514.5 nm	LD688 (EPH)	900 mW
Vigué group [46]	Verdi, 4 W @ 532 nm	LD688 (EPH)	500 mW
Ketterle group [47]	Millenia X, 10 W @ 532 nm	LD688 (EPH)	500 mW
Radiant dyes [44]	Verdi, 10 W @ 532 nm	DCM	300 mW

TABLE 1.1: Comparison of dye lasers at 671 nm. Depending on the combination of dye, solvent and pump source, Watt-class output powers were demonstrated.

Semiconductor lasers

Diode lasers are used in many ultracold atom experiments. However, a frequency-stabilized diode laser typically delivers output powers in the ten-milliwatt range, insufficient for running today's experiments. Thus, the combination of master oscillators (MOs) with power amplifiers (PAs) have been developed, rendering the intrinsically simple systems more complicated in terms of design and maintenance effort. The current ^{7}Li diode-based laser setup of the experiment at ENS is presented in Fig. 1.1. The fact that currently 12 diodes are needed to cool both ^{6}Li and ^{7}Li to quantum degeneracy demonstrates the elaborateness of the scheme. We use low-cost laser diodes manufactured for DVD players (*HITACHI HL6545MG*), delivering up to 180 mW of laser power at the room temperature design wavelength of 660 nm. These diodes are heated up to 70°C in order to shift the laser wavelength to 671 nm. To generate all the beams needed for the experiment, amplification is achieved by injection-locking further diode lasers, using the same laser diode model. The typical power per beam is 120 mW, out of which typically $\lesssim 50\%$ are coupled to single-mode fibers. However, the heating significantly reduces the diode lifetime. In a different approach, 130 mW of output power were generated by using a broad emitter laser diode as a single-pass

[†]DCM = 4-dicyanomethylene-2-methyl-6-p-dimethylaminostyryl-4H-pyran; AMX = ammonyx LO (75%) and ethylene glycol (25%) used at 10°C; COT = cycloocta- tetraene; BZ = benzyl alcohol, EPH = 2-Phenoxyethanol

amplifier [48]. The required seed power was 9.6 mW, and magneto-optical trapping of atomic lithium was successfully demonstrated, with the drawback of lower stability and mode quality.

An alternative way to amplify the MO light, or even several nearby frequencies in the same spatial mode and polarization, is to use tapered amplifiers (TAs), see for instance [49]. At present, there is only one commercial TA available to amplify 671-nm light, the *TOPTICA TA-670-0500-5*. It delivers up to 500 mW of output power, the single-mode-fiber-coupling efficiency being $\lesssim 50\%$. Thus, for a standard ultracold atom experiment including a Zeeman slower and a MOT, several TAs are needed, as in the FerMix experiment at Laboratoire Kastler Brossel [50]. Its elevated price, the questionable future availability and the limited lifetime of ≈ 1 year add up to its disadvantages.

Frequency-doubled solid state lasers

Inherent to their design, all-solid-state lasers are amongst the most stable light sources in terms of power fluctuations, frequency stability and degradation. They can deliver hundreds of Watts of ultra stable single-mode output, see for instance [51, 52]. The same holds for nonlinear frequency conversion in crystals. It is thus desirable to develop suitable single-frequency lasers in the Watt-level output power range.

Light sources emitting at 671 nm based on intra-cavity frequency-doubling of the 1342-nm emission in Nd:YVO_4 or Nd:$GdVO_4$ have been realized previously [53–62]. Up to 9.5 W of cw multi-mode output radiation was demonstrated to date [62]. However, these lasers operate longitudinally multimode, and thus are not frequency-stabilized. A solid state single-frequency laser source delivering 920 mW at around 657 nm has been presented in [63]. Single-mode operation of frequency-doubled Nd:YVO_4 lasers yielded 671-nm output powers of 580 mW [64] and 680 mW [65]. The source of [65] was tuned to the lithium D-line resonance, yielding only $\sim$200 mW of output power, the most probable power limitation being the tilt-induced etalon loss. A development of an intracavity-frequency-doubled LBO-Nd:YVO_4 laser by CrystaLaser yielded up to 250 mW of output power, and is commercially available [66].

1.3 Alternative sources at 1342 nm

The D-line transitions of the alkali atoms, the most popular species in ultracold atoms experiments, are situated in the visible range[‡]. Most laser sources are capable to emit only in a narrow spectral range. Since many suitable laser transition wavelengths are in the infrared, frequency doubling of such sources is a popular means of generating light to cool and trap atoms. For example, commercial 1560-nm telecom-range fiber lasers are convenient light sources for Rubidium experiments after being frequency doubled to 780 nm [67]. In this section, some possible alternative laser sources at 1342 nm, suitable for frequency doubling to 671 nm, are presented.

[‡]The definition of the visible range is not very well fixed. The Cesium transitions at 852 nm and 894 nm are, however, excluded.

Nonlinear planar ring oscillators

Non-planar ring oscillators (NPROs) or monolithic isolated single-mode end-pumped ring lasers (MISERs) were developed in the 1980s [68] and are commercially available from *InnoLight GmbH*. They are used at Laboratoire Kastler Brossel for sum frequency generation of 589 nm light necessary for the sodium experiment [69]. They feature a monolithic ring cavity made from Nd:YAG. Unidirectionality is forced by the Faraday effect present in YAG, and polarization re-rotation and -selection is assured by the nonplanar design and the coating of the output face. The gain medium restricts the possible laser wavelengths to 1064 nm (max. 2 W output power) and 1319 nm (max. 800 mW output power). Post-amplified versions up to 42 W at 1064 nm are available. Due to the compact cavity design, the mode spacing is large enough to assure single-mode behavior without additional intra-cavity etalons. Tunability is realized by changing the laser crystal temperature (slow timescale) and squeezing the crystal using a piezoelectric transducer (fast). The laser linewidth and amplitude noise characteristics are excellent [70].
To our knowledge, there were no developments for obtaining 1342-nm emission from NPROs. The prominent gain media emitting at 1342 nm are Nd:YVO_4 and Nd:$GdVO_4$. They both have a birefringent nature, questioning the possibility to realize the NPRO concept using these crystals. An alternative solution might be the use of Nd:YAG, employing its temperature-dependent shift of weak 1338 nm emission line.

Semiconductor lasers

Diode lasers emitting in the O-band (see section 1.3) are commercially available. Most commercial sources emit near 1310 nm at room temperature and use InGaAsP as the active medium. Output powers of nearly-diffraction-limited (Fabry-Perot) diodes reaches up to 300 mW.[§].

Assuming a standard wavelength dependence of $\partial\lambda/\partial T = 0.3\,\mathrm{nm.K^{-1}}$, one needs to heat such diodes to 120°C to push the emission wavelength to 1342 nm. However, heating to elevated temperatures significantly decreases the lifetime of laser diodes, see section 1.2. For test purposes, we bought the *Mitsubishi ML725B8F* laser diode, specified to emit 10 mW in the 1310-nm telecom range at a driving current of $I_\mathrm{d} = 25$ mA. Using a simple homemade spectrometer build of a 1200-lines/mm blazed grating and a 1-arcmin resolution turntable, we determined $\frac{\partial\lambda}{\partial T}$ to $0.38\,\mathrm{nm.K^{-1}}$. At 95°C and $I_\mathrm{d} = 40$ mA, the diode was emitting 5 mW at 1342 nm. When using the diode in an extended cavity diode laser, the output may be sufficient to seed a solid-state, semiconductor or fiber amplifier, which remains to be developed. Unfortunately, there are no commercial semiconductor tapered amplifiers available around 1300 nm.

Fiber lasers

Fiber lasers have become a powerful alternative to solid-state designs for many applications. Offering diffraction-limited emission at the highest output powers and power conversion efficiencies, they keep a compact, rugged design. Efficient heat removal even

[§]For instance, the *Thorlabs FPL1053T* diode is capable to deliver 300 mW at 1310 nm.

at the highest power levels is simple due to the large surface-to-volume ratio and completely fibered setups are possible when using fiber Bragg gratings as cavity mirrors. Kilowatt-level longitudinal-multi-mode output powers are available in a TEM_{00} mode [71]. Linearly polarized and SLM sources are available. In the domain of quantum gases, they play an important role as optical-dipole-trap lasers.

Most of the developments were made around 1064 nm (neodymium and ytterbium doped fiber lasers) and in the 1530-nm–1565-nm C-band telecom range ("conventional band", Erbium lasers). There are fewer sources available for the O-band ("original band") between 1260 nm and 1360 nm, where fiber losses are higher and erbium ions display no gain. However, dispersion is lower, which is important for telecom applications.

Glasses display a stochastic spatial structure. Thus, in contrast to laser crystals, most laser transitions are strongly broadened, yielding large pump and oscillation bandwidths. Nd-doped fiber lasers can be conventionally pumped around 800 nm using laser diodes. Broad gain curves including 1342 nm were reported [72–74]. Another possible dopant ion is dysprosium, which lases between 1300 nm and 1400 nm and can be pumped at 1064 nm [75]. Praseodymium ions in fluorozirconate fibers can lase at 1342 nm and be pumped by an Yb laser at around 1000 nm [76].

Due to the large interaction length at high intensities, Raman fiber lasers can be realized easily. A remarkable property of this kind of laser source is the spectral narrowness of the sources as compared to the pumps, which can be several nanometers wide. For the domains of cold atoms and astronomy, a sodium *D*-line source is commercially available from *TOPTICA Photonics AG*. It consists of a Raman fiber laser emitting at 1178 nm, which is subsequently frequency doubled using LBO. Up to 50 W of output power have been generated using this technology [77]. The required pump wavelength for a simple Raman shift of 15 THz in silica [78] from 1342 nm is around 1200 nm, a wavelength where for instance semiconductor disk lasers are available. Both normal and Raman gain are present in Bismuth-doped fiber lasers. Absorption and gain spectra depend on the fiber composition, and are generally wide [78–80]. 2.5 W of output power at 1330 nm were demonstrated [81], pumped at 1230 nm by another Raman laser [81]. Pumping at around 800 nm is possible without Raman gain [82].

A similar Raman source of 1.3 W at 1320 nm was presented in [83] by using a two-step Raman conversion in SiO_2 and P_2O_5 when pumped at 1064 nm. To extend this scheme to emission at 1342 nm, one would thus have to either find a different material composition offering the required Raman shift from a 1064-nm pump laser or change the pump wavelength. Based on the Raman shifts presented in [83], we infer a required pump wavelength of 1075 nm. Appropriate commercial sources are readily available in the form of ytterbium fiber lasers, as used for the dipole trap laser in the lithium experiment at ENS, presented in Part II of this thesis.

Optical parametric oscillators

Based on the rapid development of nonlinear optical devices, optical parametric oscillators (OPOs) have been realized in a large variety, both in pulsed and cw configurations, see for instance [84]. In a photon picture, they annihilate a pump photon and create two photons, whose energies are determined by energy conservation. Thus, they can

in principle generate any frequency which is below that of the pump.

Due to their enormously wide tunability, these sources feature countless applications from spectroscopy to pumping lasers and creation of all kinds of to-date-not-delivered wavelengths to generation of squeezed light and blinding infrared sensors, see for instance [64]. Phase-coherent linking near- and mid-infrared frequencies was demonstrated [85]. In the domain of atomic clocks and quantum gas experiments, they can serve to generate cooling and pumping wavelengths of exotic species, and "magic" or "anti-magic" wavelengths in optical lattices [86].

Continuous-wave OPOs (cw-OPOs) capable of producing single-frequency radiation close to 1342 nm are available commercially, as presented in Table 1.2. Typically pumped by a solid-state or a fiber laser at 1064 nm, these designs are singly-resonant, only resonating the signal wave. This concept leads to a very stable operation, and the decoupling of the signal frequency fluctuations from those of the pump. The major disadvantage of OPOs is the need for an expensive pump laser. Most often, periodically-poled lithium niobate (ppLN) is used as a nonlinear medium, featuring a large nonlinear coefficient (see Table 3.1) and negligible absorption in the infrared range. Only minor modifications in the poling period and the coatings of the optical components should be necessary to extend the multi-Watt oscillation wavelength range to 1342 nm. The corresponding idler wavelength of 5136 nm is in the transparency range of stoichiometric lithium niobate, see Table 3.1. By replacing the 1064-nm pump by a 1030-nm ytterbium fiber laser, the idler wavelength can be shifted to 4430 nm, and even further to the blue using the ytterbium 975-nm emission line, if the idler absorption should pose a problem.

cw-OPO source	**Signal emission range in μm**	**Idler emission range in μm**	**1.5-μm output power**
Linos OS 4500 [87]	1.38 – 2	2.28 – 4.67	20 mW
Kovalchuk thesis [88]	1.50 – 1.82	2.56 – 3.66	24 mW
Lockheed Martin Argos 2400-SF-15 [89]	1.46 – 1.98	2.3 – 3.9	1 W – 5 W
APE/Coherent/PTB cw-OPO project¶	1.43 – 1.87	2.47 – 4.16	4 W

TABLE 1.2: Comparison of cw-OPO sources near 1342 nm. The models printed in italic are commercially available.

More recently, cw-OPOs pumped at 532 nm by frequency-doubled Nd:YAG lasers were developed [90–93]. Nonlinear materials used are ppMgO:LN, ppSLN, ppKTP and ppSLT, and signal emission is in the red part of the visible spectrum. While having the advantages of OPO designs (wide tunability, spectral characteristics of the pump source), these designs are plagued by thermal effects in the nonlinear crystals and thus currently restricted to several-100 mW of output power. Another alternative approach is presented in [94], where an IR OPO is intra-cavity frequency doubled by a second nonlinear crystal. Several 100 mW were produced in the red wavelength region.

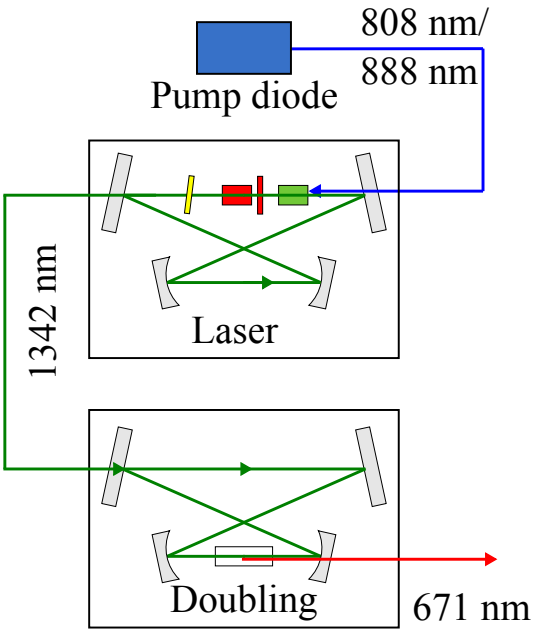

FIGURE 1.2: Schematic view of the laser system. Shown are two separate cavities, the laser and the doubling cavity. The pump diode output (blue) is focused in the Nd:YVO_4 laser crystal (green) inside the laser cavity. It furthermore contains a Faraday rotator and a $\lambda/2$-waveplate for unidirectional oscillation (both red) and two etalons (yellow) for frequency selection. The doubling cavity contains a nonlinear crystal (white) for second-harmonic generation.

1.4 General design of the laser source and outline of Part I

After consulting the possible routes to produce Watt-class single-mode output power presented before, we decided for an all-solid-state laser design using a Nd:YVO_4-based infrared laser and resonant doubling in an external buildup cavity. The overall design of the laser source is schematically represented in Fig. 1.2. It consists of a diode-pumped Nd:YVO_4 single-mode laser emitting at 1342 nm which is subsequently frequency-doubled in an external buildup cavity to produce light of 671-nm wavelength.

In Chapter 2, the Nd:YVO_4 laser will be described in detail. For pumping the active medium, we use a 808-nm-emitting, fiber-coupled diode stack whose output is focused into the laser crystal. The bow-tie cavity is formed by four mirrors, out of which two are spherically shaped to provide a stable, Gaussian cavity eigenmode. One of the two flat mirrors is used to pass the pumping light to the laser crystal, whereas the second flat mirror serves as the output coupler. To realize a single-longitudinal-mode (SLM) laser it is favorable to use a traveling-wave ring resonator. Unidirectionality is established by combining a Faraday rotator and a $\lambda/2$-wave plate, and the uniaxial laser crystal working as a polarizer. SLM operation and coarse tuning are provided using two intra-cavity etalons.

¶Co-developed by the author in the context of an internship at *APE Applied Physics and Electronics GmbH*.

As we will discuss in Chapter 3, the laser emission is mode-matched to the external doubling cavity. We again employed a unidirectional bow-tie design. Two mirrors are spherically shaped to create a focused Gaussian beam in the nonlinear crystal. One of the flat mirrors is partially transmitting, and thus used for in-coupling of the 1342-nm light. Periodically-poled potassium titanyl phosphate (ppKTP) is used for frequency doubling of the resonated radiation. For the manufacturing of the periodically-poled, nonlinear crystals, a collaboration was established with the group of Carlota Canalias at the Department of Applied Physics at Royal Institute of Technology in Stockholm, Sweden.

In Chapter 4, we will present the locking scheme to guarantee efficient second-harmonic conversion and frequency stability. A small part of the 671-nm emission from the doubling cavity is used for creating an FM-spectroscopy error signal in order to lock the cavity's resonance frequency to the laser emission wavelength via a feedback circuit. Another small part of the frequency-doubled light is employed for Doppler-free spectroscopy in a lithium vapor cell. A second feedback circuit regulates the laser emission frequency with respect to the spectroscopic lines, with an offset frequency adjustable by a double-pass acousto-optical modulator. Furthermore, Chapter 4 presents a detailed characterization of the 671-nm output light. Special emphasis is given on measuring the long-term behavior and day-to-day operation of the laser system. Finally, the implementation in the lithium experiment is described, and the first results using the laser for the Zeeman slower and the MOT are presented.

In Chapter 5, we will conclude on the first part of this thesis. A part of the material presented here was published in [95].

Chapter 2

Diode-pumped all-solid-state Nd:YVO_4 laser source

In the preceding chapter, we have presented the concept of our novel all-solid-state 671-nm laser source. In this chapter, we will discuss in detail the fundamental pump source at 1342 nm.

In this chapter, the 1342-nm laser will be presented. In Section 2.1 the Nd:YVO_4 gain medium will be introduced. We will discuss the absorption and emission spectra and detail on the thermo-optical properties whose consideration becomes necessary when designing a high-power laser system. In Section 2.2 we will present the theoretical concepts necessary for designing the laser resonator. We will detail on thermal effects and present the final design following these considerations. In Section 2.3, we will describe the method of introducing a Faraday rotator and two intra-cavity etalons to force unidirectional single-longitudinal-mode operation of the laser. We will motivate the use of a special high-field magnet design for the Faraday rotator and detail on losses introduced when tilting intra-cavity etalons. In Sections 2.4 and 2.5 we will present measurements of the output power, the output spectrum and the spatial mode. Finally, in Section 2.6 we will summarize the chapter.

A three-dimensional view of the most important parts of the mechanical setup is given in Figure 2.1.

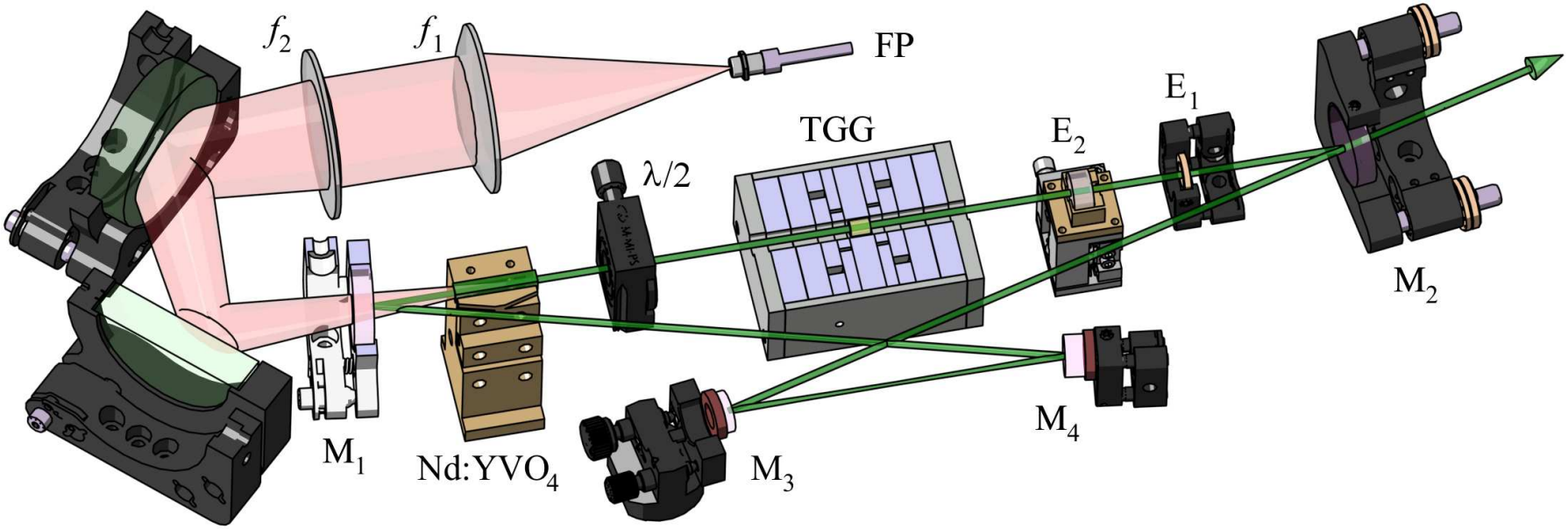

FIGURE 2.1: The laser setup, consisting of the fiber coupled pump source FP, two pump focusing lenses $f_{1,2}$, the cavity mirrors M_{1-4} and the Nd:YVO_4 active medium. The $\lambda/2$ wave plate and the TGG Faraday crystal in a magnet ensemble impose unidirectional oscillation, whereas two etalons $E_{1,2}$ establish single-mode operation and tunability. The optical path of the generated laser beam is depicted in green. For some mechanical components (mirror mounts, Nd:YVO_4 mount, TGG magnets and E_2 mount) we show a sectional view to improve visibility of the beam path. The distance between M_1 and M_2 is 295 mm. For a schematic drawing of the resonator setup see Figure 2.7.

2.1 The Nd:YVO_4 gain medium

Neodymium-doped yttrium (ortho-) vanadate (Nd:YVO_4) is a popular gain medium for both continuous wave (cw) and pulsed lasers. It has several desirable properties, the most important being the strong emission line at the desired wavelength of 1342 nm. It is being employed in many solid-state lasers and it is thus an inexpensive material available from stock from many companies. Figure 2.2 shows a simplified level scheme of the neodymium ion in the YVO_4 host material. We make use of the ${}^4F_{3/2} \rightarrow {}^4I_{13/2}$ transition, corresponding to the 1342 nm emission. In this Section, we will present the most important properties of the Nd:YVO_4 crystal.

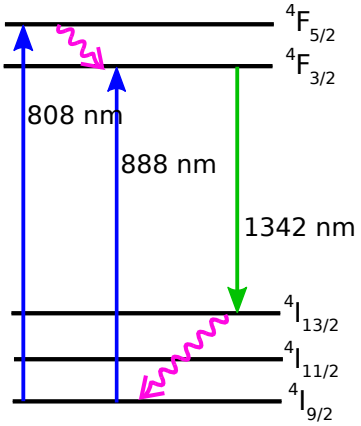

FIGURE 2.2: The simplified level scheme of the neodymium ion (Nd^{3+}). The straight lines represent photonic transitions, whereas the undulated lines denote vibrational transitions. The respective wavelengths are found in Nd:YVO_4. We will operate the laser source on the ${}^4F_{3/2} \rightarrow {}^4I_{13/2}$ transition, corresponding to 1342 nm output. Two pumping schemes to the metastable ${}^4F_{3/2}$ level are indicated, where the 808 nm transition shows significantly more absorption but also a higher contribution to heating per cycle.

2.1.1 Crystal strucure

The crystal structure of YVO_4 is of the Zircon type, see Figure 2.3. As such, it is an optically uniaxial material. Its axes are commonly termed a-,a- and c-axis. Synonyms for the c-axis are p-, π-, o- and $\|$-direction, whereas the a-axis is sometimes called s-, σ-, e- or $\perp$ axis. The axis vectors form an orthogonal system. The projection of the optical surface normal vector on the crystal axes determines the notation of the way the crystal is cut. We use a-cut crystals, meaning that we can access both the a- and c-axis by rotating the polarization of a linearly polarized beam passing the crystal.

The value for neodymium doping is commonly given in at. %, meaning that the corresponding percentage of Yttrium ions is replaced by neodymium ions. Typical values are from 0.1–3 at. %. One choses the doping such that requirements for pump absorption per unit length with respect to heating are satisfied, see Section 2.2.3.

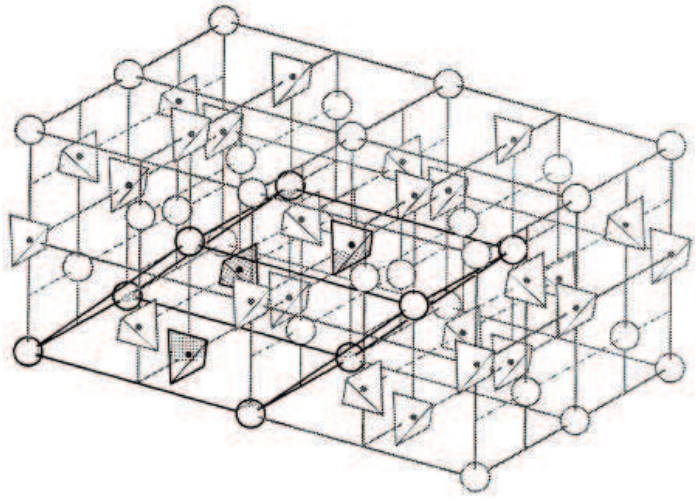

FIGURE 2.3: Crystal structure of YVO_4, which is of the zircon type, from [96]. The tetrahedra represent the VO_4^{-3} ions, balls are Yttrium atoms. The unit cell is marked in bold lines.

2.1.2 Absorption

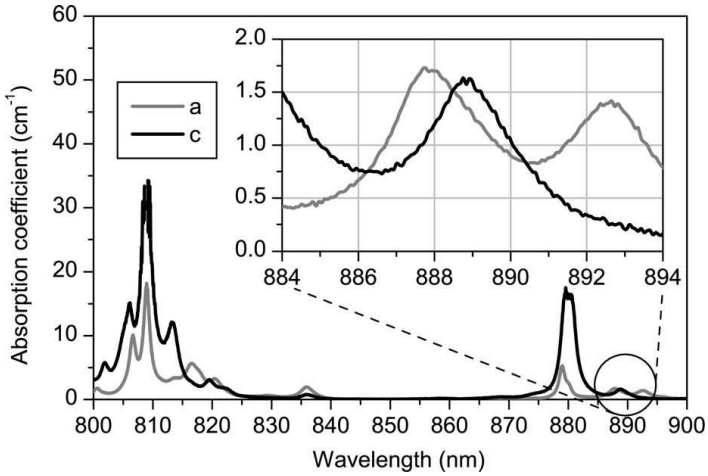

FIGURE 2.4: Absorption spectrum of 1 at. % Nd:YVO_4 for both crystal axes, from [97]. The material presents several absorption bands at 808 nm, 880 nm and 888 nm, the latter being almost polarization-independent.

One of the requirements for a gain medium is convenient pumping. We opted for laser-diode end pumping. This means that the pump beam propagates collinear to the laser beam in the active medium and provides high efficiencies. It is feasible due to the availability of bright pump sources. The absorption spectrum is shown in Figure 2.4, as published in [97]. It was measured for 1 at. % Nd:YVO_4. In the limit of small doping and thus negligible mutual influence of the neodymium ions, the absorption coefficient will scale linearly with doping.

The measurement was done for both polarizations, the values for the c-axis being significantly higher than those for the a-axis over almost the whole range. One notices several absorption bands around 808 nm, as well as two bands at 880 nm and 888 nm, conveniently addressable by commercially available laser diode stacks. When pumping at 808 nm, where the absorption coefficient has its maximum, the pump diode stacks typically need temperature stabilization in order to stabilize the emission wavelength to match the relatively narrow absorption feature.

Laser diode stacks for pumping applications are in general coupled to non-polarization-maintaining multi-mode optical fibers, facilitating handling and optical design and improving stability and ruggedness of the whole setup. The 888-nm absorption line is quasi-polarization-insensitive, which is favorable when using these pump sources, as the radiation emitted from these fibers is typically randomly polarized. Another important advantage of working at 888 nm, especially for high-power designs, is the higher quantum yield, meaning that a larger relative part of the pump photon energy is converted to laser photon energy. Thus, less pump energy is converted to heat, leading to significantly reduced thermal problems, see Section 2.2.

2.1.3 Emission

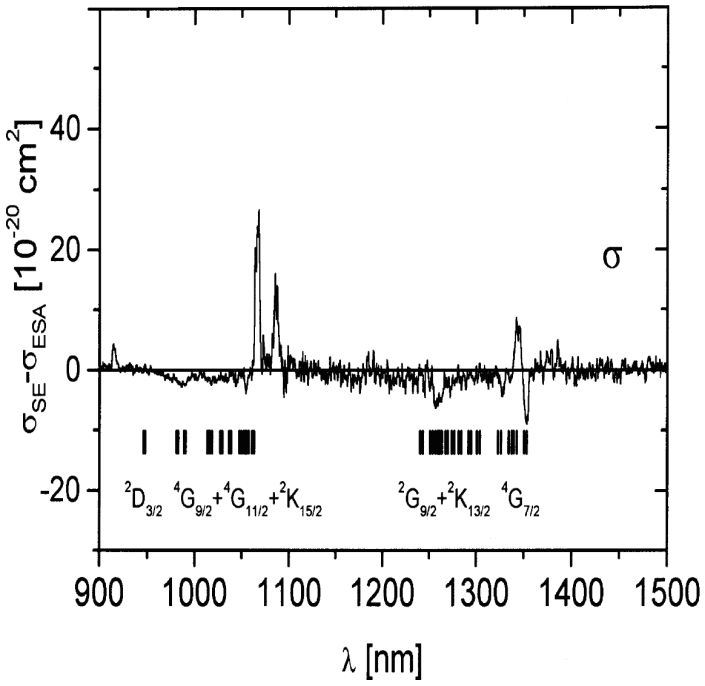

FIGURE 2.5: Nd:YVO_4 emission spectrum, c-axis, from [98]. One notices the two prominent features around 1064 nm and at 1342 nm. The spectral resolution is 2.5 nm.

The emission spectrum was measured in [98] and is presented in Figure 2.5. σ_{em} is the stimulated-emission cross section and σ_{ESA} is the cross section for absorption of light by excited ions, the so-called excited-state absorption (ESA). In a measurement as conducted in [98], one naturally measures the difference $\sigma_{\text{em}} - \sigma_{\text{ESA}}$, which is the quantity presented in the figure.

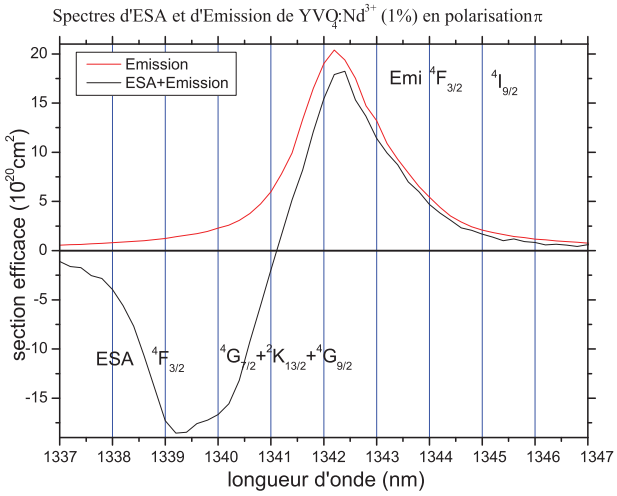

FIGURE 2.6: High-resolution 1342 nm emission peak data on the c-axis, measured by the group of R. Moncorgé [99]. At $2\lambda_{\mathrm{Li}}$ we infer an emission cross-section of $\sigma_{\mathrm{em}}(2\lambda_{\mathrm{Li}}) = 12 \times 10^{-20}\,\mathrm{cm}^2$ and an excited-state absorption cross-section of $\sigma_{\mathrm{ESA}}(2\lambda_{\mathrm{Li}}) = 3 \times 10^{-20}\,\mathrm{cm}^2$

.

Property	**Value**	**Ref.**
Typical doping	1 at.%	[100]
Atomic Density N	$2.48 \cdot 10^{26}\mathrm{m}^{-3}$	[101]
Absorption coefficient α_{abs}	35 cm^{-1} @ 808 nm	[97]
Absorption length	0.14 mm @ 808 nm	[100]
Absorption cross section	$60{\cdot}10^{-24}\,\mathrm{m}^2$ @ 808 nm	[101]
Intrinsic Loss	0.16% cm^{-1}	[102]
Peak stimulated emission cross section $\sigma_{\mathrm{em,max}}$	$18 \times 10^{-20}\,\mathrm{cm}^2$	[99]
Peak excited-state absorption cross section $\sigma_{\mathrm{ESA,max}}$	$18 \times 10^{-20}\,\mathrm{cm}^2$	[99]
Stimulated emission cross section $\sigma_{\mathrm{em}}(2\lambda_{\mathrm{Li}})$	$15 \times 10^{-20}\,\mathrm{cm}^2$	[99]
Excited-state absorption cross section $\sigma_{\mathrm{ESA}}(2\lambda_{\mathrm{Li}})$	$3 \times 10^{-20}\,\mathrm{cm}^2$	[99]
Upper-state radiative lifetime τ_{rad} (doping-dependent)	$50 - 110\,\mu$s	[103]
Upper-state radiative lifetime τ_{rad} (for 0.2 at.%)	110 μs	[103]
Upper-state fluorescence lifetime τ_{fl}	120 μs	[103]
Gain bandwidth	1.7 nm $\widehat{=}$ 280 GHz	[99]
Breakage stress	51 MPa	[1]
Refractive index temperature derivative $\mathrm{d}n/\mathrm{d}T$ (c-/a-axis)	$(8.5/2.9) \times 10^{-6}\,\mathrm{K}^{-1}$	[100]
Refractive index temperature derivative $\mathrm{d}n/\mathrm{d}T$ (c- and a-axis)	$3 \times 10^{-6}\,\mathrm{K}^{-1}$	[1]
Thermal conductivity κ (c-/a-axis)	$(5.23/5.10)\,\mathrm{W.K}^{-1}.\mathrm{m}^{-1}$	[100]

TABLE 2.1: Important material parameters of Nd:YVO_4. All values are for typical doping of 1 at.% and c-polarization, if not stated otherwise.

One notices the two features at around 1 μm and 1.3 μm typical for the neodymium ion. ESA causes dips in the emission spectrum in Figure 2.5 and has deleterious effects on laser emission. The spectral resolution of the data from [98] is only 2.5 nm. Thus, our collaboration partners from Toulouse asked the group of R. Moncorgé* to perform a more precise measurement around 1342 nm. The result is shown in Figure 2.6 and has a significantly improved spectral resolution of 0.5 nm. The value for the stimulated-emission cross section at twice the lithium vacuum wavelength,

$$2\lambda_{\mathrm{Li,vac}} = 2 \times 670.96\,\mathrm{nm} = 1341.92\,\mathrm{nm}\,, \tag{2.1}$$

is close to the peak value and can be estimated to $\sigma = 15 \times 10^{-20}\,\mathrm{cm}^2$. In the important range, the cross section is always higher for c-polarization, which is why we chose this axis as the polarization axis of the laser.

Another important spectroscopic property for a laser medium is the metastable state lifetime τ. Since the small-signal gain is proportional to the product $\sigma_{\mathrm{em}}\tau$, it is favorable to have long a lifetime. It strongly depends on density-induced fluorescence quenching and thus on doping, see [103] and references therein. For low-doped crystals ($\leq 0.4\,at.\,\%$) it yields $\tau = 110\,\mu$s, whereas the fluorescence lifetime (due to purely radiative decay) yields $\tau_{\mathrm{f}} = 120\,\mu$s. In Table 2.1 we list further important material parameters of Nd:YVO_4.

2.2 Laser theory

In this section, a brief overview of the theory of laser emission is given from the viewpoint of laser design optimization. We will start with the description of the propagation properties of Hermite-Gaussian beams to describe cavity eigenmodes. We will give analytic expressions for the output power of solid-state lasers and thermal effects occurring in the gain material. Finally, the resulting geometric design of the cavity is presented.

2.2.1 Hermite-Gaussian beams

Laser beams can be described by Hermite-Gaussian beams, see for instance [104, 105]. These form a complete basis of solutions of the paraxial Helmholtz equation for the electric field $\mathbf{E}(\mathbf{r},\mathrm{t})$ along the z-axis,

$$\left(\frac{\partial^2}{\partial x^2} + \frac{\partial^2}{\partial y^2} - 2\mathrm{i}k\frac{\partial}{\partial z}\right)\mathbf{E}(\mathbf{r},t) = 0 \tag{2.2}$$

with the wave number $k = 2\pi/\lambda$ and λ the wavelength. The general solution can be expanded on a basis of decoupled solutions

$$\mathbf{E}(\mathbf{r},t) = E_0\,\mathbf{n}\,u_l(x,z)\,u_m(y,z)\,\mathrm{e}^{-\mathrm{i}(kz-\omega t)}\,, \tag{2.3}$$

where E_0 is the field amplitude and $\mathbf{n}$ the normalized polarization vector. The eigenfunctions $u_l(x,z)$ and $u_m(y,z)$ for both transversal directions are identical. We will

*CIMAP, Université de Caen, France

thus in the following restrict ourselves to the x-coordinate. The corresponding equations for the y-coordinate are obtained by replacing the respective coordinate-index pair. The solution reads

$$u_l(x,z) = \left(\frac{2}{\pi}\right)^{\frac{1}{4}} \left(\frac{\exp\left(\mathrm{i}(2l+1)\varphi_x(z)\right)}{2^l l! w_x(z)}\right)^{\frac{1}{2}} H_n\left(\frac{\sqrt{2}x}{w_x(z)}\right) \exp\left(-\mathrm{i}\frac{kx^2}{2R_x(z)} - \frac{x^2}{w_x^2(z)}\right). \tag{2.4}$$

where $H_l\left(\frac{\sqrt{2}x}{w_x(z)}\right)$ is the Hermite polynomial of order l, $R_x(z)$ is the wavefront radius of curvature and $w_x(z)$ is the characteristic radius of the beam along direction x at z. It reads

$$w_x(z) = w_{0,x}\sqrt{1 + \left(\frac{z}{z_{\mathrm{R},x}}\right)^2}, \tag{2.5}$$

with the Rayleigh length $z_{\mathrm{R},x}$. The smallest value is obtained at $z = 0$, the waist of

$$w_{0,x} = \sqrt{\frac{\lambda z_{\mathrm{R},x}}{\pi}}. \tag{2.6}$$

$\varphi_x(z)$ is the so-called Gouy phase and reads

$$\varphi_x(z) = \arctan\left(\frac{z}{z_{\mathrm{R},x}}\right). \tag{2.7}$$

To describe the evolution of a beam propagating along z, we introduce the complex beam propagation parameter

$$q_x = z + \mathrm{i}z_{\mathrm{R},x}\,, \tag{2.8}$$

where z is the distance from the beam focus position and $z_{\mathrm{R},x}$ the Rayleigh length, where the radius of curvature $R_x(z)$ becomes minimal. The evolution of a Hermite-Gaussian beam passing through linear optical components can now be described by applying $ABCD$-matrices known from ray matrix propagation, according to the following identity:

$$q'_x = M_x * q_x \equiv \frac{A_x q_x + B_x}{C_x q_x + D_x}\,, \tag{2.9}$$

The matrices

$$M_x = \begin{pmatrix} A_x & B_x \\ C_x & D_x \end{pmatrix} \tag{2.10}$$

for standard components are readily tabulated in literature, see for instance [104, 105]. M_x can represent complete optical systems, and is created via matrix multiplication from the left for consecutive elements.

For finding the eigenmode of an optical resonator, one has to calculate the resonator matrix M_x for the two axes first. The condition for an eigenmode is self-similarity after one resonator round-trip:

$$q'_x = M_x * q_x \equiv q_x\,, \tag{2.11}$$

We define the stability parameter $p_{\mathrm{stab};x,y}$:

$$p_{\mathrm{stab},x} = \frac{A_x + D_x}{2}\,. \tag{2.12}$$

Only in the range

$$-1 < p_{\mathrm{stab},x} < 1\,, \tag{2.13}$$

can a stable cavity eigenmode exist. The stability criterion not only implies existence of eigenmodes, but also the decay of small perturbations [104].

Cavity resonance condition and Gouy Phase Shift

A laser will operate very close to the laser cavity resonance. This means that the laser beam will reproduce itself after one cavity round-trip both in terms of the transverse profile, as demonstrated before, and in terms of the phase. This condition yields for the total phase φ_{tot} acquired after one round-trip

$$\varphi_{\mathrm{tot}} \equiv 2\pi b\,, \tag{2.14}$$

with $b \in \mathbb{N}$ the longitudinal mode index. Also, higher cavity eigenmodes (TEM_{nm}), corresponding to $n, m > 0$, may occur. A Hermite-Gaussian beam experiences the so-called Gouy phase shift $\varphi_{l;x}$ compared to a plane wave of the same wavelength, see [104] and Equation (2.4):

$$\begin{aligned} \varphi_{l,x}(z) &= \left(l + \frac{1}{2}\right) \varphi_x(z) \\ &= \left(l + \frac{1}{2}\right) \arctan\left(\frac{z}{z_{\mathrm{R},x}}\right)\,, \end{aligned} \tag{2.15}$$

and for m, y similarly and $\varphi_x(z)$ as in Equation (2.7), yielding a total phase shift of

$$\varphi_{lm}(z) = \varphi_{l,x}(z) + \varphi_{m,y}(z)\,. \tag{2.16}$$

The optical path length in a cavity is defined as

$$L_{\mathrm{opt}} = \sum_i n_i t_i\,, \tag{2.17}$$

with the geometrical path lengths t_i between optical elements and their respective refractive indices n_i. The resonance criterion thus becomes

$$k_{lm} L_{\mathrm{opt}} + \varphi_{lm}(L_{\mathrm{opt}}) + \varphi_{\mathrm{off}} \equiv 2\pi b\,, \tag{2.18}$$

with the residual phase term φ_{off} due to mirrors, coatings etc., which is assumed constant for all eigenmodes. The wavenumber k_{lm} is

$$k_{lm} = \frac{2\pi}{\lambda_{lm}} = \frac{2\pi\nu_{lm}}{c}\,, \tag{2.19}$$

where c is the speed of light. The resonance condition then becomes

$$k_{lm} = \frac{1}{L_{\mathrm{opt}}}\left(2\pi b - \varphi_{lm}(L_{\mathrm{opt}}) - \varphi_{\mathrm{off}}\right)\,. \tag{2.20}$$

For the eigenfrequencies, this yields

$$\nu_b = b\nu_{\mathrm{FSR}} + \nu_{\mathrm{off}} \,. \tag{2.21}$$

The frequency spacing between neighboring longitudinal modes of identical transversal quantum numbers l, m is

$$\nu_{\mathrm{FSR}} = \frac{c}{L_{\mathrm{opt}}} \,, \tag{2.22}$$

and is commonly termed the free spectral range in the literature. Let us finally consider the frequency difference $\Delta\nu_{\Delta l \Delta m}$ between Hermite-Gaussian modes at fixed b:

$$\Delta\nu_{\Delta l \Delta m} = \frac{c}{2\pi L_{\mathrm{opt}}} \varphi_{\Delta l \Delta m}(L_{\mathrm{opt}}) \,, \tag{2.23}$$

where $\Delta l = l - l'$ and $\Delta m = m - m'$ for two modes with indices l, m and l', m', respectively. This result means that in the general case, Hermite-Gaussian resonator eigenmodes of different order are not frequency degenerate. We can advantageously make use of this result for coupling to the TEM_{00} mode of the doubling cavity, as will be described in Chapter 3.

2.2.2 Laser output power

One of the most important design parameters of a laser is its output power. Since a Watt-level output is desired for the laser presented here, this point is crucial in the design process. For a diode-pumped solid-state laser emitting at frequency $\nu = \omega/2\pi$, the output power P_{out} is [106–109]

$$P_{\mathrm{out}} = \max\left[\eta_{\mathrm{sl}} \left(P_{\mathrm{abs}} - P_{\mathrm{thr}}\right), 0\right] \,, \tag{2.24}$$

where the slope efficiency is defined as

$$\eta_{\mathrm{sl}} = \frac{\partial}{\partial P_{\mathrm{p}}} P_{\mathrm{out}} = \frac{\mathcal{T}}{\mathcal{L}} \eta_{\mathrm{p}} \eta_0 \,. \tag{2.25}$$

P_{p} is the pump power incident on the gain medium. $\mathcal{T}$ is the output coupler power transmission and $\mathcal{L}$ is the total round-trip loss

$$\mathcal{L} = \mathcal{L}_{\mathrm{pass}} + \mathcal{T} \,, \tag{2.26}$$

where $\mathcal{L}_{\mathrm{pass}}$ contains all the passive round-trip losses. The overall pump efficiency (often termed quantum yield in literature) is given as

$$\eta_{\mathrm{p}} = \frac{\omega}{\omega_{\mathrm{pump}}} \,, \tag{2.27}$$

with the pump frequency in radians $\omega_{\mathrm{pump}} = 2\pi\nu_{\mathrm{pump}}$. The overlap integral

$$\eta_0 = \frac{\left(\int \mathrm{d}V s_{\mathrm{l}}(\mathbf{r}) s_{\mathrm{p}}(\mathbf{r})\right)^2}{\int \mathrm{d}V {s_{\mathrm{l}}}^2(\mathbf{r}) s_{\mathrm{p}}(\mathbf{r})} \tag{2.28}$$

contains the power-normalized spatial distributions $s_\mathrm{l}(\mathbf{r})$ and $s_\mathrm{p}(\mathbf{r})$ of the laser and pump beams, respectively. P_abs is the pump power absorbed in the gain medium and l_med its length. We have

$$P_\mathrm{abs} = (1 - \mathrm{e}^{-\alpha_\mathrm{abs} l_\mathrm{med}}) P_\mathrm{p}\,, \tag{2.29}$$

where α_abs is the linear absorption coefficient for the pump radiation. Equation 2.30 furthermore contains the pump power at lasing threshold[†]

$$P_\mathrm{thr} = \frac{I_{sat}}{\eta_\mathrm{p} l_{med}} \mathcal{L} V_\mathrm{eff}\,, \tag{2.30}$$

The saturation intensity is defined here as

$$I_\mathrm{sat} = \frac{\hbar\omega}{\sigma_\mathrm{em}\tau_\mathrm{rad}}\,, \tag{2.31}$$

with the emission cross section σ_em and excited state lifetime τ_rad, both to be determined spectroscopically, as presented in Section 2.1. We further have

$$V_\mathrm{eff} = \left(\int \mathrm{d}V\, s_\mathrm{l}(\mathbf{r}) s_\mathrm{p}(\mathbf{r}) \right)^{-1}\,. \tag{2.32}$$

Optimizing the pump mode for maximum output power in equation (2.30) results in a narrow, ideally delta-peak-shaped distribution, which is both impossible to realize experimentally and unfavorable in the presence of any realistic active medium, as we will see in the next section.

2.2.3 Thermal effects in solid-state lasers

The most important effect restricting the scaling of diode-pumped solid-state laser designs to higher output power is the presence of thermal effects in the active medium. Absorption of pump light leads to local heating caused by phononic transitions, see for instance Figure 2.2 for a typical example of a four-level laser medium. The first relaxation process is from the highest excited state, where the system is pumped, to the metastable intermediate state, where the population inversion is created. After stimulated or spontaneous emission of a photon, the ions relax to an intermediate state in the case of four-level lasers, and from there phononically to the ground state.

A review on thermal effects in laser crystals is given in [110]. The impact of local pump-light-induced heating in an active medium is fourfold:

1. The refractive index is temperature-dependent and changes locally. This process leads to a thermal lensing effect, which changes the eigenmode of the laser cavity. In some high-power laser designs, this can actually render the laser cavity unstable at a given range of pump powers, in the sense that no eigenmode of the cavity exists [111].

[†]In References [106–109], the length of the gain medium is multiplied by 2, because it is passed twice per roundtrip in the linear cavities which the theory was developed for.

2. The local heating causes stress and strain. Since the refractive index of a material normally is stress- and strain-dependent, this represents a second effect causing thermal lensing.

3. The stress causes bulging of the end faces of the active medium, which results in a further thermal lensing effect.

4. If the stress becomes to large, it might actually reach the value of the breakage stress and thus destroy the medium.

All of these lensing effects also result in aberrations due to a nonquadratic modification of the phasefronts, finally leading to losses for a passing laser beam. The expression for the round-trip loss, Equation (2.26) thus becomes dependent on the absorbed laser power P_{abs}.

$$\mathcal{L}(P_{\mathrm{abs}}) = \mathcal{T} + \mathcal{L}_{\mathrm{pass}} + \mathcal{L}_{\mathrm{th}}(P_{\mathrm{abs}}) \tag{2.33}$$

Let us consider the steady-state heat equation

$$\nabla^2 T(\mathbf{r}, t \to \infty) = -\frac{Q(\mathbf{r})}{\kappa}\,, \tag{2.34}$$

which has the form of a Poisson equation with the temperature profile $T(\mathbf{r}, t \to \infty) = T(\mathbf{r})$, the heat source term $Q(\mathbf{r})$ and the thermal conductivity κ. The longitudinal variation on the left side of (2.34) is in general small compared to the transverse dependence. Hence, we neglect the $\partial^2/\partial z^2$-term, such that z is merely a parameter in Equation (2.34). To model these effects, we simplify the geometry and discuss a cylindrical crystal embedded in an infinite medium. The problem becomes one-dimensional and we have

$$\nabla_\rho^2 T(\rho, z) = -\frac{Q(\rho, z)}{\kappa}\,, \tag{2.35}$$

(ρ, z) being the cylindrical coordinates. It can be solved analytically for a top-hat pump beam with a flat intensity distribution of radius $w_{\mathrm{p}}^2(z)$ and a fixed temperature T_0 at the crystal edge. This is established by having good thermal contact between the crystal and its mount, and a high (infinite) thermal conductivity of the mount material. We define $\delta T(\rho, z) = T(\rho, z) - T_0$ and obtain

$$\delta T(\rho, z) = \frac{\eta_{\mathrm{las/nonlas}} P_{\mathrm{abs}}}{4\pi\kappa} \frac{\alpha_{\mathrm{abs}} \mathrm{e}^{-\alpha_{\mathrm{abs}} z}}{1 - \mathrm{e}^{-\alpha_{\mathrm{abs}} l_{\mathrm{med}}}} \times \begin{cases} \ln\left(\frac{\rho_0^2}{w_{\mathrm{p}}^2(z)}\right) + 1 - \frac{\rho^2}{w_{\mathrm{p}}^2(z)}, & \text{if } \rho \le w_{\mathrm{p}}^2(z) \\ \ln\left(\frac{\rho_0^2}{\rho^2}\right), & \text{else.} \end{cases} \tag{2.36}$$

$\eta_{\mathrm{las/nonlas}}$ is the relative amount of the pump photon energy contributing to heating. The total thermal phase shift imprinted on a laser beam passing the heated material reads

$$\varphi(\rho) = \int_0^{l_{\mathrm{med}}} \left(\frac{\partial n_\omega}{\partial T} + f_{\mathrm{stress}}(T) \right) \mathrm{d}z\,. \tag{2.37}$$

The second term inside the integral, $f_{\mathrm{stress}}(T)$, contains effects from stress, strain and end-face bulging. Since the parameters describing this term are difficult to obtain experimentally, it is normally absorbed in the $\partial n_\omega/\partial T$-prameter. This explains the different values obtained in literature, see Table 2.1.

The expression for the dioptric power D_{th} (inverse focal length f_{th}) of a laser crystal (or any material with heat deposition) is easily obtained by Taylor-expanding (2.37) near $\rho = 0$ [110, 112]:

$$D_{\mathrm{th}} = \frac{1}{f_{\mathrm{th}}} = \frac{\eta_{\mathrm{las/nonlas}} P_{\mathrm{abs}}}{\pi w_{\mathrm{p}}^2 \kappa} \frac{\partial n_\omega}{\partial T} \tag{2.38}$$

for P_{abs} as defined in Equation (2.29). $\eta_{\mathrm{las/nonlas}}$ is the fraction of absorbed power contributing to heating of the crystal. Due to the different branching ratios, one has to distinguish between the non-lasing and lasing case [103]:

$$\eta_{\mathrm{nonlas}} = \frac{P_{\mathrm{abs}} - P_{\mathrm{fl}}}{P_{\mathrm{abs}}} = \frac{\lambda_{\mathrm{p}}}{\lambda_{\mathrm{fl,mean}}} \frac{\tau_{\mathrm{fl}}}{\tau_{\mathrm{rad}}}, \tag{2.39}$$

where P_{fl} is the amount of power converted to fluorescence radiation, λ_{p} is the pump wavelength and $\lambda_{\mathrm{fl,mean}}$ is the mean fluorescence wavelength. τ_{fl} is the fluorescence lifetime and τ_{rad} the purely radiative lifetime of the metastable state in the active material. When lasing occurs instead of fluorescence, another quantity of energy per pump photon is deposited in heat. The fractional heating power changes to

$$\eta_{\mathrm{las}} = \frac{P_{\mathrm{abs}} - P_{\mathrm{las}}}{P_{\mathrm{abs}}} = 1 - \frac{\lambda_{\mathrm{p}}}{\lambda_{\mathrm{las}}} \frac{\sigma_{\mathrm{em}}}{\sigma_{\mathrm{em}} + \sigma_{\mathrm{ESA}}}, \tag{2.40}$$

where P_{las} is the amount of power converted to laser radiation, and λ_{las} the laser wavelength. One finds from (2.40) that excited state absorption not only lowers the available output power, but also detrimentally influences the thermal effects, since the excited-state decay channels are safely considered fully phonic. The ratio $\eta_{\mathrm{las}}/\eta_{\mathrm{nonlas}}$ equals the ratio between the two resulting dioptric powers. This has to be considered when designing a cavity, as will be shown in the next section.

2.2.4 Laser cavity design

In this section, we employ the theory presented above to design a laser cavity satisfying the design constraints imposed. The setup needs to offer sufficient versatility to operate the laser under a wide set of parameters due to a lack of exact knowledge of the material parameters and the approximate nature of the theory presented above. Most importantly, to facilitate single-mode operation, the total cavity length is to be chosen to be as short as possible to enlarge the longitudinal mode spacing, or free spectral range $\nu_{\mathrm{FSR}} = c/L_{\mathrm{opt}}$.

One also needs to account for the placement of the additional intra-cavity elements besides the active medium. As we will see in the course of this chapter, we require a half-wave plate, a TGG crystal and two etalons to force unidirectional single-mode operation. The most bulky element is the TGG Faraday rotator magnet ensemble with its outer dimensions of $50 \times 50 \times 65\,\mathrm{mm}^3$. Additionally, one has to include the zero-order waveplate and the two etalons needed for single-longitudinal-mode operation. To diminish these constraints, the whole laser setup was designed using the *Dassault CATIA* 3D–CAD software to diminish the cavity length. All the optics mounts were minimized in size to easily fit in the resonator. An overview drawing of the mechanical laser setup is given shown in Figure 2.1, whereas a schematic is shown in Figure 2.7.

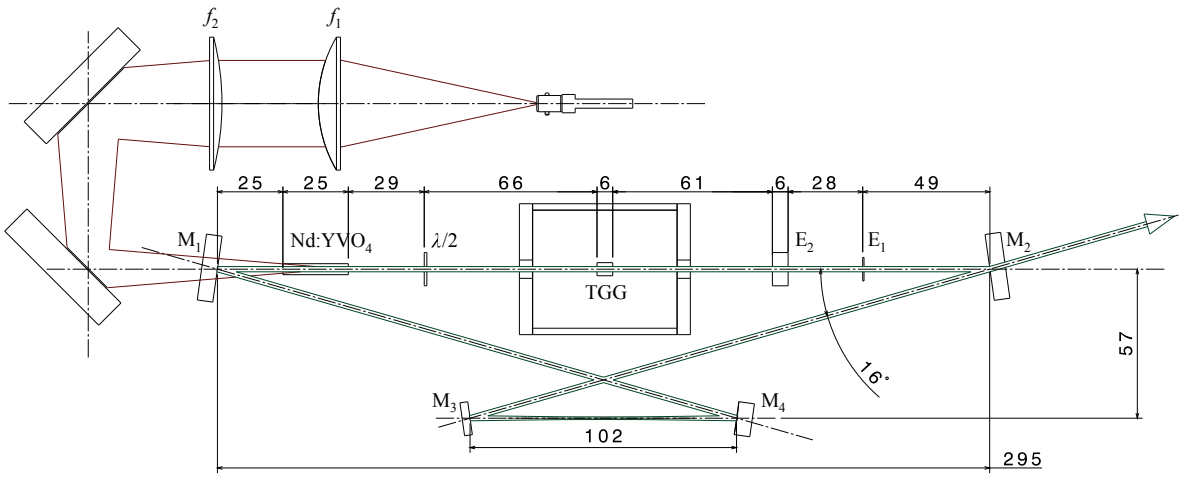

FIGURE 2.7: Schematic view of the cavity geometry chosen, including all intra-cavity elements. The pump beam dimensions are not given, since they can be varied using different sets of lenses f_1 and f_2 as a function of the desired pump spot radius w_p in the Nd:YVO_4 crystal. the cavity is formed by four mirrors M_{1--4}, where M_2 is the output coupling mirror, and M_3 and M_4 are concave. Additional elements are the half-wave plate $\lambda/2$, a TGG crystal in a magnet ensemble (large box) and two etalons $E_{1,2}$.

We decided for the popular bow-tie design because of several advantages: It features a long arm between the plane mirrors M_1 and M_2 where the beam is almost collimated. This arm offers enough space to install all the additional optical elements, including the magnet ensemble. In the shorter arm, which is situated between the two curved mirrors M_3 and M_4, the beam is strongly focused. By adjusting the distance between those two mirrors, the size of the resonator eigenmode and thus the overlap between laser and pump spatial mode profiles can be optimized, see Section 2.2.3. The focus between the two mirrors allows one the option off putting a nonlinear crystal here in order to directly intra-cavity-frequency-double the laser without the use of an external cavity. This approach was followed by our collaboration partners in Toulouse, using both lithium triborate (LiB_3O_5, LBO) and bismuth triborate (BiB_3O_6) [95]. Another advantage of bow-tie designs is the similar and small angle of incidence of the beams on the four mirrors forming the cavity. This means that the coating design of these mirrors can be identical, except for the output coupler. This facilitates interchange of mirrors and thus constitutes an inexpensive solution for the choice of mirrors. The pump coupling mirror M_1 as well as the curved mirrors M_3 and M_4 consist of fused-silica substrates which are highly-reflective coated for 1342 nm at an angle of incidence of 10° for both s- and p-polarization. The same coating allows for efficient transmission of the pump wavelengths 808 nm and 888 nm at the same angle of incidence at random polarization, and transmission of the second harmonic output at 671 nm for using the same (curved) mirrors in the doubling cavity. Accordingly, the rear sides were anti-reflective coated at both the pump and second-harmonic wavelengths.

For the output couplers we chose the slightly more expensive infrared fused silica as the substrate material, for avoidance of absorption features in normal fused silica around 1340 nm. Available values for the power transmission were 2% and 3.5% and

the values for the doubling cavity couplers 5%, 10% and 17%. The back sides of the couplers are anti-reflective coated at 1342 nm.

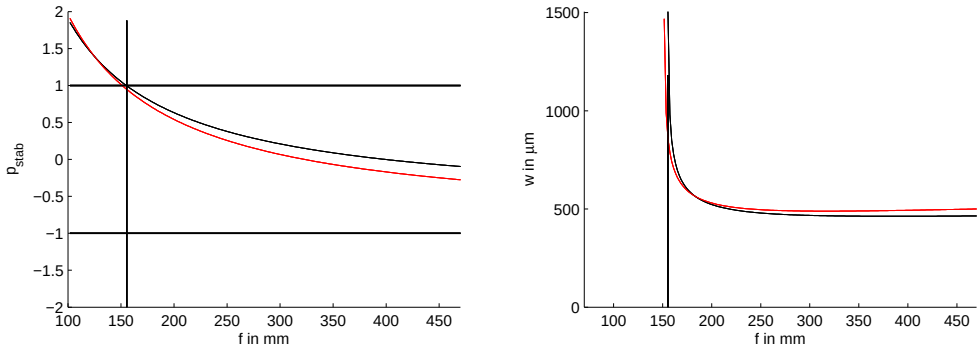

FIGURE 2.8: The stability parameters (left, see Equation 2.12) and the mode sizes (right) in the laser crystal as a function of the focal length f_{th}. The black (red) lines indicate the horizontal (vertical) direction. The vertical lines indicate the limits of cavity stability. The resonator remains stable down to $f_{\mathrm{th,min}} = 153\,\mathrm{mm}$.

The cavity eigenmode needs to be stable for two different values of the thermal lens focal length f_{th} induced in the Nd:YVO_4 crystal, both with and without lasing [111]. If it were not, lasing either could not start from fluorescence or significant intra-cavity power will not build up. From Equations (2.38), (2.39) and (2.40) we get

$$\frac{f_{\mathrm{th,nonlas}}}{f_{\mathrm{th,las}}} = \frac{D_{\mathrm{th,las}}}{D_{\mathrm{th,nonlas}}} = \frac{\eta_{\mathrm{th,las}}}{\eta_{\mathrm{th,nonlas}}}\,. \tag{2.41}$$

For the material parameters (cf. Table 2.1), we have $\tau_{\mathrm{fl}} = 110\,\mu\mathrm{s}$ for low doping. The available spectroscopic data allows a conservative estimate for the emission and ESA cross sections of $\sigma_{\mathrm{em}} = 15 \times 10^{-20}\,\mathrm{cm}^2$ and $\sigma_{\mathrm{ESA}} = 3 \times 10^{-20}\,\mathrm{cm}^2$ (cf. Figure 2.6). The stability range thus needs to extend over a focal length range of

$$\frac{f_{\mathrm{th,nonlas}}}{f_{\mathrm{th,las}}} \approx 2\,. \tag{2.42}$$

For calculating the behavior of the cavity eigenmode, we now need to solve (2.11), fulfilling condition (2.13). Figure 2.8 shows the behavior of the cavity stability and of the mode size inside the laser crystal as a function of the thermal focal length f_{th}. The cavity remains stable from infinite focal lengths (or no thermal effect, not shown) down to $f_{\mathrm{th,min}} = 153\,\mathrm{mm}$. For a pump spot diameter of $w_{\mathrm{p}} = 500\,\mu\mathrm{m}$, the cavity thus supports a maximum absorbed pump power of $P_{\mathrm{abs,max}} = 17.5\,\mathrm{W}$ for the given parameters. The f_{th}-dependence of the radius of the mode in the Nd:YVO_4 crystal is also given, reaching from $500\,\mu\mathrm{m}$ to $700\,\mu\mathrm{m}$.

The optimum mode overlap for high-power lasers ($P_{\mathrm{abs}} > 10\mathrm{W}$) is given as [108]

$$\frac{w_{\mathrm{l}}}{w_{\mathrm{p}}} \approx 0.8\,, \tag{2.43}$$

which can be easily fulfilled for a given value for f_{th} by optimizing the distance between the two curved mirrors M_3 and M_4. In practice, this is realized by mounting M_4 on a

linear translation stage and optimizing its position to optimize the output power. The calculated radii are plotted in Figure 2.9 for a focal length of $f_{\mathrm{th}} = 260\,\mathrm{mm}$, as derived in Section 2.5. The range of waists in the crystal can thus be expanded from $430\,\mu\mathrm{m}$ to $\geq 1000\,\mu\mathrm{m}$.

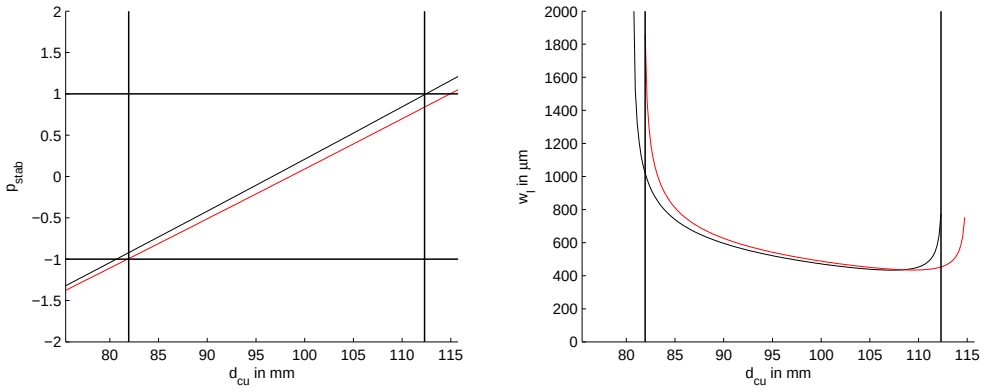

FIGURE 2.9: (Left) The stability diagram of the laser cavity by varying the distance d_{cu} between the curved mirrors M_3 and M_4. The thermal focal length is fixed to 260 mm. (Right) The mode sizes in the laser crystal $w_{\mathrm{h(v)}}$. The black (red) lines indicate the horizontal (vertical) direction, whereas the vertical lines indicate the range of stability.

The values for the stability parameters and waists presented in this section depend strongly on the distances realized in the setup, which can be measured and set with a precision around 1 mm only. The analytic model for the thermal lensing effect (2.38) does not take into account finite size effects of the system, and the material constants found in literature sometimes are contradictory, see the theoretical discussion in Section 2.2.3. We thus refer the interested reader to Section 2.5, where the measured optimized cavity eigenmode is presented.

The pump source is a commercial fiber-coupled *Coherent FAP-400* diode stack emitting up to 42.6 W at 808 nm (90% energy width: 4 nm). Its metal housing is temperature stabilized to optimize the spectral overlap between pump emission and the gain medium absorption. The fiber output (core radius: $200\,\mu\mathrm{m}$, numerical aperture $NA = 0.22$) is imaged in the gain medium using two lenses ($f_1 = 100\,\mathrm{mm}$ and $f_2 = 250\,\mathrm{mm}$) to a top-hat like spot of a radius of $w_{\mathrm{pump}} = 500\,\mu\mathrm{m}$. The Nd:$YVO_4$ crystal of dimensions $3 \times 3 \times 10\,\mathrm{mm}^3$ is 0.2 at.%-doped, a-cut and anti-reflective (AR) coated at 808 nm and 1342 nm. It is wrapped in 100-μm thick Indium foil and fixed in a solid water-cooled copper mount to efficiently remove heat. Care needs to be taken to avoid acoustic excitations of the mount due to turbulent water flow, thus only a small continuous flux of tap water was applied to prevent phase-, or equivalently, frequency fluctuations of the laser output.

The laser was mounted on a $50 -$ mm-thick breadboard. A combined aluminum-acrylic-glass housing was provided to isolate from acoustic perturbations and for keeping the setup continuously under a dry-air atmosphere to prevent dust and moisture from having detrimental effects on the long-term stability of the system.

2.3 Single-frequency operation and tunability

For our application of trapping and cooling atoms, we need single-frequency light output of the fundamental light source. In this section we will present the technical measures taken to force laser operation in a single longitudinal mode.

2.3.1 Faraday rotation and unidirectional operation

For realizing a single-longitudinal-mode laser it is favorable to avoid standing waves in the gain medium. These cause spatial hole burning in the active medium and thus partially suppress mode competition. From this point of view, running-wave lasers are preferable [104].

Two solutions exist: the twisted-mode linear cavity [113] and the unidirectional ring cavity. The first method is not feasible using a birefringent gain medium like Nd:YVO_4. For forcing unidirectional operation, several methods exist [114–116]. Because of its simplicity and reliability, we use an intra-cavity optical diode consisting of a Faraday medium and two elements for polarization selection and rotation.

The polarization rotation of φ_{rot} imposed on a light beam when traveling through a Faraday medium is

$$\varphi_{\mathrm{rot}} = \mathcal{V} I_B \,, \tag{2.44}$$

with the magnetic field integral

$$I_B = \int_0^{l_{\mathrm{F}}} B(z)\,\mathrm{d}z \tag{2.45}$$

in the medium of length l_{F}. The material- and wavelength-specific constant $\mathcal{V}$ is called the Verdet constant. For common Faraday materials, it decreases significantly when leaving the visible range towards higher wavelengths, whereas the absorption rises. It is thus favorable to use a short crystal and a strong magnetic field, while maintaining sufficient field homogeneity to not create a transversal variation in polarization.

These requirements necessitated the development of a special magnet assembly by Gérard Trénec and coworkers. The design consists of an ensemble of NdFeB ring magnets and is presented in [117]. It is optimized for Faraday media with a length of 6 mm and 5-mm diameter. The outer dimensions of the housing are $50 \times 50 \times 65\,\mathrm{mm}^3$ are the most restricting factor for the compactness of the cavity design presented in Section 2.2.4. The measured value for the magnetic field integral is $I_B = 8\,\mathrm{T.mm}$.

Terbium gallium garnet (TGG), a standard crystal for visible and near-infrared laser applications, was chosen as the Faraday medium. We performed single-pass measurements of the rotation angle for TGG samples from different suppliers. The results are presented in Table 2.2. We use the sample from FEE in our laser, since it is offering the greatest rotatory power.

Back-rotation and stable unidirectional operation at high intra-cavity powers is established by an anti-reflective-coated, zero-order $\lambda/2$-wave plate, which is preferred to multi-order wave plates because of instabilities related to thermal effects [118]. The polarizing intra-cavity element is the Nd:YVO_4 crystal which provides higher gain in

[‡]Forschungsinstitut für mineralische und metallische Werkstoffe -Edelsteine/Edelmetalle- GmbH

Supplier	**angle φ_{rot}**	**Verdet constant $\mathcal{V}$**
CLaser Photonics Inc. sample 1	$-2.7(1)^\circ$	-5.9(2) rad.T^{-1}.m^{-1}
CLaser Photonics Inc. sample 2	$-1.7(1)^\circ$	-3.7(2) rad.T^{-1}.m^{-1}
FEE[‡]	$-9.3(1)^\circ$	-20.3(2) rad.T^{-1}.m^{-1}

TABLE 2.2: Measurements of the rotative power of different samples of TGG at 1342 nm.

the c-direction as well as birefringence. The oscillation direction is chosen as indicated in Fig. 2.1 to spatially separate residual pump light from the output beam.

2.3.2 Etalons as frequency-dependent filters

To achieve single longitudinal mode (SLM) operation, several measures were taken in the laser design presented before, such as the use of a running-wave (unidirectional ring) resonator, and the compactness of the whole setup. This yields the largest possible longitudinal-mode frequency spacing, or free spectral range

$$\nu_{\mathrm{FSR,laser}} = \frac{c}{L_{\mathrm{opt}}} \approx 360\,\mathrm{MHz} \tag{2.46}$$

for the laser cavity, where L_{opt} is the round-trip optical path length and c the speed of light in vacuum. The width of the gain peak is $\approx 300\,\mathrm{GHz}$ and so three orders of magnitude larger than ν_{FSR}, showing that additional measures need to be taken to make the laser oscillate in a single longitudinal mode. Thus, small Fabry-Pérot resonators termed etalons are installed in the laser cavity to modify the cavity round-trip transmission function.

The frequency-dependent transmission function of a Fabry-Pérot resonator in the plane-wave approximation reads

$$\mathcal{T}_{\mathrm{FP}} = \left(1 + \left[\frac{2\mathcal{F}}{\pi}\sin\left(\pi\frac{\nu-\nu_{\mathrm{res}}}{\nu_{\mathrm{FSR,etalon}}}\right)\right]^2\right)^{-1}, \tag{2.47}$$

where ν_0 is a constant offset frequency depending on the additional phase shifts acquired due to the optical coatings. The so-called finesse is defined as

$$\mathcal{F} = \frac{\pi\sqrt{\mathcal{R}}}{1-\mathcal{R}}, \tag{2.48}$$

with the surface power reflectivity $\mathcal{R}$. The resonance condition $\mathcal{T}_{\mathrm{FP}} = 1$ is fulfilled for the corresponding resonance frequencies $\nu_b = b\,\nu_{\mathrm{FSR,etalon}} + \nu_{\mathrm{res}}$, $b \in \mathbb{N}$, see Equation (2.21).

In the small-signal limit, the product $\mathcal{T}_{\mathrm{cav}}(\nu) \times \sigma_{\mathrm{em}}(\nu)$ needs to be greatest for one of the laser cavity modes to suppress all the other modes from oscillating due to mode competition [104]. $\mathcal{T}_{\mathrm{cav}}(\nu)$ is the total transmission function of the cavity and reasonably approximated as constant for the frequency range considered here, except for the influence of the etalons. $\sigma_{\mathrm{em}}(\nu)$ is a measure for the gain experienced by a light

wave crossing the gain medium. If there is sufficient mode competition, provided by a unidirectional ring cavity, only the favored mode with mode index b will be oscillating.

Equations (2.47)–(2.48) contain two degrees of freedom for choosing an appropriate etalon. The first is the free spectral range $\nu_{\mathrm{FSR,etalon}}$ given by its length and the refractive index of the material. The second parameter is the finesse $\mathcal{F}$ which is given by the surface reflectivity of the etalon. One should note that up to this point, losses were not considered in our analysis. These are due to residual absorption of the substrate and coatings, scattering, surface nonparallelity and roughness and the beam walk-off.

2.3.3 Etalon walk-off loss

The loss processes mentioned before can be minimized to negligible values by carefully chosing the appropriate materials and methods in the etalon production process. However, the etalon walk-off loss is fundamental and can not be avoided. We will thus calculate its magnitude to motivate our choice of etalons presented in the next section.

The frequency-dependent etalon transmission function (2.47) is strictly valid only in the case of plane waves. The beam nature of the wave propagating through the laser cavity leads to additional loss due to wavefront curvature and the angle-dependent walk-off.

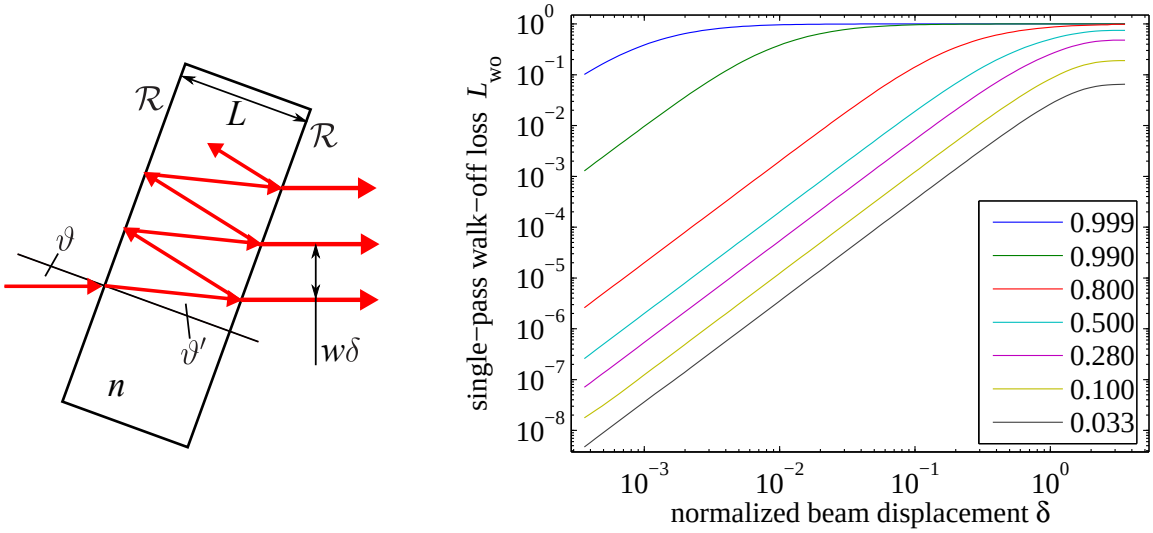

FIGURE 2.10: LEFT: Definition of the single-pass walk-off distance δ, normalized by the gaussian beam radius w. RIGHT: Calculation of the etalon single-pass walk-off loss, plotted as a function of the normalized beam displacement parameter δ for different values of the reflectivity $\mathcal{R}$ as indicated in the legend.

When the surface normal vector and the direction of propagation of a Gaussian beam form an angle of incidence ϑ, a lateral walk-off of subsequent orders of the transmitted waves occurs, see Figure 2.10 (a). The normalized beam displacement reads

$$\delta = \frac{2L}{w} \tan(\vartheta') \cos(\vartheta)\,, \tag{2.49}$$

where L is the geometric length of the etalon and w the Gaussian radius of the beam. ϑ is the angle of incidence or tilt angle of the etalon and $\sin(\vartheta)/\sin(\vartheta') = n$ with

the refractive index n of the etalon medium. δ thus gives the displacement between succeeding modes of transmission in units of the Gaussian beam radius.

The non-unity overlap integral between the cavity mode and the transmitted beam leads to insertion loss when installing the tilted etalon in a resonator. We recalculated the loss $\mathcal{L}_{\mathrm{wo}}$ according to [119][§]. The results are presented in Figure 2.10(b). The loss rises quadratically with a scaling given by the etalon surface reflectivity $\mathcal{R}$. Around $\delta = 1$, the curves level off to the maximum value $\mathcal{L}_{\mathrm{wo,max}} = 2\mathcal{R} - \mathcal{R}^2$ obtained analytically for complete separation of subsequent transmission orders. In this limit, the use of an intracavity etalon as a frequency filter becomes meaningless.

2.3.4 Etalon choice and operation

For the Toulouse laser setup, a trial was made to achieve single-mode oscillation by using an available $\mathcal{R} = 20\%$-etalon of a width of 1 mm. It was not successful, even though about 90% of the emitted power was contained in one of the two modes oscillating, and the frequency spacing to the second oscillating mode was 2 or 3 cavity free spectral ranges most of the time. Such a laser would be suitable to deliver single-frequency second-harmonic light when doubling in an external cavity by coupling only one of the laser modes to the doubling cavity. Instead, we decided to use a combination of two etalons to realize a single-frequency laser. This scheme avoids multi-mode dynamics in the laser output and thus to stabilizes the whole laser system. Single-mode operation is favored when intra-cavity frequency doubling of a laser is applied. In that case, mode competition is enhanced due to sum-frequency generation, which causes higher losses for the low-power mode [120].

To suppress the closely-spaced mode from oscillating, we employed a more selective $\mathcal{R} = 28\%$-etalon of a width of 4 mm called E_2. For suppression of the modes which are more distant, we use an uncoated etalon of $\mathcal{R} = 3.3\%$-etalon of a width of 0.5 mm. The typical frequency scales are given in Table 2.3. The material of both substrates is infrared fused silica, and the $\mathcal{R} = 28\%$-coating consists of a single layer to minimize coating-related loss. With the combination of etalons presented here, reliable every-day single-mode operation is achieved.

Figure 2.11 shows an example of a calculated transmission-gain behavior $\mathcal{T}_{\mathrm{cav}}(\nu_b) \times \sigma_{\mathrm{em}}(\nu_b)$ using the data presented in Figure 2.6. Note that the behavior presented here is valid only in the non-saturated (small-signal) regime. For this plot, the reflectivity of E_2 was set to 10% to improve visibility of its effect. One should furthermore keep in mind that the resolution of the spectroscopic data is 0.5 nm or 80 GHz, so that any additional sub-structure is washed out. The interested reader can refer to Section 2.3.6, where the single-frequency output spectrum of the laser was measured.

When installing an intra-cavity etalon perpendicularily to the eigenmode propagation direction, a set of coupled cavities will be formed. Due to fluctuations in the setup, this will lead to highly unstable behavior of the setup. Thus, one needs to account for a minimum tilt angle ϑ_{min} for any intra-cavity etalon to avoid multi-cavity behavior. It can be estimated by the cavity-eigenmode beam divergence, which is maximally

[§]The analysis given in [119] accounts only for linear resonators, so the etalon is passed twice for each roundtrip, giving approximately two times the values obtained for the single-pass case considered here.

Element	Length L	Typ. freq.	Typ. $\mathcal{R}$	Finesse $\mathcal{F}$	Q-factor
Gain profile width	-	300 GHz	-	-	-
Laser cavity	81 cm	360 MHz	96.5%	110	6×10^7
Doub. cavity	41 cm	730 MHz	93.6%	86	3×10^7
Etalon E_1	0.5 mm	210 GHz	3.3%	-	-
Etalon E_2	4 mm	26 GHz	28%	2.1	2×10^3
Etalon Toulouse	1 mm	105 GHz	20%	1.4	3×10^3

TABLE 2.3: Frequency scales in the setup. Typical frequencies are free spectral ranges ν_{FSR} as described in the text and FWHM for the gain profile from [99]. Reflectivities $\mathcal{R}$ are given for the output and input coupling mirrors in case of the two cavities and for the two etalon surfaces, respectively. The finesses $\mathcal{F}$ and Q-factors of the laser cavity and E_1 are calculated from the $\mathcal{R}$-values as stated, neglecting further losses. $\mathcal{F}$ and Q were measured for the doubling cavity, see Chapter 3, and are given for comparison only.

1.1 mrad in our case. This value is obtained for a Gaussian beam of a minimal waist radius of 400 μm, see Section 2.5. Any angular etalon tuning will start from this point towards higher tilt angles, accounting for a minimum tilt loss $\mathcal{L}_{\mathrm{wo,min}}$.

Etalon	Length L	$\mathcal{R}$	ν_{FSR}	$\mathcal{L}_{\mathrm{wo,min}}$	$\mathcal{L}_{\mathrm{wo}}(3\,\mathrm{GHz})$	$\mathcal{L}_{\mathrm{wo}}(\nu_{\mathrm{FSR,etalon}})$
E_1	0.5 mm	3.3%	210 GHz	1×10^{-7}	3×10^{-6}	0.02%
E_2	4 mm	28%	26 GHz	1×10^{-4}	0.3%	2.5%
Toulouse	1 mm	20%	105 GHz	5×10^{-6}	1×10^{-4}	0.4%

TABLE 2.4: Walk-off loss calculation for the etalons selected. For reasons of completeness, we also give the calculated loss for a typical detuning of 3 GHz. The losses remain negligible for E_1 under all reasonable circumstances, but can become important for E_2.

During the manufacturing process, the absolute value of the etalon thickness L_{etalon} can be controlled with a precision larger than the laser wavelength only. Thus, the offset frequency ν_{res} and the free spectral range $\nu_{\mathrm{FSR,etalon}}$ in the etalon transmission function (2.47) are given by an arbitrary etalon thickness offset. In the worst case one has to tune the laser system by $\nu_{\mathrm{FSR,etalon}} = c/(2nL_{\mathrm{etalon}})$ to reach the lithium resonance. Walk-off losses can be completely neglected for E_1, see Table 2.4. To avoid the higher tilt loss of E_2 ($\mathcal{L}_{\mathrm{wo}} = 2.5\%$ for angular tuning over one free spectral range of $\nu_{\mathrm{FSR}} = 26$ GHz, comparable to the output coupler transmission), we chose to keep it still at the minimum angle and to only change its temperature to tune the laser.

The mode-hop-free scan range of the laser was measured to ≈ 550 MHz, slightly higher then $\nu_{\mathrm{FSR}} = 360$ MHz, see (2.46). Tilt-tuning of the etalon was used to almost double the mode-hop-free scan range of the laser to ≈ 1.1 GHz at the cost of increased losses as described above. To realize this, the etalon was mounted on a rotation mount actuated by a piezoelectric transducer. For the highest tilt loss, at the border of the mode-hop-free scan range, this results in a drop of the output power by 30%.

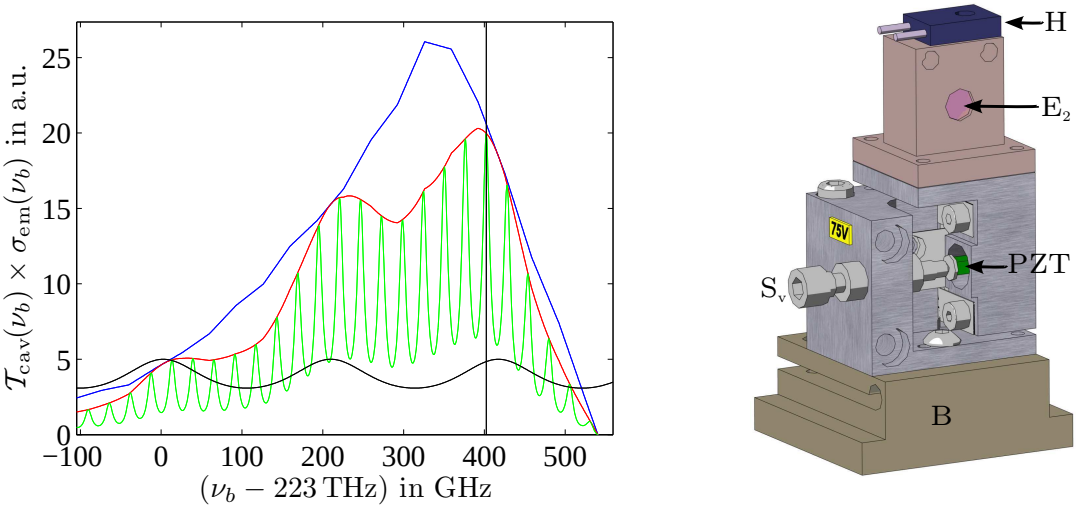

FIGURE 2.11: LEFT: Small-signal gain–transmission behavior $\mathcal{T}_{\rm cav}(\nu_b) \times \sigma_{\rm em}(\nu_b)$ for two etalons as indicated in Table 2.3, except for $\mathcal{R}_{E_2} = 10\%$. The black vertical line represents half the Li resonance frequency. The blue line is the spectroscopy data for $\sigma_{\rm em}(\nu_b)$ from [99], the red line is $\sigma_{\rm em}(\nu_b)$ modulated by E_1 only. The red line is $\sigma_{\rm em}(\nu_b)$ modulated by both etalons, and the black line is the transmission of E_1 in a.u. The cavity modes spaced by $\nu_{\rm FSR} = 360\,\mathrm{MHz}$ are not resolved here. RIGHT: Etalon mount assembly for E_2. The temperature is stabilized in a copper mount, using the heating resistor H. The *Thorlabs NanoFlex* series mount provides etalon tilt around the vertical axis via the setscrew S_v and the piezo-electric transducer PZT. The base B, made from nickel silver, provides rotation around a horizontal axis.

2.3.5 Etalon temperature tuning

As demonstrated above, tilt-tuning of E_2 should be avoided to minimize losses inherent to this method. Another, slower way to tune the resonance frequency of an etalon is to change its temperature, since both its length L and refractive index n display a temperature dependence. The change in frequency reads

$$\frac{\partial \nu_b(T)}{\partial T} = b\,\frac{\partial \nu_{\rm FSR}(T)}{\partial T} \simeq b\,\frac{\partial}{\partial T}\left(\frac{c}{2n(T)L(T)}\right) = -b\,\nu_{\rm FSR}\left(\frac{1}{n}\frac{\partial n}{\partial T} + \frac{1}{L}\frac{\partial L}{\partial T}\right), \quad (2.50)$$

where c is the speed of light and n the refractive index and L the geometric length of the etalon. The values for silica are $\frac{1}{n}\frac{\partial n}{\partial T} = 8.4 \cdot 10^{-6}\mathrm{K}^{-1}$, $n = 1.44512$ and $\frac{1}{L}\frac{\partial L}{\partial T} = 5.5 \cdot 10^{-7}\mathrm{K}^{-1}$ according to [121–123]. For E_2 we get $\Delta T \approx 26.4\,\mathrm{K}$ to detune over a full spectral range. It thus should also be temperature-stabilized to avoid drifts during the warm-up process of the laser setup.

For temperature tuning, E_2 is enclosed in a temperature-regulated copper mount stabilized to $\approx 100\,\mathrm{mK}$, see Figure 2.11. To measure the etalon-temperature dependence of the laser frequency, we single-pass frequency-doubled the output beam using a setup similar to the one presented in Section 3.3. It yields a second harmonic power of the order of 1 mW, sufficient to drive a *High Finesse WMA-6* CCD-based high resolution spectrum analyzer.

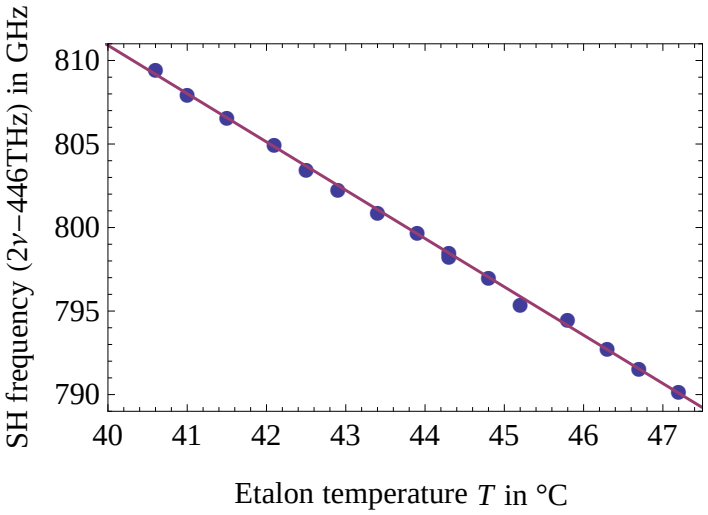

FIGURE 2.12: Temperature-tuning curve for the emission frequency of the laser. Since the frequency was measured using SHG light, we get twice the value for the slope $2\mathrm{d}\nu_b(T)/\mathrm{d}T = -2.89\,\mathrm{GHz.K^{-1}}$. This value is practical for every-day use of the frequency-doubled laser light.

The result is presented in Figure 2.12. As expected, the output frequency depends linearly on etalon temperature. The theoretical value from Equation (2.50) using the literature values as above yields $\mathrm{d}\nu_b(T)/\mathrm{d}T \approx -1.42\,\mathrm{GHz.K^{-1}}$. We fit a linear slope of

$$2\frac{\mathrm{d}\nu_b(T)}{\mathrm{d}T} = -2.89(3)\,\frac{\mathrm{GHz}}{\mathrm{K}} = 2 \times -1.45(1)\,\frac{\mathrm{GHz}}{\mathrm{K}}\,. \tag{2.51}$$

The discrepancy between these two values can be explained by differences in the glass composition for infrared fused silica, the material actually used for all etalons to avoid additional loss due to absorption. A further explanation is a possible manufacturer tolerance of the etalon lenght L.

2.3.6 Output spectrum

By changing the temperature of E_2 and optimizing the respective output power, the emission spectrum of the laser was measured, as shown in Figure 2.13.

The spectrum is smooth except for three narrow dips 1341.8 nm, 1342.1 nm and 1342.7 nm, which can probably be accounted for by absorption of water molecules in the laser cavity. At these wavelengths, the laser operation is unstable and mode-hops towards stable regions occur. The total width of the spectrum is 1.2 nm. The wavelength value corresponding to the lithium D-line resonance is well in between the two first dips, and the emitted power is close to the absolute maximum. Hence, every-day operation of the laser on the lithium resonance wavelength is accomplished easily.

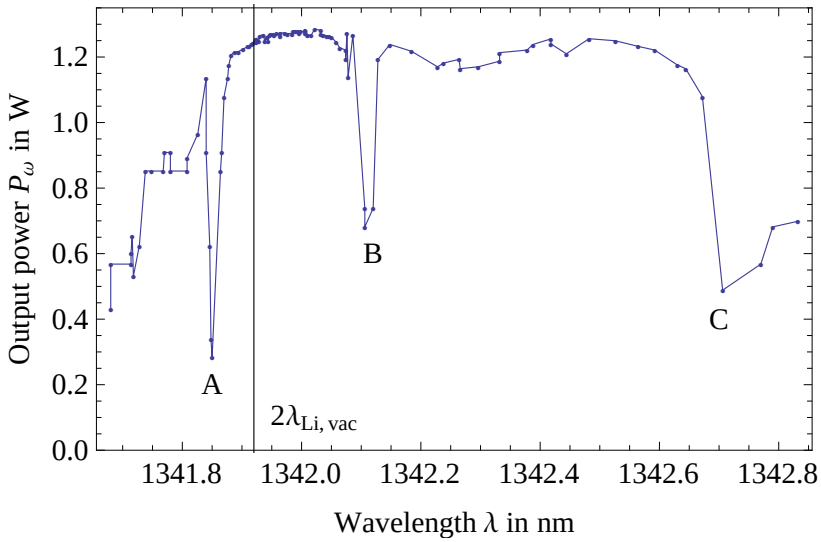

FIGURE 2.13: Output power of the laser as a function of wavelength (dots), the lines are guides for the eye only. The value corresponding to twice the lithium D-line wavelength is indicated by a vertical line. One notices the features A, B and C, where the output power drops sharply and the laser tends to mode-hop to frequencies in the higher-output-power range.

2.4 Output power

The output power of a laser is certainly one of its key parameters, determining the design as well as the possible applications of a laser. In this section, the output power measurements are presented.

The laser output power is first optimized with an empty cavity at maximum pump power, meaning that all elements not strictly necessary for lasing were removed. This includes the TGG, the half-waveplate and the two etalons. Doing so, one can optimize the spatial overlap between the pump beam and the cavity mode (see analysis in Section 2.2.3) while avoiding additional power-modulating effects due to the frequency selectivity of the etalons. Furthermore, due to the compact setup, only in the empty cavity one can introduce a powermeter behind the Nd:YVO_4 crystal to measure the pump powers incident on the laser crystal and transmitted through it. This allows the determination of the absorbed pump power P_{abs}.

Since the pump absorption coefficient depends sensitively on the wavelength, see Section 2.1.2, the pump wavelength spectrum needs to be adapted to the absorption spectrum of Nd:YVO_4. Since the pump source consists of a diode bar, one can tune its central emission wavelength by changing its temperature. This is realized using a water chiller with a variable set temperature. Due to burn-in and aging of the pump source, the chiller set temperature needs to be be optimized from time to time (approximately every two months during every-day operation), and is generally set between 26°C and 31°C.

The current passed through the diode bar is kept constant at $I_{\mathrm{p}} = 51$ A to stabilize the laser output power. All the laser parameters were optimized for this current, since it represents the maximum output of the power supply used to drive the diode. All the

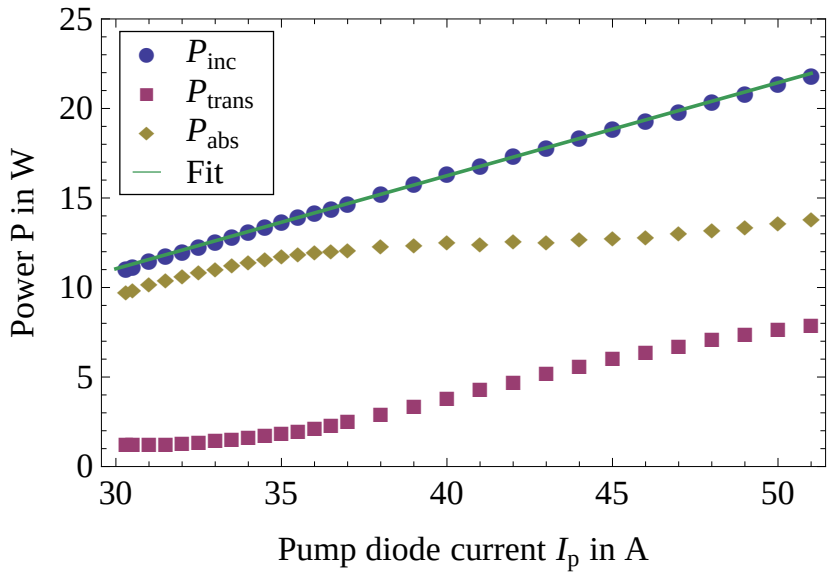

FIGURE 2.14: Absorption of the pump light. Shown are the power incident on the laser crystal P_{inc}, the transmitted power P_{trans} and the absorbed pump power P_{abs} as a function of the current I_p passing through the pump diode bar. Starting from $I_p = 33\,A$, pump light absorption saturation sets in.

measurements presented in the course of this work were taken at this value for I_p, if not otherwise stated, since no degradation of the laser parameters was observed even for highest pump powers.

Figure 2.14 shows the pump power incident on the crystal P_{inc} and the pump power transmitted through the crystal P_{trans} as a function of the pump current I_p. The difference between the two is the absorbed pump power P_{abs} due to negligible reflection of the AR-coated Nd:YVO_4 crystal. The absorbed power rises linearly with the incident pump power up to $I_p \approx 33\,A$, where either saturation in the Nd:YVO_4 crystal sets in, or the pump diode stack emission changes its spectral output characteristics. It is visible in the plateau formed for P_{abs}. The maximum absorbed pump power is 14 W.

The empty cavity output characteristics are presented in Figure 2.15(a). Since there is no TGG and waveplate present in the cavity, unidirectionality is not enforced. As such, the output power is symmetrically distributed in two beams leaving the cavity via the output coupler M_2. The power values presented here are measured for one beam only, so the total emitted power equals twice that value. The output coupler transmission was chosen out of the limited set of available values to $\mathcal{T} = 3.5\%$, so as to optimize the maximum output power at maximum pump current in the presence of all the additional intra-cavity elements. The behavior can be described by (2.30) with constant thermal loss $\mathcal{L}_{th}$, which means that there is a linear relationship between the absorbed pump power P_{abs} and the output power. Another possible explanation is that the overlap integrals (2.28) and (2.32) change accordingly in presence of $\mathcal{L}_{th}(P_{abs})$, yielding the linear behavior observed. The lasing threshold is found at $P_{thr} = 7.5\,W$ and the maximum power emitted $P_{\omega,max} = 2 \times 1.5\,W$, yielding a slope efficiency of $\eta_{sl} = 2 \times 20.4(2)\%$.

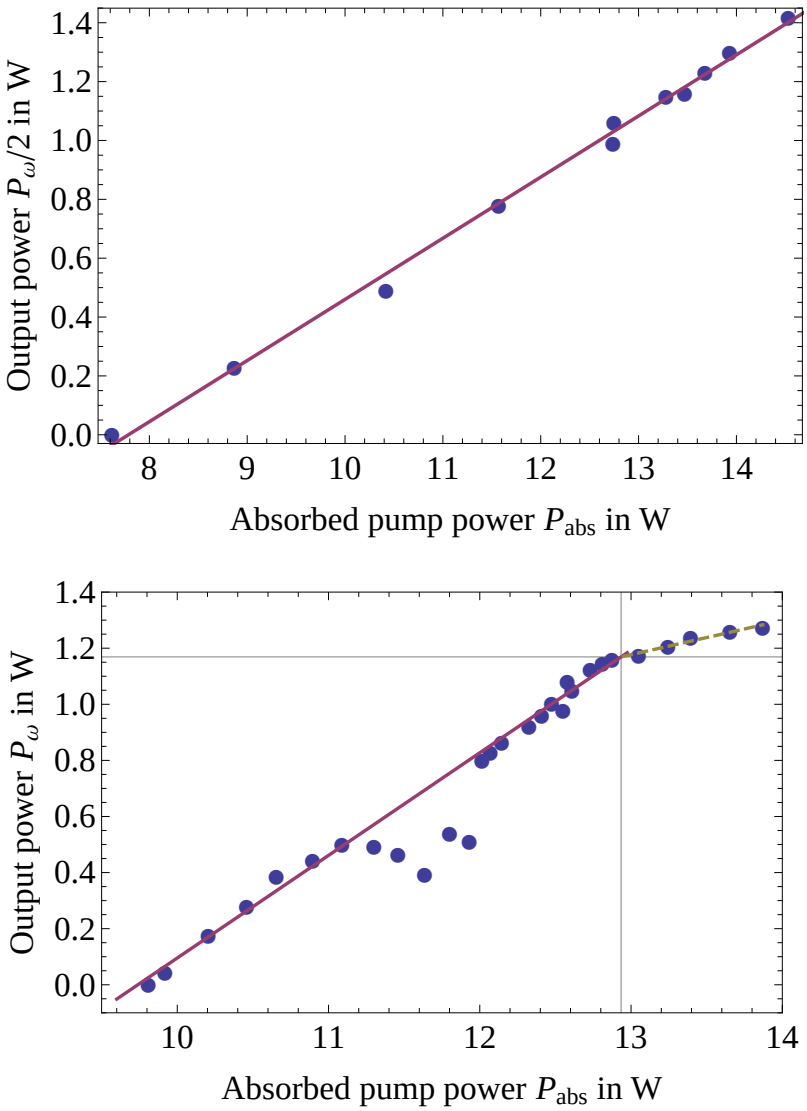

FIGURE 2.15: UPPER PANEL: One-way output power of the laser without additional intra-cavity elements (dots) and linear fit (line). In this configuration, the ring laser emits its power symmetrically distributed in two separated beams. LOWER PANEL: Single-frequency laser output power of the Nd:YVO_4 laser including additional intra-cavity elements as a function of absorbed pump power. Two regimes can be distinguished in the data (circles), and linear fits are performed (solid/dashed line) for $P_{abs} < 12.9\,W$ and $P_{abs} > 12.9\,W$. An unstable domain occurs, which can be attributed to thermal depolarization in the Faraday rotator. Points in the unstable domain near $P_{abs} = 11.5\,W$ were left out of the fit.

The output characteristics of the laser in the presence of all additional intra-cavity elements are presented in Figure 2.15. The laser was optimized at maximum pump power. The lasing threshold was found at an absorbed pump power $P_{\mathrm{abs}} = 9.8\,\mathrm{W}$. The power rises linearly above threshold with a slope efficiency of $\eta_{\mathrm{sl}} = 36.6(6)\%$. Between $P_{\mathrm{abs}} = 11\,\mathrm{W}$ and 12 W the output power departs from a linear behavior and becomes unstable. We attribute this to intracavity-power-induced heating of etalon E_2 and the related change of its resonance frequency, thereby leaving the optimum operation range of the two-etalon setup. Above $P_{abs} = 12\,\mathrm{W}$ we recover the initial slope with stable operation[¶].

As compared to the empty cavity case, the maximum output power amounts to about half the total value. The slope efficiency is lower, whereas the lasing threshold is significantly higher. These are clear indications of the losses caused by the additional intra-cavity elements. Equation (2.30) yields increase of losses of 0.3% due to the additional intra-cavity elements for passive cavity losses of 1%, as measured in [95].

At $P_{\mathrm{abs}}(P_{\mathrm{out}}) = 12.9\,\mathrm{W}$ (1.17 W) the slope efficiency drops to $\eta_{\mathrm{sl}} = 12\%$. We first interpreted this behavior as an indication of the presence of detrimental thermal effects. This was qualitatively found before, see for instance [125]. The empty-cavity measurement performed later does not display this behavior. Another possible explanation for the change of slope is the inset of thermal effects in the additional intra-cavity elements. Especially TGG is prone to display absorption-induced thermal lensing effects, see Reference [124] and references therein, causing additional loss and change in the pump-eigenmode overlap integrals discussed before.

2.5 Spatial mode

As motivated earlier, the laser design presented before is supposed to deliver a Gaussian TEM_{00} single-mode output beam. For verification, we performed a mode-quality measurement. For this, the laser beam was focused by lens of $f = 150$-mm focal length and images of the profile were taken using a *LuCam LU055M* camera which, though equipped with a Silicon CCD sensor, has a somewhat low sensitivity at 1342 nm. We measured the beam size as a function of the position of the camera along the direction of beam propagation. The beam quality factor M^2, $M^2 \leq 1$ can be extracted by fitting Gaussian distributions to the camera images obtained and performing a fit to

$$w^2(z) = \frac{\lambda z_{\mathrm{R}}}{\pi}\left[1 + \left(M^2\frac{z - z_0}{z_{\mathrm{R}}}\right)^2\right], \tag{2.52}$$

which is an extension of Equation (2.5). M^2 is unity for a pure Gaussian (TEM_{00}) beam. From the fits presented in Figure 2.16, we get $M^2_{\mathrm{h}} = 1.02(5)$ and $M^2_{\mathrm{v}} = 0.97(3)$, both

[¶]As realized recently, the dip in the power curve is due to temperature-dependent depolarization in presence of absorption of the Faraday rotator and the $\lambda/2$ waveplate, see for instance Reference [124] and references therein. The laser emits in both directions in the unstable regime. [124] states an absorption coefficient of $\alpha_{\mathrm{TGG}} = 4.8\times10^{-3}\,\mathrm{cm}^{-1}$, measured at 1053 nm. Asuming the same absorption coefficient at 1342 nm, this corresponds to a full absorbed power of around 100 mW for the full output power. The compensation of the rotation of polarization via the half-wave plate can be optimized for all pump power values to avoid the output power dip.

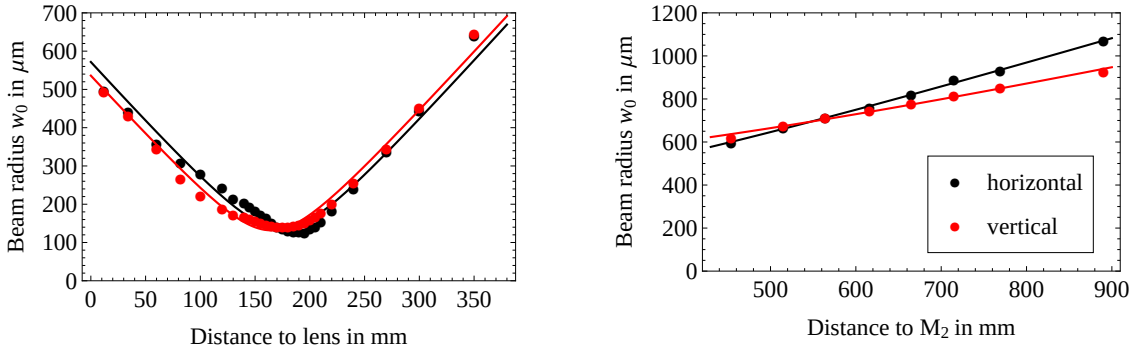

FIGURE 2.16: Spatial mode measurement performed on the laser output beam. The distances are indicated with respect to the coupling mirror M_2. LEFT: M^2 measurement, yielding values compatible to $M^2 = 1$, or pure Gaussian (TEM_{00}) output. RIGHT: measurement of the output mode. The fits assume $M^2 \equiv 1$. This measurement is used to design the coupling optics between the laser and the resonant doubling cavity. Both astigmatism and ellipticity, correctable by cylindrical lenses, are apparent.

values indistinguishable from one within experimental resolution. Thus, the output beam quality is excellent, which is important for efficient frequency doubling, as will be presented in the next chapter.

As mentioned before, due to the lack of precise knowledge of material parameters, and the over-simplification involved in the theory of thermal focusing, the laser resonator design presented in Section 2.2.4 only gives approximate results for the mode sizes $w_{h/v}$. We thus measured the mode parameters of focus position z_0 and Rayleigh length z_R with the assumption $M^2 \equiv 1$, as justified before. Precise knowledge of the shape of the output beam is crucial for the mode-matching between the laser and the doubling cavity, as will be described in the next chapter.

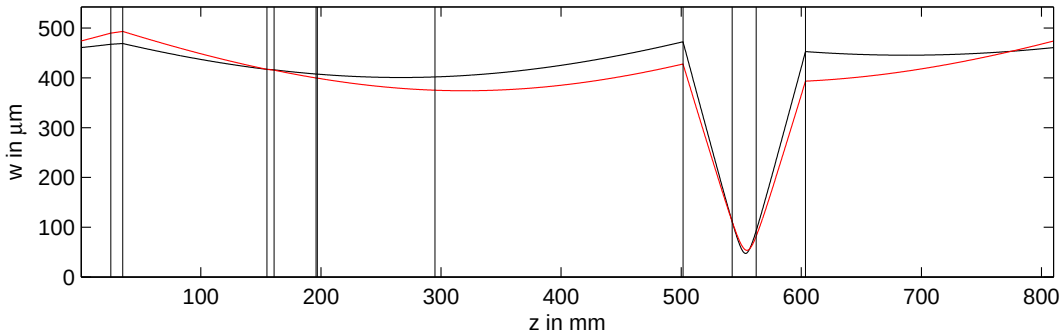

FIGURE 2.17: The laser cavity eigenmode in the wrapped-up resonator. Shown are the position-dependent widths of the laser beam for the horizontal (black) and the vertical direction (red). Horizontal lines indicate the position of optical surfaces of the intra-cavity elements. $z = 0$ is the position of the pump coupler (M_1), and the sense of propagation starts via the output coupler (M_2), which is found at 295 mm.

The measurement is realized by simply measuring the radii of the output laser beam at different positions. By comparing the fit parameters to the cavity calculations, we gain knowledge about the thermal focal length present in the gain medium under lasing conditions.

The results are given in Figure 2.16. The fits yield $z_{0,\mathrm{h/v}} = 52(7)\,\mathrm{mm} / -16(7)\,\mathrm{mm}$ and $z_\mathrm{R} = 294(8), \mathrm{mm}/540(20)\,\mathrm{mm}$ in the horizontal/vertical direction. Following the beam path upstream through the laser resonator yields a thermal focal length of $f_\mathrm{th} = 3.4\,\mathrm{m}/5.9\,\mathrm{m}$ from knowledge of the cavity geometry. The values obtained for the thermal lens are much greater than the theory value $f_\mathrm{th,theo} = 0.26\,\mathrm{m}$ obtained in Section 2.2.3. We attribute this to the oversimplifications in the theoretical analysis. We thus measure thermal effects significantly less detrimental than predicted by theory. A second interpretation presented in Section 2.4 is the onset of thermal lensing in the additional intra-cavity-elements (TGG, waveplate, etalons), which are not included in the analysis.

Comparing the Nd:YVO_4 mode size to the pump mode size, we get $w_l/w_p = 0.9/1.1$ in the vertical/horizontal direction, significantly greater than predicted by Equation (2.43). Together with the diminished thermal effect discussed before, this indicates lower aberrations even at mode-size-to-pump-size ratios close to 1.

2.6 Summary

In this chapter we have presented design and the characterization of a single-mode diode-pumped all-solid-state laser source at 1342 nm, capable of creating powerful frequency-doubled light at the lithium D-line resonances near 671 nm. We have justified the choice of Nd:YVO_4 as the active medium in our laser. We then have presented the theoretical tools needed to design a solid-state laser, concluding in the presentation of the chosen geometry. Thereafter, we have discussed the methods employed to force unidirectional operation, and to impose single-frequency operation. We have characterized the laser output in great detail. Measurements of the output power as a function of the absorbed pump power have been presented and compared to the results of the empty-cavity case. We have measured a maximum of 1.3 W of single-frequency output power, tunable from 1341.7 nm to 1342.8 nm. We have obtained a beam-quality factor of $M^2 \approx 1.0$ and characterized the output spatial mode. This measurement is indispensable for efficient coupling of the output to the doubling cavity, which will be presented in the next chapter.

Chapter 3

Second harmonic generation

To produce light at 671 nm from the laser source presented in the preceding chapter, we need to frequency-double its output radiation. Since we only have a limited amount of fundamental power available, the frequency doubling method needs to be efficient in order to meet our goals of Watt-level second harmonic output. We thus have to resort to second-harmonic generation in a resonant doubling cavity.

In this chapter, we will present the frequency-doubling setup. In Section 3.1, we will first consider briefly the theoretical aspects necessary for second-harmonic generation in a resonant doubling cavity. In Section 3.2 will then justify our selection of periodically-poled potassium titany phosphate (ppKTP) as the nonlinear medium. Thereafter, we will discuss in Section 3.3 the single-pass conversion measurements necessary for designing the resonant enhancement cavity. The design will be presented in Section 3.4. In Section 3.5 we will detail on measurements of the nonlinear conversion in the doubling cavity, and we will summarize the chapter in Section 3.6.

3.1 Theory of frequency doubling

In this section, a brief overview of the theoretical concepts needed to describe nonlinear interactions of Gaussian beams will be given. We will describe the technology of quasi phase matching and demonstrate its superiority over birefringent phase matching. We will finally present an approximate result for the temporal behavior of dephasing effects due to absorpion in optical media.

3.1.1 Nonlinear conversion

When an electro-magnetic wave is passing through a medium, the medium is polarized by the electric field $\mathbf{E}$ of the incident wave. The polarization vector $\mathbf{P} = \sum_{i=1}^{3} P_i \, \mathbf{e}_i$ reads

$$P_i = \varepsilon_0 \left(\chi_{ij}^{(1)} E_j + \chi_{ijk}^{(2)} E_j E_k + \chi_{ijkl}^{(3)} E_j E_k E_l + \ldots \right) \tag{3.1}$$

where the $\mathbf{e}_i$ are an orthonormal set, ε_0 is the the vacuum permittivity and the material-dependent tensors $\chi^{(k)}$ of rank $k+1$ account for the k-th order process. We will concentrate here on second-harmonic generation and neglect all higher-order effects, which is a good approximation in the general non-resonant case. $\chi^{(2)}$ is only non-zero in crystals without inversion symmetry. Because the coupling between fundamental waves is not important, and because of further symmetries, $\chi^{(2)}$ is reducible to a 3×6 matrix containing 10 independent elements d_{jk} [126]. We introduce the nonlinear polarizations

$$\mathbf{P}_{\omega,j}^{\mathrm{nl}}(\mathbf{r}) = 2\varepsilon_0 d_{jk} \mathbf{E}_{2\omega,k}(\mathbf{r}) \mathbf{E}_{\omega,j}^{*}(\mathbf{r}) \tag{3.2}$$

$$\mathbf{P}_{2\omega,k}^{\mathrm{nl}}(\mathbf{r}) = \varepsilon_0 d_{jk} \mathbf{E}_{\omega,j}^{2}(\mathbf{r}) \, , \tag{3.3}$$

where the indices $\omega(2\omega)$ refer to the frequency and d_{jk} is the effective nonlinear coefficient of the material with $j(k)$ the polarization of the fundamental (second harmonic) wave. One has now to solve the coupled Helmholtz equations

$$(\nabla^2 + k^2)\mathbf{E}_{\omega,j}(\mathbf{r}) = -2\varepsilon_0 \mu_0 \omega^2 d_{jk} \mathbf{E}_{2\omega,k}(\mathbf{r}) \mathbf{E}_{\omega,j}^{*}(\mathbf{r}) \tag{3.4}$$

$$(\nabla^2 + k^2)\mathbf{E}_{2\omega,k}(\mathbf{r}) = -4\varepsilon_0 \mu_0 \omega^2 d_{jk} \mathbf{E}_{\omega,j}^{2}(\mathbf{r}) \, , \tag{3.5}$$

which can be solved in the paraxial approximation. In the limit of weak conversion, or no pump depletion, this generally yields a second harmonic (SH) output power $P_{2\omega}$ in the form of

$$P_{2\omega} = \eta_{\mathrm{SHG}} P_{\omega}^{2} \, , \tag{3.6}$$

with P_ω the fundamental or pump beam power and η the conversion efficiency. In [126, 127], Boyd and Kleinman derived the following expression for η, for second harmonic interaction of Gaussian beams:

$$\eta_{\mathrm{SHG}} = \frac{2\omega^3 d_{jk}^2 L}{\pi \varepsilon_0 c^4 n_{\omega,i} n_{2\omega,j}} h(\alpha, \beta) \, , \tag{3.7}$$

where $n_{\omega(2\omega),i(j)}$ the corresponding refractive indices of the material, L the nonlinear material length and c the speed of light in vacuum. The material parameters can be recast as

$$\eta_{\mathrm{mat},jk} = \frac{d_{jk}^2}{n_{\omega,j} n_{2\omega,k}} \approx \frac{d_{jk}^2}{n_{\omega,i}^2} \, , \tag{3.8}$$

governing the doubling efficiency. The function $h(\alpha, \beta)$ is given as

$$h(\alpha, \beta) = \frac{1}{4\alpha} \left| \int_{-\alpha}^{\alpha} \frac{\mathrm{e}^{\mathrm{i}\beta\tau}}{1 + \mathrm{i}\tau} \, \mathrm{d}\tau \right|^2 , \tag{3.9}$$

with the focusing parameter $\alpha = L/2z_\mathrm{R}$, where z_R is the Gaussian beam Rayleigh length assumed here equal for both waves, yielding a waist smaller by a factor $1/\sqrt{2}$ for the second harmonic light. The phase-matching parameter

$$\beta = \beta(T) = \frac{4\pi z_\mathrm{R}}{\lambda} \left(n_{\omega,j}(T) - n_{2\omega,k}(T) \right) \tag{3.10}$$

is temperature- and polarization-dependent in the case of birefringent media, and λ is the fundamental vacuum wavelength. The derivation assumes no depletion of the fundamental wave and absence of losses. The integral in Equation (3.9) needs to be calculated numerically except for the two limiting cases $\alpha \to 0$ and $\alpha \to \infty$. It has a global maximum of $h_\mathrm{max}(2.84, 0.573) = 1.068$. The fact that the optimum β is non-zero reflects the fact that we have Gaussian beams instead of plane waves. Putting in values for the usual lengths and parameters of nonlinear media, this results in a doubling efficiency η_SHG in the %/W range at best. Thus for the available cw laser power, single pass doubling is not an option and one has to resort to resonantly enhanced intracavity doubling.

3.1.2 Quasi-phase matching

Efficient conversion requires the phase-matching parameter β to be close to zero (and exactly zero for the plane-wave limit $\alpha \to 0$). In the presence of dispersion, as present in all optical materials,this condition is not fulfilled. Thus, one has to resort to different kinds of phase-matching techniques using angular- and temperature tuning in birefringent crystals to fulfill $\beta \simeq 0$, see for instance [126]. The use of different polarization axes yields small conversion, since the off-diagonal values of d_{jk} normally are small in comparison to the diagonal elements d_{jj}.

To circumvent these complications, one can resort to quasi phase-matching. It was proposed by Bloembergen et al. [128] in 1962 and was brought to practice one year after [129]. The idea is to invert the sign of the optical axis whenever the interference between the fundamental-wave-driven dipoles and the second harmonic wave becomes destructive. The dipoles then oscillate with a phase shift of π and thus contribute constructively to the second harmonic wave. The length of the region over which constructive interference occurs is then chosen to be the poling period Λ. The accessibility of the much greater diagonal elements d_{jj} of the nonlinear tensor allows for higher single-pass efficiencies η_SHG while keeping the phase matching condition of optimum β. Quasi phase-matching using domain poling in bulk ferroelectric materials was first demonstrated in lithium niobate [130] in 1993.

Quasi-phase matching is favorable in the intracavity case because of the excellent beam quality achievable without beam walk-off [126, 131], and the avoidance of tedious angle tuning. Compared to the bulk case, the same equations (3.6)–(3.10) hold, by performing the following replacements:

$$\beta \to \beta - 2\pi z_\mathrm{R}/\Lambda \tag{3.11}$$

where Λ is the poling period and

$$d_{jk} \rightarrow d_{\text{eff}} = 2d_{jj}/\pi\,. \tag{3.12}$$

From Equations (3.8) and (3.12) we thus get an efficiency improvement of

$$\frac{\eta_{\text{SHG,QPM}}}{\eta_{\text{SHG,BPM}}} = \left(\frac{2}{\pi}\frac{d_{jj,\max}}{d_{jk,\max}}\frac{n_j(2\omega)}{n_k(2\omega)}\right)^2, \tag{3.13}$$

where the index extensions of η_{SHG} stand for quasi phase-matching (QPM) and birefringent phase-matching (BPM). In the case of potassium titanyl phosphate (KTP), using the data from [132] this yields

$$\frac{\eta_{\text{QPM}}}{\eta_{\text{BPM}}} \approx \left(\frac{2}{\pi}\frac{d_{33}}{d_{32}}\right)^2 \approx 6\,, \tag{3.14}$$

which represents a substantial increase in single-pass doubling efficiency.

3.1.3 Thermal effects and related dynamics

We want to briefly consider here the dynamic behavior of an optical material when absorbing a light beam. Heat is locally deposited in the medium, modeled by the heat source term $Q(\mathbf{r},t)$, as in Chapter 2. We have

$$Q(\mathbf{r},t) = \alpha_{\text{abs}} I(\mathbf{r},t)\,, \tag{3.15}$$

with the beam intensity $I(\mathbf{r},t)$ and the absorption coefficient α_{abs}. The heat equation reads

$$\frac{\partial}{\partial t}T(\mathbf{r},t) = \frac{\kappa}{\rho c_{\text{p}}}\nabla^2 T(\mathbf{r},t) + \frac{Q(\mathbf{r},t)}{\rho c_{\text{p}}}\,, \tag{3.16}$$

with the thermal conductivity of the medium κ, its mass density ρ and its heat capacity c_{p}. The quantity $\xi = \rho c_{\text{p}}/\kappa$ is an important material constant governing dynamic effects and should be considered when choosing a proper nonlinear medium. In the steady state, $t \rightarrow \infty$, it reduces to the Poisson equation

$$\nabla^2 T(\mathbf{r}, t\rightarrow\infty) = -\frac{Q(\mathbf{r})}{\kappa}\,, \tag{3.17}$$

which can be solved for top-hat [110] or Gaussian shapes [112] of $Q(\mathbf{r})$ in cylindrically-shaped media. The thermal conductivity should thus be high to diminish thermal gradients, which can lead to local dephasing in the phase-matching conditions (3.10) and (3.11). The solution in the cylindrically symmetric Gaussian case reads

$$\delta T(r,z) = \frac{\alpha_{\text{abs}} P_{\text{inc}}\exp(-\alpha_{\text{abs}} z)}{4\pi\kappa}\left[\ln\left(\frac{r_0^2}{r^2}\right) + E_1\left(\frac{2r_0^2}{w^2(z)}\right) - E_2\left(\frac{2r^2}{w^2(z)}\right)\right], \tag{3.18}$$

where $\delta T(r,z)$ is the temperature offset from the material edge, where the temperature is kept constant in a solid copper mount as discussed in Chapter 2. P_{inc} is the incident power of the Gaussian beam of width $w(z)$. r_0 is the radius of the material, considered

cylindrical here. E_i are exponential integral functions of degree i, where the E_2 term is negligible under all practical circumstances.

If we assume a sudden switch-on of $Q(\mathbf{r},t) = \theta(t)Q(\mathbf{r})$ in a medium of initially homogeneous temperature, $\theta(t)$ being the Heaviside function, $\nabla^2 T(\mathbf{r}, t=0) = 0$, (3.16) reduces to

$$\frac{\partial}{\partial t} T(\mathbf{r}, t=0) = \frac{Q(\mathbf{r})}{\rho c_\mathrm{p}} \,. \tag{3.19}$$

Regarding the on-axis values for $\mathbf{r} = (0,0,z)$, we introduce a typical time scale

$$\tau_\mathrm{typ} = \frac{\delta T(z, t\to\infty)}{\frac{\partial}{\partial t} T(z, t=0)} = \frac{5.9}{16\pi} \frac{\lambda L}{\arctan\left(\frac{L}{z_\mathrm{R}}\right)} \frac{\rho c_\mathrm{p}}{\kappa} \simeq 3\,\mathrm{ms} \tag{3.20}$$

for this process, where L is the length of the medium and z_R and w_0 are the parameters of the Gaussian beam, as presented in Section 2.2.1. Our geometrical parameters of $r_0/w \simeq 10$ were assumed, yielding to the numerical prefactor of 5.9. Since our crystals have cross-sections of $6 \times 1\,\mathrm{mm}^2$, and the beam is off-centered on the long axis, r_0 was set to 0.5 mm, yielding the numerical factor of 5.9 in Equation (3.20). One should note that one would have to perform a finite element analysis to get a better estimate for the temperature profile.

The meaning of Equation (3.20) is twofold: First, a fast switch-on process compared to τ_typ can occurs when a build-up cavity comes to resonance. τ_typ does not depend on the $Q(\mathbf{r})$, so it is independent of the absolute circulating power and the absorption coefficient. Even in presence of increased heating due to second-harmonic-induced fundamental absorption (often termed green-induced infrared absorption in literature), this time scale will not change. Second, under normal operation, a doubling cavity is held in resonance by a lock circuit, the circuit bandwidth should be at least on the order of magnitude of $1/\tau_\mathrm{typ}$.

3.2 Choice of the nonlinear medium

In this section, we will motivate the selection of periodically-poled potassium titanyl phosphate (ppKTP) as the nonlinear medium in the resonant doubling cavity.

As we saw in Section 3.1.2, it is advantageous to choose periodically poled (pp) materials for efficient nonlinear conversion. We will use a crystalline material with high values for d_{jk}, yielding efficient conversion, see Equation (3.7). Ferroelectricity is the property of materials to possess a spontaneous electric polarization, which can be permanently changed by applying an external electric field. It is necessary for the quasi phase-matching method treated theoretically in Section 3.1.2. This prerequisite restricts the choice to non-inversion-symmetric ferroelectric crystalline materials. The properties of three such materials (KTP = potassium triphosphate, SLT = stoichometric lithium tantalate, LN = lithium niobate) are given in Table 3.1. Standard nonlinear crystals are transparent over the whole visible range. Depending on the material, the transparency extends in the ultraviolet and infrared regions. Absorption coefficients are thus small in the region of interest. A deleterious effect, as mentioned before, is second-harmonic induced fundamental absorption (SHIFA). This effect, also termed green-induced infra-red absorption (GRIIRA), describes the increased absorption of

Material	KTP	SLT	LN
d_{33}[pm.V^{-1}]	16.9 [132]	10.0 [133]/ 14.1 [134]	27 [134]
$n_z(\lambda = 1342\,\text{nm})$	1.82 [135, 136]	2.12 [137]	2.15 [138]
$\eta_{\text{mat},33}$[pm^2.V^{-2}]	86.2	22.2/44.2	157.7
α_{abs}[%.cm^{-1}]	< 0.2 [139]		
transp. window [μm]	0.365-4.3 [138]	0.270-5.5 [138]	0.305-5.5 [138]
I_{dam}[MW.cm^{-2}]	> 37 [140]	2 [134]	0.001-2 [134]
ρ[g.cm^{-3}]	3.03 [66]	7.465 [141]	4.628 [142]
c_{p}[J.kg^{-1}.K^{-1}]	728	426 [143]	648 [143]
κ[10^{-2}W.cm^{-1}.K^{-1}]	(2.0,3.0,3.3) [144]	8.8 [133] / 5 [141] / 4.6 [145]	4.4 [143]/4.6 [133]
$\xi = \rho c_{\text{p}}/\kappa$[$10^3$ s.m^{-2}]	11.0/7.4/6.7	3.6/6.4/6.9	6.8/6.5

TABLE 3.1: Comparison of material parameters for different ferroelectric nonlinear media (KTP = potassium triphosphate, SLT = stoichometric lithium tantalate, LN = lithium niobate). The definitions of the physical quantities are given in the text. The material efficiency parameter $\eta_{\text{mat},33} \simeq d_{33}^2/n_z^2(\lambda)$ is as given as in Equation (3.8). The values for the thermal conductivity κ of KTP from [144] are for the three different axes of the KTP crystal. The different values for the dynamic parameter $\xi = \rho c_{\text{p}}/\kappa$, see Equation (3.20), were calculated with the values for $(\rho, c_{\text{p}}, \kappa)$ as given here and in the order of the different values for κ.

the fundamental wavelength in the presence of the second-harmonic light. It is detrimental especially when using resonant buildup cavities, thus restricting the use of LN ([134, 146]).

Another detrimental effect in LN is photorefractivity. It consists of a rapid shift of refractive index due to the field-induced release of charge carriers in the material. As the cavity optical length is changed abruptly, this is a catastrophic effect when trying to keep a build-up cavity frequency-locked to a pump laser.

When operating at high intensities, optical media might become subject to damage. The damage threshold intensity I_{dam} is highest for KTP, whereas it can be dangerously low for LN, depending on the crystal composition (stoichiometric or congruent, precence of dopants such as MgO, Fe). This threshold, after SHIFA and photorefractivity, further limits the high-power handling capability of LN.

KTP, on the other hand, displays a detrimental effect called gray-tracking. This effect takes its name from the appearence of visible gray tracks in the crystal. This reversible increase of absorption limiting frequency-doubling of Nd:YAG lasers at 1064 nm. Since the photon energies involved in our case are a lot lower, we have reason to believe that this effect will not occur for doubling of 1342 nm light.

The material-dependent conversion-efficiency parameter $\eta_{\text{mat},33}$ is highest for LN, but the material suffers from its higher refractive index in comparison to KTP. SLT displays the lowest conversion efficiency, but the deleterious effects mentioned above are largely suppressed [134], and its lower absorption edge extends largely in the UV, making it an interesting alternative for high-power and short-wavelength applications.

SLT is a relatively new material in which, to the best of our knowledge, the intensity-limiting effects described before are strongly reduced.

The important thermal parameter ξ is within a factor of three for the materials, and furthermore depends on the publication or crystal axis considered. The typical time scale τ_{typ} calculated in Equation (3.20) scales accordingly. Thus, a standard lock scheme using piezo-electric tuning of the doubling cavity length will allow for stabilization in all cases with a standard lock circuit bandwidth of a few kilohertz. The heat conductivity κ is somewhat low for KTP, but it only plays a significant role for the steady-state temperature profile (solution of Equation (3.17)). Since the linear absorption parameter α_{abs} is small, κ is a less important criterion for choosing the appropriate crystal.

For the reasons mentioned above, we consider ppKTP being a good trade-off between conversion efficiency and high-power-handling capability. For the poling of the crystals, we established a collaboration with the Institute of Laser Physics of the Royal Institute of Technology (Kungliga Tekniska Högskolan, KTH). The group of Carlota Canalias is specialized in electric field poling of KTP at room temperature [147], which is the poling method chosen to produce our samples. The length of the crystal used in this work is 19.2 mm, featuring an optical aperture of $6 \times 1\,\mathrm{mm}^2$. The length of the periodically-poled region is 17.25 mm. The poling period was chosen to be $\Lambda = 17.61\,\mu$m, resulting in expected plane-wave phase matching condition $\beta(T) = 0$ (Equation 3.11) at $T = 23.5°$C using the temperature-dependent Sellmeier equations from [135, 136]. This period is easily manufacturable. Both surfaces are AR coated at 1342 nm and 671 nm.

3.3 Single-pass measurements

We use a single-pass method to independently characterize the ppKTP crystal employed for intra-cavity frequency doubling in the next section. The completely automatized measurement setup is represented in Fig. 3.2.

The 1342-nm laser output was passed through a mode-cleaning fiber, resulting in a beam with a clean Gaussian profile. The output power was $\simeq 500$ mW of single-frequency infrared light, resulting in a maximum of $P_{2\omega} \simeq 2$ mW of red light output, the two beams being separated using mirror $\mathrm{M}_{\mathrm{sep}}$. The fundamental power was monitored using a Ge photodiode (PD) exploiting the finite transmission through mirror $\mathrm{M}_{\mathrm{ref}}$. The signal was calibrated against the IR power P_ω incident on the crystal. The finite transmittance of $\mathrm{M}_{\mathrm{ref}}$ at 671 nm was taken care of, and the SH power measured using a commercial power meter (Thorlabs S130A). The response of the power meter's Si photodiode at 1342 nm is negligible, and so is the corresponding transmission of $\mathrm{M}_{\mathrm{sep}}$ Thus, no infrared power is detected by the power meter. The shutter, driven at $\simeq 1$ Hz with a 50% duty cycle allowed for the determination of dark current offset drifts for both power measurements, which is of highest importance for low conversion efficiencies. The crystal is mounted on a transverse (xy-) translation stage and temperature controlled with an accuracy of ≈ 10 mK using a Peltier element and a home-made temperature controller. A set temperature ramp was applied to the controller, scanning the full 55°C range in about 30 minutes. The slow ramp allowed for adiabatic behavior of the temperature measurement, permitting independent determination of the temperature of the crystal measured by a LM35 sensor attached to the crystal mount.

The experimental results are presented in Figure 3.1. A weighted numerical fit to the Boyd-Kleinman theory (Equation (3.7)) describes the data well. The error bars

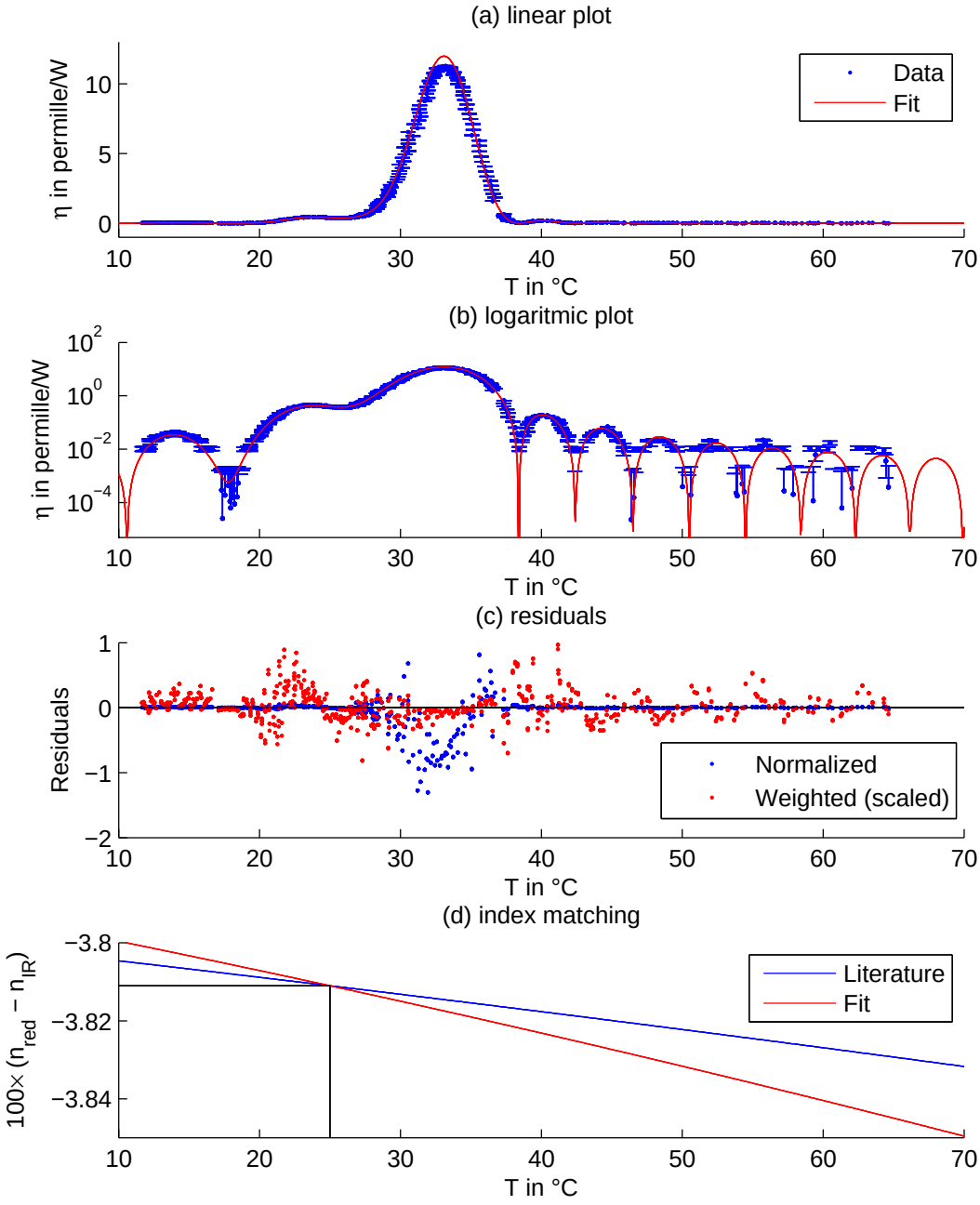

FIGURE 3.1: Temperature-dependent single-pass doubling efficiency measurements. (a) Linear and (b) logaritmic plot of the measured data (dots) and the fit (solid line). The error bars are the standard deviation of the data measured for each point. (c) shows the residuals with and without weighting, whereas (d) shows the refractive index difference from the temperature-dependent Sellmeier equations for KTP published in [135, 136] and the fit. The difference between the two was artificially set to zero at $T = 25°C$, where the non-temperature-dependent Sellmeier equation for KTP was measured in [136].

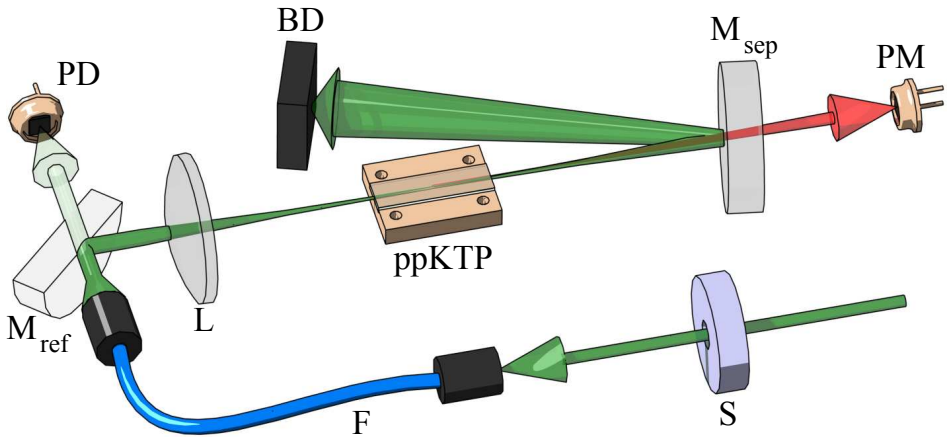

FIGURE 3.2: Setup of the single pass efficiency measurements. The laser output is sent through shutter (S) before being coupled to a PMSM mode-shaping fiber (F). The power leaking through mirror M_{ref} is referenced on a photodiode (PD), and the beam is then focussed into the ppKTP crystal by a lens (L). Mirror M_{sep} separates second harmonic from fundamental light, which is sent in a beam dump (BD), whereas the converted light power is measured with a power meter (PM).

$u(\eta(T))$, representing the fit weights $w(\eta(T)) = (u(\eta(T)))^{-2}$, stem from the standard deviation of the measured power data. The temperature dependence of the phase matching parameter β is taken into account up to quadratic order. The full 99%-width of the peak of 0.7°C allows the use of standard temperature controllers. However, the optimum phase-matching temperature of 33.2°C differs slightly from the theoretical value of 23.5°C. This can be explained by a small difference to the Sellmeier equations as presented in [135, 136] and a non-perfect alignment between pump beam and crystal axis. In Figure 3.1 (d) we plot the fitted refractive index difference $n_{2\omega,3} - n_{\omega,3}$, which according to (3.10) is a measure of the slope of the phase matching parameter β as a function of temperature. It is about twice as high as the temperature-dependent Sellmeier-equations prediction.

Since we performed a weighted fit, there are deviations visible between the fit curve and the measured data points around the peak value (blue dots in Figure 3.1 (c)), where the error bars $u(\eta(T))$ are largest. This can be explained by thermal effects due to linear absorption and SHIFA, leading to local dephasing due to heating and the non-zero pump depletion. The fit yields $\eta_{SHG}(T_{opt}) = 1.20\%/W$ at the optimal temperature $T_{opt} = 33.1°C$ for $\alpha = 3.53$.

The maximum measured single pass efficiency of 1.13%/W represents 74% of the theoretical maximum of 1.53%/W from Equation (3.7) with the parameter $\alpha = 3.53$ as fitted and d_{33} for KTP from [132]. This can be explained by imperfections of the domain poling, most probably deviations from perfect periodicity, or the 50% duty cycle. We thus derive an effective nonlinear coefficient of $d_{eff} = 9.2\,pm/V$ for our crystal, significantly lower than the literature value of $16.9\,pm.V^{-1}$ [132].

3.4 Doubling cavity design

In Section 3.1 we saw from Equations (3.6) to (3.12) that the single-pass doubling efficiency of the chosen KTP crystal is in the %/W range, which is why we need to use a resonant doubling cavity to build up a strong fundamental wave and to thus convert efficiently.

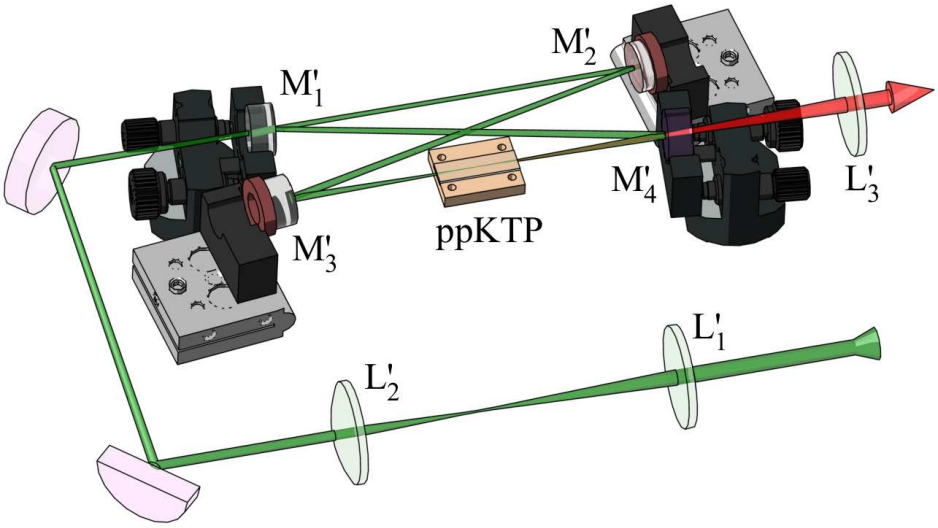

FIGURE 3.3: The doubling cavity setup consisting of the four mirrors M'_{1-4} and the ppKTP nonlinear crystal. The light is coupled to the TEM_{00} cavity eigenmode using lenses $L'_{1,2}$, whereas L'_3 collimates the second harmonic output. Some mechanical components are sectioned to improve visibility of the laser (second harmonic) beam, depicted in green (red). The distance between M'_3 and M'_4 is 93 mm. The piezoelectric transducers underneath M'_2 and M'_3, used for changing the cavity length, are pictured in dark red. Dimensions of the coupling light paths are not to scale.

The doubling cavity mechanical setup is similar to the one presented in [69] and depicted in Figure 3.3. As for the laser, a four-mirror-folded-ring cavity is used. The pump light is coupled through the plane mirror M'_1 for which several reflectivity values $\mathcal{R}_c$ are available. All other mirrors are highly reflective at 1342 nm and transmitting at 671 nm. M'_3 and M'_4 are concave with a radius of curvature of 75 mm. Mode matching between the laser output and the cavity was accomplished using a set of spherical lenses. The crystal mount is identical to the one described in Section 3.3. The frequency doubled light is transmitted through M'_4 and collimated using a lens of $f'_3 = 150$ mm focal length, yielding a Gaussian $1/e^2$ beam radius of 0.9 mm.

The cavity design is presented in Figure 3.4. We chose the distance $d_{cu} = 93$ mm between the two curved mirrors M'_3 and M'_4, where all requirements are fulfilled: We work on a position well centered (but slightly shifted) in the stability range and a large enough waist of $w_0 \simeq 55\,\mu$m. It avoids frequency degeneracy of higher-order transverse cavity eigenmodes and the TEM_{00} mode. It also accounts for a circular beam in the crystal and thus for a circular SH output. The weaker-than-optimal focusing leads to a slightly reduced $h(\alpha = 1.22, 0.818) = 0.865$, or a fraction $h/h_{max} = 81\%$ of the optimum value, yielding $\eta = 0.92\%/W$. This choice represents a trade-

off between maximum single-pass doubling efficiency and intensity-related detrimental effects such as nonlinear and SH-induced absorption (SHIFA, [148]) and possible gray-tracking [149].

The doubling cavity is kept under a dry-air atmosphere in an aluminum-acrylic-glass housing to prevent dust and moisture from deteriorating the quality of the optical surfaces, and to shield from thermal and acoustic perturbations.

3.4.1 Mode matching and intra-cavity loss

We can change the length of the doubling cavity by δL when applying a voltage to the piezoelectric transducers mounted below the cavity mirrors M_2' and M_3' (cf. Figure 3.3). In the absence of nonlinear loss the intra-cavity power $P(\delta L)$ reads

$$P(\delta L) = \sum_{lm} \frac{P_{lm}}{1 + F \sin^2 (\varphi_{lm} + \omega \delta L / c)} , \tag{3.21}$$

where F is a parameter related to the cavity Finesse and thus to the losses, see Equation (2.47). P_{lm} are the contributions from the TEM_{lm} modes, and c is the speed of light in vacuum. The constant cavity round-trip phase of φ_{lm} depends on the cavity geometry and should be chosen such as to not be degenerate (modulo $2\pi/N_{\mathrm{int}}$ for low integer numbers N_{int}), as mentioned before. This avoids simultaneous presence of higher-order modes in the cavity and thus keeps the SH output of TEM_{00} mode quality.

We define the mode-matching efficiency as

$$\eta_{\mathrm{mm}} = \frac{P_{00}}{\sum P_{lm}} . \tag{3.22}$$

A cavity scan measurement was performed for low intra-cavity powers of up to $\approx$ 500 mW and the crystal temperature tuned far from the optimum phase matching value, so that nonlinear conversion can be neglected. M_3' is glued on a slow piezoelectric transducer (PZT), allowing to act on the cavity length in the $2 - \mu$m range, see Figure 3.3. While scanning the cavity length by δL, we measured a power signal leaking through M_2', which is proportional to $P(\delta L)$ and allows for simultaneous determination of both the cavity losses and mode-matching efficiency. Examples of such measurements are given in Figure 3.5.

The mode-matching efficiency was maximized to $\eta_{\mathrm{mm}} = 92\%$ using two telescopes composed of spherical lenses only. One of the two telescopes is shown in Figure 3.3. The linear cavity round-trip losses $\mathcal{L}_{\mathrm{emp(tot)}}$ can be quantified from the fit parameter F, where emp(tot) means the empty cavity (cavity including ppKTP crystal). The results are presented in Table 3.2. Inserting the crystal rises the losses by $\mathcal{L}_{\mathrm{cr}} \simeq 1\%$. This can be accounted for by residual absorption and scattering in the ppKTP crystal and imperfections of its AR coatings. The empty cavity loss for the 5% coupler account to more than 6%, which is a significant deviation from the manufacturer's specifications. Within the errors of our measurement, we will refer to it as the $\mathcal{R}_{\mathrm{c}} = 94\%$ coupler from now on.

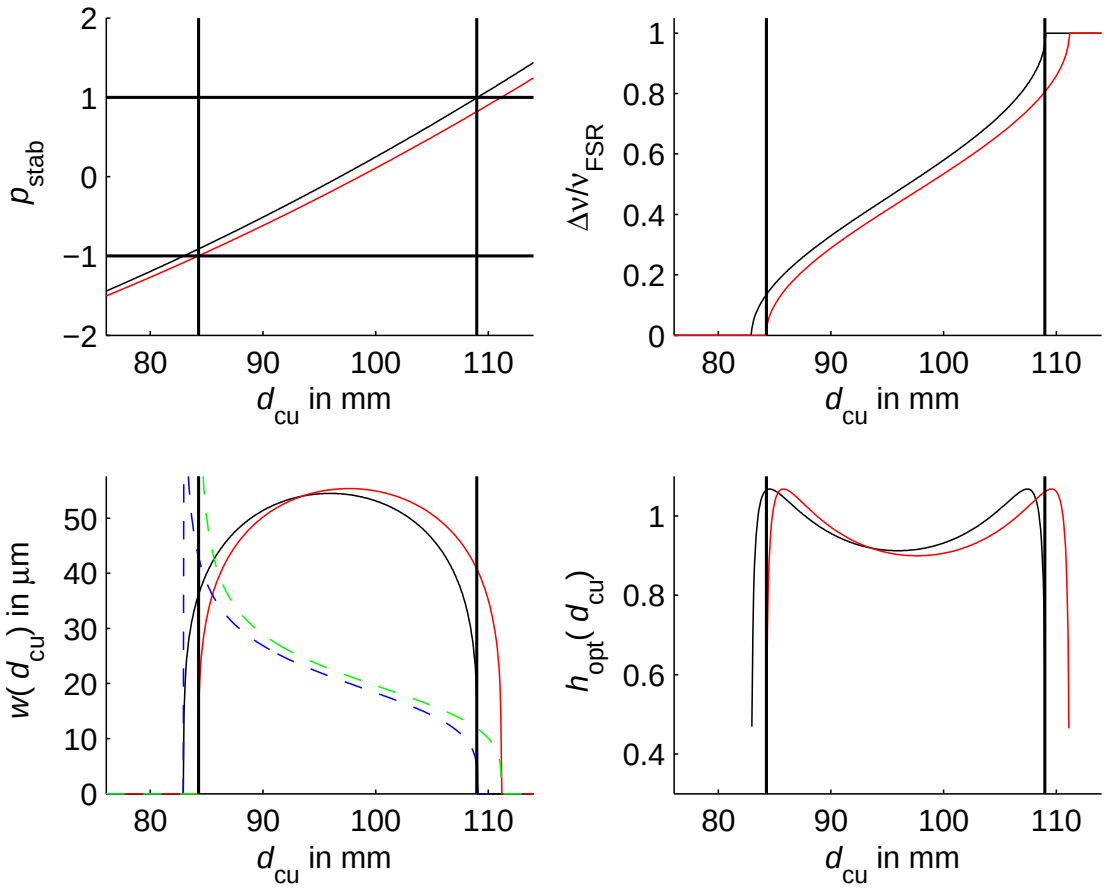

FIGURE 3.4: Geometric design of the doubling cavity, the variation parameter is the distance d_{cu} between the two curved mirrors M_3' and M_4'. Black (red) lines indicate the horizontal (vertical) direction in the setup. UPPER LEFT: The stability parameters p_{stab} of the cavity, which remains stable between $d_{\mathrm{cu}} = 84.3\,\mathrm{mm}$ and $d_{\mathrm{cu}} = 109.0\,\mathrm{mm}$. UPPER RIGHT: The relative mode spacing $\Delta\nu/\nu_{\mathrm{FSR}}$, defined between the TEM_{00} mode and the modes TEM_{10} (horizontal) and TEM_{01} (vertical). LOWER LEFT: The waist sizes in the doubling crystal (continuous lines). We also show the waist radii in the coupling arm (dashed lines, blue [green] stands for the horizontal [vertical] direction) between M_1' and M_2', the values being devided by a factor of ten for better visibility. LOWER RIGHT: The optimized Boyd-Kleinman function $h_{\mathrm{opt}}(\alpha) \to h_{\mathrm{opt}}(d_{\mathrm{cu}})$, see Equation (3.9). We chose the point $d_{\mathrm{cu}} = 93\,\mathrm{mm}$ where both waists in the crystal are degenerate, yielding a round SH beam, and where the relative mode spacing is around 0.4.

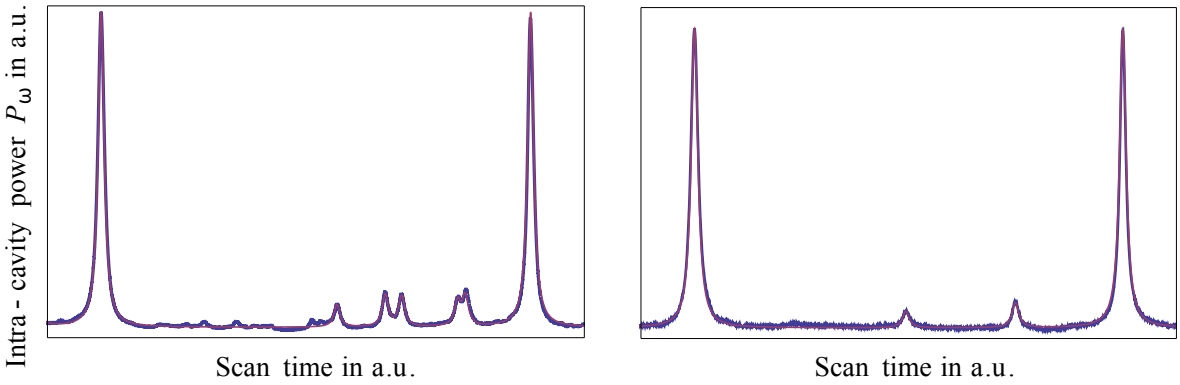

FIGURE 3.5: Examples of cavity scan measurements of the circulating power $P(\delta L)$ without (left) and with (right) the ppKTP present. Blue dots are data, while the purple lines represent fits to Equation (3.21), with the fit parameters P_{lm}, F, φ_{lm}, ω and a variable offset to compensate the voltage offset inherent to our measurement. We fit to six (three) modes in the left (right) panel. In presence of the crystal, the mode matching improves, whereas the cavity loss increases, so the resonance lines get slightly broader. From the width of the resonances we can deduce the cavity round-trip loss.

$1-\mathcal{R}_c$	$\mathcal{L}_{emp}$	$\mathcal{L}_{tot}$	$\mathcal{L}_{cr}$
5%	6.4%	7.1%	0.7%
10%	10.4%	11.2%	0.9%
17%	17.9%	19.0%	1.3%

TABLE 3.2: Passive losses in the doubling cavity measured from cavity transmission spectra at low power and conversion efficiency. $(1-\mathcal{R}_c)$ is the specified coupler power transmission, $\mathcal{L}_{emp}$ are the measured empty-cavity round trip power losses, $\mathcal{L}_{tot}$ are losses including the ppKTP crystal, and $\mathcal{L}_c$ are the inferred crystal insertion losses according to $\mathcal{L}_c$ = 1-(1-$\mathcal{L}_{tot}$)/(1-$\mathcal{L}_{emp}$).

3.4.2 Impedance matching

Impedance matching is the process of optimizing the reflectivity of the output coupler in presence of nonlinear conversion and passive round-trip loss in order to optimize the second-harmonic output for a given fundamental input power.

If we now take into account nonlinear conversion, the fundamental-mode-intra-cavity power $P_{00} = P_\omega$ at TEM_{00} resonance (referred to as cavity resonance) is a solution of

$$P_\omega = \frac{(1-\mathcal{R}_c-\mathcal{L}_1)\eta_{mm}P_{in}}{\left(1-\sqrt{\mathcal{R}_c(1-\mathcal{L}_{tot})(1-\eta_{SHG}P_\omega)}\right)^2}, \tag{3.23}$$

where P_{inc} is the fundamental pump power incident on M'$_1$, $\mathcal{L}_1$ is the coupling mirror (M$'_1$) transmission loss and $\mathcal{L}_{tot}$ is the total cavity passive loss excluding the coupler transmission. The single-pass doubling efficiency η_{SHG} is calculated according to Equation (3.7) with d_{33} as measured in Section 3.3 and $h(\alpha)$ as given by the cavity design, see Figure 3.4. The solution can be calculated analytically using *Mathematica*, yielding an expression of a length of several pages. Thus, we will not present it in this work. The

second-harmonic output power is then simply calculated according to Equation (3.6), and we define the cavity doubling efficiency as

$$\eta_{\mathrm{cav}} = \frac{P_{2\omega}}{P_{\mathrm{in}}} = \frac{\eta_{\mathrm{SHG}} P_{\omega}^2}{P_{\mathrm{in}}}\,, \tag{3.24}$$

The results are depicted in Figure 3.6. Setting $\mathcal{L}_{\mathrm{tot}} = \mathcal{L}_{\mathrm{cr}}$ and $\mathcal{L}_1 = 0$, the solution of Equation (3.23) yields a maximum SH power of 710 mW at the maximum available pump power of $P_{\mathrm{in}} = 860\,\mathrm{mW}$. It is currently limited by the quality of the AR coatings of the optical elements in the coupling pathway between the laser and the doubling cavity, and can thus easily be improved to reach values close to the maximum laser output power. This conversion is accomplished for an optimized coupling mirror reflectivity of $\mathcal{R}_{\mathrm{c,opt}} = 92\%$, yielding a total conversion efficiency of $\eta_{\mathrm{cav}} = 84\%$. For the $\mathcal{R}_{\mathrm{c}} = 94\%$ coupler we get satisfying results up to the maximum available pump power $P_{\mathrm{in}} = 860\,\mathrm{mW}$.

3.5 Second harmonic output power and limitations

In this section we will present a measurement which characterizes the resonant conversion process. We will then demonstrate limiting effects and discuss measures to circumvent them to allow scaling to higher powers.

3.5.1 Cavity characterization

After locking the cavity to the laser, as will be described in Chapter 4, the second harmonic output power $P_{2\omega}$ was measured versus the intra-cavity fundamental power P_{ω} and the 1342 nm pump power P_{in}, using the $\mathcal{R}_{\mathrm{c}} = 94\%$ input coupler. This measurement allows for a complete characterisation of the cavity, and is presented in Figure 3.7.

As expected from Equation (3.6), the conversion shows quadratic behavior for low power values. However, at elevated power levels, starting from the values $(P_{\mathrm{in}}, P_{\omega}, P_{2\omega})_{\mathrm{crit}} = (730\,\mathrm{mW}, 9.0\,\mathrm{W}, 640\,\mathrm{mW})$, only a slow linear rise in SH power with intra-cavity power is obtained, reaching its maximum at $(P_{\mathrm{in}}, P_{\omega}, P_{2\omega}) = (860\,\mathrm{mW}, 10.7\,\mathrm{W}, 670\,\mathrm{mW})$. At the same time, we notice increased intensity noise and oscillations of the error signal. We attribute this behavior to fast intensity-dependent detrimental effects. These points are thus excluded from further analysis.

We perform a fit to Equation (3.24), the solution of Equation (3.23) and η_{SHG} and $\mathcal{L}_{\mathrm{tot}}$ as fit parameters. The fit yields a single-pass efficiency of $\eta_{\mathrm{SHG}} = 0.78\%.\mathrm{W}^{-1}$ at the conversion maximum (lower left panel in Figure 3.7), slightly lower than the theoretical prediction $\eta_{\mathrm{SHG}} \approx 1.1\%.\mathrm{W}^{-1}$. The direct measurement, presented in the lower left diagram of Figure 3.7, gives slightly higher values of up to $\eta_{\mathrm{SHG}} = 0.86\%.\mathrm{W}^{-1}$ for low powers. However, it decreases with increasing power to $\eta_{\mathrm{SHG}} = 0.78\%.\mathrm{W}^{-1}$, the same value as obtained from the fit before. We attribute this change in single-pass doubling efficiency to absorption-induced heating of the crystal, leading to local dephasing of fundamental and second harmonic radiation, hence to a reduced conversion.

The fits to the second harmonic power and total conversion versus pump power in the two right panels of Figure 3.7 describe the data well. The intra-cavity losses

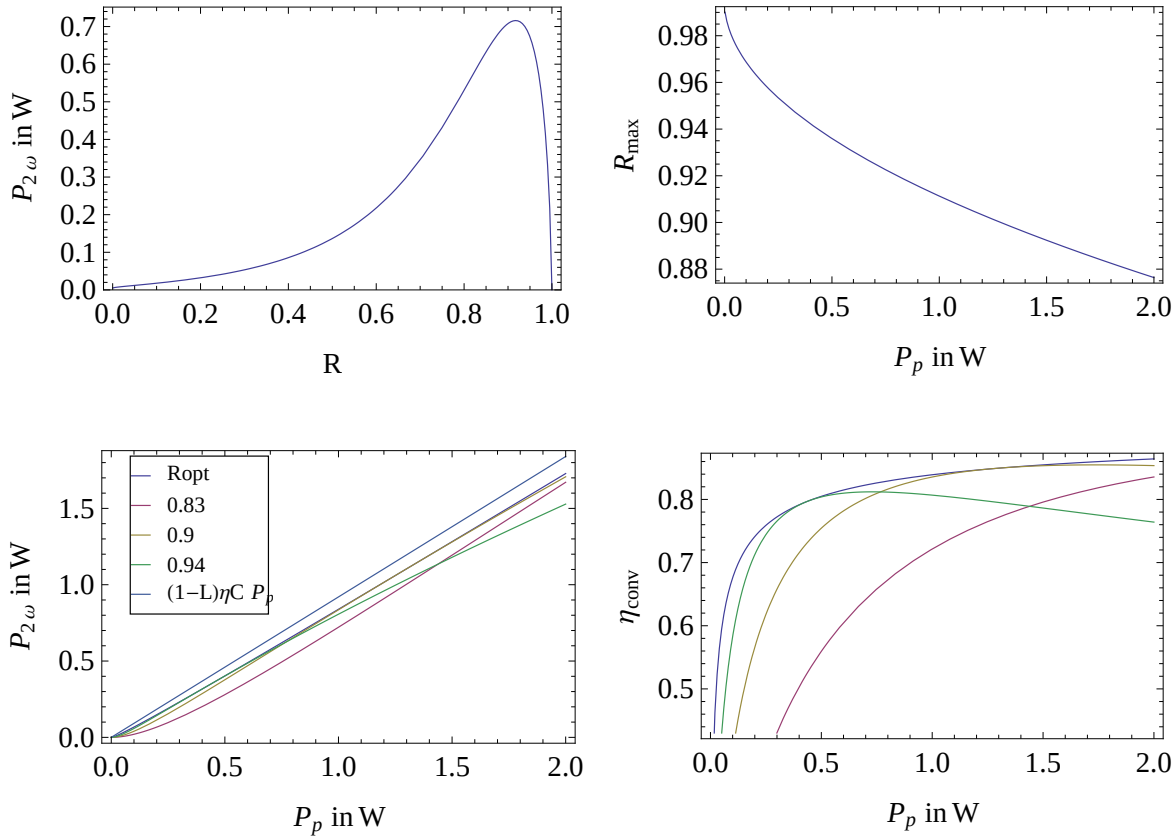

FIGURE 3.6: Calculations for the intra-cavity conversion with the parameters η_{SHG}, $\mathcal{R}_{\mathrm{c}}$ and $\mathcal{L}_{\mathrm{tot}}$ measured before. UPPER LEFT: The achievable SH power at maximum available pump power $P_{\mathrm{in}} = 860\,\mathrm{mW}$ as a function of the coupling mirror (M_1') reflectivity $\mathcal{R}_{\mathrm{c}}$. UPPER RIGHT: The optimum pump coupler reflectivity $\mathcal{R}_{\mathrm{c,opt}}$ as a function of the available pump light. LOWER LEFT: The SH output power as a function of available pump power for different values of the coupler reflectivity. Shown are the curves for $\mathcal{R}_{\mathrm{c,opt}}$ as before, the three experimentally available couplers and, as a reference, the power of the pump light coupled to the TEM_{00} mode $1-\mathcal{L}_1\eta_{\mathrm{c}}P_{\mathrm{p}}$. LOWER RIGHT: Doubling efficiencies for the same coupler reflectivity values as before. The $\mathcal{R}_{\mathrm{c}} = 94\%$ coupler allows satisfactory conversion for all pump powers up to the maximum value $P_{\mathrm{in}} = 860\,\mathrm{mW}$, while keeping a good conversion efficiency at lower powers. For higher pump powers, a lower-reflectivity pump coupler should be chosen.

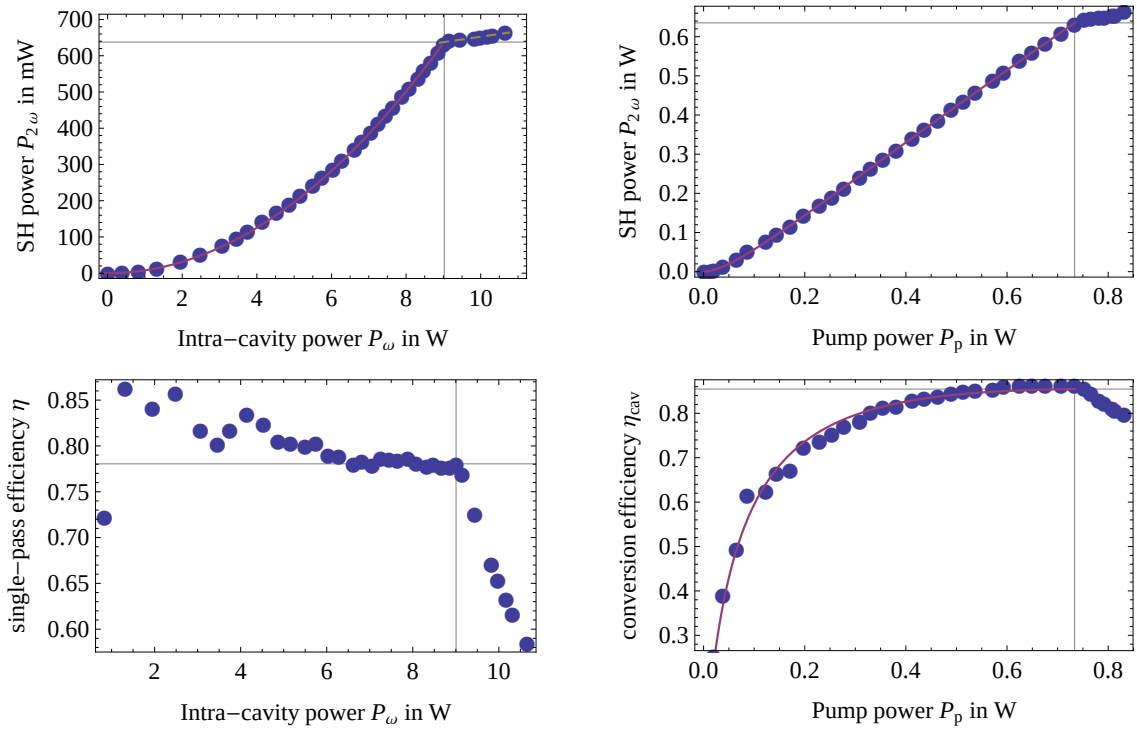

FIGURE 3.7: Cavity doubling efficiency measurements, points are measured data and lines are fits. The crossed orthogonal lines mark the onset of the lock instability, as described in the text. UPPER LEFT: The second harmonic output power versus the intra-cavity power. At $(P_{in}, P_\omega, P_{2\omega})_{crit} = (730\,\text{mW}, 9.0\,\text{W}, 640\,\text{mW})$, the conversion becomes less efficient (dashed line), these points are thus excluded from all fits. UPPER RIGHT: $P_{2\omega}$ versus pump power P_p, following the behavior predicted from theory, see Figure 3.6. LOWER LEFT: The crystal single-pass efficiency as a function of the pump power, yielding $\eta = 0.78\%.\text{W}^{-1}$ at maximum conversion efficiency. LOWER RIGHT: The total doubling efficiency η_{cav}, maximizing to 86% at high pump powers before inset of the lock instabilities. The fits yield a total passive round-trip loss of $\mathcal{L}_{tot} \simeq 0.5\%$.

of $\mathcal{L}_{tot} = 0.5\%$ fitted with this method are lower than those obtained from the low-power characterization presented in Section 3.4.1, where we had $\mathcal{L}_{cr} = 0.7\%$ for the crystal only using the $\mathcal{R}_c = 94\%$ coupler. We thus regard the latter values as upper limits. Hence, the losses of the three highly-reflective cavity mirrors are smaller than the experimental resolution.

A maximum measured doubling efficiency of $\eta_{conv} = 86\%$ is obtained just below the threshold of instability, compatible with the theoretical prediction of $\eta_{conv} = 84\%$. The fact that the measured value is slightly higher than the theory value also points to low intra-cavity loss of $\simeq 0.5\%$.

3.5.2 Measurements of thermal effect and further optimization

The abrupt change in doubling efficiency at $(P_{in}, P_\omega, P_{2\omega})_{crit} = (730\,\text{mW}, 9.0\,\text{W}, 640\,\text{mW})$ presented above indicates the presence of intensity-related effects in the doubling crystal. The cavity lock error signal becomes very noisy above threshold. In

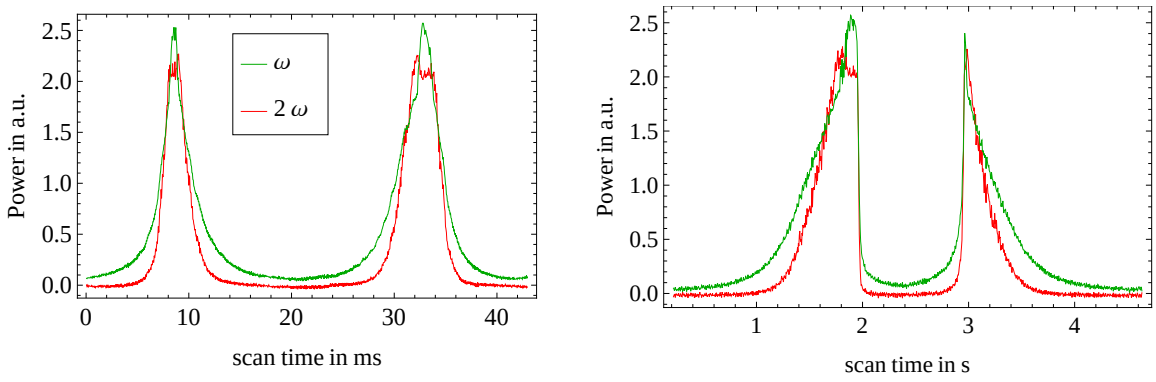

FIGURE 3.8: Thermal behavior of the crystal while scanning back and forth over cavity resonance, where on the left (right) side in each panel the cavity length is reduced (enlarged). The indices ω and 2ω refer to fundamental and second-harmonic power, respectively. Notice the different scan time scales. The direction of the scans is inverted in the middle of the data. δL (Equation (3.21)) is decreasing on the left-hand side and increasing on the right-hand side. (a) Fast scan, the two peaks are almost symmetric. (b) Slow scan, an asymmetry as reported in [150] becomes apparent. In both cases, the second-harmonic peak displays an additional plateau-like structure.

contrast to [140, 150], the cavity remains locked at all power levels.

A Fourier analysis of the error signal in the high-power range, as presented in Section 3.5.1, shows a first broad peak at 700 Hz and a second broad peak at around 1400 Hz. The corresponding time scales are within the order of magnitude of the typical time scale of the cavity buildup thermal effects, see Section 3.1.3. However, the oscillation frequencies of the cavity lock, using only the slow piezo-electric transducer, is typically located at these frequencies, as will be presented in the next chapter.

Figure 3.8 shows a fast and a slow scan over the cavity resonance. In both cases, thermal effects are clearly visible by deviations from a smooth and symmetric peak structure. The asymmetric behavior in the slow scan was already reported for ppKTP in [150], where also a significant asymmetry between the back- and forward scan was discussed. Compared to this publication, the asymmetry is not very pronounced in our case. The peak of the cavity resonance is not very sharp in the fast case, but rather forms a plateau-like structure with ripples. Since an error signal is created from the second-harmonic signal, the erratic structure can lead to the lock instability observed earlier.

When changing the pump power, the second harmonic output follows without observable hysteresis. Long-term degradation is not observed, indicating the absence of gray-tracking. However, for further characterization the setup is operated just below threshold to avoid the related rise in intensity noise.

We saw that the lower-than-optimal focusing represents a good choice in the doubling cavity design, given that the intra-cavity loss is small. By further enlarging the radius of the Gaussian mode passing the doubling crystal, one would lose in single-pass efficiency η_{SHG}. The resulting compatibility with higher intra-cavity powers should

allow for higher output powers at higher pump power values. Further optimization, not presented in the analysis above, yielded 840 mW of 671-nm output power without observation of the detrimental effects. This was achieved by finding another position in the ppKTP crystal where the beam passes. The available pump power of $P_{\mathrm{in}} \approx 1\,\mathrm{W}$ was not sufficient for observation of the intensity-related instabilities described before.

Power-scaling of the doubling section in the 671-nm light source could also be achieved using another nonlinear medium. Insertion of a crystal of periodically-poled stoichiometric lithium tantalate (ppSLT, for its material properties see Table 3.1) of the same length as the ppKTP crystal might lead to higher power tolerance. For this material, to the best of our knowledge, second-harmonic or fundamental-power-induced detrimental effects play a minor role. Calculations show that the current cavity setup could be kept without even changing the mode- or impedance matching. The eigenmode is only slightly altered, and the lower single-pass efficiency is compensated by the higher power tolerance.

3.6 Summary

In this chapter, we have presented the design and characteristics of a resonant buildup cavity, capable of efficient frequency doubling of the 1342 nm output radiation of the Nd:YVO_4 laser presented in Chapter 2. This doubling cavity is thus an essential building block to create powerful 671-nm radiation.

We first have presented the theoretical tools to design the doubling cavity including the nonlinear medium. We then have justified our choice of periodically-poled potassium titanyl phosphate as the nonlinear medium by comparing its material parameters to those of alternative crystals. The crystal's single-pass doubling efficiency and the cavity's passive losses have been measured independently. This has allowed the theoretical modeling of the cavity in terms of spatial mode and impedance matching, necessary for obtaining high power-conversion efficiencies.

The final setup has been presented and characterized. We have measured a maximum conversion efficiency of 86%, and a maximum of 840 mW of 671-nm output power. This measurement has allowed to find an upper limit of 0.5% for the doubling cavity passive roundtrip loss. We further have discussed power scaling limitations observed as well as prospects including the use of different nonlinear crystals.

Chapter 4

Frequency stabilization, characterization and implementation

In the preceding chapters, we have discussed the building blocks of an all-solid-state laser system to cool and trap Lithium atoms magneto-optically. We will present here the opto-electronic system designed to frequency-stabilize the laser system, characterize the frequency-locked output and present its implementation in the lithium experiment at Laboratoire Kastler Brossel.

In Section 4.1, we will discuss pathways of frequency-stabilization of laser systems and justify our choice for the practical realization. We will present the subsystems, the doubling cavity lock and the spectroscopy lock on the lithium D-line transitions. In Section 4.2, a full characterization of the laser system output in terms of relative intensity noise, linewidth and spatial mode quality will be presented. Special attention will be given to the presentation of the long-term stability and the every-day use of the source. In Section 4.3, we will demonstrate the implementation of the laser system in the existing Lithium experiment, and the additional setup needed to create different frequencies and to redistribute the laser light. Finally, results of the operation of the Zeeman slower and the magneto-optical of the lithium experiment at Laboratoire Kastler Brossel trap will be discussed. We will thus prove the practical applicability of the laser system for laser-cooling applications. We will summarize the chapter in Section 4.4.

4.1 Lock system

Our objective is to generate light which is frequency-stabilized with respect to the lithium D-line transitions. In laser systems, several noise sources like temperature drifts, acoustic noise and fluctuations inherent to the pump source are present, causing derivations of the resonance frequencies of optical cavities. Thus, one requires feedback loops to keep the entire laser system frequency-locked. For the combination of the Nd:YVO_4 laser and external doubling cavity presented in Chapters 2 and 3, several requirements need to be fulfilled:

1. The doubling cavity needs to be resonant with the Nd:YVO_4 laser for ensuring a good second harmonic efficiency. Practically, this means that the doubling cavity length needs to be stabilized such that its resonance frequency matches the Nd:YVO_4 laser frequency.

2. The Nd:YVO_4 laser output frequency needs to be locked such that its doubled frequency equals that of the desired optical transition. In practice, one changes the length of the laser cavity to adjust and stabilize the output frequency.

3. For cooling and trapping applications, one normally wants to lock the light frequency with a fixed offset with respect to the atomic transitions.

We thus first lock the doubling cavity resonance frequency with respect to the free-running Nd:YVO_4 laser frequency to perform Lithium spectroscopy. We afterwards lock the Nd:YVO_4 laser frequency with respect to one of the spectroscopy lines. The complete locking setup is presented in Figure 4.1.

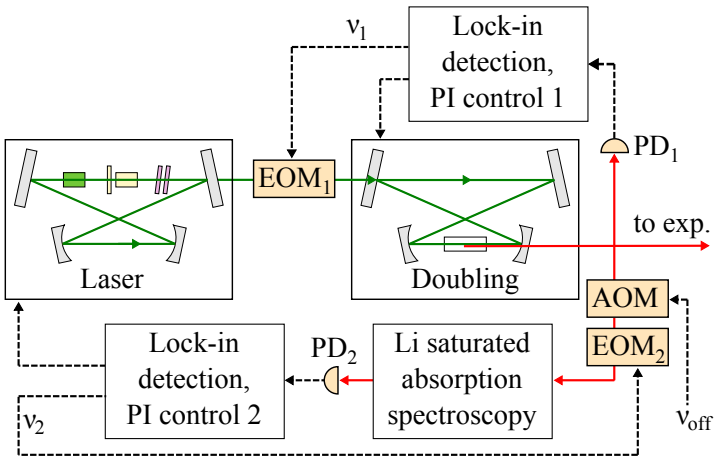

FIGURE 4.1: Locking scheme. Straight lines depict light paths, dashed lines electronic signals. First the doubling cavities resonance frequency is locked with respect to the free-running Nd:YVO_4 laser using control circuit components indexed 1. A part of the second harmonic light is used for Lithium spectroscopy. In a second step this reference serves to lock the double Nd:YVO_4 laser output frequency with respect to one of the Lithium resonance frequencies, using control circuit 2. A frequency offset between the atomic resonance and the output frequency is determined by twice the double pass AOM driving frequency ν_{off}.

4.1.1 Cavity length actuation

Actuating on an optical cavity resonance frequency is performed by changing its optical length L_{opt}. This is done by either moving cavity mirrors or changing the refractive index of intra-cavity elements. The trade-off between actuator range and feedback speed led us to the implementation of a two-way actuator system by putting two mirrors per cavity on piezo-electric transducers (PZTs):

1. To slowly actuate L_{opt} with a large range, a standard mirror made of a 12.7-mm diameter/6-mm thickness substrate is glued on a high-voltage PZT stack. This arrangement is used for mirror M_4 of the Nd:YVO_4 laser cavity (Figure 2.7) and M_3' of the doubling cavity (Figure 3.3). It allows one to move the mirror by around $2\,\mu$m for the full dynamic range of 0...150 V provided by a commercial high-voltage amplifier (*Falco Systems WMA-280*). The lowest resonance frequency of the feedback circuit is found at $\simeq 400$ Hz, which is attributable to the slow PZT discussed here. We thus operate it in the range from 0 Hz to $\nu_{3\,\mathrm{dB,slow}} = 72$ Hz, where $\nu_{3\,\mathrm{dB,slow}}$ is the cut-off frequency of a simple low-pass filter.

2. For actuating L_{opt} more quickly, a slim mirror of 12.7-mm diameter/3-mm thickness is glued on a PZT stack. We use M_3 for the laser and M_2' for the doubling cavity. It can be controlled using a standard operational amplifier of -15...+15 V dynamic range, yielding a mirror displacement of $\simeq 50$ nm. The operational frequency range was chosen, using appropriate filters, between $\simeq 0$ Hz and $\nu_{3\,\mathrm{dB,fast}} = 34$ kHz. In the low frequency range up to the slow PZT cutoff, the gain of the fast PZT is negligible compared to the slow PZT gain.

The electronic circuitry discerning the different frequency ranges and distributing it to the respective outputs is included in the lock circuitry boards.

4.1.2 Doubling cavity lock

To frequency-lock the doubling cavity to the laser frequency, an error signal needs to be generated. For doubling cavities, two methods are common: the Hänsch-Couillaud [151] method or phase/frequency modulation techniques. We use the latter, avoiding zero-offset drifts due to the involved polarizing components.

An electro-optical modulator (EOM_1 in Fig. 4.1) phase-modulates the infrared pump light at a modulation frequency of $\nu_1 = 1$ MHz. The phase modulation is also present in the second-harmonic light*. Using a fast photodiode, the modulated signal is detected from second harmonic light leaking out of the doubling cavity. It is demodulated using a homemade synchronous detection circuit. This allows one to produce an error signal with a 3 dB-bandwidth of 100 kHz, which is fed into the controller circuit.

The homemade controller circuit consists of a proportional-integral (PI) circuit and a separation circuit distinguishing the frequency ranges for the two actuator PZTs. The implementation of the re-locking scheme of Reference [152] renders the doubling cavity lock significantly more stable to external disturbances. The cavity transmission

*The sidebands are well within the lithium D-lines' natural linewidth $\Gamma_{\mathrm{Li}} \simeq 2\pi \times 6$ MHz. They are also very small in amplitude and do not cause any problem even for more demanding applications like absorption imaging.

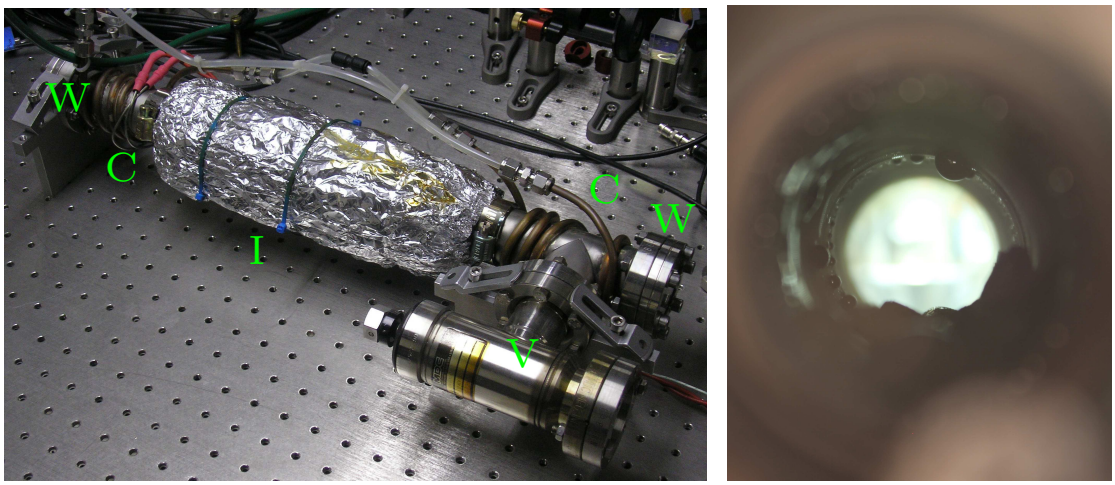

(a) (b)

FIGURE 4.2: (a) The lithium saturated absorption spectroscopy cell. It consists of a 50 cm long CF-40 tube closed by two optical quality windows (W). The third, sideways connector of the tube is shut by a valve (V), which is used for evacuation and setting of the correct argon buffer gas pressure to about 100 mTorr. A *Thermocoax* heating wire is wound directly around the central part of tube and covered by thermally insulating tin foil (I). For cooling the end parts of the vacuum tube, a copper tube was wrapped around these sections and brazed to the stainless steel tube (C). (b) Photograph of the interior of the spectroscopy cell. Migration of lithium is demonstrated by droplet condensation on colder places of the tube wall.

signal provides a reliable reference for this method. When scanning the laser frequency via the slow PZT (M_4), the ramp signal (modified by an adjustable gain) is fed forward to the lock signal, thus minimizing lock deviations and stabilizing output power.

4.1.3 Saturated absorption spectroscopy and laser lock

A small fraction of the frequency-doubled light is sent through a 200-MHz acousto-optic modulator (AOM) double-pass setup to frequency-shift the light used for spectroscopy by $2\nu_{\text{off}}$. It is employed to perform saturated-absorption frequency modulation spectroscopy [153] in an atomic lithium vapor cell. The required vapor pressure is obtained by heating a metallic lithium sample of natural isotope composition (8% ^{6}Li, 92% ^{7}Li) up to 330°C (up to 360°C in the case of the ^{6}Li D1 line) under vacuum. Our group's standard spectroscopy cell design consists of a 50-cm-long CF-40 tube with broadband AR-coated windows, shown in Figure 4.2.

The final sections of the tube are water-cooled to prevent the CF-40 flanges and windows from becoming too hot. In practice, it turned out that the water cooling is not necessary owing to the limited heat conductivity of the stainless steel tube. Nickel gaskets are employed because of their chemical inertness to lithium vapor. A small amount of argon buffer gas is used to force collisions of lithium atoms with the cold side walls and stick there before arriving at the window surfaces. The argon pressure is kept low enough to not cause significant collisional broadening of the saturated spectroscopy

lines[†]. This is established by slowly pumping out the argon of the pre-baked vacuum tube while monitoring the spectroscopy lines. When the saturated absorption lines stop narrowing, the valve is closed. A metallic mesh put inside the tube covers the tube walls to recycle condensed lithium from the colder parts, exploiting the temperature-dependent surface tension. Lithium is thus efficiently kept in the center of the tube, preventing it from being lost and chemically attacking the windows and gaskets. The tube was kept hot and in operation for almost two years, and we never observed any coating of the windows or worsening of the saturated absorption spectroscopy signal.

The spectroscopy beam $1/e^2$-radius is $\simeq 1\,\mathrm{mm}$, the pump power is of the order of 10 mW, of which typically 50% is transmitted through the lithium cell on atomic resonance. The beam then passes through EOM_2, which serves to phase-modulate the remaining light at $\nu_2 = 20\,\mathrm{MHz}$. A quarter-wave plate and a mirror retro-reflect the beam with a polarization rotated by 90°, thus creating the probe beam of $\sim 200\,\mu\mathrm{W}$ remaining power after passing back and forth through an ND filter. Around $100\,\mu\mathrm{W}$ of probe light are detected on a fast photodiode (*Newport 1801*) After passing through the spectroscopy cell again. Lock-in detection using a commercial amplifier (*Toptica PD110*) allows us to generate a dispersive error signal. A typical example of a $\simeq$ 600 MHz-scan over a part of the lithium lines is shown in Figure 4.3. The hyperfine structure of both lithium isotopes is clearly resolved and error signals of SNR ≥ 100 in a 1-MHz bandwidth are detected.

The lock saturated spectroscopy transmission signal can serve as the auto re-lock reference, see [152]. This requires a well pronounced peak or dip structure as satisfied for some (but not all) of the spectroscopy lines.

To lock the laser frequency with respect to one of the resonances, a two-way PI circuit similar to the one used for locking of the doubling cavity is employed. The AOM frequency and thus the lock offset frequency can be changed by a few tens of megahertz while keeping the laser locked.

4.1.4 Alternative locking schemes

The lock system provides sufficient short- and long-term stability, as will be demonstrated in the following section. To further improve stability, the Nd:YVO_4 laser could be locked to a reference cavity, as is normally the case for dye laser sources. Another option would be to generate a small amount of second harmonic light from the Nd:YVO_4 laser output using a single-pass method, as demonstrated in Section 3.3. It is easy to separate the second harmonic output (for spectroscopy and lock) from the remaining fundamental light (for efficient doubling in the external cavity), and use the visible light for spectroscopically generating an error signal for the laser lock. Owing to the resulting decoupling of both feedback loops, the system should behave more stably, and if one of the two loops falls out of lock, the second one is not necessarily affected.

[†]The typical value for collisional line broadening is $10\,\mathrm{MHz.Torr}^{-1}$. We therefore infer an argon pressure value of about 100 mTorr.

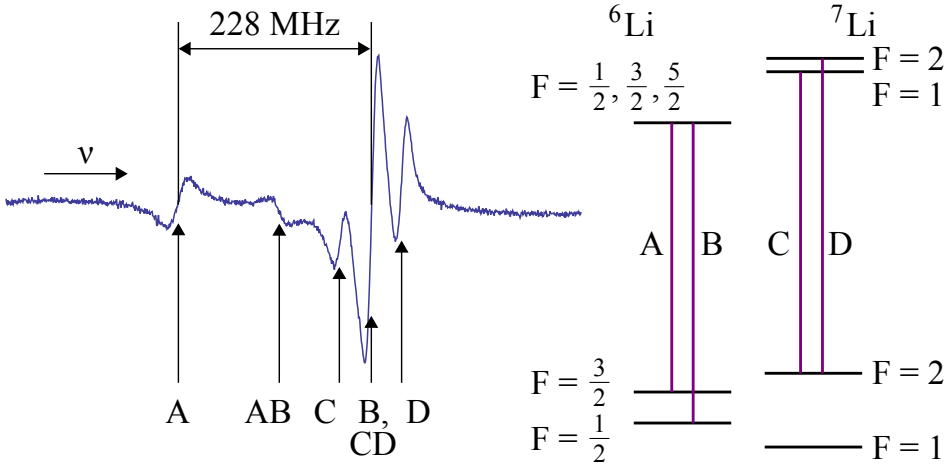

FIGURE 4.3: (a) Lock-in saturated absorption spectroscopy of lithium vapor, and corresponding transitions (b). The transitions are $2\,^2S_{1/2} \rightarrow 2\,^2P_{3/2}$ for ^{6}Li (D2) and $2\,^2S_{1/2} \rightarrow 2\,^2P_{1/2}$ for ^{7}Li (D1). Not all levels are shown, and the hyperfine structure of the ^{6}Li excited state remains unresolved. Double indices mark crossover lines, where XY marks the crossover between transitions X and Y.

4.2 Characterization

We present relative intensity noise measurements falling to the shot noise limit above 300 kHz. Offset-locking of the output frequency with respect to the Li *D*-lines is demonstrated, offering long-time stable operation. The laser linewidth is measured to $0.2^{+0.4}_{-0.2}$ MHz by imaging a cloud of ultra-cold ^{7}Li atoms in the Paschen-Back regime. Furthermore, the excellent spatial mode quality is confirmed by coupling >90% of the ouput power into a single-mode optical fiber.

4.2.1 Relative intensity noise

The relative intensity noise spectral density $S_{\mathrm{RIN}}(\nu)$ of the second harmonic output was measured by shining a beam of $\simeq 120\,\mu W$ on a low-noise photodiode (*Newport 1801*, 125-MHz bandwidth) and recording the signal using a digital oscilloscope (*Pico Technology PicoScope 4424*, 80-MHz bandwidth) in AC mode, yielding the relative power fluctuations $\varepsilon(t)$ after normalization, where $I(t)/\langle I\rangle_T = 1+\varepsilon(t)$ with $I(t)$ the intensity and $\langle I\rangle_T$ its temporal average. The definition of $S_{\mathrm{RIN}}(\nu)$ is

$$S_{\mathrm{RIN}}(\nu) = \lim_{t_{\mathrm{m}}\to\infty} \frac{1}{t_{\mathrm{m}}} \left\langle \left| \int_0^{t_{\mathrm{m}}} \varepsilon(t) \mathrm{e}^{\mathrm{i}2\pi\nu t}\, \mathrm{d}t \right|^2 \right\rangle \tag{4.1}$$

with the measurement time t_{m} and $\langle ...\rangle$ denoting temporal averaging. It was realized employing a time-discrete Fourier transformation method and averaging over 100 spectra.

The result is shown in Fig. 4.4. The broad peak at $\simeq 100$ kHz can be attributed to the laser relaxation oscillations. The structure in the 10 kHz region can be attributed to the locking system's fast PZTs. Above 300 kHz S_{RIN} drops to the photon shot-noise

level, as indicated by the spectrum of a noncoherent source producing an equivalent photocurrent (spectrum B in Figure 4.4). The narrow peaks at 1 MHz and harmonics stem from the phase modulation of the pump light, see Section 4.1.2. The square root of the integral of $S_{\mathrm{RIN}}(\nu)$ from 1 kHz to 5 MHz (1 kHz to 0.9 MHz) yields a RMS relative intensity noise of 1.1×10^{-3} (0.8×10^{-3}), where we have excluded the contribution from the modulation in the second interval.

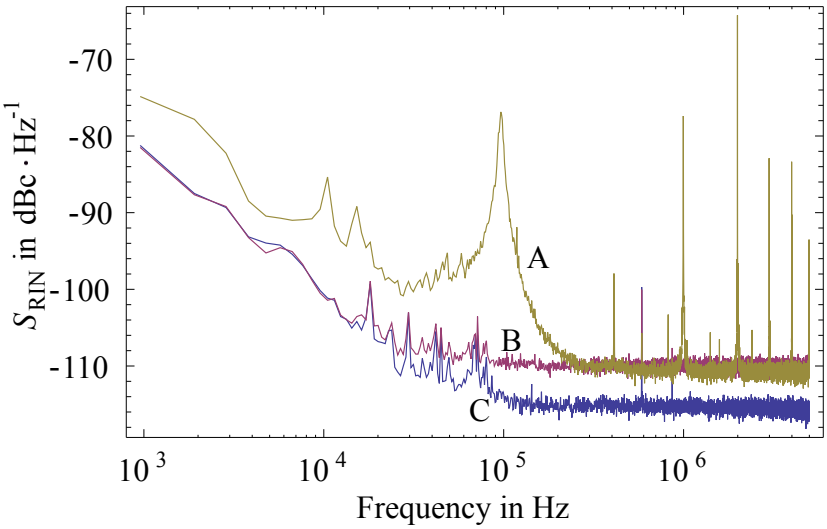

FIGURE 4.4: The second harmonic relative intensity noise spectrum (A), noise for an equivalent photocurrent from a non-coherent source (B) and noise of the detection circuit with no photocurrent (C).

4.2.2 Linewidth

The laser setup was used as an absorption imaging light source for our lithium quantum gas experiment, as will be described in Part II. A sample of around 1.2×10^5 ^{7}Li atoms above Bose-Einstein condensation threshold was prepared in an elongated optical dipole trap. In the presence of a 700-G magnetic offset field, the internal electronic states of the atoms can be described in the Paschen-Back regime, where spin and angular momentum degrees of freedom are decoupled. The corresponding lifting of degeneracy of the $F = 2 \rightarrow F' = 3$ transition frequencies results in a cycling transition. By applying a laser frequency detuning $\delta\nu$ with respect to atomic resonance using the offset lock as described in Section 4.1.3, one detects a different atom number $N(\delta\nu)$ according to

$$\frac{N(\delta)}{N(0)} = \left[1 + \left(\frac{2\delta\nu}{\Gamma}\right)^2\right]^{-1}, \tag{4.2}$$

while assuming constant atom numbers for each realization of the experiment. Γ is the measured linewidth of the transition and $N(0)$ the atom number detected at resonance.

The results are presented in Figure 4.5. A least-squares fit according to Equation (4.2) results in a linewidth of $\Gamma_{\mathrm{fit}} = 2\pi \times 6.1(4)$ MHz, a value compatible with the natural linewidth of $2\pi \times 5.872(2)$ MHz of [154]. The deviation of the fit for large

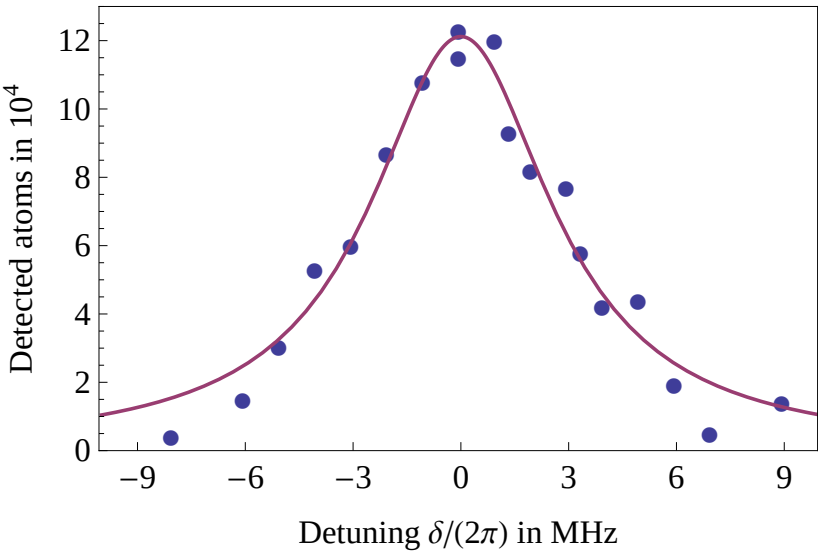

FIGURE 4.5: In-situ absorption imaging of ultra-cold atoms in a weak optical dipole trap. The laser was detuned by $\delta\nu$ from the atomic resonance using the offset lock described in Section 4.1.3, varying the detected atom number (circles). A Lorentzian of width $\Gamma_{\mathrm{Fit}} = 2\pi \times 6.1(4)$ MHz is fitted to the data (solid line).

detunings can be explained by unreliable atom counting at low optical densities. We infer that the laser linewidth is much smaller than the natural linewidth of the atomic transition. Assuming a Lorentzian lineshape for the laser, the linewidth can be given as 200^{+400}_{-200} kHz.

4.2.3 Spatial mode quality

The spatial mode of the second harmonic output has, as expected, an excellent TEM_{00} character. This is confirmed by coupling $> 90\%$ of the red output power through a single-mode optical fiber.

4.2.4 Long-term stability and every-day operation

For making a laser system attractive for ultra-cold atom experiments, a strict requirement is the long-term stability of the source in terms of output power and frequency. Figure 4.6 shows a typical long-term stability plot of the laser system under laboratory conditions. The system remained locked during the entire measurement time of $\simeq 8.5$ hours. The second harmonic output power drops by 7% and shows small modulations of a period of $\simeq 15$ minutes. This is attributed to slight angular tilts when the cavity's slow PZTs ($\mathrm{M}_4/\mathrm{M}_3'$) are driven. This effect, changing the alignment, is confirmed by monitoring the laser output power, which drops by 5% in the same time interval and displays the same modulations. The regulation signals of the slow cavity piezos are also displayed in Figure 4.6 and show exactly the same $\simeq$ 15-minute periodicity as the power signals. We thus infer that these modulations stem from the air conditioner used in our lab. Eventually, after $\simeq$8.5 hours, the PZT used for locking the

Nd:YVO_4 laser cavity reached the end of its dynamic range and the laser system fell out of lock. This effect can be avoided by using a PZT with a larger dynamic range.

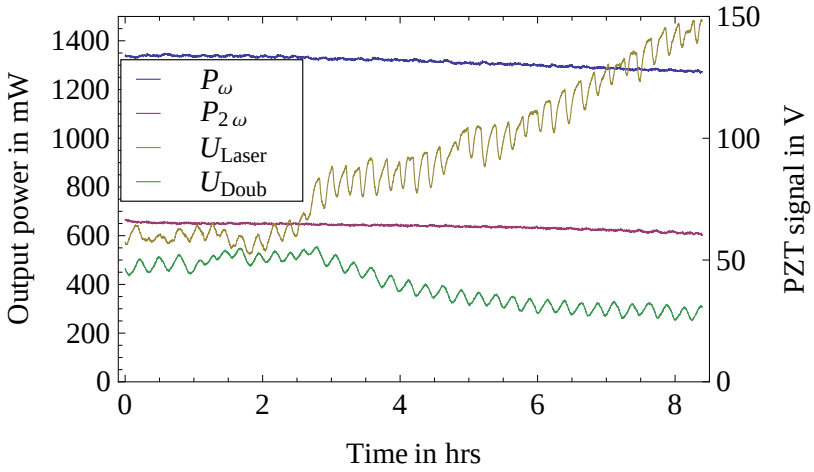

FIGURE 4.6: Long-term stability measurement of the laser system. It stays locked for the entire measurement time of ≃8.5 hours, displaying small variations of the Nd:YVO_4 laser output power P_ω and the doubling cavity output power $P_{2\omega}$ on a ≃ 15-minute time scale. This is due to the room temperature regulation by an air conditioner, as demonstrated by the corresponding slow PZT regulation signals V_ω and $V_{2\omega}$ for the laser cavity and the doubling cavity, respectively.

After ≈ 1h of warm-up, the system typically remains locked during an entire day. The laser system is currently situated in a separate room, well-shielded from perturbations. In every-day use, the system does not need any power optimization, as apparent from Figure 4.7. It was used for several months as the source for the lithium experiment Zeeman slower. Once optimized, the setup can remain untouched for about a month, while losing ≃10 mW of second harmonic output power on average per day. We found that the most important effect for regaining the old laser output power is the cleaning of the pump-sided Nd:YVO_4 crystal face. We observed this effect for crystals from *Castech Inc.* with the AR coatings either applied by the manufacturer or by *Layertec GmbH*.

4.3 Implementation in the current lithium experiment

The light source was used for laser cooling and trapping in the lithium quantum gas experiment at LKB, presented in Chapter 7. Here, we will motivate the use of a resonant electro-optic modulator (EOM) to create sidebands for repumping light. We then present the design of the optical system allowing for the generation of additional frequencies needed for operation of a Zeeman slower and a magneto-optical trap (MOT). Finally, experimental results on the realization of a MOT and a Zeeman slower are given.

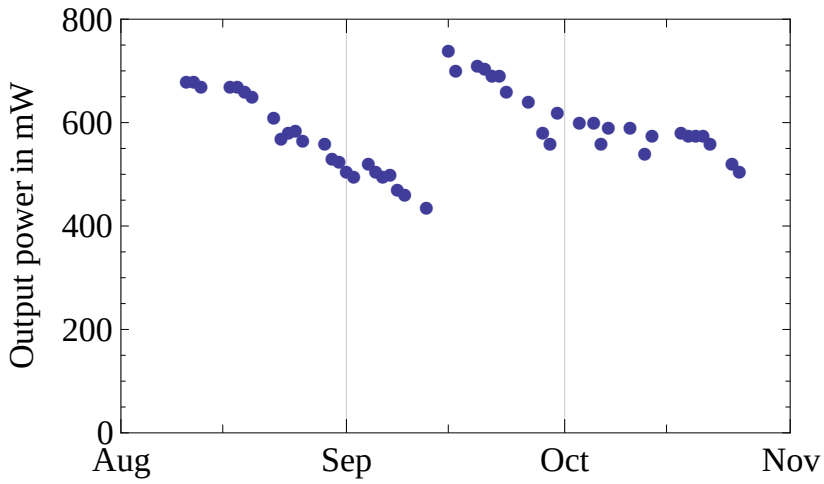

FIGURE 4.7: Every-day operation of the laser system during more than two months. The laser system was switched on and locked and remained untouched apart from that. On the 12th of September, the Nd:YVO_4 crystal was cleaned and the laser cavity was realigned.

4.3.1 EOM sideband creation

The *D*-line transitions in alkali atoms are not perfect cycling transitions. The excited state (P-state) energy splittings are too small to completely neglect excitation of states of non-maximal total angular momentum by the MOT laser, termed principal laser. Hence, in a MOT, an atom will eventually be pumped in the ground state of non-maximal total angular momentum and be lost from the cooling process. One thus needs an additional laser frequency in the MOT beams to pump the atoms back to the ground state involved in the "cycling transition". This laser is called repumper laser.

In the case of lithium, the corresponding excited state splittings are of the order of the natural linewidth $\Gamma_{\mathrm{Li}} \simeq 2\pi \times 6\,\mathrm{MHz}$, see Figure 7.1. The decay probabilities to each of the two ground states are thus of the same order of magnitude, requiring significant repumper power P_{R} of about 30% of the principal power P_{P} for a ^{7}Li MOT. We define the power ratio

$$\alpha_P = \frac{P_{\mathrm{R}}}{P_{\mathrm{P}}}\,. \tag{4.3}$$

In the first common method, the generation of the repumper beam is realized by splitting the principal laser beam, sending a portion of it through an acousto-optic modulator (AOM) setup and recombining the two beams. Since it is favorable to couple the light to single-mode polarization-maintaining optical fibers, one looses a large amount of laser power when recombining the two beams using the mandatory polarizer[‡]. The minimum loss depends on the power ratio α_P, see for instance Reference [155]. The efficiency

$$\eta_P = \frac{P_{\mathrm{out}}(\alpha_P)}{P_{\mathrm{in}}} = \frac{1+\alpha_P^2}{(1+\alpha_P)^2} \tag{4.4}$$

[‡]When seeding a tapered amplifier, however, this disadvantage is avoided, since only $\approx 20\,\mathrm{mW}$ of seed power per beam are needed.

between the sum of the powers in both frequencies $P_{\text{out}} = P_{\text{P}} + P_{\text{R}}$ and the available single-frequency power P_{in}. The second equality holds in the case of the AOM splitting and recombination method. The efficiency is only significantly higher than 50% for values of $\alpha_P < 0.2$, see Figure 4.8(b). A more efficient repumper creation scheme is therefore desirable.

A second approach for generating additional frequencies is sinusoidal phase-modulation using electro-optical modulators (EOM), symmetrically creating sidebands of the input (carrier) frequency, split by the modulation frequency. The obvious advantage of this method is that the polarization and spatial profile of the laser beam remain unchanged. In other words, the beam is only split spectrally, not spatially. When coupling to fibers, one thus avoids losses intrinsic to the AOM method. The drawback of this method is the power delivered to the non-used sidebands, yielding an efficiency η_P lower than unity. Here, we will compare both methods.

Phase-modulation of laser beams is a standard method in optics laboratories. We start by the Jacobi-Anger expansion [153]

$$\mathrm{e}^{\mathrm{i}(\omega t + M\sin(\Omega t))} = \mathrm{e}^{\mathrm{i}\omega t} \sum_{k=-\infty}^{\infty} J_k(M)\mathrm{e}^{\mathrm{i}k\Omega t}\,, \tag{4.5}$$

for the time dependence of a phase-modulated wave, where ω is the input laser (carrier) frequency, M is the phase modulation amplitude and Ω its frequency, and J_k the k-th order Bessel function. The power is symmetrically delivered from the carrier frequency ω to the $\pm k$-th order sideband of frequency $(\omega \pm k\Omega)$, since $J_k(M) = (-1)^k J_{-k}(M)$. We are only interested in power distribution efficiencies, we read directly from Equation (4.5) that the normalized power in the k-th order sideband is

$$p_k(M) = \frac{P_k(M)}{P_{\text{in}}} = J_k^2(M)\,, \tag{4.6}$$

with P_k the power in the k-th order sideband. In Figure 4.8(a) the corresponding relative powers are plotted for different modulation amplitudes. As can be seen from the green curve the power transferred to second- and higher-order sidebands remains negligible for a modulation index up to 1, so almost all of the power lost remains in the unused first-order sideband.

The results of our calculation are presented in Figure 4.8(b). Even by neglecting additional AOM-related loss due to spatial beam profile degradation, the phase-modulation method is superior to the AOM method over the whole range of power aspect ratios α_P necessary to consider. In the EOM method, the efficiency decreases much more slowly than the in the AOM case, where the curve drops rapidly to the asymptotic value of 50%. The distance between the two curves is greater than 10% for all practical purposes. While for $\alpha_P = 0.2$, η yields around 85%, it drops to 60% for $\alpha_P = 1$.

A practical issue is the need of a high modulation amplitude M of the order of one (Figure 4.8(b)). It reads

$$M = mU\,, \tag{4.7}$$

where U is the EOM drive voltage and m the modulation depth, a device-dependent parameter. For the typical 50 Ω-coupling and the maximum specified radio-frequency

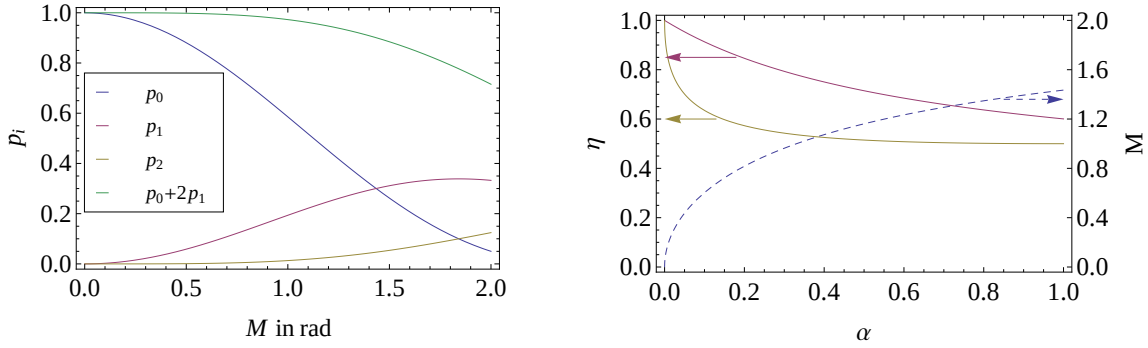

FIGURE 4.8: Calculation of the efficiency of the EOM sideband generation method. (a) Normalized powers $p_k(M) = P_k(M)/P_{\text{in}} = J_k^2(M)$ in the k-th order sideband as a function of the modulation amplitude M. (b) M (blue), the efficiencies of the EOM method η_P (purple), and the efficiency of the AOM method [cf. Reference [155] and Equation (4.4)] (yellow) as a function of the power ratio α_P between repumper and principal power. The EOM method offers significantly higher efficiencies over the whole useful range.

(RF) power of around $P_{\text{RF}} = 10\,\text{W}$ (and $U = \sqrt{50\,\Omega P_{\text{RF}}}$) this yields $M_{\max} = 2\,\mu\text{rad}$ for the common $m = 0.1\mu\text{rad/V}$ of devices in the 0.25-2 GHz range [156]. We thus needs to resort to resonant devices.

A third alternative approach for repumper generation are fiber-based EOM designs, offering higher modulation amplitude for a given RF power. Unfortunately these devices are limited to the 1 mW-optical power range. A further disadvantage of these systems is the fiber insertion loss due to the mode mismatch between the optical fiber and the lithium niobate waveguide used for phase modulation [157].

A promising technique is the sawtooth-modulation technique presented in References [158, 159], which offers the possibility to deliver almost all of the incident power to only one sideband. It involves a fiber-based device and thus the associated power restrictions. However, this is an interesting way to generate repumper light if applicable to standard (non-fiber-based) modulators. This would require wideband-modulation depth and common phase shift at Ω and harmonics, otherwise the sawtooth-shape of the RF signal and thus the modulation efficiency would suffer.

4.3.2 Additional frequencies and light delivery

After the efficiency considerations in the previous section, we decided to create the repumper beam using a resonant electro-optic modulator (EOM, *Qubig EO-Li7-3L*). This allows us to work with relatively low radio-frequency (RF) power while keeping a reasonable modulation index M and thus high enough repumper power P_{R}. The setup is presented in Figure 4.9. For reasons of flexibility, we decided for a completely fiberized setup fitting on a small ($60 \times 30\,\text{cm}^2$) breadboard.

The single-frequency light power available at the output of the optical fiber F_{in} is around 500 mW. At this power level we did not observe any thermal problems in

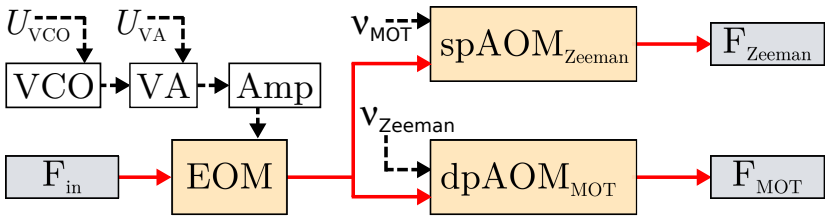

FIGURE 4.9: Creation of the laser frequencies needed for driving Zeeman slower and MOT from a single frequency laser source entering via the fiber F_{in}. White boxes mark RF components, orange boxes are optical modulators and grey boxes are optical fibers. Sidebands of variable frequency are created using a resonant electro-optic modulator (EOM). The frequency difference of the sidebands and the relative power ratio is set using a voltage controlled oscillator (VCO) and a variable attenuator (VA) before amplifying (Amp) the RF signal. The modulated light is then frequency shifted using acousto-optic modulators (AOMs, sp and dp stands for single- and double-pass, respectively) before being coupled to the respective fibers F_{Zeeman} and F_{MOT} guiding the light to the experimental room.

the lithium niobate (LN) crystal of the EOM, so we did not need to use a high-power potassium titanyl phosphate (KTP) version, which has the drawback of a lower modulation index for a given RF level.

The resonance frequency of the EOM is tunable by around ±10% of its center frequency of 800 MHz using a setscrew. The frequency and the amplitude of the modulated sidebands can be independently set using the the voltage-controlled oscillator (VCO, *Mini-Circuits ZOS-1025+*) and the variable attenuator (VA, *Mini-Circuits ZX73-2500-S+*), controlled by a respective voltage signal. The RF output power of the amplifier (Amp, *Mini-Circuits ZHL-2-8*) can thus be set between 14 dBm and 29 dBm, corresponding to a relative repumper fraction of $\alpha_P = 0.5\%...35\%$.

As presented in Section 4.1, the laser light from F_{in} is frequency-offset-locked with respect to the ^{7}Li D2 transitions using a double-pass AOM ($+2\times120$ MHz). The modulated light is then split up and sent to the acousto-optic modulator (AOM) stages for frequency shifting. We use a double-pass configuration for the MOT light ($dpAOM_{MOT}$, $+2\times80$ MHz) because of its superior performance in terms of extinction when using the AOM as a switch. For the Zeeman-slower light, we use a single-pass setup ($spAOM_{Zeeman}$, -1×200 MHz) because of its higher power efficiency.

The setup presented here creates all the frequencies needed for operation of our Zeeman slower and MOT. It is remarkably simple, stable and compact and allows total control over the necessary parameters (detunings and power balance). Both the detuning of the Zeeman slower repumper beam and its realtive power with respect to the Zeeman principle beam are fixed by the RF drive of the EOM, which is optimized for operation of the MOT. This drawback is minor because of the high magnetic fields inside the Zeeman slower, except for the spin-flip region. Most of the time, the atoms are well within the Paschen-Back regime. The photonic transitions are thus well separated and almost perfect cycling transitions. However, in the spin-flip region the amount and frequency of repumper light in the Zeeman beam is sufficient to not lose the atoms to the repumper state.

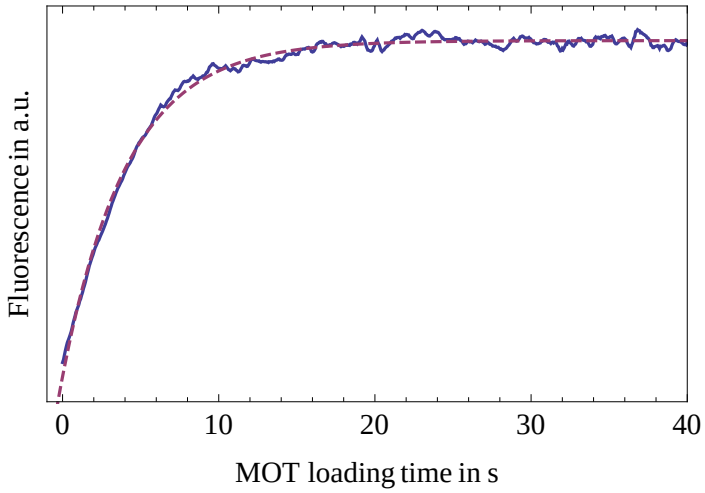

FIGURE 4.10: Zeeman slower loading of the ^{7}Li MOT in our setup, using the novel laser source for the slower. The solid line is the measured fluorescence power signal of the MOT. The dashed line is a fit to an exponential law, resulting in a loading time of 4,16(3) s. From the loading time and the final number of atoms of $\approx 10^{10}$, we deduce an atomic flux of $2 \times 10^9\,\mathrm{s}^{-1}$. We typically charge the MOT during 10 s before starting the experimental sequence.

4.3.3 Operation of Zeeman slower and MOT

The Zeeman slower of the ENS lithium experiment consists of an oven containing a sample of metallic lithium with natural abundance of the isotopes. We heat it to 400°C to provide sufficient atomic flux. An atomic beam is formed by a collimation tube of 6-mm diameter. The tube walls are covered by a stainless-steel mesh, which is wrapped inside the tube. The purpose of this mesh is identical to the one used in the spectroscopy cell (cf. Section 4.1.3): In presence of a temperature gradient, the resulting difference in surface tension of liquid lithium droplets pushes these back to the high-temperature region. Condensed lithium is thus recycled, and blocking of the tube is efficiently circumvented. The Zeeman slower is of the spin-flip type. This concept efficiently reduces size and electric power consumption of the setup, and keeps the Zeeman-induced magnetic field and gradient close to zero at the position of the MOT.

We found it more convenient to restrict ourselves to the use of our novel laser source for the Zeeman slower only, since this did not require any change in the control sequence and allowed us to gain knowledge and confidence into its usability on a day-to-day basis. In a first approach, we use the MOT as a tool for characterization of the flux of the Zeeman slower. The total power of the beam entering the Zeeman slower was ≈ 150 mW, consisting of different frequency contributions depending on the EOM sideband generation method presented in the previous section. We experimentally found the optimum power balance between repumper and principal contribution to be $\alpha_P \approx 1/3$, see Equation (4.3). We optimize the Zeeman-slower flux by observing the slope of the MOT fluorescence while periodically switching on and off the MOT. In the limit of low densities, the MOT fluorescence is proportional to the atom number. A

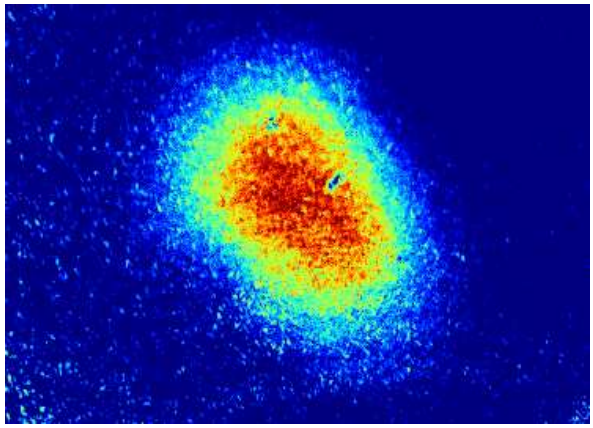

FIGURE 4.11: In-situ image (MOT laser on) of a ^{7}Li magneto-optical trap. The number of atoms is about 10^{10}.

typical loading curve is presented in Figure 4.10. The data points shown are moving-averaged points. We fit an exponential law to the loading curve,

$$\frac{N(t)}{N_0} = 1 - \exp\left(-\frac{t}{t_{\text{load}}}\right) , \tag{4.8}$$

where N_0 is the final atom number. The fit yields a loading time of 4,16(3) s. Our final atom number of $\approx 10^{10}$ can be estimated from absorption imaging of the MOT. We can therefore deduce a Zeeman slower flux of $\dot{N}_{\text{Zeeman}} = N_0/t_{\text{load}} \approx 2 \times 10^9\,\text{s}^{-1}$.

We typically charge the MOT during 10 s to assure having a maximum number of atoms available before starting the experimental cycle. With the amount of laser power entering the Zeeman slower, we work in a saturated regime. We therefore cannot observe any influence of small changes in laser power on the atomic flux.

In an earlier approach, we used the light from the repartitioning breadboard presented in the previous section to run a ^{7}Li MOT. The light coupled out of the MOT fiber (≈150 mW sum of all frequency contributions) was shone in the MOT section of our experiment using a flip mirror mount. Thus, alignment was simplified and comparison and exchange with the old diode-based laser system is feasible by just flipping one mirror. The result is presented in Figure 4.11. We took an in-situ absorption image (MOT laser on) of the trapped cloud. Since the imaging transition is saturated by the MOT beams, atom counting from the imaged optical density is not reliable. However, given the density limitation occuring in MOTs, and the observed size of the cloud, we can estimate the number of trapped as being of the order of 10^{10} atoms.

4.4 Summary

In this chapter, we have presented the electro-optical system built to frequency-lock the novel all-solid-state laser system discussed in Chapters 2 and 3. At first, we have discussed the theoretical considerations for the design of the frequency-stabilizing system. We then have presented our choice of solutions, including a lithium spectroscopy setup to lock the laser output frequency with respect to the D-lines.

Furthermore, we have characterized the output radiation of the frequency-locked laser system carefully. We have demonstrated reliable high-power operation of the system at a fixed but tunable output frequency, and we have characterized the laser system in detail. We have measured the relative intensity noise of the source, dropping to the shot-noise level above 300 kHz, and estimated the laser linewidth to be 200^{+400}_{-200} kHz. Long-term measurements have demonstrated the stability of the frequency-stabilized source for a time-span of more than eight hours. We have presented its every-day performance and marginal maintenance for more than two months.

Finally, we have discussed different methods of generating beams of different frequencies necessary to run a Zeeman slower and a MOT of lithium atoms in terms of their intrinsic loss. We have realized a simple power-efficient fiberized setup used to generate all the beams. We have given results of the operational characteristics of these subsystems used for cooling and trapping of lithium atoms.

Chapter 5

Conclusion to Part I

Summary

In the first part of this thesis we have presented the design and the characterization of a novel all-solid-state frequency-doubled laser source, delivering record-level output power of light suitable for magneto-optical cooling and trapping of lithium atoms.

We have first introduced the design and operation of the fundamental laser source, a diode-pumped Nd:YVO_4 unidirectional ring laser emitting 1.3 W of radiation at 1342 nm. The laser has a transversal mode quality factor of $M^2 = 1$ on both beam axes. Its longitudinally-single-mode operation is imposed by forcing unidirectionality and placing two etalons in the cavity. It can be tuned from 1341.7 nm to 1342.8 nm.

We have then demonstrated efficient frequency doubling of the infrared laser in an external buildup cavity. We have shown the design and the operation of this second-harmonic-generation stage, where we have employed ppKTP as the nonlinear medium. Up to 840 mW of single-mode output power have been generated, and the maximum measured fundamental-to-second-harmonic power efficiency was measured to be 86%. We have also observed power limitations in the doubling process, and discussed how to circumvent them.

Given the tuning range of the fundamental source, any of the lithium D-line transitions is conveniently adressable after frequency doubling. The laser system of the laser cavity and the doubling cavity has been frequency-locked with respect to these transitions. To do so, we have built a saturated-absorption spectroscopy setup and the necessary electro-optical locking systems. The system is of a remarkable stability, and typically stays locked for a whole working day.

We have afterwards introduced the characterization of the second-harmonic output. By performing spectroscopy on ultracold samples of lithium atoms, the narrow-band operation resulting from the single-mode operation of the system could be proven, and we have measured a linewidth of 200^{+400}_{-200} kHz. We have determined the relative intensity noise, which drops to the photon shot noise level above 300 kHz.

We have furthermore demonstrated operation of a magneto-optical trap for lithium using the novel laser source. In its first phase of implementation in the lithium setup at ENS, we have used the laser as a light source for the Zeeman slower. We have done so for more then six months on a daily basis. Apart from occasional maintenance, typically once per month, the only operations necessary are the switch-on and lock in the morning, and the switch-off in the evening.

We thus have demonstrated the suitability of the system as a laser source for experiments involving cooling and trapping of lithium species, where it can serve as a single high-power source delivering all the laser beams to run such an experiment. It is a flexible source in the sense that it can be used in different applications, as we have discussed in detail. Given that the system is entirely made of solid-state components, it should age very slowly and stay highly powerful over many years.

Perspectives

In ultracold atom experiments, quantum degeneracy can only be reached if a sufficient initial number of atoms are available. The signal-to-noise ratio is increased with more atoms present in the degenerate sample. The initial number, on the other hand, depends on the available output power of the sources employed for the cooling and trapping beams. It is thus preferable to have the highest possible output power. Hence, we will present ways to further improve the output power of the laser source discussed here.

As it has been demonstrated in [1], Nd:YVO_4 lasers can deliver longitudinal multimode $M^2 \approx 1$ output with output powers in the 20-W range at 1342 nm. It is thus possible to scale the output power by one order of magnitude. However, this would require a re-design of the laser cavity, and single-longitudinal-mode operation cannot be guaranteed at these power levels.

Further increase of the output power of the existing setup is feasible using a pump source emitting at 888 nm [1, 97]. This efficiently reduces the amount of defect energy per lasing cycle of the ions, where the non-optical transitions are phonic transitions. Thus, the defect energy finally results in heating of the laser crystal. It has been shown in this thesis that thermal lensing and the losses related to this effect need to be very well mastered to achieve efficient operation of Nd:YVO_4 lasers at 1342 nm. Currently, there are efforts performed in our group to establish a similar powerful laser using 888-nm pumping. Promising preliminary results surpassing the Nd:YVO_4 laser in terms of longitudinal output power have been obtained already.

A multi-mode high-power laser similar to the one presented in [1] could also prove very useful when using it as an injection-locked slave laser, see for instance [51, 160]. The infrared laser presented in this thesis could be used as the injection-lock source. This approach is followed by our coworkers from Toulouse.

To overcome the limitations arising in the frequency doubling process, one could change the geometric design of the doubling cavity in order to enlarge the fundamental mode size in the nonlinear crystal. The lower intensity resulting from this approach will suppress detrimental effects, and the lower single-pass efficiency can be overcome by the possible increase in infrared laser power, and a revised impedance matching. As we have discussed before, the intra-cavity round-trip passive loss is well below 1%, and thus not limiting this kind of power scaling. We have also purchased nonlinear crystals of a different material, namely ppSLT, which should, to the best of our knowledge, tolerate higher powers, by providing a sufficient single-pass efficiency. Calculations show that the crystals can be inserted in the existing doubling cavity without having to adjust the cavity geometry or the pump-beam mode matching.

Finally, the source is presently used as the Zeeman slower laser, where it served

bravely and filled the operators with confidence. In terms of output power, it has the potential to replace all of the laser sources presently used for manipulating ^{7}Li in the lithium setup at ENS. It should thus be fully implemented as soon as the experimental situation allows for it.

Part II

Three-body loss in the unitary Bose gas

Chapter 6

Introduction to Part II

The interacting Bose gas

During the quest to reach Bose-Einstein condensation of dilute atomic gases, the importance of interactions between the constituent particles quickly became apparent. Even though condensation itself is a purely statistical process, and as such occurs in noninteracting systems, interactions play a decisive role in the behavior of ultracold gases. Whereas a great deal of experimental situations can be well approximated by weakly-interacting or even ideal gases, the situation changes dramatically with the onset of high phase-space densities and resonant interactions. It is thus of great interest to understand and manipulate the interplay between ultracold atoms.

In general, interatomic potentials have complicated shapes, making the ab-initio description of an ensemble of interacting particles a challenging task. In the dilute ultracold regime however, interactions between particles can be characterized by s-wave scattering of two particles [161], which is characterized by a single parameter, the s-wave scattering length a. In this limit, the scattering cross-section for indistinguishable bosons is

$$\sigma = 8\pi \left| \frac{1}{\frac{1}{a} + ik + \frac{1}{2}k^2 r_\mathrm{e} + O(k^4)} \right|^2 , \tag{6.1}$$

where k is the reduced wave number of the two-particle relative motion and r_e is the effective range of the interaction, which is typically on the order of the van-der-Waals length. Since k tends to zero at ultracold temperatures, the cross-section becomes $8\pi a^2$. Because the behavior of systems of any kind of indistinguishable particles is identical whenever they share the same value of a, this regime is called the *universal* regime. In systems offering magnetic Feshbach resonances [17, 162–165], a can be tuned arbitrarily, allowing one to precisely control interactions over many decades [17, 166, 167]. From Equation (6.1) it follows that on resonance, where a diverges, the scattering cross-section reads

$$\sigma = \frac{8\pi}{k^2} . \tag{6.2}$$

Since this is the maximum value permitted by quantum mechanics in the s-wave channel, the limit $ka \to \infty$ is called the *unitary limit*.

The interaction strength in ultracold many-body systems is typically characterized by the dilution parameter $n|a|^3$, where n is the particle density. In the range where $n|a^3| \ll 1$, the behavior of gases can be described by a mean-field theory [168]. Using

Fano-Feshbach resonances, properties of gases with relatively large $n|a|^3$ were accessed experimentally right after the observation of these resonances in atomic systems [166]. An example of the modified behavior of quantum gases in presence of interactions is the interaction-induced change of the critical temperature for Bose-Einstein condensation, predicted theoretically (see [169]and references therein) and measured in [170–173]. In [174], corrections to the (weakly-interacting) mean-field theory for the bosonic zero-temperature equation of state become apparent, as predicted in 1957 [175].

The unitary Bose gas

It is thus a logical step to try to pursue increasing the interactions in ultracold gases towards the unitary limit. In fermionic systems, the unitary gas is a well-established (meta-)stable system in both experimental and theoretical contexts. The predicted collisional stability [176] when crossing a Feshbach resonance was found in early experiments on ^{6}Li [177–179] and ^{40}K [180].

Intriguing properties were predicted for the Bose gas when tuning the interactions towards the unitarity limit. In the homogeneous case at zero temperature, a and $n^{-1/3}$ deliver the only length scales for the problem. However, since a diverges, it drops from the description of the system. Dimensional considerations lead to the only remaining energy scale: the Fermi energy $E_\mathrm{F} = (\hbar^2/2m)(3\pi^2 n)^{2/3}$ [181] for a noninteracting Fermi gas. It is quite remarkable that a maximally interacting bosonic system should behave like a non-interacting fermionic system, the only difference being the type of quantum statistics. The zero-temperature chemical potential is thus expressed as $\mu(T = 0) = \xi E_\mathrm{F}$ with ξ being a universal constant. Several theoretical predictions exist for the value of ξ [181–183], and a lower experimental bound was recently proposed in our group [174]. However, this measurement could not prove the existence of the finite-temperature unitary Bose gas at quasi-equilibrium.

Three-body loss and quasi-stability

It became clear from early experiments on Bose-Einstein condensates on the $a < 0$ side, that a mechanical instability due to the effective attraction occurs [184–187], leading to a collapse, commonly termed the Bose-nova. Reference [183] theoretically deduced such instabilities for both sides of a Feshbach resonance.

Even more severely, the gaseous state is not a ground state, but a metastable state of resonantly interacting bosons. This is due to the presence of molecule formation, occuring in collisions of $N > 2$ particles. Thus, we have to see on which timescales we can study the gas under conditions of *quasi-equilibrium*. A criterion of quasi-equilibrium is that the elastic two-body collision rate γ_2 is much greater than the largest contribution to the molecule formation rate, the inelastic three-body recombination event rate γ_3,

$$\frac{\gamma_2}{\gamma_3} \gg 1\,. \tag{6.3}$$

As predicted theoretically, γ_3 has an overall a^4 dependence [188, 189]. Systematic measurements were performed in [166, 190–192], quantitatively justifying the predictions. However, when a diverges, a *three-body recombination unitary limit* exists, posing a quantum-mechanical limitation on the three-body recombination rate. As

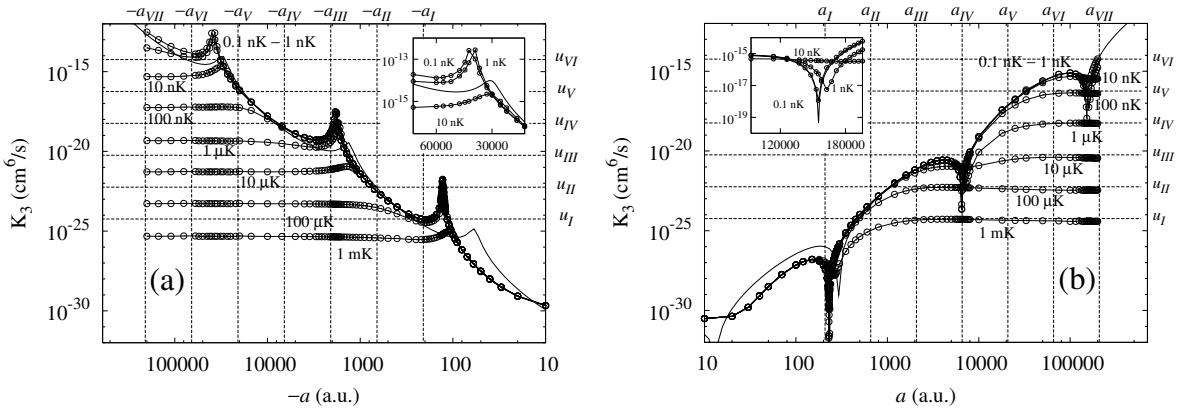

FIGURE 6.1: Theoretical prediction of the three-body recombination rate constant spectra $K_3(a) = \gamma_3(a)/n^2$, figure from [201], where the temperature of the sample is treated as a parameter. One notices the increase (decrease) of K_3 whenever a new Efimovian state appears at threshold for $a < 0$ ($a > 0$). However, for finite temperatures, the curves level off to a constant rate when approaching the Feshbach resonance.

will be shown in this work, this results in a $1/T^2$ law for γ_3, predicted theoretically in [193–195]. We will demonstrate that the predicted coefficient agrees well with our observations. Thus, for sufficiently high temperatures, a quasi-equilibrium state can always be reached. The resulting phase diagram of the quasi-stable, finite-temperature strongly-interacting Bose gas was recently addressed theoretically in [196].

The Efimov effect

As it was predicted theoretically by Vitaly Efimov in 1970, there exist infinitely many universal three-body bound states for the resonant three-boson system [197–199]. The subject remained under theoretical debate for decades. No experimental proof of the existence of these states could be found, mostly due to the non-tunable interaction parameters in nuclear systems.

The theoretical predictions for the observability of Efimovian features in the three-body loss spectra of tunable ultracold atoms experiments showed the limitations arising at finite temperatures [200, 201]. These, on one hand, include contributions of higher channels of nonzero angular momenta, possibly masking the loss minima on the $a > 0$ side. On the other hand, a limit on the maximum value of γ_3 arises,

$$\gamma_3(T, n) = \frac{72\sqrt{3}\pi^2\hbar^5 n^2}{m^3 k_B^2 T^2}\,, \tag{6.4}$$

whose measurement is one of the major objectives of this thesis.

Apart from being detrimental, three-body loss in ultracold gases became a field of important scientific interest. The milestone 2006 paper of the Innsbruck group [202] clearly revealed Efimov physics for the first time in an experimental context. The appearance of an Efimov state at threshold enhanced the three-body loss rate. Improved measurements of three-body loss spectra were accomplished using ^{39}K [203] and

^{7}Li [204, 205]. The full universality of Efimov's theory was revealed in these measurements. Efimov physics is also present in fermionic spin mixtures [206–208]. A review on the subject can be found in [209, 210].

The present work

In Chapter 7, we will present the experimental apparatus used to perform experiments on the unitary Bose gas. We will give a brief outline of how we produce and probe ultracold gaseous samples of lithium atoms. As discussed before, the unitary Bose gas is difficult to prepare because of the presence of strong three-body recombination. We establish a new method of rapidly transferring atomic clouds to the strongly-interacting state with minimized three-body loss. This is realized using RF transfer from a weakly-interacting state. We will detail the methods used to realize the finite-temperature unitary Bose gas. In Chapter 8 we will present the experimental results. Before addressing the actual measurement of the equation of state, we have to quantitatively understand losses in the system. Whereas previous studies of three-body recombination were restricted to finite values of a, we present in this manuscript a measurement of the temperature dependence of three-body loss at unitarity. We use a method developed earlier in our group to present a first measurement of the equation of state of the unitary Bose gas. We will conclude in Chapter 9, and discuss further perspectives.

Chapter 7

Experimental setup

In this chapter, we will discuss the experimental apparatus used to create ultracold, strongly-interacting samples of bosonic ^{7}Li. The lithium apparatus at Laboratoire Kastler Brossel has been extensively presented before in the theses written in our group [211–218]. Thus, we will only give a brief outline of how we produce and probe ultracold gaseous samples of lithium atoms. We will emphasize the changes made to the setup in order to create samples of finite-temperature, strongly-interacting Bose gases. Because the measurement of the three-body loss coefficients presented in the next chapter depends sensitively on the values of the trap frequencies, we will detail on their precise calibration.

Originally, the setup was designed to trap both the bosonic (^{7}Li) as well as the fermionic (^{6}Li) isotope of lithium. In the RF evaporation stage, the bosons can be used to sympathetically cool the fermions. Due to the absence of collisions between identical fermions at ultracold temperatures, this is an elegant way of producing degenerate Fermi gases. It also offers great versatility in creating Bose-Fermi mixtures or to use one of the species as a temperature probe for the other [217]. Since the work presented here relies only on the bosons, we will exclude the fermions from further presentation.

The final hybrid trap, in which the measurements are performed, is formed by two independent trapping potentials. A magnetic curvature field to provide relatively weak confinement in the axial direction, and a focused dipole trap laser yields strong confinement in the radial direction. Both axial and radial trap frequencies can be tuned over a large range. The magnetic offset field in the trap center can be tuned freely to address magnetic Feshbach resonances, allowing one to change the interactions between ultracold atoms at will.

The chapter is organized as follows: In Section 7.1 we will give the important physical properties of ^{7}Li. In Section 7.2 we will present the experimental steps performed to load the final trap, which will be detailed in Section 7.3. In Section 7.5.2, we will present the radio-frequency setup used to transfer atoms between magnetic substates of the ground-state manifold, and give the magnetic field calibrations obtained. We will present the imaging scheme in Section 7.4 and summarize the chapter in Section 7.6.

7.1 The ^{7}Li atom

The lithium atom exists in the form of two stable isotopes, the bosonic isotope ^{7}Li and the fermionic isotope ^{6}Li. The natural abundances are $\simeq 92\%$ for ^{7}Li and $\simeq 8\%$ ^{6}Li [219]. The low saturated vapor pressure [219] makes it necessary to operate the sources at elevated temperatures, up to 500°C in our case, in order to obtain sufficient vapor pressure. This strongly favors the use of Zeeman-slowing schemes from thermal beams out of an oven in order to load a MOT*.

^{7}Li has a mass of 7 a.u., which is about 1.162×10^{-26} kg. It is thus the lightest bosonic isotope of the alkali group. The ground state has the electron configuration $1s^2 2s$. The D-line transitions, corresponding to the lowest excited state, $2s \rightarrow 2p$, have wavelengths of around 671 nm.

7.1.1 Energy level scheme

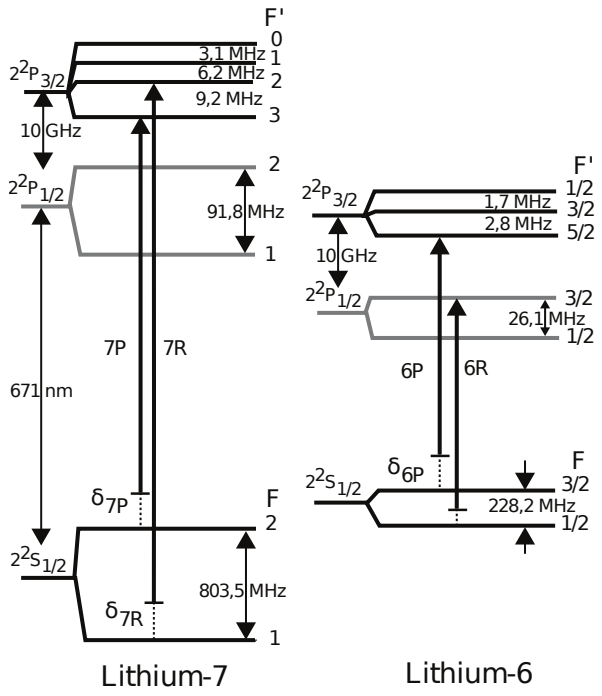

FIGURE 7.1: The ^{7}Li level scheme, figure from [215]. The scheme of ^{6}Li is shown for completeness. The $2^2S_{1/2} \rightarrow 2^2P_{1/2}$ or D_1 transition of ^{7}Li is almost degenerate in frequency with respect to the $2^2S_{1/2} \rightarrow 2^2P_{3/2}$ or D_2 transition of ^{6}Li.

The energy level scheme of both stable isotopes of lithium is given in Figure 7.1, where the ground (excited) hyperfine states are labeled by their total angular momentum quantum number $F(F')$. We use the $2^2S_{1/2} \rightarrow 2^2P_{3/2}$ or D_2 transition for Zeeman slowing and magneto-optical trapping of the atoms. As shown in the figure, we keep the nomenclature of cooling and repumper frequencies as introduced in

*In contrast to this, operation of a lithium 2D-MOT was demonstrated in Reference [220].

Chapter 4, although both beams require almost the same amount of power for efficient operation of a MOT[†]. The principal beam frequency is red-detuned from all the $F = 2 \rightarrow F' = 1, 2, 3$ transitions, whereas the repumper frequency is red detuned from all three $F = 1 \rightarrow F' = 0, 1, 2$ transitions. The upper-state ($2p$) lifetime was measured in [154] to be $\tau = 27.102(2)$ ns, corresponding to a natural linewidth of $\Gamma = 2\pi \times 5.872(2)$ MHz.

7.1.2 Hyperfine-ground-state energies

The energies of the magnetic sublevels $|F, m_F\rangle$ of the ground states depend on the value of the magnetic field B. F is the total angular momentum of the valence electron-nucleus system, and m_F its projection on the quantization axis. However, at high fields the angular momenta decouple. We will therefore use the common notation $|1\rangle$, $|2\rangle$, $|\ldots\rangle$ for the states, with an energy ordering starting from the lowest energy state. The energies can be calculated according to the Breit-Rabi formalism [221]. We show the result in Figure 7.2.

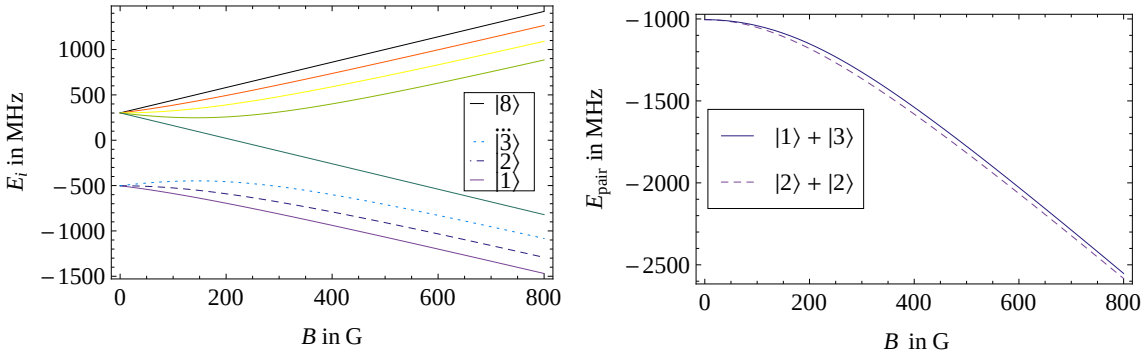

FIGURE 7.2: (a) The magnetic-field dependence of the ground-state energies of the ^{7}Li atom. The states that are important in our experiment are labeled in the legend. (b) The sum of the energies of two atoms in the $|2\rangle$ state ($|2\rangle + |2\rangle$) and one atom in the $|1\rangle$ and one in the $|3\rangle$ state ($|1\rangle + |3\rangle$). Since $E_{|1\rangle+|3\rangle}(B) > E_{|2\rangle+|2\rangle}(B)$ for all $B > 0$, spin-changing collisions of atoms in the $|2\rangle$ state are energetically forbidden.

The high-field regime is called the Paschen-Back regime, where the electron spin decouples from the nuclear spin. One asymptotically finds

$$E_{|i\rangle}(B) \xrightarrow[B\to\infty]{} \pm\frac{g_J}{2}\mu_B B \pm \frac{m_I}{2(2I+1)}E_{\text{hf}}, \tag{7.1}$$

where $g_J \approx 2$ is the Landé factor of the electron, μ_B is the Bohr magneton, $I = 3/2$ is the nuclear angular momentum, $m_I = -3/2, -1/2, 1/2, 3/2$ its projection on the quantization axis and $E_{\text{hf}} \approx h \times 803.5$ MHz the ground-state hyperfine splitting with h

[†]In [50] it was shown experimentally that for ^{6}Li, the optimum power ratio between repumper and principle beam is $\approx 1/8$. The situation is slightly different for ^{7}Li due to the different level structure, see Figure 7.1.

being Planck's constant, see Figure 7.1 and [222]. The plus or minus sign depends on the spin orientation of the valence electron. Equation (7.1) describes a decoupled system where the spin contribution to the Hamiltonian is that of the free electron and the second term is a constant correction depending on the spin state of the nucleus. This contribution does not depend on B, which means that in the high-field regime, magnetic potentials are nuclear-spin insensitive, since they only depend on the derivative of the energy with respect to B.

The states are commonly labeled $|1\rangle$, $|2\rangle$, $|\ldots\rangle$, starting from the lowest energy state. Exoenergetic collisions can occur when the spin state changes between initial and final states of the collision partners. As shown in Figure 7.2(b), in a gas of ^{7}Li atoms in the $|2\rangle$ state, the sum of energies of two atoms is lower than that of a pair where one atom is in the $|1\rangle$ state and the other one is in the $|3\rangle$ state. Since we only work with the two lowest states $|1\rangle$ and $|2\rangle$, spin-exchange collisions are energetically forbidden. The gas is thus stable against two-body collisions.

7.1.3 The 737.8-G magnetic Feshbach resonance

The $|1\rangle$ ground state of ^{7}Li displays a broad Feshbach resonance near 740 G. Its parameters were determined in [204, 218, 223–225]. The first measurements [223, 224] employed a trap-loss method, exploiting the enhanced trap loss at large values of a. This method is relatively imprecise. In [204], the size of a BEC was determined and compared to mean-field theory (including a beyond-mean-field Lee-Huang-Yang correction) in order to infer $a(B)$. However, the most precise method of determining the parameters of a Feshbach resonance is RF spectroscopy. Here, on the $a > 0$ side of the resonance, shallow dimers are associated using B-field modulations. The measurements were performed in [218, 225]. Throughout this work, we use the parameters obtained in our experiment [218] in order to calculate the s-wave scattering length $a(B)$ as a function of the magnetic field B. In the vicinity of the Feshbach resonance, the value of the scattering length as a function of B can be parametrized as[‡]

$$a(B) \approx \frac{\Gamma_\mathrm{F}}{B_0 - B}, \tag{7.3}$$

with the parameters $\Gamma_\mathrm{F} = 3550(100)\, a_0.\mathrm{G}$, the resonance center field $B_0 = 737.8(2)\,\mathrm{G}$ and the Bohr radius $a_0 \simeq 5.292 \times 10^{-11}\,\mathrm{m}$. We plot Equation (7.3) in Figure 7.3. The $|2\rangle$ state also displays Feshbach resonances, all of them located above 800 G [226] and thus not affecting our experiments, since all of them are performed at magnetic field values below 740 G.

[‡]A more general formula for the magnetic-field dependent scattering length is

$$a(B) \simeq a_\mathrm{bg}\left(1 - \frac{\Delta}{B - B_0}\right), \tag{7.2}$$

where Δ is a measure for the resonance width and a_bg is the background value, that is, the value of a far from resonance. In the case of ^{7}Li in the $|1\rangle$ state, $a_\mathrm{bg} \approx 5\, a_0$ [17]. We state the simplified expression (7.3) because it is valid close to resonance, where the calibration of [218, 225] was performed.

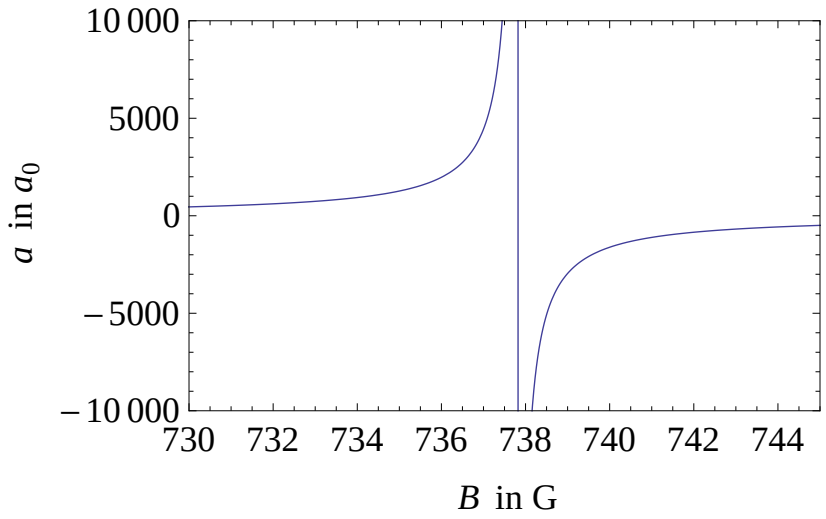

FIGURE 7.3: The s-wave scattering length $a(B)$ as a function of the magnetic field B around the 740-G Feshbach resonance of the $|1\rangle$ state in ^{7}Li. We use the parametrization of [218].

7.2 Experimental procedure

In this section, we will briefly present the experimental steps from the MOT loading, which produces samples of pre-cooled atoms, until the transfer in the final hybrid trap

7.2.1 Zeeman slower, MOT and CMOT

The Zeeman slower and magneto-optical trap (MOT) stages were presented before in Section 4.3.3. In short, the slower consists of an oven containing a sample of metallic lithium with natural abundance of both isotopes. It is heated to up to 500°C to provide sufficient atomic flux out of a collimation tube of a 6-mm internal diameter. The slower is a spin-flip Zeeman slower, meaning that there is a zero-crossing of the magnetic field along the length of the slower. This concept efficiently reduces size and electric power consumption of the setup, and keeps the Zeeman-induced magnetic field and gradient close to zero at the position of the MOT. It also involves a large detuning of the Zeeman-slower beams compared to the MOT beams, thus the MOT is not affected by the presence of the Zeeman-slower light. The laser setup for producing the light beams necessary for operation of the Zeeman-slower, MOT, further manipulation and probing of the atoms is presented in Figure 1.1. Here, the lasers necessary for driving the Zeeman slower were replaced by the laser system presented in Part I of this thesis.

The MOT is formed by three pairs of counterpropagating laser beams. The three pairs form an orthogonal setup. Each beam has a diameter of about 2.5 cm and an intensity of about one saturation intensity $I_{\mathrm{sat},D_2} \simeq 2.5\,\mathrm{mW.cm^{-2}}$. The detuning of both beams is about $6\,\Gamma$, and we trap about 10^{10} atoms at a few millikelvin. The full loading phase of the MOT takes about 10 s, after which the Zeeman slower is switched off.

Due to the excited-state level structure, there is no significant sub-Doppler cool-

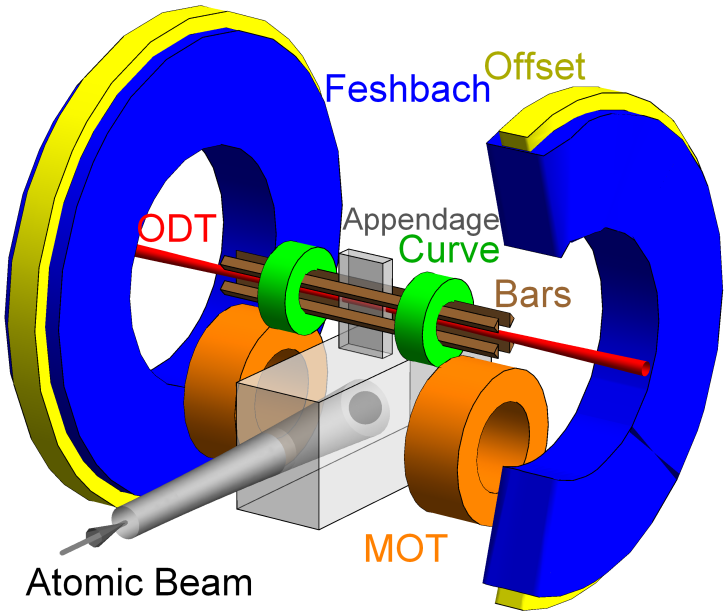

FIGURE 7.4: The central experimental setup, figure taken from [174]. Atoms from the Zeeman-slowed atomic beam are captured in the MOT, at the central point between the MOT coils. Using the MOT and the Feshbach coils, the atoms are magnetically elevated to the Ioffe-Pritchard trap, formed of the magnetic fields produced by the Ioffe bars for radial confinement, and the curvature (Curve) coils for axial confinement. Here, Doppler-cooling and RF-evaporation takes place. The atoms are afterwards loaded in the final trap, consisting of a dipole trap laser beam (ODT) for the radial confinement and the curvature-, Feshbach- and offset coils to provide both axial confinement and a freely tunable magnetic offset field. The right-hand side Feshbach and offset coils are sectioned to improve visibility.

ing present in our system. To improve the phase-space density, a compressed-MOT (CMOT) phase follows the MOT phase. During 8 ms, the beam detuning is changed to about half of the value used for the MOT phase, and the power in the repumper beam is ramped to zero. The atoms are thus efficiently pumped in the $|F = 1\rangle$ ground state, cf. Figure 7.1. After the CMOT phase, we end up with about half the initial MOT atom number at a temperature significantly below 1 mK.

7.2.2 Quadrupolar magnetic trapping and transport

To further improve the phase-space density, we use evaporative cooling in conservative traps. For magnetic traps, Wing's theorem forbids trapping of the lowest ground-

state atoms, because they are high-field seeking [227]. Maxwell's equations forbid the existence of magnetic field minima in free space. Thus, using static magnetic fields, one can only trap low-field seeking states. Identical atoms in stretched states cannot experience spin-changing, exoenergetic collisions[§]. Therefore we optically pump the atoms to the $|8\rangle$ state using a small offset field and a circularly-polarized light beams of frequencies resonant to the transitions from both $F = 1$ and $F = 2$ states, cf. Figure 7.1.

For creating the quadrupole magnetic field trapping the atoms, the current in the MOT coils (cf. Figure 7.4) is ramped to a higher value. By then ramping down the MOT-coil current and simultaneous ramping up of the Feshbach-coil currents in quadrupolar configuration, the atoms are magnetically transported to the appendage of the experimental cell. Due to the small inner dimensions of the appendage (inner width of 5 mm), about half of the atoms are lost during the transport stage.

7.2.3 Ioffe-Pritchard trap

After magnetic transport of the atoms to the appendix, the Ioffe-Pritchard trap is switched on. Four Ioffe bars positioned only 1 mm from the appendage walls yield a strong radial confinement, whereas the axial confinement is provided by the curvature (pinch) coils. The background s-wave scattering length is small and negative for the $|8\rangle$ state. One can show that the scattering cross-section and, following therefrom, the scattering and rethermalization rates are drastically reduced in the millikelvin range [212]. To overcome this issue, a double Doppler-cooling stage was included in the experimental procedure. The movement of the atoms in the radially linear trapping potentiel is coupled. Thus, and because of the remaining collisional redistribution of energy, one only needs a single light beam for Doppler cooling in a quadrupolar magnetic field. For a large bias field of about 500 G, the optical transition from state $|8\rangle$ to the excited state $|F', m_{F'}\rangle = |3, 3\rangle$ is an almost perfect cycling transition. The duration of both Doppler stages is about 1 s, and for the second stage the Ioffe-Pritchard trap is compressed in both radial and axial directions. We ramp the cooling laser beams to full power in ≈ 100 ms to avoid the excitation of sloshing of the cloud in the trap. We end up with about 50% of the atoms at $\approx 200\,\mu$K.

After the Doppler cooling, we perform RF evaporation in the Ioffe-Pritchard trap to further increase phase-space density. We drive the $|8\rangle \rightarrow |1\rangle$ transition to the high-field seeking, lowest-energy ground state. At the end of this stage, we end up with $\approx 10^6$ atoms at temperatures of a few tens of microkelvin, depending on the evaporation trajectory and most importantly on the final RF frequency chosen.

7.3 Hybrid dipolar-magnetic trap

To control the interactions between different species of atoms via magnetic Feshbach resonances, one needs to tune the magnetic offset field at the trap center. The limits imposed here using magnetic traps can be overcome by using optical dipole traps. In

[§]However, dipolar relaxation can occur.

our setup, we use a hybrid dipolar-magnetic trap consisting of a powerful, focused laser beam and a magnetic curvature field, providing additional axial confinement.

The spatial profile of the trapping laser is well approximated by a cylindrically-symmetric Gaussian laser beams, see Section 2.2.1. In a single-beam dipole trap, one thus has three free design parameters, the waist radius w_0, the power P and the detuning from resonance $\Delta = \omega - \omega_0$. Here, ω is the dipole trap laser frequency and ω_0 is the resonance frequency of the atoms, corresponding to the lithium D-lines in our case. The atoms are attracted to high-intensity regions in the case of negative detunings. The trap depth U_0 is proportional to $P/(\Delta w_0^2)$, whereas the photon scattering rate is proportional to $P/(\Delta^2 w_0^2)$. Thus, high-power lasers with large detunings are favorable, resulting in a large choice of trap depths and negligible photon-scattering-induced heating. The trap frequencies scale with the design parameters like

$$\omega_\rho = 2\pi\,\nu_\rho \propto \sqrt{\frac{P}{-\Delta w_0^4}} \tag{7.4}$$

$$\omega_z = 2\pi\,\nu_z \propto \sqrt{\frac{P}{-\Delta w_0^6}} \tag{7.5}$$

We use a 120-W ytterbium fiber laser from *IPG Photonics Corp.*, having a central emission wavelength of 1073 nm. The detuning of ≈ 400 nm is much larger than the atomic fine structure. The power at the trap position is controlled by passing the beam through a high-power acousto-optic modulator (AOM), and the waist at the trap position is $w_0 \approx 35\,\mu$m.

After RF evaporation in the Ioffe-Pritchard trap, the atoms are loaded in the hybrid dipolar-magnetic trap by adiabatically switching on and off the respective traps. The atoms are then transfered from the low-field seeking state $|8\rangle$ to the high-field seeking state $|1\rangle$ using a Landau-Zener sweep consisting of a fixed RF knife and a magnetic field ramp. This requires a switch of the sign of the magnetic field curvature. During this stage, trapping is purely due to the high-power dipole trap.

Further evaporation in the dipole trap is obtained by lowering the laser power and thus diminishing U_0. Thus, the atoms are efficiently evaporated along the radial direction. Using the wide 740-G Feshbach resonance presented in Section 7.1.3, we can tune the scattering length a in state $|1\rangle$ at will. We typically evaporate at $200\,a_0$ in the hybrid dipolar-magnetic trap. Depending on the chosen parameters, we obtain samples of $\approx 10^5$ atoms in the microkelvin range. Evaporating further, Bose-Einstein condensates of $\approx 2 \times 10^4$ atoms at $200\,a_0$ without distinguishable thermal background can be produced.

7.3.1 Trap frequency calibration 1: axial direction

The dipole-trap laser beam is focused to a waist size of $\approx 35\,\mu$m in the center of the trap, providing a reasonably large trapping volume for efficient loading from the Ioffe-Pritchard trap. However, this results in very weak axial trapping. We thus have to resort to additional trapping along the z-axis. We use a constant magnetic curvature field generated by the curvature coils, providing harmonic axial magnetic trapping.

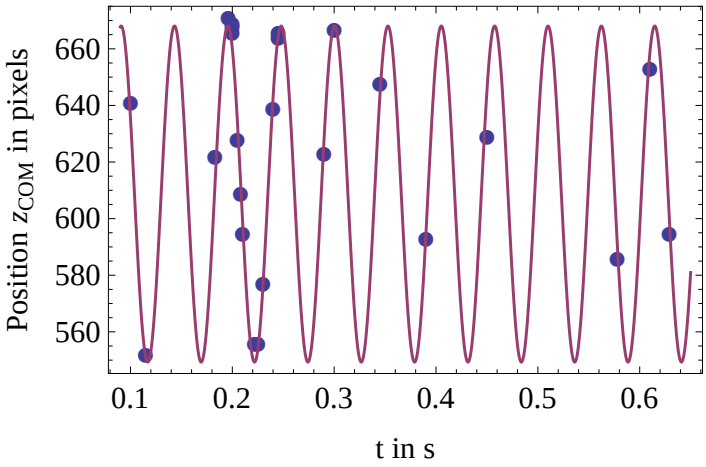

FIGURE 7.5: Axial frequency measurement. The center-of-mass position z_{COM} is determined as a function of the wait time after excitation (dots). The line represents a fit to a sinusoidal [Equation (7.7)] for obtaining the axial frequency ω_z.

This is characterized by the frequency $\omega_{z,\mathrm{mag}}$. In presence of the dipole trap laser of power P, the axial frequency reads

$$\omega_z = \sqrt{\omega_{z,\mathrm{mag}}^2 + \alpha P}, \tag{7.6}$$

where α is a constant depending on the trap geometry. For determination of the atomic densities in our trap, we need precise knowledge of the trap frequencies in both radial and axial directions. Both frequencies depend on the power of the dipole trap laser. Although all the trap parameters can be obtained from first principles, we calibrate our trap by measuring the frequencies as a function of the dipole trap laser power, as will be presented in the next section.

The movement of the center-of-mass coordinate z_{COM} can be separated from the N-body problem. Thus, by simply exciting an axial movement and measuring $z_{\mathrm{COM}}(t)$ as a function of the wait time t after excitation, one observes harmonic oscillations of the cloud in the trap. The oscillation frequency then equals the trap frequency $\omega_z/2\pi$.

We typically prepare a sample of $\approx 10^5$ atoms in the $|1\rangle$ state at $\approx 6\,\mu$K and 720 G, or $a/a_0 = 200$. We performed the excitation by a 20-ms switch-off of the dipole trap laser[¶]. The cloud is then attracted by the center of the magnetic curvature field, whose alignment is not perfect with respect to the laser waist. After re-switch-on, oscillations were observed, see Figure 7.5. We fit gaussian density distributions to the absorption images obtained from the thermal clouds. This yields the center-of-mass coordinate z_{COM} as a function of wait time. The result is presented in Figure 7.5. We fit the data to a simple harmonic-oscillator trajectory

$$z_{\mathrm{COM}}(t) = A\sin(\omega_z t + \varphi) + C, \tag{7.7}$$

where A is the oscillation amplitude, φ a constant phase and C a constant offset of the cloud position. The power P of the trapping laser is measured by shining the beam

[¶]A similar method used occasionally is a fast off-on-switching process of the magnetic field.

on a bolometer after it has passed the experimental glass cell. This method is rather slow, but precise[‖]. According to Equation (7.6), the axial trapping frequency depends on P. We thus repeated the experiment for different values of P and measured the axial frequency. In the evaporation process, P also determines the temperature and atom number for the frequency measurement. The results are presented in Figure 7.6. A fit to Equation (7.6) yields the parameters $\omega_{z,\mathrm{mag}} = 2\pi \times 17.5(3)\,\mathrm{Hz}$ and $\alpha = (2\pi)^2 \times 84(6)\,\mathrm{Hz}^2.\mathrm{W}^{-1}$.

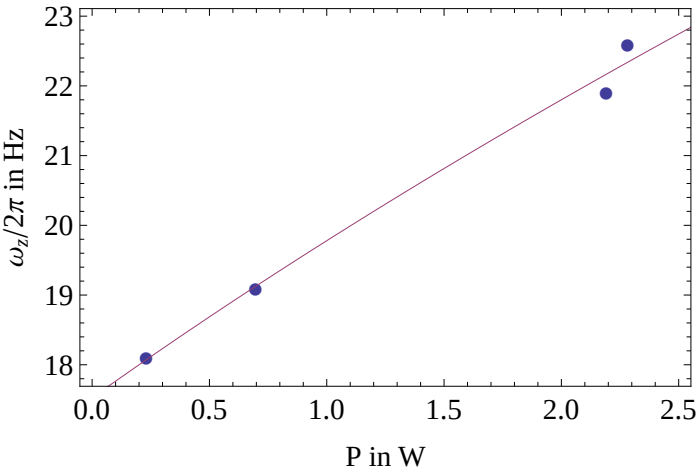

FIGURE 7.6: Axial frequency ω_z as a function of the dipole trap laser power P. The data points stem from several measurements, as presented in Figure 7.5. By fitting the results to Equation (7.6), we obtain the parameters $\omega_{z,\mathrm{mag}} = 2\pi \times 17.5(3)\,\mathrm{Hz}$ and $\alpha = (2\pi)^2 \times 84(6)\,\mathrm{Hz}^2.\mathrm{W}^{-1}$ to calibrate our trap in the axial direction. The fit is represented by the solid line.

7.3.2 Trap frequency calibration 2: radial direction

When applying the method of excitation of a sloshing mode described before for measuring the radial frequency, we faced important practical limitations due to the limited timing resolution of the control system. An alternative method of determining trap frequencies is the parametric excitation of the trapped atoms to higher vibrational states. This is achieved by modulating the trap frequency with a modulation frequency ω_{mod}. This process causes heating and results in atom loss due to evaporation. It becomes resonant at $\omega_{\mathrm{mod}} = 2\omega_\rho$.

We prepare an initial sample of $\approx 6\times10^4$ atoms in the $|1\rangle$ state at $6\,\mu$K and 720 G, or $a/a_0 = 200$, and $P = 1.97\,\mathrm{W}$. We then sinusoidally modulate the laser power P during a hold time of 1 s. The modulation depth is chosen to be less than 10%. We then take time-of-flight images of the remaining atoms to determine the temperature T and the number of atoms remaining. The results are presented in Figure 7.7. We fit a Lorentzian to the data points to obtain the central frequency of the feature, which is two times

[‖]We used the values obtained with this method to calibrate a photodiode that measures the laser power leaking through a mirror used to steer the beam. With the help of the photodiode signal, we can monitor the laser power on shorter time scales.

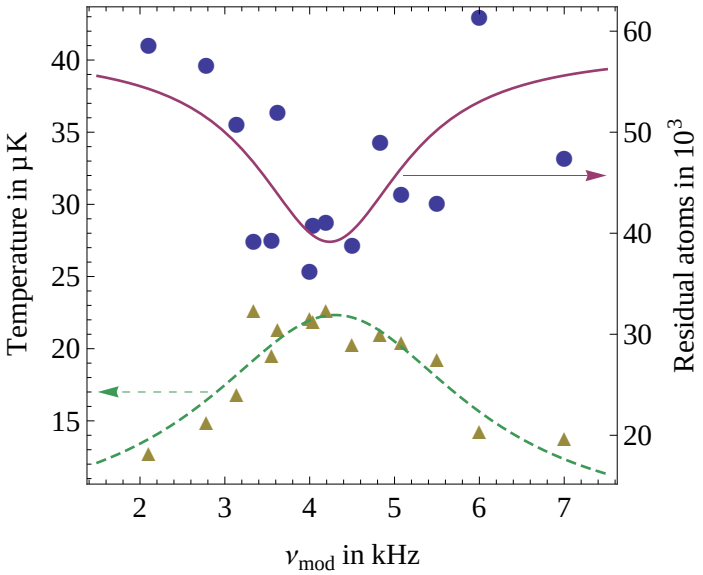

FIGURE 7.7: Radial frequency measurement. By parametric sinusoidal modulation of the trapping laser power at the modulation frequency $\omega_{\mathrm{mod}} = 2\pi\nu_{\mathrm{mod}}$, the atoms gain energy and leave the trap due to evaporation. We measure the temperature T (triangles) and the remaining number of atoms (dots) and fit a Lorentzian to the data (dashed/solid line). The frequency determination from the temperature measurement yields the smallest fitting error, we therefore deduce $\omega_\rho(P = 1.97\,\mathrm{W}) = 2\pi \times 2.15(5)\,\mathrm{kHz}$ from the temperature data.

the radial frequency ω_ρ. Due to the smaller amount of scattering in the temperature data, the fit error is substantially lower than for the remaining-atom-number data. For $P = 1.97\,\mathrm{W}$, we find $\omega_\rho = \omega_c/2 = 2\pi \times 2.15(5)\,\mathrm{kHz}$ from the temperature measurement. The radial frequency can therefore be obtained for arbitrary power by using the simple $\sqrt{P}$ scaling law, cf. Equation (7.4). When changing the dipole trap laser power, the simple scaling law (7.4) now provides the radial trap frequency.

7.4 Imaging

We use a standard absorption imaging technique to probe the atomic samples produced in our setup. The coordinate system given by the hybrid dipolar-magnetic trap is presented in Figure 7.8.

While passing the atom cloud along the y-direction, the resonant probe light is absorbed and statistically reemitted. Thus, the probe beam intensity $I(x, z)$ contains a shadow which carries information about the atomic density distribution. We measure $I(x, z)$ by imaging the beam on a CCD camera. For intensities well below the lithium D_2 saturation intensity $I_{\mathrm{sat}} \simeq 2.5\,\mathrm{mW.cm^{-2}}$, we define the optical density

$$OD(x, z) = \ln\left(\frac{I_0(x, z)}{I(x, z)}\right) = \sigma_{\mathrm{abs}} \int n(\mathbf{r})\,\mathrm{d}x_3, \tag{7.8}$$

where $I_0(x, z)$ is a reference image taken without atoms, $n(\mathbf{r})$ the 3D atom density distribution and σ_{abs} the absorption cross-section. Precise knowledge of the value of σ_{abs} is necessary to derive the column density $n(x, z) = \int n(\mathbf{r})\,\mathrm{d}y$. The value used throughout this thesis, as well as the size calibration, stems from former calibrations of using interacting Bose gases [174, 218]. The validity of the Lambert-Beer law (7.8) is justified for in-situ imaging: Even at peak densities of $10^{12}\,\mathrm{cm}^3$, the product $k_{\text{L}} d_{\text{mean}}$ is much larger than one, where k_{L} is the light wavenumber vector and d_{mean} is the mean distance between atoms [228].

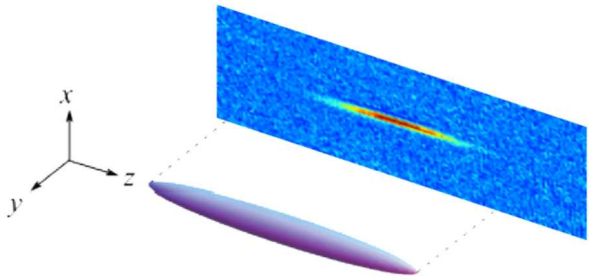

FIGURE 7.8: Schematic of the imaging apparatus and definition of the coordinate system, where the origin is in the center of the cloud. We perform in-situ imaging af the cloud along the y-axis. Time-of-flight imaging along the z-axis is useful to independently measure temperatures and populations. Figure from [218].

We perform in-situ imaging of the atoms along the y-axis, whereas the z-axis time-of-flight imaging can be used to determine temperatures and populations. The frequencies of the probe beams are chosen to match the according transitions of the states to be imaged under the given magnetic field conditions. For in-situ imaging, we obtain a spatial resolution of about $5\,\mu$m. Thus, for Bose-condensed samples, no details of the spatial distribution can be inferred along the x-direction. Due to the limited optical access for the time-of-flight imaging, the remaining numerical aperture results in a spatial resolution of $10\,\mu$m, sufficient to reliably determine temperatures and atom numbers.

7.5 Creating strongly-interacting Bose gases

As discussed in Chapter 6, three-body loss restricts the lifetime of Bose gases at large values of the scattering length. Thus, the transfer of the precooled samples to the strongly-interacting regime needs to be *fast* in order to keep a significant amount of atoms in the trap. Thus, we generally prepare pre-cooled samples at an intermediate scattering length of $200a_0$ and transfer them to the strongly-interacting state. In the following, we will present two fast methods employed by us to create ultracold, strongly-interacting Bose gases.

7.5.1 Magnetic field sweeps

The technique of magnetic field sweeps has been presented in detail in [218]. In brief, a pre-cooled atomic sample is produced in the $|1\rangle$ state at $a = 200a_0$. One then ramps

the magnetic field closer to the Feshbach resonance to increase the interactions. The Feshbach coils display a large inductance, thus their contribution to the field is kept constant, and the sweeps are mediated by the faster offset coils. The limitations of this method are obvious: The magnetic field has to be swept by 20 G to change the value of the scattering length from $200\,a_0$ to the center of the Feshbach resonance. Due to inductive coupling, an absolute field stability of $\lesssim 100$ mG can be provided after $\gtrsim 50$ ms only when using fast sweeps on the order of 100 ms. Since the atoms pass a long time interval at large values of a, an important fraction of the atoms is lost from the trap due to the strongly increased three-body loss.

7.5.2 RF transfers

To mitigate the limitations described before, a second method to produce strongly-interacting Bose gases is radio-frequency (RF) transfer. As before, the samples are initially prepared in the $|1\rangle$ state at $200a_0$. However, before going to the strongly-interacting regime, we apply an RF-induced adiabatic-rapid-passage technique (also called Landau-Zener sweep) to transfer the atoms to the $|2\rangle$ state. We use an antenna close to the appendage to couple RF radiation to the atoms. We then ramp the offset field to the unitarity value of the $|1\rangle$ state corresponding to 737.8 G and let the current overshoot settle afterwards. In the $|2\rangle$ state, the atoms are weakly interacting at this field value and no additional losses are observed during the ramp. Using a powerful RF-pulse, the atoms are then transferred from state $|2\rangle$ to the strongly-interacting state $|1\rangle$ by keeping the magnetic field value fixed. We match the antenna setup to give strongest coupling at the $|2\rangle \rightarrow |1\rangle$ transition frequency of 174.878 MHz at the Feshbach resonance center. The duration of the pulse is chosen such as to obtain the largest number of atoms in the strongly-interacting state in the presence of three-body loss. We apply a 10 ms RF pulse, transferring about 40% of the atoms in the maximally-interacting state $|1\rangle$. Due to the maximum collision rate of the atoms at unitarity, the transfer here is incoherent, and we could not observe Rabi oscillations.

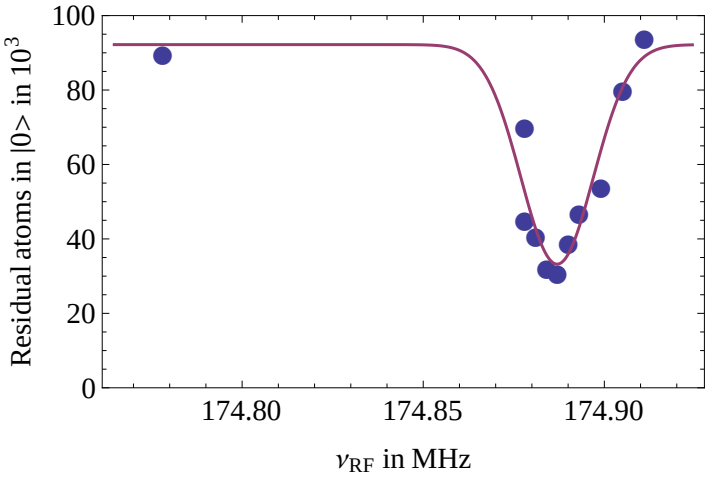

FIGURE 7.9: Transfer $|2\rangle \rightarrow |1\rangle$ at unitarity field. We measure the remaining fraction in the $|2\rangle$ state and fit a Gaussian of 10(2) kHz standard deviation to the data.

We characterize the RF transfer efficiency by measuring the residual number of atoms in the $|2\rangle$ state. The results are presented in Figure 7.9. We fit a Gaussian with a standard deviation of 10(2) kHz. Assuming constant experimental conditions, the remaining number of atoms in the $|2\rangle$ state can serve as a reference for the number of atoms transfered to the $|1\rangle$ state. Even though the transfer efficiency is not unity, the number of strongly-interacting atoms obtained at well-defined fields is superior to the field-sweep method described before.

Since we rapidly transfer the atoms between states of different axial trapping frequencies, we need to be careful to not excite axial breathing of the cloud. The magnetic field contribution $\omega_{z,\mathrm{mag}}$ to the axial trap frequency as defined in Equation (7.6) is proportional to the magnetic field derivative of the internal energy $E_{|i\rangle}(B)$ of an atom in state i with respect to B. We thus have a relative frequency difference at the Feshbach resonance field B_0:

$$\frac{\omega_{z,\mathrm{mag},|1\rangle}}{\omega_{z,\mathrm{mag},|2\rangle}} = \frac{\partial E_{|1\rangle}(B_0)}{\partial B} \Big/ \frac{\partial E_{|2\rangle}(B_0)}{\partial B} \approx 1.0339, \tag{7.9}$$

where the indices refer to the hyperfine states. This small difference is further reduced in the presence of additional dipolar trapping along the slow axis, see (7.6). Indeed, throughout the measurements presented in the course of this work, we never observed axial breathing of the cloud, which would be attributable to the sudden change of the axial trapping frequency when transferring to the strongly-interacting state.

7.5.3 Magnetic field stability

The data presented in Chapter 8 was taken over a period of seven months. During that time, the experimental setup was sensitive to drifts of the magnetic offset field on many timescales. We therefore performed regular magnetic field calibrations by RF spectroscopy to be able to compensate these drifts. We drive $|2\rangle \rightarrow |3\rangle$ RF transitions, cf. Figure 7.2, and measure the fractional transfer efficiency by absorption imaging the populations in both states. We chose the RF power to give 50% transfer at resonance. We fit Gaussians to the fractional transfer data, yielding a standard deviation of $\approx$1.5 kHz. We therefore ensure a magnetic field standard deviation of $\Delta B \approx$100 mG around the unitarity value during the course of each measurement. With the Feshbach resonance calibration presented in Chapter 7, and Equation (7.3), the absolute value of the scattering is larger than

$$|a| \gtrsim \frac{\Gamma}{2\Delta B} \approx 1.8 \times 10^4 a_0 \tag{7.10}$$

within a probability of 95%. At typical densities of $10^{11}\,\mathrm{cm}^{-3}$, we therefore have $|na^3| \gtrsim 0.08$. At the lowest temperatures of $T \approx 1\,\mu$K, we find for the inverse of the thermal wavenumber

$$\frac{1}{k_{\mathrm{th}}} = \sqrt{\frac{2\pi k_{\mathrm{B}} m T}{\hbar^2}} \approx 2000 a_0 \ll |a|\,, \tag{7.11}$$

where k_{B} is Boltzmann's constant and m is the particle mass. In the non-degenerate regime, as it is the case in the studies presented here, k_{th} is the relevant length scale. This proves that our assumption of unitarity is fulfilled, cf. Equation (A.27).

7.6 Summary

In summary, we have presented the experimental tools necessary to produce ultracold samples of bosonic ^{7}Li at unitarity, that is at the Feshbach resonance at 737.8 G. We have introduced the properties of the ^{7}Li atom which are of importance for our measurement. We have then presented the experimental procedure of creating pre-cooled atomic clouds, and the final trap where the experiments are performed. We have performed precise calibration of the trap frequencies along the axial and radial direction, which will be of high importance for the measurements presented in the next chapter. We have then focused on two methods used to quickly transfer the sample to unitarity. With the RF method, we have been capable of transferring 40% of an atomic sample initially in state $|2\rangle$ to the unitary state $|1\rangle$. Finally, we have discussed the imaging method for probing the gas. In the next chapter, we will present measurements of the collisional stability of the unitary Bose gas.

Chapter 8

The unitary Bose gas: Results and discussion

We will present here the results obtained for the finite-temperature unitary Bose gas.

In Section 8.1, we measure the three-body loss rate in the unitary Bose gas as a function of temperature. We will compare the results to existing theory of the unitarity-limited three-body recombination rate, and we will show good agreement without adjustable parameters. We will demonstrate in particular that in the high temperature limit, three-body recombination is strongly suppressed and allows for the introduction of a criterion of quasi-equilibrium in the unitary Bose gas. The experimental fulfillment of this criterion has allowed us to measure the finite-temperature equation of state of the unitary Bose gas, which will be presented in Section 8.2. These results will justify the assumptions imposed for the three-body loss rate measurements. Finally, the chapter will be summarized in Section 8.3.

8.1 Three-body loss in the unitary Bose gas

In this section, we will present the results obtained for the three-body loss rate as a function of temperature of the unitary Bose gas. For practical reasons, we used two methods, magnetic field ramps and RF transfers, in order to transfer the initial sample to unitarity, as presented in Section 7.5.

8.1.1 Experimental procedure

We first prepare non-Bose-condensed samples at different temperatures T_{evap}. Both T_{evap} and the number of remaining atoms are given by the evaporation trajectory, which is stopped at a given power P_{evap} of the dipole trap laser. To avoid atom loss due to residual evaporation, the trap is then radially recompressed by adiabatically ramping the power to $P = 2 \cdot P_{\mathrm{evap}}$ in 500 ms. As discussed in Section 7.3, this increases the trap depth by a factor of 2, and the radial frequency by a factor of $\sqrt{2}$. We then use either of two methods presented in Section 7.5, a magnetic field sweep to the unitarity field value in the $|1\rangle$ state, or an RF transfer from the $|2\rangle$ state to the $|1\rangle$ state at constant magnetic field, to transfer the sample to unitarity.

From imaging along the y-axis, see Figure 7.8, we obtain the atomic line density

$$\bar{n}_{1\mathrm{D}}(z) = \int_{-\infty}^{\infty} \mathrm{d}x\mathrm{d}y\, n(\mathbf{r})\,, \tag{8.1}$$

where the integration over y is naturally established by the absorption imaging process, cf. Figure 7.8*. The number of atoms is calculated according to

$$N_{\mathrm{at}}(t) = \int_{-\infty}^{\infty} \mathrm{d}z\, \bar{n}_{1\mathrm{D}}(z,t)\,. \tag{8.2}$$

We then fit Gaussians to $\bar{n}_{1\mathrm{D}}(z)$. The results are presented in Figure 8.1. The temperature T of the sample is obtained from the in-situ axial halfwidth and the calibrated axial frequency according to the relation

$$T(\sigma_z) = \frac{m\omega_z^2\sigma_z^2}{k_{\mathrm{B}}} \tag{8.3}$$

for the ideal classical gas, where k_{B} is the Boltzmann constant. We will justify this method in Section 8.2.

Due to the density-dependence of higher-order losses (see Equation (8.4) in the next section), atoms are preferentially lost in the trap center, where low-energy atoms accumulate. This process was termed "anti-evaporation" heating in literature [192]. A second loss-induced heating process occurs when the recombination products, a dimer and a free atom in the three-body case, stay in the trap. By colliding elastically with

*In the x direction, we sum over sufficient pixel lines N_{lines} to fulfill $N_{\mathrm{lines}} d_{\mathrm{pix}} > 2\sigma_\rho$, where d_{pix} is the pixel size and σ_ρ the radial width of the cloud obtained from the images. σ_ρ has a lower limit given by the spatial resolution of $\approx 5\,\mu$m. The background signal is obtained from the mean over the same amount of pixel lines N_{lines} above and below the position of the atoms (leaving a gap of σ_ρ between the background regions and the region containing the atomic density signal), and subtracted from the raw data to obtain $\bar{n}_{1\mathrm{D}}(z)$.

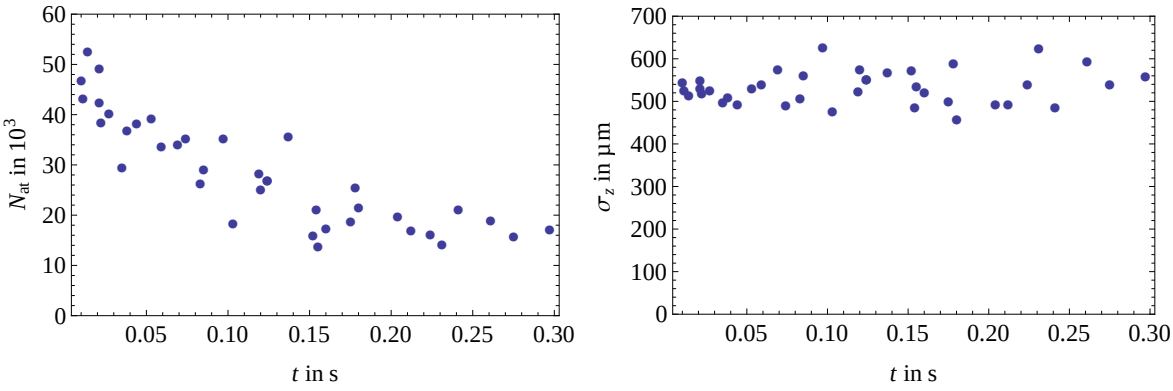

(a) (b)

FIGURE 8.1: Typical decay measurement. (a) The number $N_{\mathrm{at}}(t)$ of remaining atoms as a function of the wait time t after transfer to unitarity. (b) Measurement of the half-width of the atomic density distribution by fitting Gaussians to the line density $\bar{n}_{1\mathrm{D}}$ from the data presented before. No breathing or sloshing can be observed after the transfer to unitarity. For the first 10 ms after the transfer, we observe anti-evaporation heating. Therefore, we neglect these points in the further analysis. After 10 ms, we obtain a mean temperature of 3.3(5) μK.

atoms in the cloud, energy is exchanged, resulting in heating of the cloud. This process is called recombination heating [192]. Since the shallow-dimers state vanishes at unitarity, atoms can only recombine to deeply-bound states in three-body collisions. It is therefore safe to assume that the release energy is sufficient to expel the recombination products from the trap without causing recombination heating.

In the first 10 ms after transfer to unitarity, we observe an expansion of the cloud until mechanical stability sets in. After this wait time, we do not observe anti-evaporation heating within our experimental resolution. The data points up to 10 ms are thus neglected in the further analysis. The scattering of the width data is larger for longer wait times. We attribute this to the lower fitting precision in the low-density regime. No breathing or sloshing excitations of the cloud can be observed. Determination of the temperature is therefore realized by calculating the mean value of the clouds' halfwidths and inserting it into Equation 8.3. For the example data presented in Figure 8.1(b), we obtain $\sigma_{z,\mathrm{mean}} = 520(50)\,\mu$m, corresponding to a temperature of 3.3(5) μK.

8.1.2 Decay rate equations

Many processes lead to atom loss in conservative traps. They can be classified by N, the number of identical particles involved in a loss event. The single-particle case $N = 1$ is due to collisions with molecules of the residual background gas or residual resonant light. In the case of $N > 1$, a collision of N identical particles leads to loss. These collisions can be exoenergetic due to the formation of molecules or changing the internal state of the atoms. The released energy can be orders of magnitude larger than the trap depth, so the atoms are expelled in absence of further collisions. In a mesoscopic picture of the homogeneous gas, atom loss is expressed as decrease in

the atomic density n. Since the probability of finding N particles in the infinitesimal volume $\mathrm{d}V$ is proportional to n^N, one generally writes

$$\dot{n} = \frac{\mathrm{d}}{\mathrm{d}t} n(t) = -\sum_{N=1}^{\infty} L_N n^N(t)\,, \tag{8.4}$$

The solution of (8.4) is a decay curve. In principle, its shape allows one to distinguish between loss processes of different order N.

We perform measurements on trapped samples of atomic cloud, where the density distribution is not homogeneous. We assume Gaussian density distributions in the high temperature limit, as we will justify in Section 8.2. Thus,

$$n(\mathbf{r},t) = \frac{N_{\mathrm{at}}(t)}{(2\pi)^{3/2}\bar{\sigma}^3(t)} \exp\left[-\frac{1}{2}\left(\frac{x^2}{\sigma_x^2(t)} + \frac{y^2}{\sigma_y^2(t)} + \frac{z^2}{\sigma_z^2(t)}\right)\right], \tag{8.5}$$

where $\bar{\sigma} = (\sigma_x\sigma_y\sigma_z)^{1/3} = (\sigma_\rho^2\sigma_z)^{1/3}$ is the geometric average of the Gaussian half-width of the cloud. The spatial average reads

$$\langle X(t)\rangle \equiv \frac{\int_{\mathrm{trap}} \mathrm{d}V\, n(\mathbf{r},t)\, X(\mathbf{r},t)}{\int_{\mathrm{trap}} \mathrm{d}V\, n(\mathbf{r},t)}\,, \tag{8.6}$$

for any function $X(\mathbf{r},t)$. A simple calculation for three-dimensional Gaussian distributions yields

$$\langle n(t)\rangle = \frac{N_{\mathrm{at}}(t)}{(4\pi)^{3/2}\bar{\sigma}^3(t)}\,, \tag{8.7}$$

which is a fraction $2^{-3/2}$ of the peak density n_{peak}. From absorption imaging along the y-axis, see Section 7.4, we obtain σ_z. At the same time, due to the limited optical resolution along the x-axis, we hardly gain any knowledge about the radial width, which is on the order of magnitude of the optical resolution. On the other hand, the energy-equipartition theorem results in the condition

$$\frac{\sigma_\rho}{\sigma_z} = \frac{\omega_z}{\omega_\rho}\,. \tag{8.8}$$

We therefore get

$$\bar{\sigma}^3 = \left(\frac{\omega_z}{\omega_\rho}\right)^2 \sigma_z^3\,. \tag{8.9}$$

8.1.3 Suppression of $N \neq 3$-order loss

In the following we will show that loss processes of order N different from three can be neglected under our experimental conditions.

- $N = 1$: As in any ultracold-atom experiment, the trap lifetime is limited by loss events caused by collisions with residual background atoms. This effect is represented by the $N = 1$ term in (8.4). At low scattering lengths, we measured the lifetime due to this restriction to be $\gtrsim 90\,\mathrm{s}$. This value is more than two orders of magnitude above any timescale considered in our three-body loss measurements. Thus, $N = 1$-body loss is neglected in further the analysis.

- $N = 2$: In order to conserve energy and momentum, one needs N bodies to form a molecule consisting of $N-1$ atoms.[†] It is thus easy to see that molecule creation is not possible in pure two-body collisions of ground-state atoms. An example of a two-body loss processes are spin-changing collisions, where atoms fall to deeper $|F, m_F\rangle$ ground states. Since we work with atoms in the lowest energy state $|1,1\rangle = |1\rangle$, the process is energetically forbidden. In a mixture of $|1\rangle$ and $|2\rangle$ atoms, dipolar relaxation is strongly suppressed, see Section 7.1.2. We could not observe any signature of such a process. Finally, evaporation also is a two-body process. Due to the experimental procedure, in which we ramp the trap depth back to twice the final evaporation value, we suppress this loss process efficiently.

- $N \geq 4$: The theory of the unitarity limit of N-body scattering, see Equation A.23, allows the calculation of the four-body contribution $L_4 n_{\mathrm{peak}}^4 = 4k_4 n_{\mathrm{peak}}^4$ in (8.6). Assuming a unitary-limited three-body loss rate, the relative magnitude of the four-body contribution is

$$\frac{4K_4 n_{\mathrm{peak}}^4}{3K_3 n_{\mathrm{peak}}^3} \leq \frac{35 \cdot 2^{7/6}\pi^2}{\sqrt{3}} \frac{n_{\mathrm{peak}}}{k_{\mathrm{th}}^3} = \frac{35}{2^{11/6}\sqrt{3}\pi} n_{\mathrm{peak}} \lambda_{\mathrm{th}}^3, \tag{8.10}$$

  where $\lambda_{\mathrm{th}} = \sqrt{2\pi\hbar^2/(mk_{\mathrm{B}}T)}$ is the thermal wavelength. The relative 4-body contribution is lower than 2% for all experimental situations considered, and we can thus safely neglect it and all higher orders.

We are left with the three-body term dominating the decay. We obtain the mean density points $\langle n(t)\rangle$ from Equation (8.7) and the knowledge of atom number and the mean Gaussian halfwidth presented in Figure 8.1(b). We assume that

$$\langle n(\mathbf{r},t)\rangle = N_{\mathrm{at}}(t)\ \langle f(\mathbf{r})\rangle\,, \qquad \frac{\partial}{\partial t} f = 0\,. \tag{8.11}$$

This assumption, equivalent to $T = \text{const.}$ in the case of an ideal classical density distribution, is justified from the width measurements, see Section 8.1.1. We furthermore use the identity

$$\frac{\langle n^N\rangle}{\langle n\rangle^N} = \frac{2^{3N/2}}{(N+1)^{3/2}} \tag{8.12}$$

for three-dimensional Gaussian density distributions. In the exclusive presence of three-body loss, and under the assumption (8.11) of constant temperature, the solution of (8.6) reads

$$\langle n(t)\rangle = \left(\frac{16}{3^{3/2}} L_3 \cdot (t - t_0) + \frac{1}{\langle n_0\rangle^2}\right)^{-1/2}, \tag{8.13}$$

using the (8.12) and separation of the variables. As we have justified in Section 8.1.1, the $t < 10\,\mathrm{ms}$ data is excluded from the analysis. The result is presented in Figure 8.2.

[†]When forming one molecule of $N-1$ identical atoms, a fraction $(N-1)/N$ of the binding energy released in the recombination process is delivered to kinetic energy of the free atom, and the rest to kinetic energy of the molecule.

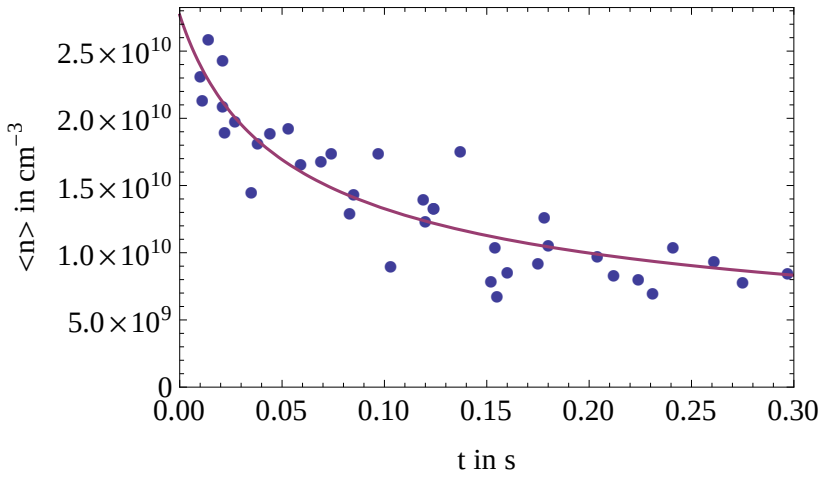

FIGURE 8.2: Decay curve for the densities obtained from the data presented before (circles). We neglected the $t < 10\,\text{ms}$ data (triangles), as described in the text. We fit the data to (8.13) and obtain the three-body loss rate constant $L_3 = 1.4(7) \times 10^{-20}\,\text{cm}^6.\text{s}^{-1}$ at $3.3(5)\,\mu\text{K}$.

Equation (8.13) nicely fits the data and we obtain a three-body loss constant of $L_3 = 1.4(7) \times 10^{-20}\,\text{cm}^6.\text{s}^{-1}$ at a temperature of $3.3(5)\,\mu\text{K}$.

The temperature error bar is obtained from the standard deviation of the width data. The error bar of $L_3(T)$ contains a contribution of the fit routine used, and a contribution from the systematic uncertainty on $\langle n \rangle$. According to Equation (8.7), the mean density has a strong σ_z^{-3} dependence on the cloud width. We thus take into account the second order for the derivation of the error of $L_3(T)$. Its relative value is of the order of 60%[‡]. The fact that the mean density depends sensitively on σ_z and the trap frequencies demonstrates the importance of the trap frequency calibration presented in Section 7.3. By fitting the data to a solution of Equation (8.6) including a four-body term, we find no significant contribution from four-body loss, as predicted from Equation 8.10. This method, however, yields the same values for L_3. Thus, we cannot distinguish $N \geq 4$-body loss.

8.1.4 Temperature-dependent results

The experiment was repeated for different temperatures T from 1.6–7.9 μK to obtain the three-body loss rate $L_3(T)$. We used different trapping laser powers P and the recompression by a factor of two in power, as discussed before. The result is presented in Figure 8.3, where the blue points are obtained using the magnetic field sweep method, and the green triangles result from the magnetic field sweep method.

[‡]If $u(X)$ is the absolute error of a physical quantity X, we get up to second order:

$$\frac{u(\langle n \rangle)}{\langle n \rangle} \simeq \frac{1}{\langle n \rangle} \left| \left(\frac{\partial}{\partial \sigma_z} \langle n \rangle \right) u(\sigma_z) + \left(\frac{1}{2} \frac{\partial^2}{\partial \sigma_z^2} \langle n \rangle \right) u^2(\sigma_z) \right| = \left| -3 \frac{u(\sigma_z)}{\sigma_z} + 6 \left(\frac{u(\sigma_z)}{\sigma_z} \right)^2 \right| \approx 30\% \,. \quad (8.14)$$

The relative value for the error of L_3 is thus about twice this value, since according to Equation (8.13), $L_3 \propto \langle n \rangle^{-2}$.

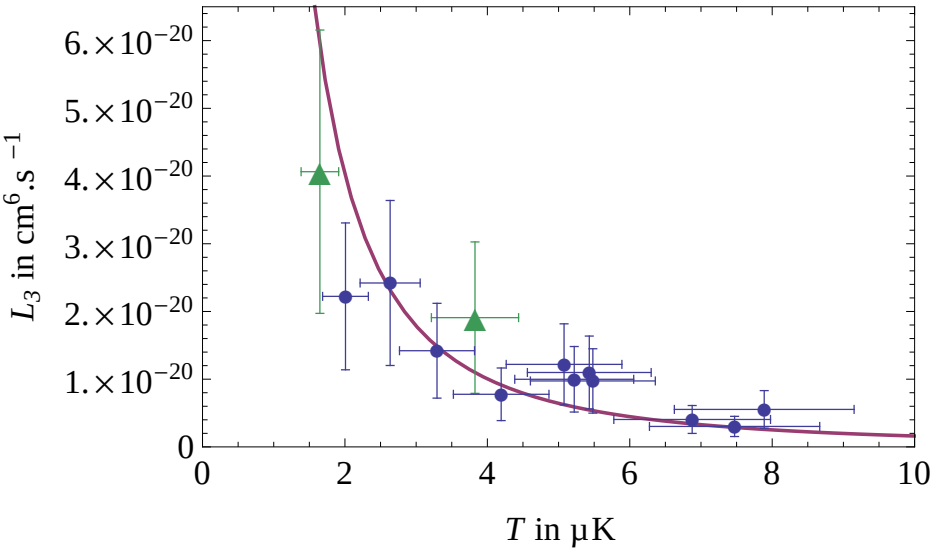

FIGURE 8.3: Measurement of the three-body loss rate constant $L_3(T)$ as a function of temperature obtained from the magnetic field sweep method (circles) and the RF transfer method (triangles). The error bars represent the standard deviation from the decay curve fits to (8.13), and a systematic contribution from the uncertainty of the density, see text. The solid line is the theoretical prediction of the unitarity-limited loss rate from Equation (8.15), which describes the data without adjustable parameters.

We also plot in Figure 8.3 the theoretical prediction of the unitarity-limited three-body recombination loss rate constant from Equation (A.36) and References [200, 201],

$$L_{3,\mathrm{lim}}(T) = 3 \cdot K_{3,\mathrm{lim}}(T) = \frac{216\sqrt{3}\pi^2\hbar^5}{m^3 k_\mathrm{B}^2 T^2}, \tag{8.15}$$

which represents the $J = 0$ contribution, where J is the total angular momentum of the three-body system, cf. Appendix A. The limit is in good agreement with the data points. The experimental data is therefore well described by theory without adjustable parameters. A fit of the data points to $L_3(T) = \chi \cdot L_{3,\mathrm{lim}}(T)$ yields the fit parameter $\chi = 0.7(1)$. However, in this fit method using an inverse-square law, the low-temperature points get a strong weight due to the larger values of $L_3(T)$.

To gain further insight, we calculate the ratio $\chi(T) = L_3(T)/L_{3,\mathrm{lim}}(T)$ of the same data points and the theoretical values of the unitarity-limited three-body loss rate from Equation (8.15). The result is shown in Figure 8.4, where the solid line at $\chi(T) = 1$ marks the theoretical expectation, around which the data is scattered. To calculate a weighted average, we weight each point according to its uncertainty on $\chi(T)$. We thus have

$$\chi_\mathrm{rel} = C_N \sum_i \frac{\chi(T_i)}{w_i}\,. \tag{8.16}$$

with the normalization constant

$$C_N = \left(\sum_i \frac{\chi(1)}{w_i}\right)^{-1} \tag{8.17}$$

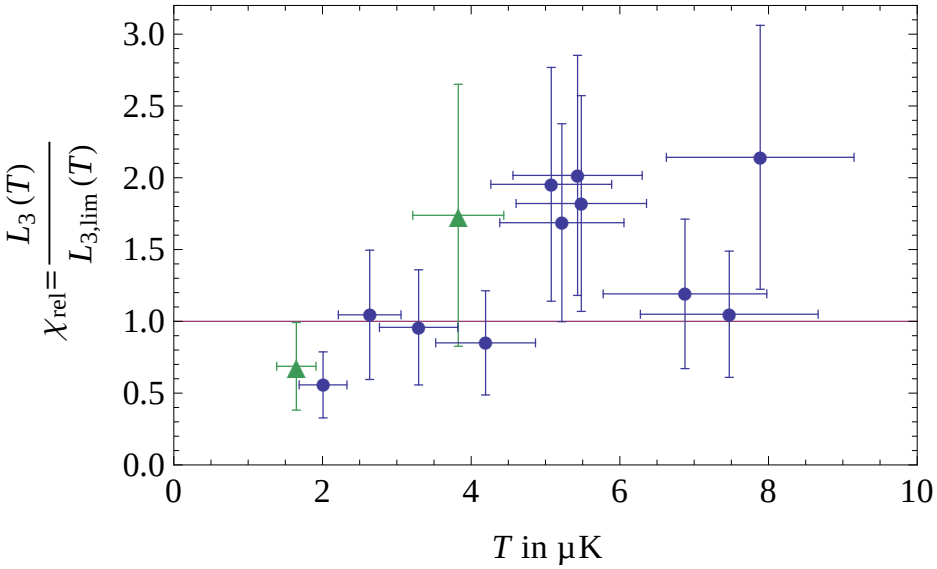

FIGURE 8.4: Relative loss rate coefficients as a function of temperature. We obtain these data points by normalizing the data presented in Figure 8.3 according to $\chi(T) = L_3(T)/L_{3,\mathrm{lim}}(T) = 1$. $L_{3,\mathrm{lim}}(T)$ is the theoretical prediction (8.15) of the unitarity-limited three-body loss rate coefficient, and is indicated by the solid line. By performing a weighted average of the data points (see text), we get $\chi_{\mathrm{rel}} = 1.1(3)$.

and the weights $w_i = u^2(\chi_i(T))$, where $u(\chi_i(T))$ is the error of the i-th point. Analogously, we find a weighted standard deviation to obtain an error bar. From the result of $\chi_{\mathrm{rel}} = 0.9(2)$, we infer that the theory presented in Appendix A describes the data well within the experimental error bars.

The derivation of the unitarity-limited three-body loss rate (8.15) assumes pure S-wave (total angular momentum J=0) contribution. Therefore, $\chi(T)$ is independent of temperature. However, the data points in Figure 8.4 may show a systematic growth with temperature. Measurements at higher temperatures should eventually show the onset of contributions from higher orders of J. References [229, 230] predict the next-highest order contribution to originate from the $J = 2$ channel. Using model potentials for three-body recombination of helium atoms, the onset temperature is predicted to be in the microkelvin range [201]. In [231], secondary collisions are discussed, leading to the expulsion of more than three atoms per three-body recombination event. Since the magnitude p of the effect is proportional to $\langle n \rangle \cdot l$, where $l \propto \bar{\sigma}$ is a typical lengthscale, and $\langle n \rangle \propto \bar{\sigma}^{-3}$, we get $p \propto \bar{\sigma}^{-2} \propto T^{-1}$. We infer that secondary collisions can not explain larger-than-predicted loss at high temperatures.

8.1.5 A criterion of collisional quasi-equilibrium

As discussed in Chapter 6, three-body loss can pose strict constraints on the possibility to realize strongly-interacting gases, because the gaseous state is not a ground state of the system. To achieve quasi-equilibrium, we will have to find a regime in which three-body loss is sufficiently suppressed. This is established when the atoms execute more elastic than inelastic collisions. The resulting criterion of collisional quasi-equilibrium

can be stated as

$$\frac{\gamma_2}{\gamma_3} \gg 1\,, \tag{8.18}$$

where the γ_N are the single-particle N-body collision rates. Their unitarity-limited values are given in Equations (A.31) and (A.37). The results presented in this section confirm the theoretical prediction of the unitarity-limited, temperature-dependent three-body recombination rate $L_3(T)$ [232], from which γ_3 is obtained easily. We therefore have

$$\frac{\gamma_2}{\gamma_3} = \frac{8}{9\sqrt{3}} \frac{(mk_\mathrm{B}T)^{3/2}}{\pi^{3/2}\hbar^3 n} = \sqrt{\frac{2^9}{3^5}} \frac{1}{n\lambda_\mathrm{th}^3} \approx 1.45 \frac{1}{n\lambda_\mathrm{th}^3}\,, \tag{8.19}$$

Fulfilling (8.19) allows the study of thermodynamic quantities of the unitary Bose gas. This criterion restricts the quasi-equilibrium area of the phase diagram to the non-degenerate regime, see for instance [196]. For all the data presented in this thesis, the ratio γ_2/γ_3 of elastic to inelastic collisions is larger than 500, therefore the criterion of collisional quasi-equilibrium (8.18) is fulfilled.

8.2 Low-fugacity unitary Bose gas equation of state

In this section, we will present the results obtained on the equation of state (EoS) of the finite-temperature, unitary Bose gas. Apart from its own interest, this measurement delivers information about the atomic density distribution in the trap, justifying the assumptions made in Section 8.1.2.

Since we took in-situ images for the three-body loss measurements presented in Section 8.1, we can use this data for determining the EoS. The equation of state is a thermodynamic quantity defined for gases in (quasi-)equilibrium. Considering the ratio of elastic versus inelastic collisions, condition 8.18 is fulfilled for all our data, as demonstrated in Section 8.1.5. To attain quasi-equilibrium in a *trapped* sample of atoms, another limitation arises: The atoms are oscillating in the trap, and the slowest trap frequency, ω_z in our case, defines a typical timescale for achieving global quasi-equilibrium in the ensemble:

$$\tau_z = \frac{1}{\omega_z}. \tag{8.20}$$

Only after the sample passed at least this amount of time in the strongly-interacting state, it can be regarded as being in quasi-equilibrium. This process is of general nature and independent of the other timescales presented before. We thus make sure that the gas is indeed in an equilibrium state by using data taken after of a minimum wait time $t \geq 20\,\mathrm{ms} > \tau_z$. This also ensures settling of the magnetic field after the current overshoots occuring when ramping to the unitarity value.

Assuming validity of the local density approximation, we measure the EoS from the 1D-line density $\bar{n}_\mathrm{1D}(z)$, see Equation (8.1)

$$P(\mu(z)) = \frac{m\omega_\rho^2}{2\pi}\,\bar{n}(z), \tag{8.21}$$

represented by the pressure $P(\mu)$, where

$$\mu(z) = \mu_0 - V(z), \tag{8.22}$$

is the local chemical potential in presence of the trapping potential $V(z) = m\omega_z^2 z^2/2$. This elegant method was proposed in [233–235] and successfully applied for the first time in [217].

We have obtained the integrated line density $\bar{n}_{1D}(z)$, see Equation (8.1) from 85 images taken at 3 different mean temperatures. From $\bar{n}_{1D}(z)$, we have measured the total atom number N_{at} and the temperature T [Equations (8.2) and (8.3)]. As we will see later, the EoS and thus the density distribution can well be described by an ideal classical gas. Therefore, for each image we can determine the lowest value ζ_0 of the inverse fugacity from the ideal classical EoS:

$$\zeta_0 = \exp\left(-\frac{\mu_0}{k_B T}\right) = \frac{(k_B T)^3}{\hbar^3 \omega_z \omega_\rho^2 N_{at}} \,. \tag{8.23}$$

The spatial variation of the inverse fugacity follows from Equation (8.22) and the known trap potential along z

$$\zeta(z) = \zeta_0 \, \exp\left(-\frac{m\omega_z^2}{2k_B T} z^2\right) \,. \tag{8.24}$$

From $\bar{n}_{1D}(z)$ and (8.21), (8.23) and (8.24), we obtain an EoS consisting of 17000 $(\zeta, P(\zeta))$ tuples. The result is presented in Figure 8.5. The raw data points show a large scattering, mostly due to shot noise of the CCD camera used for absorption imaging[§]. To reduce the noise, we perform a moving average over 1200 subsequent

[§]The CCD noise could in principle be reduced using a camera equipped with a cooled sensor. However, an even stronger limitation arises from interference fringes occurring in our imaging scheme. This effect is a general problem when imaging with coherent light sources. However, it was shown in Reference [236] that these fringes can efficiently removed using image post-processing.

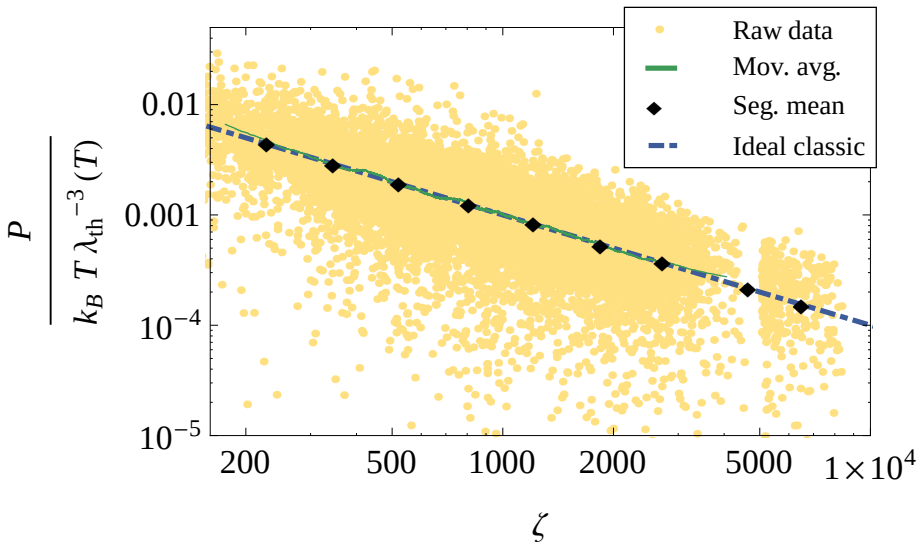

FIGURE 8.5: Equation of state (EoS) of the finite-temperature unitary Bose gas. The raw data consists of 17000 points. By using two averaging methods, moving average and mean of equally-spaced segments, we are able to significantly reduce the noise. The dash-dotted line marks the EoS of the ideal classical gas.

data points (green solid line in Figure 8.5). Since the distribution of the data points on the $\log(\zeta)$ axis is not homogeneous, regions of high data point density are favored. Therefore, in a second approach, we divide the dataset in segments of equal spacing on the $\log(\zeta)$ axis. We calculate the mean values of $(\zeta, P(\zeta))$ for each of these, represented by black diamonds in Figure 8.5. Both methods decrease the noise by orders of magnitude.

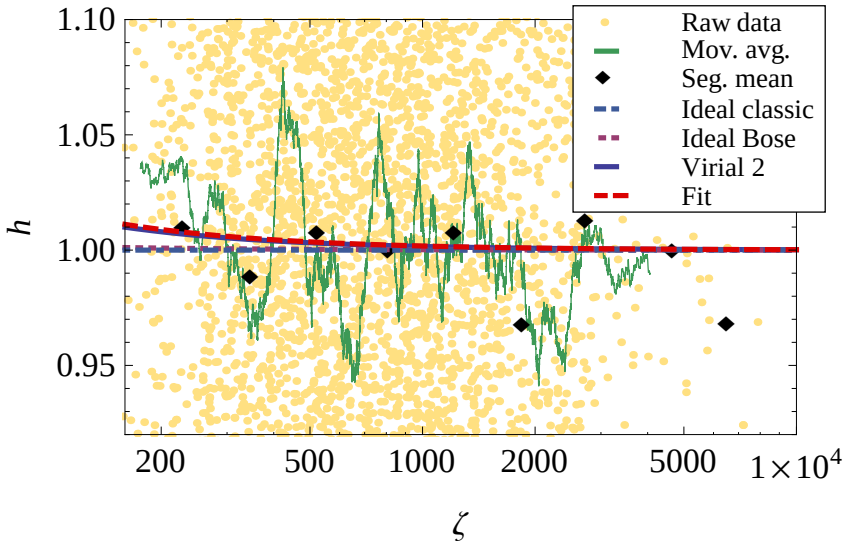

FIGURE 8.6: Relative representation of the equation of state (EoS) of the finite-temperature unitary Bose gas with respect to the ideal classical gas. We experimentally obtained 17000 data points, which display a large scattering. Two methods of averaging the data, as presented in the text, are shown (Moving average and mean of equally-spaced segments). A fit of the raw data to a second-order virial EoS yields a virial coefficient of $b_2 = 1.8(2.7)$, close to the prediction [237] of $b_2 \approx 1.59$, but also compatible with zero within experimental error bars. The predicted second-order virial EoS is also shown.

We gain further information by plotting the EoS normalized with respect to the ideal classical gas,

$$h(\zeta) = \frac{P(\zeta)}{P_{\mathrm{ic}}(\zeta)}\,, \tag{8.25}$$

in Figure 8.6, where $P_{\mathrm{ic}} = k_{\mathrm{B}}T/(\lambda^3\zeta)$. We get a reduced-noise EoS by averaging, as described before. We also include theoretical predictions from the ideal Bose gas and the virial expansion. The mean value of all data points is $h = 1.0(9)$. We get $h = 1.00(3)$ and $h = 1.01(4)$ for the moving average and average over the equally-spaced segments, respectively. Within our error bars, we do not observe any deviation from the ideal classical gas EoS. Comparing with the predictions for the ideal Bose gas and the second-order virial expansion for the unitary Bose gas [237] in Figure 8.6, related corrections to the EoS should vanish in the noise. The standard deviation of the moving average amounts to 3%. Imposing this value, we expect a second-order

virial correction of the same order below $\zeta_0 = 50$, which can be obtained in our setup[¶]. The stability criterion (9) shows a $T^{3/2}/n$ behavior, whereas the ideal classical inverse fugacity (8.23) goes like T^3/n. Therefore, while keeping the gas in quasi-equilibrium by lowering the density, we do not find a principal limitation on the inverse fugacity.

Furthermore, we fit the complete dataset to the normalized second-order virial EoS

$$h_2(\zeta) = \frac{P_{\mathrm{v2}}(\zeta)}{P_{\mathrm{ic}}(\zeta)} = 1 + \frac{b_2}{\zeta}\,, \tag{8.26}$$

with the coefficient b_2 as a fit parameter. We obtain $b_2 = 1.8(2.7)$, a value which is remarkably close to the theoretical prediction $b_2 = 9\sqrt{2}/8 \approx 1.59$ [237]. It is compatible with zero within error bars. Therefore, we cannot observe any deviation from the ideal classical gas, or any other theory for the EoS presented. This result allows one to define an upper limit of $b_2 < 4.5$ for the second-order virial coefficient of the unitary Bose gas.

Apart from its own interest, the measurement of the EoS of the unitary Bose gas justifies the assumptions made in Section 8.1. The fact that our samples can be described by the ideal classical Boltzmann gas EoS is a proof of our assumption of Gaussian density distributions made in Section 8.1.

8.3 Summary

In summary, in the first section of this chapter we have presented our measurements of the temperature-dependent, unitarity-limited three-body loss rate constant in the resonantly interacting Bose gas. We have introduced the method of analyzing the data and discussed the negligible influence of $N \neq 3$ loss processes. Our measurements are well described by the theory presented in Appendix A within experimental error bars. The theory is free of adjustable parameters and represents the fastest-possible loss rate. We have furthermore discussed processes leading to higher losses than predicted.

The second section of this chapter is dedicated to the measurement of the equation of state (EoS) of the finite-temperature unitary Bose gas. We have briefly discussed the method of obtaining the EoS from the in-situ data obtained when measuring the three-body loss coefficients. We have compared the data of the normalized pressure to theory, and we have observed no departure from the ideal classical gas within our experimental signal-to-noise ratio. To observe corrections to the ideal classical EoS, one would have to decrease the inverse fugacity ζ, which can possibly be achieved by reaching lower temperatures and higher atom numbers, while maintaining a quasi-equilibrium situation in our trap. The EoS measurement furthermore justifies the measurement of the three-body loss rate coefficient presented before.

[¶]We obtained a preliminary result of $\zeta_0 < 40$ without recompressing the sample after evaporation to P_{evap}.

Chapter 9

Conclusion to Part II

Summary

In the second part of this thesis, we have presented results obtained on the Bose gas at strongest-possible s-wave interaction, that is, at unitarity. We have first introduced the theoretical tools of the N-body scattering problem and given applications to the two- and three-body situation necessary to understand our measurements.

We have then briefly discussed the present experimental apparatus of the lithium experiment at ENS, where we have detailed on the newly-established method of RF transfers, bringing $\approx 40\%$ of the atoms initially in the weakly-interacting state $|2\rangle$ to the unitary state $|1\rangle$ at constant magnetic field. We are thus capable of producing and probing finite-temperature Bose gases of macroscopic atom numbers. The frequencies of the final trap depend on the power of the dipole trap laser, which is varied. We have presented a careful calibration to obtain reliable values for the mean spatial densities of atoms in the trap.

We then have presented our measurement of the three-body loss constant in the unitary Bose gas as a function of temperature. We have detailed on the methods of data analysis. Based on the theory presented, we can explain our experimental findings without any adjustable parameter. These results are universal in the sense that they are valid for any unitary Bose gas with short-range interactions. The experimental verification of the theory of losses allows the definition of the quasi-equilibrium range for the unitary Bose gas: The condition for quasi-equilibrium in any gas is that a particle executes more elastic collisions than inelastic ones. This yields the ratio

$$1 \ll \frac{\gamma_2}{\gamma_3} = \frac{8}{9\sqrt{3}} \frac{(mk_{\mathrm{B}}T)^{3/2}}{\pi^{3/2}\hbar^3 n} = \sqrt{\frac{2^9}{3^5}} \frac{1}{n\lambda_{\mathrm{th}}^3} \approx 1.45 \frac{1}{n\lambda_{\mathrm{th}}^3},$$

between the elastic two-body collision rate γ_2 and the inelastic three-body collision rate γ_3. The condition for quasi-equilibrium is that this rate is larger than one*. This condition for the existence of a quasi-equilibrium state of the homogeneous, finite-temperature unitary Bose gas can only be stated after the experimental characterization of the three-body loss rate, an essential ingredient for the the three-body scattering rate per particle γ_3, which was presented in this part of the present thesis. We recall

*Note that for the right-hand side of Equation 9 to be valid, temperatures need to be in microkelvins and densities in cm^{-3}.

that the theory contains no adjustable parameters. It represents the fastest-possible formation of molecules in the S-wave channel. The fact that the reaction rate constant rises when lowering the temperature is an evident contradiction of the Arrhenius equation[†].

We have then employed the data collected for the loss experiment for measuring the equation of state (EoS) of the finite-temperature unitary Bose gas down to inverse fugacities of $\zeta \approx 200$. In the low-fugacity limit, where the gas is very dilute, the EoS is that of an ideal classical gas because of the absence of important interactions and correlations. The EoS we have measured does not contain features allowing to distinguish it from the classic ideal gas within the experimental signal-to-noise ratio. We have performed a fit in order to determine a value for the second-order virial coefficient. The result $-0.9 \leq b_2 \leq 4.5$ is compatible to the theoretical prediction $b_2 \approx 1.6$ [237] and allows for the definition of an upper bound of b_2.

Perspectives

The subject of how the three-body losses can be described in the finite-temperature unitary Bose gas has been elucidated by the measurements presented in this thesis. However, open questions still remain. An obvious one is the onset of contributions from higher angular momenta. Being frozen out at ultracold temperatures analogously to the two-body case, these depend on the detailed shape of the three-body potential. Theoretical predictions indicate [201, 230] their onset at what is normally considered ultracold temperatures, that is in the 10-mK range for lithium. A further question is the comparison of the behavior of the three-body loss rate to the theoretical calculations across the Feshbach resonance. Reference [201] predicts a step-like behavior of the three-body loss rate when crossing the Feshbach resonance, where k_3 drops to less then one tenth of the unitarity limit on the $a < 0$ side. We could not observe this phenomenon even within the finite magnetic field stability in our setup. More profound examination needs to be pursued here. However, for fermionic systems it is now well known that properties of the system change smoothly when crossing a Feshbach resonance.

Further examination the RF transfer method introduced in this thesis should reveal interesting physics. In the mean-field regime, the population dynamics can be described by a Josephson-like Hamiltonian, which includes a transition from the well-known Rabi oscillations to interaction-induced population self-trapping [238, 239]. Since in our case, the atoms in state $|1\rangle$ have strongest-possible interactions, the mean-field description breaks down. Thus, we expect modified behavior, possibly described by quantum-Zeno-effect-like dynamics.

The equation of state (EoS) measurements have been limited by the finite amount of data on hand for very low temperatures. This imposes a given signal-to-noise ratio, ideally being lower than the corrections to the EoS of the ideal classical gas. These are predicted to have a relative amplitude of 1% for the highest fugacities we could observe. Another option for observing these effects is to work in a range where higher corrections are observable. To keep the condition of quasi-equilibrium for a given fugacity and

[†]The Arrhenius equation for the chemical reaction rate constant is commonly stated as $K = A \exp[-E_a/(k_B T)]$, where the constants A and E_a depend on the system under consideration.

temperature, and the resulting three-body loss rate, a promising experimental step is the increase of the slowest frequency. Thus, the increase the magnetic curvature to increase the axial frequency, and simultaneous decrease of the radial frequency allows to keep a low enough density. The faster equilibration resulting from this change of the experimental parameters would allow to keep significantly more atoms to proceed deeper inside the interesting correlated regime of high fugacities [196, 237].

The present setup, where both fermionic and bosonic lithium atoms can simultaneously be present in the same trap at ultracold temperatures not only provides an interesting testbed for mixed-quantum-statistics manybody theories. It also permits to access boson-fermion Efimov physics [240, 241], a field completely uncovered in current experimental literature.

General conclusion

In the first part of this thesis, a novel all-solid state laser source emitting 840 mW of output power at 671 nm was presented. The very satisfying performance of the source is emphasized by the fact that soon after its completion, the laser was used for driving the Zeeman slower in the lithium experiment at ENS. Apart from occasional maintenance, it remained operational in this role, and its remarkable stability has impressed its operators for more than six months now.

In the second part of this thesis, we have reported on measurements of the three-body loss rate in the finite-temperature unitary Bose gas. The loss rate constant L_3 was measured as a function of temperature. We have found that it is well described by the limiting value imposed by quantum mechanics. Using this result, we have been capable of establishing a stability criterion for the homogeneous gas. In the regime of quasi-stability, we measured the equation of state.

In the lithium experimental apparatus, we have the possibility of studying ultracold isotopic mixtures of fermionic ^{6}Li and bosonic ^{7}Li. Thus, Bose-Fermi Efimov physics [240, 241] can be explored experimentally. Since the datasets needed for these studies require a great number of experimental points, reliable laser sources are a key issue here. Experiments on strongly-interacting Bose-Fermi mixtures will provide further insight in mixed-statistic many-body Hamiltonians [242–244], for example in the study of the bosonic polaron [245–247]. The lithium isotope shift is $\approx$10 GHz, we are therefore building a similar second laser source to bridge this frequency gap and drive a dual-species MOT of ^{6}Li and ^{7}Li.

Appendix A

A glance on theory

The knowledge of the scattering problem of identical Bosons is of major importance for the work presented in this thesis. We will thus detail on the N-particle scattering problem, from which we will deduce results for the case of two and three particles. This allows to discuss the possibility of establishing a quasi-equilibrium state of the unitary Bose gas.

A.1 The N-body scattering problem

We will present the nonrelativistic treatment of the N-body scattering problem. Since we consider N particles in three-dimensional space, the problem is a priori $3N$-dimensional. Separation of the center-of-mass coordinate, however, allows to reduce the problem to $d = 3(N-1)$ dimensions.

We formally introduces hyperspherical coordinates in the center-of-mass system. We assign to any d-dimensional vector $\mathbf{r}$ a hyperradius r,

$$r^2 = \frac{1}{N} \sum_{i<j} r_{ij}^2 \,, \tag{A.1}$$

where r_{ij} is the distance between particles i and j. r is thus a measure of the size of the system. We are left with $d-1$ hyperangles, combined in the quantity $\check{r}$:

$$\mathbf{r} \to \{r = |\mathbf{r}|, \check{r} = \mathbf{r}/|\mathbf{r}|\} \tag{A.2}$$

For d-dimensional wavenumber vectors $\mathbf{k}$, we have accordingly

$$\mathbf{k} \to \{k = |\mathbf{k}|, \check{k} = \mathbf{k}/|\mathbf{k}|\} \tag{A.3}$$

A great choice of the hyperangular subset $\check{r}$ of hyperspherical coordinate systems exists. Since we will only consider quantities integrated or averaged over the angular coordinates, the choice is arbitrary and of no further importance.

The results of the treatment presented here was published in [248] and [249]. It is the straightforward generalization of the 2-body theory presented e.g. in [161]. In the asymptotic limit $r \to \infty$, the wave function is of the form

$$\Psi_a \propto \mathrm{e}^{\mathrm{i}\mathbf{k}\mathbf{r}} + f(\mathbf{k}, \mathbf{k}') \frac{\mathrm{e}^{\mathrm{i}kr}}{r^{\frac{d-1}{2}}} \,, \tag{A.4}$$

where the first term represents the incoming part, a plane wave. The second term describes an outgoing hyperspherical wave, whose relative amplitude is fixed by the scattering amplitude $f(\mathbf{k},\mathbf{k}')$. Furthermore, we can develop d-dimensional functions in terms of hyperspherical harmonics $Y_{\lambda\mu}(\check{r})$ [250]

$$\Psi_b = \sum_{\lambda\mu} A_{\lambda\mu} Y_{\lambda\mu}(\check{r}) \left[j_{d,\lambda}(kr)\cos\delta_\lambda - n_{d,\lambda}(kr)\sin\delta_\lambda \right] , \tag{A.5}$$

where $\lambda \in \mathbb{N}_0$ and $-\lambda \leq \mu \leq \lambda$, $\lambda \in \mathbb{Z}$ are quantization numbers of the hyperspherical harmonics. $A_{\lambda\mu}$ are constants of the development, and δ_λ is the scattering phaseshift [161]. The d-dimensional hyperspherical Bessel (Neumann) functions $j_{d,\lambda}(kr)$ ($n_{d,\lambda}(kr)$) read [250]

$$j_{d,\lambda}(kr) = \frac{\Gamma(\alpha)}{(d-4)!!}\frac{J_{\alpha+\lambda}(kr)}{(kr)^\alpha} \xrightarrow[kr\to\infty]{} \sqrt{\frac{2}{\pi}}\frac{2^{\alpha-1}\Gamma(\alpha)}{(d-4)!!}\frac{\cos\left(kr - \frac{2\alpha+2\lambda-1}{2}\pi\right)}{(kr)^{\alpha+1/2}}, \tag{A.6}$$

$$n_{d,\lambda}(kr) = \frac{\Gamma(\alpha)}{(d-4)!!}\frac{N_{\alpha+\lambda}(kr)}{(kr)^\alpha} \xrightarrow[kr\to\infty]{} \sqrt{\frac{2}{\pi}}\frac{2^{\alpha-1}\Gamma(\alpha)}{(d-4)!!}\frac{\sin\left(kr - \frac{2\alpha+2\lambda-1}{2}\pi\right)}{(kr)^{\alpha+1/2}}, \tag{A.7}$$

where Γ is the Riemann zeta function, and $J_{\alpha+\lambda}$ ($N_{\alpha+\lambda}$) are the usual one-dimensional Bessel (Neumann) functions. We also introduced $\alpha = d/2-1$. $Y_{\lambda\mu}$ are eigenfunctions of the d-dimensional total angular momentum operator $\Lambda^2 \equiv -\sum_{i>j}^{d}(x_i\partial_j - x_j\partial_i)^2$,

$$[\Lambda^2 - \lambda(\lambda+d-2)]Y_{\lambda\mu}(\check{k}) = 0\,. \tag{A.8}$$

Obviously, the eigenvalues are $\lambda(\lambda+d-2)$. We now can compare the expressions for Ψ_a and Ψ_b to distinguish the ingoing and outcoming contributions similarily to the case of two particles [161]. By using the hyperspherical Fourier transform [250]

$$\mathrm{e}^{\mathrm{i}\mathbf{kr}} = (d-2)!!\frac{2\pi^{d/2}}{\Gamma(d/2)}\sum_\lambda \mathrm{i}^\lambda j_{d,\lambda}(kr) Y^*_{\lambda\mu}(\check{k}) Y_{\lambda\mu}(\check{r})\,, \tag{A.9}$$

and the "lucky guess" of

$$A_{\lambda\mu} = (d-2)!!\frac{2\pi^{d/2}}{\Gamma(d/2)}\mathrm{i}^\lambda Y^*_{\lambda\mu}(\check{k})\exp(\mathrm{i}\delta_\lambda)\,, \tag{A.10}$$

we can calculate the difference

$$\Psi_b - \mathrm{e}^{\mathrm{i}\mathbf{kr}} = f(\mathbf{k},\mathbf{k}')\frac{\mathrm{e}^{\mathrm{i}kr}}{r^{\frac{d-1}{2}}}\,, \tag{A.11}$$

We find for the scattering amplitude

$$f(\mathbf{k},\mathbf{k}') = \left(\frac{2\pi}{k}\right)^{\frac{d-1}{2}} \sum_{\lambda\mu,\lambda'\mu'} \mathrm{e}^{-\mathrm{i}\pi(d+\lambda-3)/2} Y^*_{\lambda\mu}(\check{k}) Y_{\lambda'\mu'}(\check{k}')(S_\lambda - 1)\,, \tag{A.12}$$

where $S_\lambda = \mathrm{e}^{2\mathrm{i}\delta_\lambda}$ is the so-called S matrix. By allowing coupling between the (λ,μ) channels, we get

$$f(\mathbf{k},\mathbf{k}') = \left(\frac{2\pi}{k}\right)^{\frac{d-1}{2}} \sum_{\lambda\mu,\lambda'\mu'} \mathrm{e}^{-\mathrm{i}\pi(d+\lambda-3)/2} Y^*_{\lambda\mu}(\check{k}) Y_{\lambda'\mu'}(\check{k}')(S_{\lambda\mu,\lambda'\mu'} - \delta_{\lambda,\lambda'}\delta_{\mu,\mu'})\,, \tag{A.13}$$

An important physical quantity is the scattering cross-section for distinguishable particles

$$\sigma_{\text{dist}} = \left\langle \int \mathrm{d}\check{k}\, |f(\mathbf{k}, \mathbf{k}')|^2 \right\rangle_{\check{k}} . \tag{A.14}$$

To calculate it from (A.13), we integrate over the final hyperangles $\check{k}'$ using the orthonormality relation

$$\int \mathrm{d}\check{k}\, Y^*_{\lambda\mu}(\check{k}) Y_{\lambda'\mu'}(\check{k}) = \delta_{\lambda,\lambda'}\delta_{\mu,\mu'} \tag{A.15}$$

and averaging over the initial hyperangles $\check{k}$ according to

$$\langle X \rangle_{\check{k}} = \frac{\int \mathrm{d}\check{k}\, X}{\int \mathrm{d}\check{k}} = \frac{\int \mathrm{d}\check{k}\, X}{I(d)} . \tag{A.16}$$

$I(d)$ is the d-dimensional solid angle [250]

$$I(d) = \frac{2\pi^{d/2}}{\Gamma(d/2)} , \tag{A.17}$$

and Γ is the Riemann-Zeta function. This is appropriate to our experimental situation, where we do not measure the initial or final hyperangles, but rather deal with a uniform distribution. The result is

$$\sigma_{\text{dist}} = \frac{1}{I(d)} \left(\frac{2\pi}{k}\right)^{d-1} \sum_{\lambda\mu,\lambda'\mu'} |S_{\lambda\mu,\lambda'\mu'} - \delta_{\lambda,\lambda'}\delta_{\mu,\mu'}|^2 . \tag{A.18}$$

In the case of indistinguishable particles, one has to include permutation (anti-)symmetry and therefore gets the modified cross-section

$$\sigma_{\text{indist}} = N_p \sigma_{\text{dist}} . \tag{A.19}$$

For instance, for N indistinguishable particles, we have $N_p = N!$. The N-body collision rate constant is obtained from σ_{indist} by multiplying it by the hyperradial velocity,

$$K_N(k) = \frac{\hbar k}{\mu_N} \sigma_{\text{indist}} = \frac{\hbar k}{\mu_N} \cdot \frac{N_p}{I(d)} \left(\frac{2\pi}{k}\right)^{d-1} \sum_{\lambda\mu,\lambda'\mu'} |S_{\lambda\mu,\lambda'\mu'} - \delta_{\lambda,\lambda'}\delta_{\mu,\mu'}|^2 , \tag{A.20}$$

where we used the definition of the N-body reduced mass in d dimensions,

$$\mu_N = \left(\frac{\prod_{i=1}^N m_i}{\sum_{i=1}^N m_i}\right)^{\frac{1}{N-1}} = \frac{m}{N^{\frac{1}{N-1}}} . \tag{A.21}$$

Unitarity implies that the sum in (A.20) is replaced by $\sum_J (2J+1) s_J(k)$ [248, 249], where we introduced the total angular momentum J and the contribution $s_J \leq 1$ of channel J. We end up with

$$K_{N,\text{unit}} = N_p N^{\frac{1}{N-1}} \, \Gamma\left(\frac{3(N-1)}{2}\right) \frac{\hbar}{m} \left(\frac{4\pi}{k^2}\right)^{\frac{3N-5}{2}} \sum_J (2J+1) s_J(k) . \tag{A.22}$$

In the ultracold regime, higher angular moment are "frozen out". The only remaining contribution originates from $L = 0$:

$$K_{N,\max} = N_p N^{\frac{1}{N-1}} \, \Gamma\left(\frac{3(N-1)}{2}\right) \frac{\hbar}{m} \left(\frac{4\pi}{k^2}\right)^{\frac{3N-5}{2}} , \tag{A.23}$$

The same result for $L = 0$ was found independently using a generalized N-body optical theorem [251]. The N-body scattering event rates per particle are calculated as follows:

$$\gamma_N = K_N n^{N-1} , \tag{A.24}$$

where n is the number density of a gas assumed uniform here.

A.1.1 Two-body elastic scattering

To form a molecule in a collision of N ground state* atoms, one needs $N + 1$ collision partners to conserve energy†. In the case of $N = 2$, it is thus easy to see that all collisions need to be of elastic nature, except for the cases that have been discussed in Section 8.1. We also do not need to take into account higher partial waves, $l \neq 0$, which is easy to see from the fact that in alkali-atoms, the term of lowest order in r of the interatomic potential is $-C_6/r^6$. The large-distance potential thus reads

$$V(r) = -\frac{C_6}{r^6} + \frac{\hbar^2 l(l+1)}{2mr^2} . \tag{A.25}$$

This potential features a rotational barrier with a height of

$$V_\mathrm{b} = \frac{1}{3\sqrt{6C_6}} \cdot \left(\frac{\hbar^2 l(l+1)}{m}\right)^{3/2} . \tag{A.26}$$

As we will see later, p-wave scattering is symmetry-forbidden for bosons. For ^{7}Li, the next-higher contribution comes from the d-wave channel, or $l = 2$. With the C_6 of [154], this yields a d-wave barrier of a height of 9 mK, a value three orders of magnitude above the typical energy scale in our experiments.

The elastic s-wave scattering amplitude reads [161]

$$f_s(k) = -\frac{1}{\frac{1}{a} + ik + \frac{1}{2}k^2 r_\mathrm{e} + O(k^4)} , \tag{A.27}$$

where r_e is the effective range of the potential. In the ultracold limit, $k \to 0$, the r_e term and all higher orders disappear. Thus, the scattering process is fully described by a single parameter, the s-wave scattering length a.

$$a = -\lim_{k\to 0} \frac{\tan\delta_o(k)}{k} , \tag{A.28}$$

*The use of the term ground-state atom is ambiguous. As it is the convention in atomic physics, we will refer to all states in the $|F, m_F\rangle$ manifold of the $2^2S_{1/2}$ state of ^{7}Li as ground states. Since we will work with atoms in the absolute ground state $|1, 1\rangle$, inelastic two-body collisions that necessarily change the internal state of the collision partners are energetically forbidden.

†The $(N-1)/N$-fold of the binding energy released in the recombination process is delivered to the free atom.

f_s does not have any angular dependence. Owing to the fact that the description of the interaction does not depend on the microscopic parameters, this regime is called the *universal* regime.

Unitarity of the two-body scattering matrix is achieved when

$$a \to \infty \tag{A.29}$$

The unitarity-limited cross section than reads

$$\sigma = N_p \frac{4\pi}{k^2}\,, \tag{A.30}$$

and we have $N_p = 2$ for identical bosons, $N_p = 0$ for identical fermions and $N_p = 1$ for distinguishable particles. Thus, because of (anti)symmetrization of the 2-body wavefunction for indistinguishable particles, identical fermions do not scatter in the s-wave channel. For the same reason, the scattering amplitude for identical bosons does not have a p-wave contribution. From this result and (A.23), (A.24), we get the unitarity-limited collision rate for identical Bosons

$$\gamma_2 = \frac{\hbar k}{\mu_2}\sigma n = \frac{4\pi\hbar n}{mk} = \frac{64\sqrt{\pi}\,\hbar^2 n}{\sqrt{m^3 k_\mathrm{B} T}}\,, \tag{A.31}$$

Another intriguing feature of short-range interactions is the existence of a shallow universal dimer for $a > 0$, which is the weakest bound state of the molecular potential. Its energy reads

$$E_\mathrm{d} = \frac{\hbar^2}{ma^2}. \tag{A.32}$$

Because the universal dimer disappears at unitarity, it does not provide a decay path for our measurements.

A.1.2 Unitarity-limited three-body loss

From Equation (A.23) we readily get the expression for $K_3(E)$:

$$K_3(E) = \frac{144\sqrt{3}\pi^2\hbar^5}{m^3E^2}\sum_J (2J+1)s_L(E)\,, \tag{A.33}$$

where we used the identity $E = \hbar^2k^2/(2\mu_3)$. To account for our experimental situation, where we control the temperature T of an atomic cloud instead of the collision energy, we need to average over an energy distribution. In the non-condensed regime, we get [230, 252][‡]

$$K_3(T) = \frac{\displaystyle\int_0^\infty \mathrm{d}E\, K_3(E)\, E^2 \exp\left(-\frac{E}{k_\mathrm{B}T}\right)}{\displaystyle\int_0^\infty \mathrm{d}E\, E^2 \exp\left(-\frac{E}{k_\mathrm{B}T}\right)}\,. \tag{A.34}$$

[‡]Note that the according Equation (4) given in [252] is wrong, the factor 2 needs to be in the denominator instead of the numerator.

The integration is straightforward and it follows

$$K_{3,\mathrm{lim}}(T) = \frac{72\sqrt{3}\pi^2\hbar^5}{m^3 k_\mathrm{B}^2 T^2}\,, \tag{A.35}$$

where we assumed exclusive unitarity-limited $J = 0$ contribution. We assume now that any three-body collision described here leads to the formation of a dimer. These states rapidly decay to (nonuniversal) two-body deeply-bound states. The binding energy liberated in this process is converted to kinetic energy of the dimer and the free atom. It is orders of magnitude above the typical depth of the traps used to confine the atoms, so both the free atom and the dimer will be lost directly from the trap, if no further collisions happen. To calculate the three-body *loss* rate constant from the *event* rate constant, we have to multiply it by the number of lost particles per event, which is three:

$$L_{3,\mathrm{lim}}(T) = \frac{216\sqrt{3}\pi^2\hbar^5}{m^3 k_\mathrm{B}^2 T^2} \tag{A.36}$$

This allows to define a scattering rate per particle according to (A.24):

$$\gamma_{3,\mathrm{lim}}(T,n) = K_{3,\mathrm{lim}}(T)n^2 = \frac{72\sqrt{3}\pi^2\hbar^5 n^2}{m^3 k_\mathrm{B}^2 T^2}\,. \tag{A.37}$$

A.2 Equation of state of the finite-temperature unitary Bose gas

Three-body loss can pose strict constraints on the possibility to realize strongly-interacting gases, because the gaseous state is not a ground state of the system. We will have to find a regime in which three-body loss is sufficiently suppressed for the gas to be in quasi-equilibrium. This is established when the atoms execute significantly more elastic than inelastic collisions, which can be stated as

$$\frac{\gamma_2}{\gamma_3} \gg 1\,. \tag{A.38}$$

The γ_i are defined in Equations (A.31) and (A.37).

$$\frac{\gamma_2}{\gamma_{3,\mathrm{lim}}} = \frac{8}{9\sqrt{3}}\frac{(mk_\mathrm{B}T)^{3/2}}{\pi^{3/2}\hbar^3 n} = \sqrt{\frac{2^9}{3^5}}\frac{1}{n\lambda_\mathrm{th}^3} \approx 1.45\,\frac{1}{n\lambda_\mathrm{th}^3}\,, \tag{A.39}$$

which needs to be larger than one in quasi-equilibrium. For the definition of Equations (A.31) and (A.39) we used the thermal de-Broglie wavelength

$$\lambda_\mathrm{th} = \frac{2\pi}{k_\mathrm{th}} = \sqrt{\frac{2\pi\hbar^2}{mk_\mathrm{B}T}}\,. \tag{A.40}$$

The pressure P can be defined as

$$P = f(T,z)\,, \tag{A.41}$$

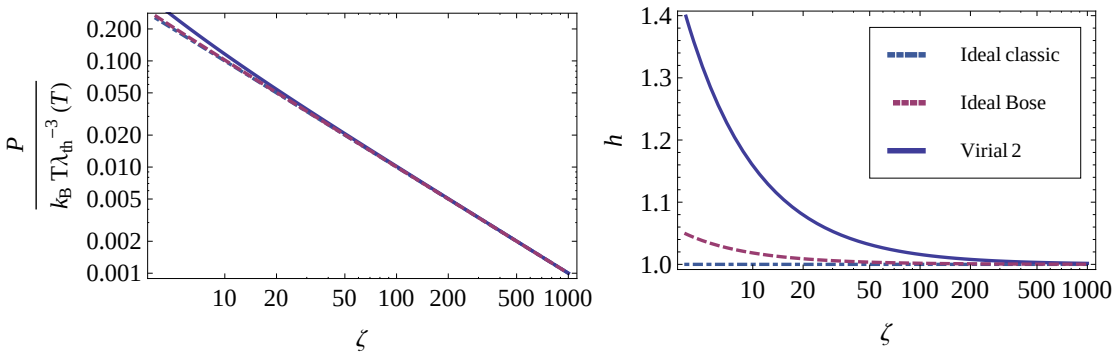

FIGURE A.1: The equations of state from Equations (A.42), (A.44) and (A.47).

where $z = \exp[\mu/(k_\mathrm{B}T)]$ is the fugacity and μ is chemical potential. The function $P(T, z)$ over its variable range is called the equation of state (EoS) of a gas. We will give a few examples here.

In the case of no interaction-free particles and classical statistics, the EoS reads

$$P_\mathrm{ic} = \frac{k_\mathrm{B}T}{\lambda_\mathrm{th}^3} z \,, \tag{A.42}$$

the EoS of the idel classical or Boltzmann gas. For more realistic systems in the high-temperature limit, one can perform a development of the pressure in terms of powers of the fugacity:

$$P = \frac{k_\mathrm{B}T}{\lambda_\mathrm{th}^3} \sum_{n=1}^{\infty} b_n z^n \,. \tag{A.43}$$

This development is called virial development, and the coefficients b_n are accordingly called the n-th order virial coefficients. As it is obvious, in the ideal classical case all coefficients are zero except for $b_1 = 1$. Since any gas of sufficiently low fugacity can always be described by an ideal classical gas, because interactions and correlations do not play a role anymore, $b_1 = 1$ holds for any gas. The ideal Bose gas above condensations threshold displays the EoS

$$P_\mathrm{iB} = \frac{k_\mathrm{B}T}{\lambda_\mathrm{th}^3} \mathrm{Li}_{5/2}(z) \,, \tag{A.44}$$

where the polylogarithm is defined as

$$\mathrm{Li}_s(z) = \sum_{q=1}^{\infty} \frac{z^q}{q^s} \tag{A.45}$$

It is immediately clear from this definition that the virial coefficients of the ideal Bose gas read

$$b_n = n^{-5/2} \,. \tag{A.46}$$

Using the known analytic solution of the two-body problem in a trap, the second virial coefficient for the unitary Bose gas has been determined to be [237]

$$b_2 = \frac{9}{8}\sqrt{2} \approx 1.59 \,. \tag{A.47}$$

The EoSs (A.42), (A.44) and (A.47) are shown in Figure A.1.

Appendix B

Publications

We will present here work published in peer-reviewed journals in the framework of this thesis.

Article A:

A. Ridinger, S. Chaudhuri, T. Salez, U. Eismann, D. Fernandes, K. Magalhães, D. Wilkowski, C. Salomon and F. Chevy, *Large atom number dual-species magneto-optical trap for fermionic* ^6Li *and* ^{40}K *atoms*, The European Physical Journal D **65**, 223-242 (2011)

Eur. Phys. J. D (2011)
DOI: 10.1140/epjd/e2011-20069-4

THE EUROPEAN PHYSICAL JOURNAL D

Regular Article

Large atom number dual-species magneto-optical trap for fermionic ^{6}Li and ^{40}K atoms

A. Ridinger[1,a], S. Chaudhuri[1], T. Salez[1], U. Eismann[1], D.R. Fernandes[1], K. Magalhães[2], D. Wilkowski[3,4], C. Salomon[1], and F. Chevy[1]

[1] Laboratoire Kastler Brossel, École Normale Supérieure, CNRS, Université Pierre et Marie-Curie, 24 rue Lhomond, 75231 Paris Cedex 05, France
[2] Instituto de Física de São Carlos, Universidade de São Paulo, Caixa Postal 369, 13560-970 São Carlos-SP, Brazil
[3] Centre for Quantum Technologies, National University of Singapore, 117543 Singapore, Singapore
[4] Institut Non Linéaire de Nice, Université de Nice Sophia-Antipolis, CNRS, 06560 Valbonne, France

Received 29 January 2011 / Received in final form 16 February 2011
Published online 27 April 2011 –

Abstract. We present the design, implementation and characterization of a dual-species magneto-optical trap (MOT) for fermionic ^{6}Li and ^{40}K atoms with large atom numbers. The MOT simultaneously contains 5.2×10^9 ^{6}Li-atoms and 8.0×10^9 ^{40}K-atoms, which are continuously loaded by a Zeeman slower for ^{6}Li and a 2D-MOT for ^{40}K. The atom sources induce capture rates of 1.2×10^9 ^{6}Li-atoms/s and 1.4×10^9 ^{40}K-atoms/s. Trap losses due to light-induced interspecies collisions of ∼65% were observed and could be minimized to ∼10% by using low magnetic field gradients and low light powers in the repumping light of both atomic species. The described system represents the starting point for the production of a large-atom number quantum degenerate Fermi-Fermi mixture.

1 Introduction

The study of ultracold atomic Fermi gases is an emerging research field aiming to understand many-body quantum phenomena occurring in various fields, such as condensed matter systems, disordered systems, quark-gluon plasmas or astrophysics (neutron stars) [1,2]. They provide a unique opportunity to create strongly correlated many-body systems with a high degree of experimental control. One intends to realize analog quantum simulators in Feynman's spirit [3], with which many-body Hamiltonians could be solved.

In the field of ultracold Fermi gases the study of mixtures of two different fermionic species with different mass is gaining interest. Both theoretical and experimental aspects motivate this study. Such mixtures are predicted to exhibit a rich phase diagram such as phase separation [4], crystalline phases [5], exotic pairing mechanisms [6] and long-lived trimers [7]. They further allow the creation of polar molecules, which have a long-range dipole-dipole interaction [8,9]. Two different atomic species yield additional tunable parameters, such as the mass imbalance and species-specific potentials. The mass-imbalance can be varied in an optical lattice, where the effective mass of each species depends on the optical lattice parameters.

The mixture ^{6}Li-^{40}K is a prime candidate for these studies. ^{6}Li and ^{40}K are the only stable fermionic alkali isotopes and thus belong to the experimentally best-mastered class of atoms. Moreover, both species have bosonic isotopes which can also be used to create boson-fermion gases. Furthermore, the mass difference between the two species is large leading to a large electric dipole moment for heteronuclear diatomic molecules (3.6 D) [10]. Finally, many of the above-mentioned predicted quantum phases require strong interspecies interactions and a universal behavior of the gas. It was recently reported [11] that it is possible to reach the universal regime for the ^{6}Li-^{40}K-mixture due to the existence of a 1.5 gauss-wide Feshbach resonance.

The starting point of most mixture experiments is a dual-species magneto-optical trap. It is desirable to capture a large number of atoms at this stage for the following reasons. First, large atom numbers allow to anticipate the losses induced by the subsequent evaporative cooling procedure, which needs to be applied to reach the quantum degenerate regime. Second, a large initial atom number makes the evaporation procedure more efficient. Third, the Fermi temperatures of the gas are larger for larger atom numbers and thus quantum phenomena can be observed at higher temperatures. Finally, a large atom number leads to better signal-to-noise ratios and a greater robustness in day-to-day operation.

A dual-species magneto-optical trap with large atom numbers also allows an efficient creation of ultracold heteronuclear molecules via photoassociation. Using this technique, we have been able to create excited

[a] e-mail: armin.ridinger@gmail.com

heteronuclear ^{6}Li-^{40}K* molecules with a formation rate of $\sim 5 \times 10^7 s^{-1}$. The results of this experiment will be the subject of a separate publication [12].

In this article we describe the design, implementation and characterization of a dual-species magneto-optical trap for ^{6}Li and ^{40}K with large atom numbers. In a dual-species MOT, the atom number is in general reduced compared to single-species MOTs due to additional interspecies collisions and to experimental constraints, such as the imperative to use the same magnetic field for both species or common optics. In other groups working with the ^{6}Li-^{40}K mixture the following atom numbers have been achieved: in the Munich group [13] the dual-species MOT is loaded from a Zeeman slower for ^{6}Li and a vapor for ^{40}K, resulting in atom numbers of $\sim 4 \times 10^7$ (^{6}Li) and $\sim 2 \times 10^7$ (^{40}K). In the Innsbruck group [14] the dual-species MOT is loaded from a multi-species Zeeman slower and atom numbers of $\sim 10^9$ (^{6}Li) and $\sim 10^7$ (^{40}K) are achieved. In the group in Amsterdam [15] two separate 2D-MOTs allow to load $\sim 3 \times 10^9$ (^{6}Li) and $\sim 2 \times 10^9$ (^{40}K). In our setup, the dual-species MOT is loaded from a Zeeman slower for ^{6}Li and a 2D-MOT for ^{40}K. It simultaneously contains 5.2×10^9 ^{6}Li-atoms and 8.0×10^9 ^{40}K-atoms, which represents a substantial atom number improvement.

For our application in particular a large atom number in the ^{40}K-MOT is of interest, since we intend to sympathetically cool ^{6}Li with ^{40}K, where ^{40}K will be prepared and cooled in two different spin states. This approach has been implemented by Tiecke et al. [11] and proved to be an efficient cooling method, as it can be realized in a magnetic trap. In this cooling process mostly ^{40}K-atoms will be lost.

In future experiments, the atoms stored inside the dual-species MOT will be polarized and magnetically transported to an ultra-high vacuum (UHV) environment with large optical access. There the atom cloud will be evaporatively cooled to quantum degeneracy in an optically plugged magnetic quadrupole trap. Finally it will be transferred into an optical trap to investigate many-body phenomena in lower dimensions.

This article is organized as follows. In Section 2 the experimental setup, including the vacuum assembly and the laser systems, is described. In Section 3 we present the design and the performance of the atom sources, which are used to load the dual-species MOT, i.e. a Zeeman slower for ^{6}Li and a 2D-MOT for ^{40}K. In Section 4, the dual-species MOT is characterized and a study of light-induced interspecies collisions is presented.

2 Experimental setup

2.1 Vacuum system

A three-dimensional view of the vacuum system is shown in Figure 1. It consists of two atom trap chambers and three flux regions. The first chamber is a central octagonal chamber where the ^{6}Li-^{40}K dual-species MOT is prepared.

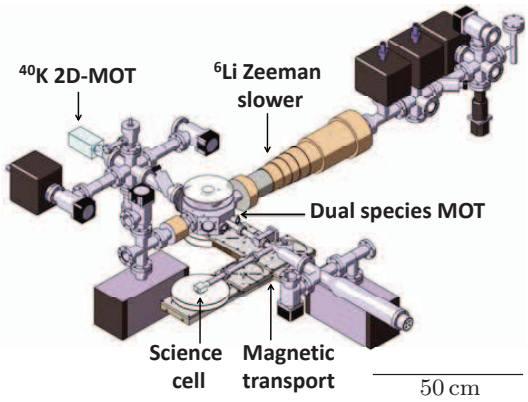

Fig. 1. (Color online) Schematics of the vacuum assembly. The dual-species MOT is loaded from a 2D-MOT for ^{40}K and a Zeeman slower for ^{6}Li. A magnetic transport allows to transfer the cloud to a UHV science cell with large optical access.

The second chamber is a glass science cell, in which we will evaporatively cool the mixture to quantum degeneracy.

The three flux regions are all connected to the octagonal chamber and are divided in two parts. First, the atom sources, namely a 2D-MOT for ^{40}K and a Zeeman slower for ^{6}Li. Second, a magnetic transport connecting the octagonal chamber to the final science cell. This magnetic transport consists of a spatially fixed assembly of magnetic coils which creates a moving trapping potential of constant shape by applying time-varying currents [16]. It has already been implemented in our system and will be described in a separate publication.

The octagonal chamber can be isolated from the source regions and the science cell by all-metal UHV valves, which allow for separate baking and trouble-shooting. The 2D-MOT and the Zeeman slower region are pumped by one and three 20 L/s ion pumps, respectively. The octagonal chamber is pumped by a 40 L/s ion pump and the science chamber by a 40 L/s ion pump and a titanium sublimation pump. Differential pumping tubes connect the source regions to the octagonal chamber in order to create a high vacuum environment in the octagonal cell. In a similar way, the science chamber is connected to the octagonal chamber via a combination of standard CF16- and homemade vacuum tubes of 1 cm diameter to further increase the vacuum quality. The glass science cell has a large optical access and permits the installation of an objective for high-resolution imaging.

2.2 Laser systems

The dual-species MOT requires separate laser systems and optics for the two different atomic transition wavelengths 671 nm (Li) and 767 nm (K). The laser systems provide several beams with different frequencies and intensities for slowing, trapping and probing each atomic species. A sketch of the energy levels of the atomic species and the

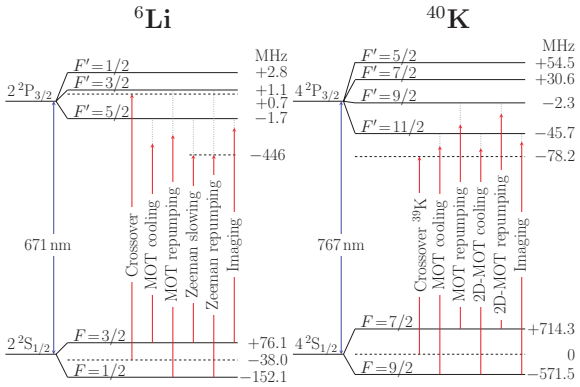

Fig. 2. (Color online) Level diagrams for the ^{6}Li and ^{40}K D_2-lines with their respective hyperfine structures, showing the frequencies required for the dual-species MOT operation. The diode lasers are locked to the indicated saturated absorption crossover signals $2S_{1/2}(F=1/2, F=3/2) \rightarrow 2P_{3/2}$ of ^{6}Li and $4S_{1/2}(F=1, F=2) \rightarrow 4P_{3/2}$ of ^{39}K.

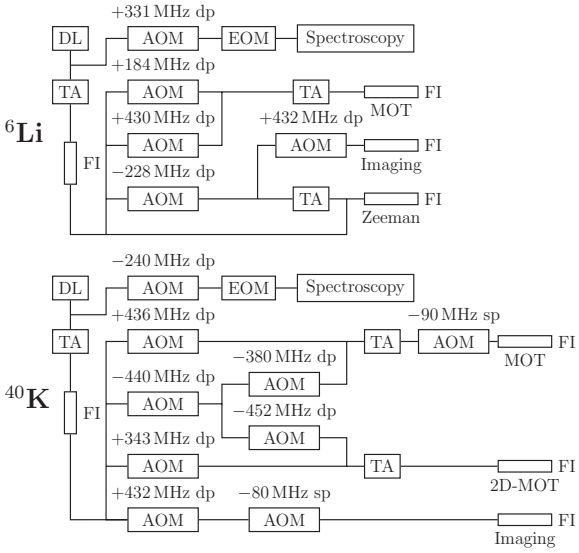

Fig. 3. Laser systems for ^{6}Li and ^{40}K. The frequencies and amplitudes of the various beams are controlled by AOMs in single pass (sp) or double pass (dp) configuration. The EOMs are used to phase modulate a part of the beam for the diode laser's frequency stabilization. Single mode polarization maintaining fibers (FI) are used for beam shaping and spatial filtering. The indicated AOM frequencies allow to generate the required beam frequencies (see Fig. 2).

frequencies of interest are shown in Figure 2. The laser systems are set up on separate optical tables and the generated laser beams are transferred to the main experimental table using optical fibers. A simplified scheme of the laser systems is shown in Figure 3. Each one consists of a single low output-power frequency-stabilized diode laser (DL) and three tapered amplifiers (TAs) used for light amplification. Due to the small hyperfine splittings of both ^{6}Li and ^{40}K, the required frequencies of the various laser beams are conveniently shifted and independently controlled by acousto-optical modulators (AOMs).

The diode lasers are homemade tunable external cavity diode lasers in Littrow configuration. The laser diode for Li (Mitsubishi, ref. ML101J27) is of low-cost due to its mass production for the DVD industry. Its central free running output wavelength at room temperature is 660 nm which can be shifted into the range of 671 nm by heating the diode to 80 °C. In external cavity configuration its output power is 40 mW at a driving current of 150 mA. Under these conditions the laser diode reaches a typical lifetime of 6 months. It can be mode hop-free tuned over a range of 5 GHz. The laser diode for K is an anti-reflection coated Ridge-Waveguide Laser (Eagleyard, ref. EYP-RWE-0790-0400-0750-SOT03-0000), whose central free running output wavelength at room temperature corresponds to the desired wavelength. In external cavity configuration its output power is 35 mW at 90 mA and it has a typical lifetime of one year. It can be mode hop-free tuned over a range of 10 GHz.

The tapered amplifiers are commercial semiconductor chips which are mounted on homemade supports. We developed compact support designs with nearly no adjustable parts, which allow for a quick temperature stabilization, do not require running water for heat dissipation and allow for an easy installation process. The support designs are described in detail in the appendix.

We have also developed an all-solid-state laser for lithium delivering more than 630 mW output power, with which we intend to increase further the number of laser-cooled Li atoms. The setup of this light source is described elsewhere [17].

The frequency of each diode laser is stabilized via saturated absorption spectroscopy for which a small part of the DL's output is used (see Fig. 3). A 20 MHz electro-optical modulator (EOM) is employed to modulate the phase of the spectroscopy laser beam yielding the derivative of the absorption signal through a lock-in detection. The resulting error signal is transferred to both the diode's current (via a high frequency bias-tee), and, via a PID-controller, to a piezo that adjusts the external cavity's length with a 4 kHz bandwidth. An AOM is used to offset the frequency of the diode laser with respect to the absorption line used for locking. It allows for fine adjustments of the frequency while the laser is locked.

The Li diode laser frequency is shifted by −331 MHz from the ^{6}Li $2S_{1/2}(F=1/2, F=3/2) \rightarrow 2P_{3/2}$ crossover signal and the K diode laser frequency is shifted by +240 MHz from the conveniently located $4S_{1/2}$ ($F=1$, $F=2$) $\rightarrow 4P_{3/2}$ crossover signal of ^{39}K. Note that the small excited state hyperfine structures of both ^{6}Li and ^{39}K are unresolved in the spectroscopy.

The saturated absorption spectroscopy for lithium is realized in a heat pipe of 50 cm length, in which a natural Li sample (with the isotopic abundances ^{7}Li: 92%,

^{6}Li: 8%) is heated to 350 °C to create a sufficiently high vapor pressure for absorption. The heat pipe consists of a standard CF40 tube with the Li-sample placed at its center. The tube is heated with a pair of thermocoax cables which are wound around the tube in parallel with opposite current directions in order to prevent magnetic fields to build up. Condensation of lithium atoms on the cell windows needs to be inhibited as Li chemically reacts with glass. This is achieved by adding an argon buffer gas at ∼0.1 mbar pressure, as Ar-Li collisions prevent Li to reach the cell windows in ballistic flight. The optimum argon pressure was chosen such that it provides enough collisions, but does not substantially collision-broaden the absorption spectrum. Water cooling of the metallic parts close to the windows leads to condensation of the diffusing lithium-atoms before those can reach the windows. To avoid that lithium slowly migrates to the colder surfaces, the inside of the tube is covered with a thin stainless steel mesh (Alfa Aesar, ref. 013477), which induces capillary forces acting on the condensed atoms. Since the surface tension of liquid lithium decreases with increasing temperature [18], the capillary forces cause the atoms to move back to the hotter surfaces.

The saturated absorption spectroscopy for potassium is realized in a cylindrical glass vapor cell of 5 cm length, in which a natural K-sample (with the isotopic abundances ^{39}K: 93.36%, ^{40}K: 0.012%, ^{41}K: 6.73%) is heated to 40 °C. Here, a small non-heated appendix of the cell serves as a cold point to prevent condensation of K-atoms on the surfaces crossed by the laser beam.

In both laser systems the frequency stabilized master laser beam is immediately amplified by a first TA and subsequently injected into a single-mode polarization maintaining optical fiber (FI) for beam shaping and spatial filtering (see Fig. 3). The output beam of the optical fiber is split by a series of polarizing beam splitters into several beams whose frequencies and intensities are independently shifted and controlled with AOMs in single or double pass configuration. The various beams are then recombined with a pair of polarizing beam splitters to linearly polarized bichromatic beams consisting of one cooling and one repumping frequency. Those are then either directly injected into a fiber or into another TA for further amplification. The fibers finally transfer the beams to the main experimental table.

The injection of a bichromatic beam into a TA, whose gain-medium is non-linear, is accompanied with the creation of sidebands [19]. The sideband creation is due to parametric amplification of the gain medium by the beating between the two injected frequencies. In general, sidebands represent a loss of the power available in the injected frequencies and can excite unwanted transitions. In our case, where the two injected beam components have significantly different powers and frequencies (differing by ∼228 MHz for ^{6}Li and by ∼1286 MHz for ^{40}K), the power losses are below 10%. No unwanted transitions are excited by the amplified bichromatic beams, except for the Zeeman slower beam, as that is detuned close to an integer multiple of 228 MHz and would thus perturb the atoms in the MOT. For this beam the injection of both frequency components into the same TA was thus avoided (see Fig. 3).

Acoustically isolated homemade mechanical shutters are placed in front of each fiber on the optical tables allowing to switch off the laser beams when required. The shutters consist of a low-cost solenoid-driven mechanical switch (Tyco Electronics, ref. T90N1D12-12) and a razor blade attached to it via a small rigid lever arm. These shutters typically have a closing time of ∼100 μs when placed in the focus of a laser beam and a sufficiently reproducible time delay of the order of 3 ms.

3 Atom sources

Magneto-optical traps can be loaded in different ways. The most efficient is the loading from a beam of slow atoms. This scheme allows isolating the MOT from the atom source region with a differential pumping tube, through which the beam is directed. The MOT thus can be located in a UHV chamber where collisions with the residual gas are minimized. Furthermore, the MOT will be quickly loaded when the atomic beam is cold and has a high flux. The most efficient methods to create such beams are Zeeman slowers and 2D-MOTs. For both atomic species ^{6}Li and ^{40}K, both, Zeeman slowers [14,20,21] and 2D-MOTs [22], have been realized in the past. In our setup we chose to implement a Zeeman slower for ^{6}Li and a 2D-MOT for ^{40}K.

3.1 ^{6}Li Zeeman slower

3.1.1 Introduction

Zeeman-tuned slowing represents one of the earliest and most widely used techniques to slow down atoms from an oven [23]. A Zeeman slower longitudinally decelerates an atomic beam using the radiative force of a counter-propagating resonant laser beam. The Doppler effect accumulated during the deceleration is compensated by the Zeeman effect, induced by an inhomogeneous magnetic field, which maintains the atoms on resonance and provides a continuous deceleration.

Two types of Zeeman slowers are commonly used: the positive-field and the sign-changing field ("spin-flip") Zeeman slower [24]. We have implemented a spin-flip Zeeman slower since it brings about several advantages. First, a smaller maximum absolute value of the magnetic field is required. Second, the Zeeman laser beam is non-resonant with the atoms exiting the slower and thus does not push them back into the slower, neither it perturbs the atoms trapped in the ^{6}Li-MOT. However, the spin-flip Zeeman slower requires repumping light in the region where the magnetic field changes sign and thus makes the optics system slightly more complicated.

3.1.2 Experimental setup

The Zeeman slower consists of two distinct parts: the oven, which creates an atomic beam of thermal atoms, and an assembly of magnetic field coils. In the oven a nearly pure ^{6}Li sample (5 g) is heated to 500 °C and an atomic beam is extracted through a collimation tube. The magnetic field coils create an inhomogeneous magnetic field along the flight direction of the atoms.

The oven consists of a vertical reservoir tube (diameter: 16 mm, length: 180 mm) and a horizontal collimation tube (diameter: 6 mm, length: 80 mm), which is attached to it (see Fig. 1). The upper end of the reservoir tube and the free end of the collimation tube are connected to CF40-flanges. The flange of the reservoir tube is sealed and allows connecting a vacuum pump for baking purposes. The flange of the collimation tube connects the oven to the rest of the vacuum chamber. All parts of the oven are made of stainless steel of type 302L and connected using nickel gaskets instead of copper gaskets as they stand higher temperatures and react less with lithium. The heating of the oven is realized with two high power heating elements (Thermocoax, ref. SEI 10/50-25/2xCM 10), wound around both, the reservoir and the collimation tube.

The temperature of the oven needs to be stabilized precisely, since the atomic flux critically depends on the temperature. This is accomplished by an active stabilization circuit and an isolation with glass wool and aluminum foil. Along the collimation tube a temperature gradient is maintained in order to recycle lithium atoms sticking to the inner tube walls through capillary action, as explained above. In order to amplify the effect of capillary action, a thin stainless steel mesh with a wire diameter of 0.13 mm (Alfa Aesar, ref. 013477) is placed inside the tube. This wire decreases the effective diameter of the collimation tube to ∼5 mm. For the operating temperature of 500 °C, the vapor pressure of lithium in the oven amounts to 4×10^{-3} mbar.

A computer controlled mechanical shutter (Danaher Motion, ref. BRM-275-03) in front of the oven allows to block the atomic beam during experiments or when the ^{6}Li-MOT is not in operation.

The oven is pumped through the collimation tube with a 20 L/s ion pump and isolated from the main chamber via three differential pumping stages and the tube of the Zeeman slower. The pumping efficiency through the collimation tube is ∼0.19 L/s resulting in a pressure drop of a factor ∼100. The second and third differential pumping tubes both have a length of 100 mm and a diameter of 5 mm and 10 mm, respectively. A 20 L/s ion pump is placed after each tube. In total a pressure drop of a factor of $\sim 2.5 \times 10^6$ between the oven and the main chamber is obtained.

The assembly of the oven is a three-step procedure. First, the metallic parts of the oven are pre-baked at 600 °C during 48 h. Then, the oven is filled with the lithium sample under air atmosphere and baked again at 600 °C during 12 h in order to eliminate the impurities in the lithium sample (mostly LiH). Typically 50% of the sample is lost during this procedure. Then, the oven is connected to the rest of the vacuum chamber under an argon atmosphere, since argon does not react with lithium. Since argon damages ion pumps, the vacuum chamber is first pumped by a turbo molecular pump during 12 h before the ion pumps are finally launched and the oven is operational.

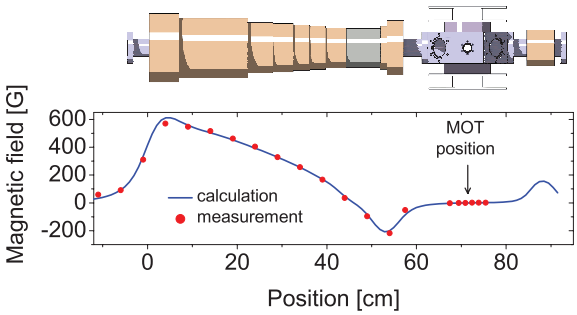

Fig. 4. (Color online) ^{6}Li Zeeman slower coil assembly and generated axial magnetic field profile. The thermal atoms coming from the ^{6}Li-oven enter the coil assembly at the position 0, and a fraction of them is slowed down and finally captured in the ^{6}Li-MOT, which is located at 71.4 cm. A compensation coil placed on the opposite side of the MOT (at 84.1 cm) ensures that the magnetic field is zero at the position of the MOT.

The Zeeman slower coils are mounted on a 65 cm long standard CF40 tube placed between the oven and the MOT chamber. A sketch of the coil assembly and the generated axial magnetic field profile are shown in Figure 4. The coil assembly extends over $L = 55$ cm and is separated from the position of the MOT by 16 cm. The coils are connected in series and were designed such that the desired magnetic field profile is generated for a moderate driving current of 12 A. The axial magnetic field of the slower along the flight direction of the atoms is measured to be 570 G at the entrance and −220 G at the exit.

The magnetic field of the Zeeman slower is non-zero at the position of the MOT and hence compensated by a coil placed opposite to the slower coils at a distance of 12.7 cm from the MOT (see Fig. 4). The compensation coil consists of 4 coil layers wound around a 10 cm long CF40 standard tube. They are powered by a separate power supply for fine adjustments. When compensated, the magnetic field has an axial gradient of 0.5 G/cm at the position of the MOT.

The cables of the Zeeman slower coils (APX France, ref. méplat cuivre émaillé CL H 1.60×2.50) stand bake out procedures up to 200 °C. One layer of a heating cable (Garnisch, ref. GGCb250-K5-19) is permanently placed underneath the magnetic field coils for these bake out procedures. To avoid heating of the vacuum parts during the Zeeman slower's operation, two layers of water coils were wound underneath the coil layers.

Slowing and repumping light for the Zeeman slower is derived from a bichromatic laser beam which is provided by an optical fiber originating from the laser system.

It has a total power of $P_{\rm fiber} = 50$ mW and its frequencies are both red detuned by $\Delta\omega_{\rm slow} = \Delta\omega_{\rm rep} = 75\ \Gamma$ from the $2S_{1/2}(F = 3/2) \rightarrow 2P_{3/2}(F' = 5/2)$ slowing and the $2S_{1/2}(F = 1/2) \rightarrow 2P_{3/2}(F' = 3/2)$ repumping transition (see Fig. 2). The intensity $I_{\rm slow}$ of the slowing light is 8 times bigger than the intensity $I_{\rm rep}$ of the repumping light. Both beam components have the same circular polarization (σ^+ at the position where the atoms enter the slower).

The detuning of the slowing light and the axial magnetic field at the entrance of the coil assembly define the so-called capture velocity $v_{\rm cap}^{\rm Zee}$ of the Zeeman slower. All atoms with a velocity smaller than $v_{\rm cap}^{\rm Zee}$ are expected to be decelerated to the same final velocity $v_{\rm fi}^{\rm Zee}$ at the exit of the slower, provided that they initially populate the correct internal atomic state. The resonance condition for the atoms inside the slower yields $v_{\rm cap}^{\rm Zee} \sim 830$ m/s and $v_{\rm fi}^{\rm Zee} \sim 90$ m/s. The exit velocity of the slower is thus larger than the capture velocity of the ^{6}Li-MOT, which is estimated to be ∼50 m/s. However, the atoms are still decelerated significantly in the region between the slower exit and the MOT and are thus expected to be captured by the MOT. The capture velocity of the Zeeman slower is smaller than the most probable thermal speed of the atomic beam, which is given by $v_p = \sqrt{2k_{\rm B}T/m} = 1464$ m/s at $T = 500$ °C, where $k_{\rm B}$ denotes the Boltzmann constant and m the mass of the ^{6}Li-atoms.

The bichromatic Zeeman slower beam is expanded and focused by a lens pair. The focusing of the beam accounts for the divergence of the atomic beam and the loss of beam power due to absorption and thus yields an efficient utilization of the available laser power. In addition, it induces a small cooling effect along the transverse direction [24]. The $1/e^2$-diameter at the position of the MOT is 31 mm and the focus is at a distance of 120 cm from the MOT, 10 cm behind the oven.

The divergence of the atomic beam is an important parameter characterizing the Zeeman slower. Three factors contribute to it: first, the geometry of the oven's collimation and the subsequent differential pumping tubes, second the atom's deceleration inside the slower, and third the transverse heating due to the scattered photons during the slowing process. In order to estimate the divergence of the atomic beam, we calculate the maximum possible deflection of an atom which exits the oven with a longitudinal velocity $v_{\rm cap}^{\rm Zee}$. An atom with this velocity needs ∼1.1 ms to reach the exit of the Zeeman slower and additional ∼1.8 ms to reach the MOT. Due to the geometry of the collimation and differential pumping tubes it can have a maximum transverse velocity of ∼16 m/s. The change in transverse velocity due to the heating is calculated to be ∼2.5 m/s [25] and is thus negligible with respect to the maximum transverse velocity determined by the tube geometry. The final transverse displacement of the atom with respect to the beam axis at the position of the ^{6}Li-MOT would thus be ∼5 cm, resulting in an effective beam divergence of ∼90 mrad. This divergence requires ^{6}Li-MOT beams of a large diameter.

Table 1. Optimized values for the parameters of the ^{6}Li Zeeman slower, yielding a ^{6}Li-MOT capture rate of $\sim 1.2 \times 10^9$ atoms/s at an oven temperature of 500 °C. The definition of the symbols is given in the text. The natural linewidth of ^{6}Li is $\Gamma/(2\pi) = 5.87$ MHz. The length of the Zeeman slower coil assembly is 55 cm.

	^{6}Li Zeeman slower
$P_{\rm fiber}$ (mW)	50
$\Delta\omega_{\rm slow}$ (Γ)	–75
$\Delta\omega_{\rm rep}$ (Γ)	–75
$I_{\rm rep}/I_{\rm slow}$	1/8
$B_{\rm max}$ (G)	570

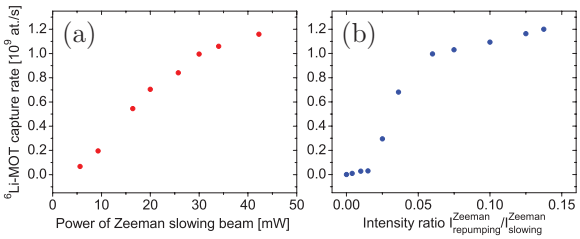

Fig. 5. (Color online) ^{6}Li-MOT capture rate as a function of (a) the power of the Zeeman slowing light for a constant repumping light power of 5.6 mW and (b) the intensity ratio between repumping and slowing light of the Zeeman slower for a constant slowing light power of 45 mW. The intensities of the superimposed beams depend on the position inside the slower, since the beams are focused toward the oven. At the position where the magnetic field changes sign, a power of 10 mW corresponds to an intensity of 2.5 $I_{\rm sat}$, with the saturation intensity $I_{\rm sat}$ given in Table 3.

3.1.3 Experimental results

For our application the essential parameter which characterizes the performance of the Zeeman slower is the capture rate of the ^{6}Li-MOT. We studied its dependence as a function of several Zeeman slower parameters, such as: the temperature of the oven, the power of the slowing light, the magnitude of the magnetic field and the intensity ratios between the repumping and slowing light. The optimized values of these parameters are displayed in Table 1, leading to a ^{6}Li-MOT capture rate of $\sim 1.2 \times 10^9$ atoms/s. The capture rate was deduced from a very short loading of the MOT, for which atom losses can still be neglected (∼250 ms).

Figure 5a shows the dependence of the ^{6}Li-MOT capture rate on the power of the Zeeman slowing light. The curve increases with increasing beam power and indicates saturation for higher powers. In the experiment the slowing light power is 45 mW, for which the curve in Figure 5a starts to saturate, demonstrating that the size of the slowing beam is well chosen. In particular it shows that the beam is not absorbed significantly by the atoms inside the slower.

The dependence of the ^{6}Li-MOT capture rate on the intensity ratio between repumping and slowing light of the Zeeman slower is depicted in Figure 5b. The curve

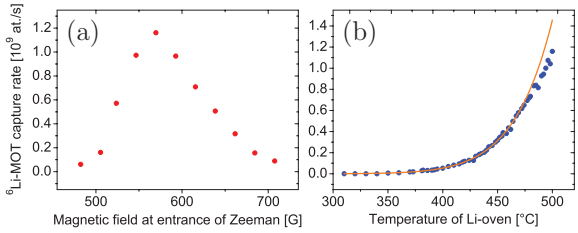

Fig. 6. (Color online) ^{6}Li-MOT capture rate as a function of (a) the axial magnetic field of the Zeeman slower and (b) the temperature of the Li-oven. Circles represent the experimental data and the solid curve the theoretical prediction from equation (3).

increases with increasing repumping intensity and saturates for higher intensities. For the intensity ratio $I_{\rm rep}/I_{\rm slow} \sim 0.1$ the repumping intensity in the region where the magnetic field of the Zeeman slower changes sign, is of the order of the saturation intensity. Therefore the transition probability of the repumping transition saturates at $I_{\rm rep}/I_{\rm slow} \sim 0.1$, explaining the behavior in Figure 5b. The graph shows that the Zeeman slower only requires a small repumping intensity. It is important that the repumping light has the same circular polarization as the slowing light, since it helps to optically pump the atoms to the cycling transition used for slowing.

Figure 6a shows the ^{6}Li-MOT capture rate as a function of the magnitude of the axial magnetic field of the Zeeman slower. The position of the maximum depends on the detuning of the slowing light.

Figure 6b shows the dependence of the ^{6}Li-MOT capture rate on the oven temperature T (circles) as well as a (scaled) theoretical prediction (solid curve) for the experimental data. The curve shows a nearly exponential increase of the capture rate with the temperature. The theoretical prediction is based on a model which assumes no collisions between the atoms (i.e., no intrabeam collisions and no collisions between the beam and the MOT atoms). It is derived as follows.

In the absence of collisions, the normalized velocity distribution of the Zeeman-slowed atoms exiting the slower does not depend on the temperature of the oven. Assuming that the ^{6}Li-MOT captures mainly atoms which have been slowed by the Zeeman slower, the capture rate $\dot{N}_{\rm M}$ of the ^{6}Li-MOT is a temperature-independent fraction of the flux $\dot{N}_{\rm Z}$ of the Zeeman-slowed atoms: $\dot{N}_{\rm M}(T) = \kappa_1 \dot{N}_{\rm Z}(T)$. The proportionality constant κ_1 depends on the divergence of the atomic beam and the capture velocity of the ^{6}Li-MOT. The flux of the Zeeman-slowed atoms $\dot{N}_{\rm Z}$ is given by the flux of the oven atoms which have a speed smaller than the Zeeman slower's capture velocity $v_{\rm cap}^{\rm Zee}$ and which are in the correct internal atomic state to be decelerated by the Zeeman slower (i.e. $F = 3/2$, $m_F = 3/2$). Assuming the oven to be in thermal equilibrium, $\dot{N}_{\rm Z}$ is given by [22,26]

$$\dot{N}_{\rm Z}(T) = \kappa_2 n_{\rm s}(T) A \int_0^{\Omega_{\rm Z}} d\Omega \frac{\cos\theta}{4\pi} \int_0^{v_{\rm cap}^{\rm Zee}} v f(v,T) dv, \quad (1)$$

with a temperature-independent constant κ_2, which equals the fraction of atoms which are in the correct internal atomic state. $n_{\rm s}(T)$ is the atomic density in the oven, $A = 2 \times 10^{-5}$ m^2 the aperture surface of the oven, $\Omega_{\rm Z} = A'/l^2 = 5 \times 10^{-4}$ the solid angle of the atomic beam (with A' the aperture surface of the last differential pumping tube and l the distance between the two aperture surfaces A, A') and $d\Omega = 2\pi \sin\theta d\theta$, with θ the emission angle with respect to the oven axis. $f(v,T)$ is the normalized speed distribution function given by

$$f(v,T) = \sqrt{\frac{2m^3}{\pi k_{\rm B}^3 T^3}} v^2 \exp\left(-\frac{mv^2}{2k_{\rm B}T}\right). \quad (2)$$

Since the solid angle of the atomic beam is small, it is $\cos\theta \approx 1$ and thus $\int_0^{\Omega_{\rm Z}} d\Omega \cos\theta \approx \Omega_{\rm Z}$.

The explicit temperature dependence of the ^{6}Li-MOT capture rate is then obtained via $\dot{N}_{\rm M}(T) = \kappa_1 \dot{N}_{\rm Z}(T)$ by substituting into equation (1) the ideal gas equation $n_{\rm s}(T) = p_{\rm s}/(k_{\rm B}T)$ and the relation $p_{\rm s} = p_{\rm a} \exp[-L_0/(k_{\rm B}T)]$ for the saturated vapor pressure $p_{\rm s}$, with $p_{\rm a} = 1.15 \times 10^8$ mbar and the latent heat of vaporization $L_0/k_{\rm B} = 18\,474$ K [27]. This relation applies to the temperature range 300–500 °C with an accuracy of 5%. Thus, we have

$$\dot{N}_{\rm M}(T) = \kappa A \Omega_{\rm Z} p_{\rm a} \sqrt{\frac{m^3}{8\pi^3 k_{\rm B}^5 T^5}} e^{-\frac{L_0}{k_{\rm B}T}} \int_0^{v_{\rm cap}^{\rm Zee}} v^3 e^{-\frac{mv^2}{2k_{\rm B}T}} dv, \quad (3)$$

with $\kappa = \kappa_1 \kappa_2$. Scaling equation (3) to the experimental data for a given (low) temperature ($T = 350$ °C) yields the theoretical prediction for the curve shown in Figure 6. The scaling yields $\kappa = 10^{-3}$, thus 0.1% of the atoms, which enter the Zeeman slower with a velocity smaller than $v_{\rm cap}^{\rm Zee}$, are captured by the ^{6}Li-MOT.

The main contribution to the small value of κ is the large divergence of the slowed atomic beam: κ is proportional to the ratio of the atomic beam cross section and the capture surface of the ^{6}Li-MOT, which is estimated to $\sim 10^{-2}$ (assuming the ^{6}Li-MOT capture surface to be a circle of 1.1 cm diameter). Two-dimensional transverse laser cooling of the atomic beam could vastly increase the value of κ. The remaining 10% are due to an inefficient capture of the ^{6}Li-MOT and to a significant fraction of oven atoms occupying the incorrect internal atomic states.

The obtained theoretical prediction agrees well with the experimental data for temperatures below 475 °C (see Fig. 6b). For temperatures above 475 °C, the experimental data deviate from the prediction indicating that intrabeam collisions or collisions between the atoms in the beam and the MOT become important. We found that for $T = 500$ °C collisions between the thermal ^{6}Li beam and the trapped ^{6}Li-MOT atoms indeed take place, which we verified by measuring the lifetime of the ^{6}Li-MOT in presence and absence of the thermal ^{6}Li beam, making use of the mechanical block placed at the exit of the oven. The lifetime was found 10% larger for the case where the thermal ^{6}Li beam was blocked. In a similar way the thermal ^{6}Li beam also affects the lifetime of the ^{40}K-MOT.

In order to avoid a reduction of the number of trapped ^{40}K atoms in the dual-species MOT, we therefore limit the ^{6}Li-oven temperature to 500 °C.

With the help of equation (1) the lifetime of the oven can be estimated. Assuming that the collimation tube of the oven recycles all atoms sticking to its wall and the vacuum pumps have no impact on the Li pressure in the oven, the total atomic flux through the collimation tube is obtained by replacing $A' = A$, $v_{\mathrm{cap}}^{\mathrm{Zee}} = \infty$ and $l = 8$ cm (the length of the collimation tube) in equation (1). For the working temperature $T = 500$ °C the lithium vapor pressure is $p_s = 4.8 \times 10^{-3}$ mbar, corresponding to a density $n_s = 4.5 \times 10^{19}$ m^{-3}. Thus, the atom flux through the collimation tube is $\dot{N}_{\mathrm{O}} = 3.5 \times 10^{14}$ s^{-1} $\hat{=}$ 3.5×10^{-12} kg/s. With 3 g of ^{6}Li this corresponds to an oven lifetime of $\tau_{\mathrm{oven}} \sim 25$ years. (The importance of the recycling becomes manifest when comparing this value to the hypothetical lifetime of the oven, would the collimation tube be replaced by an aperture of the same surface. In this case the atom flux through this aperture would be $\dot{N}_{\mathrm{O}}^{\mathrm{hyp}} = (\pi l^2/A)\dot{N}_{\mathrm{O}} \sim 1000\dot{N}_{\mathrm{O}}$ and thus $\tau_{\mathrm{oven}}^{\mathrm{hyp}} \sim 10$ days.)

3.2 ^{40}K 2D-MOT

3.2.1 Introduction

2D-MOTs have been widely used over the past years to produce high flux beams of cold atoms [14,22,28–31]. In some cases they offer advantages over the more common Zeeman slowers. Even though Zeeman slowers can produce higher fluxes and are more robust, they have the following disadvantages. They produce unwanted magnetic fields close to the MOT which need to be compensated by additional fields, they require a substantial design and construction effort and are space consuming. The atomic beam source of Zeeman slowers needs to be operated at higher temperatures than the vapor cell used as source for 2D-MOTs and the material consumption can be high. In the case of the rare isotope ^{40}K, this drawback is major: no pure source of ^{40}K exists and enriched ^{40}K samples are very expensive (4000 Euros for 100 mg of a 4% enriched sample). Therefore a ^{40}K Zeeman slower would be very costly. A 2D-MOT can be operated at lower pressures and is thus more economic. In addition it allows separating ^{40}K from the more abundant ^{39}K, since it produces an atomic beam which nearly only contains the slowed atoms (i.e. no thermal background). These considerations motivated us to implement a 2D-MOT for ^{40}K.

3.2.2 Principle of operation

In a 2D-MOT, an atomic vapor is cooled and confined transversally and out-coupled longitudinally through an aperture tube. The role of the aperture tube is two-fold. First, it isolates the 2D-MOT from the MOT chamber by differential pumping, and second, it acts as a geometric velocity filter, since only atoms with a small transverse velocity pass through. As the transverse cooling is more efficient for atoms which have a small longitudinal velocity – since those spend more time in the cooling region – most of the transversally cold atoms are also longitudinally cold. Thus, the filter indirectly filters atoms also according to their longitudinal velocity. A 2D-MOT thus produces an atomic beam which is transversally and longitudinally cold.

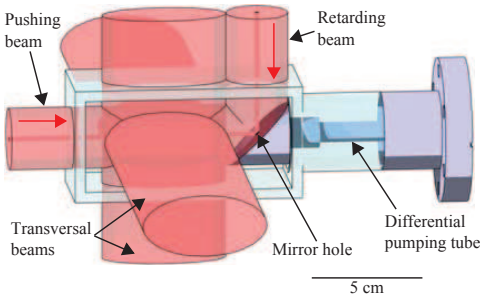

Fig. 7. (Color online) Sketch of the parallelepipedical glass cell used for the ^{40}K 2D-MOT. A mirror is placed inside the vacuum chamber to allow an independent control over the longitudinal beam pair. The mirror has a hole in its center and creates a dark cylindrical region in the reflected beams.

The flux of a 2D-MOT can be improved by adding a longitudinal molasses cooling to the 2D-MOT configuration [28]. Thus, the atoms spend more time in the transverse cooling region due to the additional longitudinal cooling. The longitudinal beam pair is referred to as the pushing and the retarding beam, where the pushing beam propagates in the direction of the atomic beam (see Fig. 7). We implemented such a configuration, making use of a 45°-angled mirror inside the vacuum chamber. This mirror has a hole at its center which creates a cylindrical dark region in the reflected retarding beam. In this region, the atoms are accelerated along the longitudinal direction by the pushing beam only, which allows an efficient out-coupling of the atomic beam.

3.2.3 Experimental setup

The vacuum chamber of the 2D-MOT consists of standard CF40 components and a parallelepipedical glass cell (dimensions 110 mm × 55 mm × 55 mm), which is depicted in Figure 7. Its long axis is aligned horizontally, parallel to the differential pumping tube and the direction of the produced atomic beam. The mirror inside the vacuum chamber is a polished stainless steel mirror with an elliptical surface (diameters 3.0 cm and 4.2 cm). It is attached to the differential pumping tube inside the vacuum. It allows to overlap the two longitudinal laser beams whose powers and orientations can thus be independently controlled externally. The mirror's material has a reflectivity of only 50%, but inhibits chemical reaction of potassium with its surface. The differential pumping tube intercepts the mirror at its center. The tube has a diameter of 2 mm over a distance of 1.5 cm and then stepwise widens up to 10 mm over a total distance of 22 cm. The ^{40}K-MOT

is located 55 cm away from the 2D-MOT center. Assuming a ballistic flight of the atoms, the geometry of the differential pumping tube defines an upper limit of the divergence of the atomic beam, which is calculated to be ∼35 mrad. The atomic beam thus is expected to have a diameter of ∼2 cm when it reaches the ^{40}K-MOT. The differential pumping tube has a conductance of 0.04 L/s. The generated pressure ratio between the 2D-MOT and the 3D-MOT chambers is $\sim 10^3$.

The potassium source is an isotopically enriched ^{40}K sample (containing 4 mg of ^{40}K, 89.5 mg of ^{39}K and 6.5 mg of ^{41}K, from Technical Glass Inc., Aurora, USA), placed at a distance of 20 cm from the glass cell. It was purchased in a small ampule which was broken under vacuum inside a modified stainless steel CF16 bellow. The small vapor pressure of potassium at room temperature (10^{-8} mbar) requires heating of the entire 2D-MOT chamber. We heat the source region to 100 °C, all intermediate parts to 80 °C and the glass cell to 45 °C. The gradient in temperature ensures that the potassium migrates into the cell and remains there. The resulting K-pressure in the glass cell was measured by absorption of a low intensity probe. We found 2.3×10^{-7} mbar, which implies a partial pressure of the ^{40}K-isotope of 1×10^{-8} mbar. In contrast to lithium, the source lifetime is mainly determined by the pumping speed of the ion pump. At the measured pressure the lifetime of the source is estimated to ∼2 years.

Four air-cooled rectangular shaped elongated racetrack coils (dimensions 160 mm × 60 mm) are placed around the glass cell to produce a 2D quadrupole field with cylindrical symmetry and a horizontal line of zero magnetic field. This racetrack coil geometry allows an independent control of the transverse position of the magnetic field zero, and minimizes finite coil fringe effects at the coil ends. The coils are controlled by four separate power supplies. For optimized operation, the transverse magnetic field gradients are $\partial_x B = \partial_y B = 11$ G/cm.

Cooling and repumping light for the 2D-MOT is derived from a bichromatic laser beam which is provided by an optical fiber originating from the laser system. It has a total power of $P_{\text{fiber}} = 450$ mW and its frequencies are red detuned by ∼3.5 Γ from the $4S_{1/2}(F = 9/2) \rightarrow 4P_{3/2}(F' = 11/2)$ cooling and by ∼2.5 Γ from the $4S_{1/2}(F = 7/2) \rightarrow 4P_{3/2}(F' = 9/2)$ repumping transition (see Fig. 2). The beam is separated into four beams and expanded by spherical and cylindrical telescopes to create the transverse and longitudinal 2D-MOT beams. The transverse beams have an elliptical cross section ($1/e^2$-diameters: 27.5 mm and 55 mm), are circularly polarized and retro-reflected by right-angled prisms, which preserve the helicity of the beams. The power losses in the surface of the glass cell and the prisms weaken the power of the retro-reflected beams by ∼17% (the loss contribution of the absorption by the vapor is negligible due to the high laser power). This power imbalance is compensated by shifting the position of the magnetic field zero. The longitudinal beams are linearly polarized and have a circular cross section ($1/e^2$-diameter: 27.5 mm). 75% of the fiber output power is used for the transverse beams, 25% for the longitudinal beams. The intensity ratio between pushing and retarding beam along the atomic beam axis is ∼6 (for reasons explained below).

Table 2. Optimized values for the parameters of the ^{40}K 2D-MOT, yielding a ^{40}K-MOT capture rate of $\sim 1.4 \times 10^9$ atoms/s. The definition of the symbols is given in the text. The natural linewidth of ^{40}K is $\Gamma/(2\pi) = 6.04$ MHz.

	^{40}K 2D-MOT
P_{fiber} (mW)	450
$\Delta\omega_{\text{cool}}$ (Γ)	–3.5
$\Delta\omega_{\text{rep}}$ (Γ)	–2.5
$I_{\text{rep}}/I_{\text{cool}}$	1/2
$I_{\text{push}}/I_{\text{ret}}$	6
$\partial_x B, \partial_y B$ (G/cm)	11
K vapor pressure (mbar)	2.3×10^{-7}

3.2.4 Experimental results

For our purpose the essential parameter which characterizes the performance of the 2D-MOT is the capture rate of the ^{40}K-MOT. We studied its dependence as a function of several 2D-MOT parameters, such as: the vapor pressure in the 2D-MOT cell, the total cooling light power, the detuning of the cooling frequency and the intensity ratios between the repumping and cooling light and between the pushing and retarding beam. The optimized values of these parameters are displayed in Table 2, leading to a ^{40}K-MOT capture rate of $\sim 1.4 \times 10^9$ atoms/s.

The mean velocity of the atoms in the atomic beam can be estimated as follows. It is approximately given by the average time required for the atoms of the 2D-MOT region to reach the 3D-MOT. This time was measured by recording the time delay of the onset of the ^{40}K-MOT loading after switching on the 2D-MOT beams. We measured a time delay of ∼23 ms and deduce a mean longitudinal velocity of the captured atoms of ∼24 m/s. At this velocity, the displacement due to gravity of the beam of atoms from the ^{40}K-MOT center is ∼2.6 mm, which is negligible compared to the size of the ^{40}K-MOT beams and the divergence of the atomic beam.

Figure 8a shows the dependence of the ^{40}K-MOT capture rate on the detuning $\Delta\omega_{\text{cool}}$ of the 2D-MOT cooling light. The curve has a maximum at $\Delta\omega_{\text{cool}} = -3.5\ \Gamma$ and a full width at half maximum (FWHM) of 2.7 Γ. The maximum is the result of two opposing effects: the scattering force of the 2D-MOT beams decreases with increasing detuning whereas the capture velocity increases [24]. The first effect implies a less efficient transverse cooling whereas the second leads to a more efficient capture of atoms. An additional effect might influence the shape of the curve: since the scattering force of the pushing beam depends on the detuning, also the mean-velocity of the atomic beam depends on it [28,29,31]. Since we measure the ^{40}K-MOT capture rate rather than the flux of the 2D-MOT, the mean-velocity might exceed the capture velocity of the ^{40}K-MOT. However, as shown in references [28,29,31], the mean-velocity of the beam only

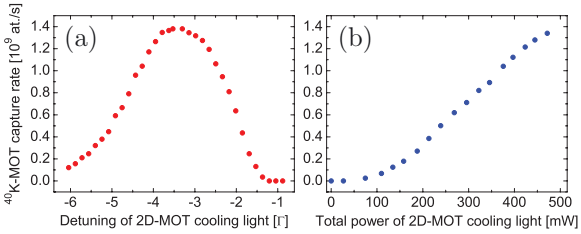

Fig. 8. (Color online) ^{40}K-MOT capture rate as a function of (a) the detuning and (b) the total power of the cooling light used for the 2D-MOT (for a constant intensity ratio between the cooling and repumping light). The total power refers to the sum of the powers in the six 2D-MOT beams, where a power of 470 mW corresponds to a total intensity of $\sim 47\, I_{\rm sat}$ at the center of the 2D-MOT, with the saturation intensity $I_{\rm sat}$ given in Table 3.

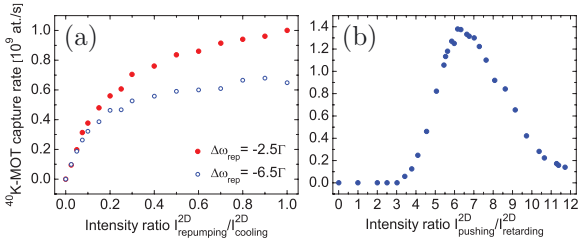

Fig. 9. (Color online) ^{40}K-MOT capture rate as a function of the intensity ratio between (a) repumping and cooling light of the 2D-MOT for two different repumping detunings $\Delta\omega_{\rm rep}$ and a constant total cooling light power of 300 mW (which corresponds to a total intensity of $\sim 30\, I_{\rm sat}$) and (b) the pushing and the retarding beams of the 2D-MOT. The intensities of the pushing and retarding beams refer to the intensities along the atomic beam axis.

Table 3. Characteristic parameters of the dual-species ^{6}Li-^{40}K-MOT.

	^{40}K-MOT	^{6}Li-MOT
$P_{\rm fiber}$ (mW)	220	110
$\Delta\omega_{\rm cool}$ (Γ)	–3	–5
$\Delta\omega_{\rm rep}$ (Γ)	–5	–3
$\Gamma/(2\pi)$ (MHz)	6.04	5.87
$I_{\rm cool}$ per beam ($I_{\rm sat}$)	13	4
$I_{\rm sat}$ (mW/cm^2)	1.75	2.54
$I_{\rm rep}/I_{\rm cool}$	1/20	1/5
$\partial_z B$ (G/cm)	8	8
$N_{\rm single}$ ($\times 10^9$)	8.9	5.4
$N_{\rm dual}$ ($\times 10^9$)	8.0	5.2
$n_{\rm c}$ ($\times 10^{10}$ at./cm^3)	3	2
T (μK)	290	1400

slightly changes with the detuning, such that we expect this effect to only weakly influence the curve. From the shape of the curve we conclude that the ^{40}K-MOT capture rate is not very sensitive to changes of $\Delta\omega_{\rm cool}$.

The dependence of the ^{40}K-MOT capture rate on the total power of the 2D-MOT cooling light is depicted in Figure 8b. The total power refers to the sum of the powers in the six 2D-MOT beams. According to the chosen beam sizes, the maximum power of 470 mW corresponds to a total intensity of $\sim 47\, I_{\rm sat}$ (for zero detuning) at the center of the 2D-MOT, with the saturation intensity $I_{\rm sat}$ given in Table 3. The curve almost linearly increases with light power without a clear indication of saturation. The increase is due to two effects. First, the 2D-MOT capture velocity increases with laser power due to the power broadening of the atomic spectral lines. Second, the scattering force increases, resulting in a steeper transverse confinement, which facilitates the injection of the atoms into the differential pumping tube. At some point, the curve is expected to saturate, since the temperature of the cooled atoms and light-induced collisions between them increase with light power. These effects, however, are less limiting in a 2D-MOT as compared to a 3D-MOT, since the atomic density in a 2D-MOT is typically three orders of magnitude smaller due to the absence of a three-dimensional confinement. Thus, in a 2D-MOT a high light power would be required to reach the regime of saturation.

Figure 9a shows the dependence of the ^{40}K-MOT capture rate on the intensity ratio between the cooling and repumping light of the 2D-MOT for the two different repumping detunings $\Delta\omega_{\rm rep}^{(1)} = -2.5\ \Gamma$ and $\Delta\omega_{\rm rep}^{(2)} = -6.5\ \Gamma$ and for a constant total cooling light power of 300 mW. The graph shows that for both frequencies the ^{40}K-MOT capture rate increases with increasing repumping intensity and that it saturates at high intensities. It also shows that the maximum capture rate is bigger for the smaller detuning. The intensity dependence of the curves results from the likewise intensity dependence of the transition probability for an atomic transition. The maximum capture rate is bigger for the smaller detuning, since this detuning contributes more efficiently to the cooling process. In our experiment, a fixed total laser power is available for both repumping and cooling light. It is distributed such that the resulting capture rate is maximized. It was found to be maximum for an intensity ratio of $I_{\rm rep}/I_{\rm cool} \sim 1/2$. For that ratio the detuning $\Delta\omega_{\rm rep}^{(2)} = -2.5\ \Gamma$ also yields the maximum capture rate.

The dependence of the ^{40}K-MOT capture rate on the intensity ratio between pushing and retarding beam is depicted in Figure 9b. The curve has a maximum at $I_{\rm push}/I_{\rm retard} \sim 6$. It is zero for values of $I_{\rm push}/I_{\rm retard}$ between 0 and 3, then increases until the maximum and falls off again with a smaller slope. From the curve we can extract information about the importance of the reflectivity of the mirror inside the vacuum and of the size of its hole. For a given intensity ratio $I_{\rm push}/I_{\rm retard}$ along the (horizontal) direction of the atomic beam, the mirror's reflectivity determines the intensity ratio $I^*_{\rm push}/I^*_{\rm retard}$ along the vertical direction above the reflecting surface of the mirror (see Fig. 7). If $I^*_{\rm push}/I^*_{\rm retard}$ differs from 1, the atomic beam can experience a vertical deflection in this region. The hole inside the mirror creates a dark cylinder in the pushing beam after its reflection, so that in the region above the hole only light from the retarding beam has a

vertical direction, which can also give rise to a vertical deflection of the atomic beam.

In the following we estimate the deflection of the atomic beam, which is induced by the unbalanced retarding beam in the small region above the hole. Assuming the atomic beam to have reached its final longitudinal velocity of 24 m/s when entering into the hole, the atoms spend 85 μs in the region above the hole. Neglecting Doppler shifts and the presence of the pushing beam along the horizontal direction (no transverse beams are present in the region above the mirror), the atoms will scatter $N_{\mathrm{ph}} = R_{\mathrm{sc}} \times (85\ \mu s) \sim 75$ photons, with R_{sc} being the scattering rate [24] for the given detuning $\Delta\omega_{\mathrm{cool}} = -3.5\ \Gamma$ and peak intensity $I^*_{\mathrm{retard}} = 2.5 I_{\mathrm{sat}}$. The recoil velocity of ^{40}K being given by $v_{\mathrm{rec}} = 0.013$ m/s, each atom will accumulate a transverse velocity of $v_{\mathrm{dev}} \sim 1$ m/s. This leads to a downwards deflection of the atomic beam by an angle of ∼40 mrad, which is more than a factor two bigger than the maximum deflection angle allowed by the differential pumping tubes. The atoms will thus not reach the ^{40}K-MOT.

This deflection needs to be anticipated by an intensity imbalance $I^*_{\mathrm{push}} > I^*_{\mathrm{retard}}$ in the region above the reflecting surface of the mirror, as that results in an upwards deflection of the atomic beam. For the given mirror reflectivity of 50%, $I^*_{\mathrm{push}} > I^*_{\mathrm{retard}}$ is equivalent to $I_{\mathrm{push}}/I_{\mathrm{retard}} > 4$, which corresponds to the experimental observation depicted in Figure 9b. The deflection of the atomic beam in the region above the hole could be avoided using a beam block which creates a dark cylinder in the region above the mirror which overlaps with the one in the pushing beam. In this configuration the position of the curve optimum in Figure 9b would change from $I_{\mathrm{push}}/I_{\mathrm{retard}} = 6$ to $I_{\mathrm{push}}/I_{\mathrm{retard}} = 4$. For mirrors with a reflectivity close to 100% the position of the curve optimum could thus even be changed to $I_{\mathrm{push}}/I_{\mathrm{retard}} = 1$, for which the longitudinal optical molasses cooling would be most efficient leading to a maximum 2D-MOT flux. Due to the polarization gradients generated by the transverse 2D-MOT beams the longitudinal optical molasses cooling is, however, still very efficient even in case of an intensity imbalance of 6 along the atomic beam axis.

We now study the dependence of the ^{40}K-MOT capture rate on the vapor pressure of potassium (all isotopes) in the 2D-MOT cell, which is shown in Figure 10 (circles) together with a fit to a theoretical model (solid curve). The vapor pressure was measured by recording the absorption profile of a low intensity probe. The curve in Figure 10 has a maximum at a vapor pressure of 2.3×10^{-7} mbar. In the absence of collisions, the curve should increase linearly with pressure, which is indeed observed for low pressures. For high pressures, collisions become important and limit the ^{40}K-MOT capture rate. The dependence of the ^{40}K-MOT capture rate L on the pressure p can be described by the function [31]

$$L = L_0 \exp\left[-\left(\Gamma_{\mathrm{coll}} + \beta \int n^2(\mathbf{r}) d^3r\right) \langle t_{\mathrm{cool}} \rangle\right], \qquad (4)$$

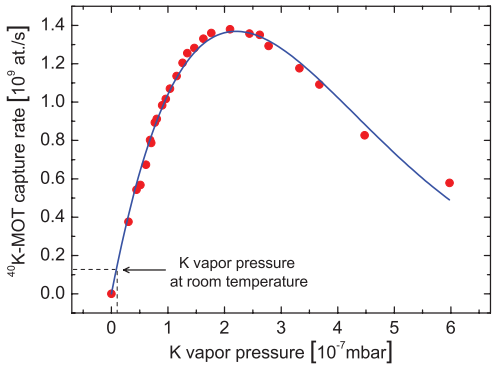

Fig. 10. (Color online) ^{40}K-MOT capture rate as a function of the potassium vapor pressure (all isotopes). Circles: experimental data, solid curve: fit of the experimental data by equation (5). Due to the low abundance of the ^{40}K-isotope in our potassium sample (4%), the ^{40}K-MOT capture rate is limited by collisions between the ^{40}K-atoms and the other K-isotopes in the 2D-MOT cell. At room temperature the potassium vapor pressure is 1×10^{-8} mbar.

where L_0 denotes the hypothetical capture rate of the ^{40}K-MOT in the absence of collisions in the 2D-MOT chamber, Γ_{coll} denotes the collisional loss rate due to collisions in the 2D-MOT chamber between the cooled atoms and the background atoms, $\langle t_{\mathrm{cool}} \rangle$ is the average time which the atoms spend inside the 2D-MOT cooling region, $n(\mathbf{r})$ is the position-dependent atomic density in the atomic beam, and β is the two-body loss rate coefficient which describes the cold collisions between the ^{40}K atoms in the atomic beam. L_0 is proportional to the atomic density n_{K} in the vapor cell, and $\Gamma_{\mathrm{coll}} = n_{\mathrm{K}} \sigma_{\mathrm{eff}} \langle v \rangle$, where σ_{eff} is the effective collision cross section, and $\langle v \rangle \sim 400$ m/s the mean velocity of the thermal potassium atoms. The term describing the cold collisions is approximately proportional to n_{K}^2 due to the small density obtained in the 2D-MOT. For the investigated pressure range, the ratio p/n_{K} only changes slightly with temperature and can thus be considered constant. Therefore equation (4) can be written as

$$L(p) = \kappa_1 p \exp\left(-\kappa_2 p - \kappa_3 p^2\right), \qquad (5)$$

with the constants $\kappa_1, \kappa_2, \kappa_3$, which are obtained from the fit shown in Figure 10. At the curve's maximum, the fit yields $\kappa_2 p/\kappa_3 p^2 = 8$, showing that the collisions which limit the ^{40}K-MOT capture rate are mainly the collisions with the hot background atoms, consisting mostly of ^{39}K.

The background atoms are predominantly potassium atoms. These can collide either with the excited or the non-excited ^{40}K-atoms of the atomic beam. Depending on the isotopes of the colliding partners, these collisions have different cross sections. Collisions between an excited and a non-excited atom of the same isotope usually have a very large cross section due to the strong resonant dipole-dipole interaction, described by a C_3/R^3-potential. In 2D-MOT systems of other atomic species these collisions have been identified as the ones which limit the

flux of the 2D-MOT [28,29,31]. In the case of ^{40}K, the scattering rate for these collisions is reduced by the small abundance of ^{40}K in the vapor. Therefore other collisions might limit the flux. In order to identify the flux-limiting collisions we calculate the cross section of different possible collisions and deduce the corresponding collision rates. The cross sections can be calculated using the approach described in reference [32] for losses out of a cold atom cloud. The cross section for collisions involving an excited and a non-excited ^{40}K-atom is given by [32]

$$\sigma_{\mathrm{eff}}^{40,40^*} = \pi \left(\frac{4C_3}{m v_{\mathrm{esc}} \langle v \rangle} \right)^{2/3}, \tag{6}$$

where m is the mass of the ^{40}K-atom, $v_{\mathrm{esc}} \sim 1$ m/s is the estimated transverse velocity kick needed to make an atom miss the ^{40}K-MOT, and $C_3 = 5.4 \times 10^{-48}$ J m^3 is the dispersion coefficient for the resonant dipole-dipole interaction [33]. The cross section for collisions involving a non-excited ^{40}K-atom and a non-excited K-atom of the different isotopes is given by [32]

$$\sigma_{\mathrm{eff}}^{40,39} \sim \sigma_{\mathrm{eff}}^{40,41} \sim \sigma_{\mathrm{eff}}^{40,40} = \pi \left(\frac{15\pi C_6}{8 m v_{\mathrm{esc}} \langle v \rangle} \right)^{1/3}, \tag{7}$$

where $C_6 = 3.7 \times 10^{-76}$ J m^6 is the dispersion coefficient for the underlying van der Waals interaction [33]. Substituting the experimental parameters, one obtains: $\sigma_{\mathrm{eff}}^{40,40^*} = 2.7 \times 10^{-16}$ m^2 and $\sigma_{\mathrm{eff}}^{40,39} \sim \sigma_{\mathrm{eff}}^{40,41} \sim \sigma_{\mathrm{eff}}^{40,40} = 1.3 \times 10^{-17}$ m^2. The resulting collision rates are proportional to the atomic densities n_{39}, n_{40} and n_{41} of the corresponding isotopes in the vapor and the relative number of excited ^{40}K-atoms in the atomic beam, which was estimated to $P \sim 0.1$ for the given beam detunings and intensities. One obtains

$$\Gamma_{\mathrm{coll}}^{40,40^*} = P n_{40} \sigma_{\mathrm{eff}}^{40,40^*} \langle v \rangle = 4.4 \times 10^{-16} n_{\mathrm{K}}, \tag{8}$$

$$\Gamma_{\mathrm{coll}}^{40,39} = (1-P) n_{39} \sigma_{\mathrm{eff}}^{40,39} \langle v \rangle = 4.4 \times 10^{-15} n_{\mathrm{K}}, \tag{9}$$

$$\Gamma_{\mathrm{coll}}^{40,40} = (1-P) n_{40} \sigma_{\mathrm{eff}}^{40,40} \langle v \rangle = 2.0 \times 10^{-16} n_{\mathrm{K}}, \tag{10}$$

$$\Gamma_{\mathrm{coll}}^{40,41} = (1-P) n_{41} \sigma_{\mathrm{eff}}^{40,41} \langle v \rangle = 3.0 \times 10^{-16} n_{\mathrm{K}} \tag{11}$$

(n_{K} denoting the atomic density of potassium in the vapor cell). The dominant collision rate here is $\Gamma_{\mathrm{coll}}^{40,39}$ (Eq. (9)) for collisions involving a non-excited ^{40}K-atom and a non-excited ^{39}K-atom from the background. The largest collision rate for collisions between two ^{40}K-atoms, $\Gamma_{\mathrm{coll}}^{40,40^*}$, is by a factor of 10 smaller than $\Gamma_{\mathrm{coll}}^{40,39}$. Therefore, collisions involving two ^{40}K-atoms are not the collisions which limit the flux of the 2D-MOT. This is in contrast to 2D-MOT systems of other species. From the difference between $\Gamma_{\mathrm{coll}}^{40,40^*}$ and $\Gamma_{\mathrm{coll}}^{40,39}$ we conclude that the flux of the 2D-MOT for ^{40}K could still be improved by about a factor of 10 by using a potassium sample of a higher isotopic enrichment.

4 ^{6}Li-^{40}K dual-species MOT

4.1 Introduction

Previously, several groups have studied samples of two atomic species in a magneto-optical trap [13–15,34–37]. Here we report on the implementation and performance of our ^{6}Li-^{40}K dual-species MOT and on the study of collisions between atoms of the different species. After a description of the experimental setup, we start with a characterization of the single-species MOTs and then focus on the collisions in the dual-species MOT.

4.2 Principle of operation

In a magneto-optical trap six counter-propagating red-detuned overlapping laser beams cool and magneto-optically confine atoms in a magnetic quadrupole field around its zero [24]. MOTs for alkali-atoms require laser light of two frequencies, namely the cooling and the repumping frequency. The latter ensures that the atoms stay in the cycling transition used for cooling. Typically the repumping light has a much lower power than the cooling light as the atoms principally occupy the states belonging to the cooling transition. For ^{6}Li, however, the power of the repumping light needs to be relatively high, since ^{6}Li has a very small hyperfine structure in the excited state manifold (of the order of the linewidth). When laser cooled, ^{6}Li-atoms thus very likely quit the cooling transition. Therefore, the repumping light needs to contribute to the cooling process. As a consequence it needs to be present in all six directions with the same polarization as the cooling light. Therefore, we use bichromatic MOT-beams containing both cooling and repumping frequencies. We adapt the same strategy also for ^{40}K.

4.3 Experimental setup

Light for the dual-species MOT is derived from two bichromatic laser beams, containing each a cooling and a repumping frequency, which are provided by two separate optical fibers originating from the respective laser systems. The beams are superimposed using a dichroic mirror and then expanded by a telescope to a $1/e^2$-diameter of 22 mm. All subsequent beam reflections are realized by two-inch sized broadband mirrors (Thorlabs, ref. BB2-E02-10). The beam is separated by three two-inch sized broadband polarization cubes (Lambda Optics, ref. BPB-50.8SF2-550) into four arms that form a partially retro-reflected MOT, in which only the vertical beam pair is composed of independent counter-propagating beams. Each retro-reflected MOT beam is focused with a lens of focal length 10 cm, placed at a distance of ∼11 cm in front of the retro-reflecting mirror, in order to increase the intensity and therefore compensate for the losses in the optics and the light absorption by the trapped atoms. The distribution of the light power over the MOT beams is independently

adjusted for the two wavelengths using a pair of custom-made wave plates, placed in front of each broad-band splitting cube. The wave plate pair consists of a $\lambda/2$ plate of order 4 for the wavelength 767 nm and a $\lambda/2$ plate of order 4 for the wavelength 671 nm. To a very good approximation each of these wave plates can turn the polarization direction for one wavelength without affecting the polarization for the other one (since it is $4.5 \times 767 \approx 5 \times 671$ and $4.5 \times 671 \approx 4 \times 767$). The circular polarization of the MOT beams is produced by first order $\lambda/4$ plates for 767 nm, which work sufficiently well also for 671 nm. All four frequency components thus have the same circular polarizations in each beam. A mechanical shutter is placed in the focus of the telescope allowing to produce total extinction of the MOT light in addition to the partial and fast switching by the AOMs.

The bichromatic beam for the ^{40}K-MOT has a total power of $P_{\text{fiber}} = 220$ mW and its frequencies are red-detuned by $\sim 3\ \Gamma$ from the $4S_{1/2}(F = 9/2) \rightarrow 4P_{3/2}(F' = 11/2)$ cooling and by $\sim 5\ \Gamma$ from the $4S_{1/2}(F = 7/2) \rightarrow 4P_{3/2}(F' = 9/2)$ repumping transition (see Fig. 2). The intensity of the cooling light is $\sim$20 times bigger than that of the repumping light. The bichromatic beam for the ^{6}Li-MOT has a total power of $P_{\text{fiber}} = 110$ mW and its frequencies are red-detuned by $\sim 5\ \Gamma$ from the $2S_{1/2}(F = 3/2) \rightarrow 2P_{3/2}(F' = 5/2)$ cooling and by $\sim 3\ \Gamma$ from the $2S_{1/2}(F = 1/2) \rightarrow 2P_{3/2}(F' = 3/2)$ repumping transition (Fig. 2). The power of the cooling light is $\sim$5 times bigger than that of the repumping light.

The magnetic field for the dual-species MOT is created by a pair of coils in anti-Helmholtz configuration. The magnetic field gradient along the vertically directed symmetry axis is $\partial_z B = 8$ G/cm. This gradient yields an optimum atom number for the ^{40}K-MOT.

The atoms in the dual-species MOT are probed by absorption imaging. In order to obtain a two-dimensional density profile of the atom cloud, three pictures are taken and recorded by a CCD-camera (PCO imaging, ref. Pixelfly qe). The first picture is taken with the imaging beam tuned near resonance and thus records the shadow cast by the atom cloud on the CCD-chip of the camera. The second picture is taken with the imaging beam tuned far off resonance (by $-10\ \Gamma$) and records the intensity profile of the imaging beam. The third picture is taken in absence of the imaging beam and records the background signal. The change of frequency of the imaging beam allows to take the first two pictures with a short time delay (2 ms), while keeping the imaging beam at the same frequency would require to wait for the atom cloud to disappear before the second picture could be recorded. Thus, the intensity fluctuations of the imaging beam during the recording process are minimized and both pictures can be taken with the same intensity.

Each atomic species requires its own imaging beam, which is provided by a separate optical fiber originating from the respective laser system (see Fig. 3). The two imaging beams are superimposed using a dichroic mirror and expanded by a telescope to a $1/e^2$-diameter of 27.5 mm. The imaging beams have low intensity ($I_{\text{img}} \sim 0.01 I_{\text{sat}}$ in the beam center), are circularly polarized and pass through the MOT along the horizontal direction, perpendicular to the axis of the quadrupole magnetic field of the MOT. No bias magnetic field is applied when absorption pictures are taken. The best atom number estimate from the measured absorption pictures is thus given by using an averaged squared Clebsch-Gordan coefficient, which is $C^2 = 0.5$ for ^{6}Li and $C^2 = 0.4$ for ^{40}K. Both beams are red detuned by $2\ \Gamma$ from the $4S_{1/2}(F = 9/2) \rightarrow 4P_{3/2}(F' = 11/2)$ and the $2S_{1/2}(F = 3/2) \rightarrow 2P_{3/2}(F' = 5/2)$ cooling transitions of ^{40}K and ^{6}Li, respectively (see Fig. 2), so as to reduce saturation effects. For the chosen length of the imaging pulses (100 μs) no repumping is required during the imaging process (we verified for ^{6}Li that even in the case of a resonant imaging beam, the presence of a repumping beam would yield an increase of the detected atom number of only 8%, which would be even less for ^{40}K). In order to image the total number of atoms in the MOTs the atom clouds are exposed for 500 μs to only the repumping light before the image is taken in order to optically pump all atoms to the hyperfine ground state which is imaged. The overall uncertainty of the absolute atom number determination is estimated to be 50%.

4.4 Experimental results

In single-species operation we characterized the MOTs using the parameters for the optimized dual-species operation. We determined the atom numbers, the atomic densities in the cloud center, the loading times and the temperatures. Furthermore, we studied for each atomic species the dependence of the steady-state MOT atom number on the following parameters: the power and detuning of the cooling light and the intensity ratio between the repumping and cooling light. In dual-species operation, we studied the dependence of heteronuclear light-induced cold collisions on the laser power used for the MOT-beams. The optimum parameters, which lead to atom numbers of $N_{\text{single}} \sim 8.9 \times 10^9$ in the ^{40}K-MOT and $N_{\text{single}} \sim 5.4 \times 10^9$ in the ^{6}Li-MOT, are displayed in Table 3 together with the characteristics of the MOTs (in dual-species operation, the atom numbers only slightly change due to the additional interspecies collisions to $N_{\text{dual}} \sim 8.0 \times 10^9$ in the ^{40}K-MOT and $N_{\text{dual}} \sim 5.2 \times 10^9$ in the ^{6}Li-MOT). The $(1 - 1/e)$-loading times of the MOTs are $\sim$5 s for ^{40}K and $\sim$6 s for ^{6}Li.

Magneto-optical traps with large atom numbers have a high optical density and are optically dense for weak resonant laser beams. Therefore, when determining the atom number via absorption imaging, the frequency of the imaging beam has to be detuned, so not to "black out" the image.

Figures 11a, 11b depict the *detected* atom number of the two MOTs (circles) as a function of the detuning of the imaging beam. The detected atom number was derived from the measured optical density assuming the imaging beam to be resonant. The curves are expected to have the shape of a Lorentzian with the peak centered around zero detuning. The experimental data shown in

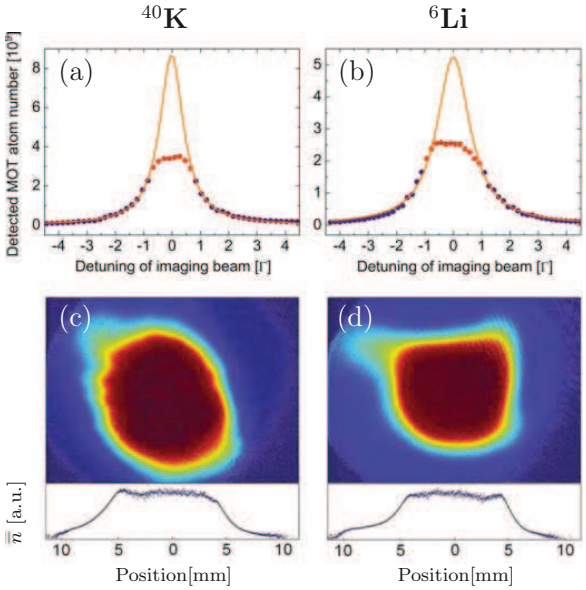

Fig. 11. (Color online) (a), (b) Detected atom number in the MOTs as a function of the detuning of the imaging beams. Circles correspond to the experimental data and solid curves to Lorentzian fits of the curve wings with an imposed width, which was determined by another measurement. (c), (d) Absorption images of the MOTs and the doubly-integrated optical density profile $\overline{\overline{n}}$, recorded with a resonant imaging beam. The graphs (a, c) relate to the ^{40}K-MOT and (b), (d) to the ^{6}Li-MOT. The flat top of $\overline{\overline{n}}$ in the graphs (c), (d) and the saturation of the detected atom number for small magnitudes of the detuning in the graphs (a), (b) demonstrate that the MOTs are optically dense for the imaging beam when the detuning is small. Their (extrapolated) central optical densities for a resonant imaging beam are ∼20 for ^{40}K and ∼15 for ^{6}Li.

Figures 11a, 11b clearly deviate from a Lorentzian behavior – they saturate for small magnitudes of the detuning. This deviation demonstrates that the MOTs are optically dense for small detunings. A correct estimate of the atom number is obtained from an extrapolation of the experimental data to zero detuning based on a Lorentzian fit of the curve wings (solid curves). A reliable extrapolation, however, requires imposing the width of the Lorentzian fit. In order to determine this width, an additional experiment was done (not shown): the data in Figures 11a, 11b were again recorded and fitted by a Lorentzian for a MOT with a small atom number and a low optical density (obtained by a short loading of 250 ms). The widths found by this additional measurement were 1.05 Γ for ^{40}K and 1.5 Γ for ^{6}Li. For ^{40}K this width corresponds to the natural linewidth of the exited state addressed by the imaging transition. For ^{6}Li the width is larger than the natural linewidth, since the small excited hyperfine structure is unresolved and thus its width (∼0.5 Γ) and the natural linewidth add up (this line broadening does not occur when a bias magnetic field is applied and a closed transition is used for imaging). The peak values of the Lorentzian fits in Figures 11a, 11b finally yield the atom numbers in the MOTs, given in Table 3.

Figures 11c, 11d show images of the MOTs and their doubly-integrated optical density profiles $\overline{\overline{n}}$ for the case of a resonant imaging beam. The flat top of $\overline{\overline{n}}$ as a function of position shows that the MOTs are optically dense. Their central optical densities for the resonant imaging beam are determined to be ∼20 for ^{40}K and ∼15 for ^{6}Li by the extrapolation technique described above. In addition, the density profiles in Figures 11c, 11d show that the MOTs have spatial extensions of the order of 1 cm.

The atomic density in the MOT center is extracted from the recorded two-dimensional density profile as follows. The recorded profile is proportional to the atomic density $n(x, y, z)$ integrated along the imaging beam direction z: $g(x, y) \propto \int n(x, y, z)dz$. When assuming that the MOT has cylindrical symmetry (with the symmetry axis along the x-direction), the local atomic density n_c at the MOT center is given by the maximum of the inverse Abel transform of $g(x_c, y)$, where x_c is the x-coordinate of the MOT center

$$n_c = \max_r \left(-\frac{1}{\pi} \int_r^\infty \left(\frac{\partial g(x_c, y)}{\partial y} \right) \frac{dy}{\sqrt{y^2 - r^2}} \right), \qquad (12)$$

with $r = \sqrt{y^2 + z^2}$ denoting the distance to the MOT center [38]. Since the derivative $\partial g/\partial y$ is very sensitive to noise, the density profile g is smoothened before its derivative is calculated. We obtain $n_c^K \sim 3\times10^{10}$ atoms/cm^3 and $n_c^{Li} \sim 2 \times 10^{10}$ atoms/cm^3, respectively.

The temperature of the MOTs in single-species operation was determined by the time-of-flight method [24]. The ^{40}K-MOT has a temperature of 290 μK and the ^{6}Li-MOT of 1.4 mK. Both temperatures are higher than the Doppler cooling limit, because of the high intensity in the MOT beams. In addition, for ^{6}Li, the unresolved excited hyperfine structure (see Fig. 2) inhibits sub-Doppler cooling effects. The same temperatures are found in dual-species operation. The measured temperatures and atomic densities yield the peak phase space densities $D_K = n_c^K \Lambda_K^3 \sim 1.2\times10^{-7}$ and $D_{Li} = n_c^{Li} \Lambda_{Li}^3 \sim 1.3\times10^{-7}$ with the thermal de Broglie wavelength $\Lambda = \sqrt{2\pi\hbar^2/(mk_BT)}$, respectively.

The dependence of the MOT atom number on the detuning of the cooling light is depicted in Figures 12a, 12b. The atom number is maximum at $\Delta\omega_{cool}^K = -3\ \Gamma$ for ^{40}K and at $\Delta\omega_{cool}^{Li} = -5\ \Gamma$ for ^{6}Li, and has a FWHM of 2.3 Γ and 4.1 Γ, respectively.

Figures 12c, 12d show the dependence of the MOT atom number on the power of the cooling light per MOT beam. In the figures, a power of 10 mW corresponds to an on-resonance peak intensity of ∼3 I_{sat} (Fig. 12c) and ∼2 I_{sat} (Fig. 12d) in each of the six MOT beams. The atom number increases with increasing light power and saturates for higher powers. The saturation is due to several effects. First, the absorption probability for the cooling light saturates for high intensities. Second, the repulsive forces between the atoms due to rescattered photons and the temperature of the cloud increase with increasing light

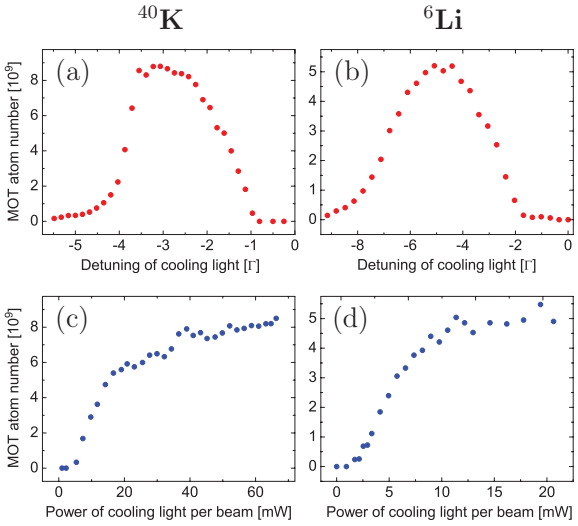

Fig. 12. (Color online) MOT atom number as a function of (a), (b) the detuning and (c), (d) the power of the cooling light per MOT beam for a constant intensity ratio between the cooling and repumping light. The graphs (a), (c) relate to the ^{40}K-MOT and (b), (d) to the ^{6}Li-MOT. For ^{40}K a power of 45 mW corresponds to an intensity of 13 $I_{\rm sat}$, for ^{6}Li a power of 20 mW corresponds to an intensity of 4 $I_{\rm sat}$, with the respective saturation intensities $I_{\rm sat}$ given in Table 3.

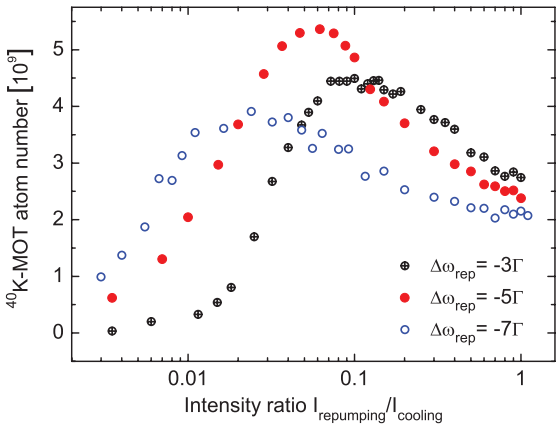

Fig. 13. (Color online) ^{40}K-MOT atom number as a function of the intensity ratio between repumping and cooling light for three different repumping detunings $\Delta\omega_{\rm rep}$ and a constant cooling light power of 18 mW per MOT beam (which corresponds to an intensity of 6 $I_{\rm sat}$).

power [32]. Finally the scattering rate for light-induced cold collisions increases with increasing light power.

Figure 13 shows the dependence of the ^{40}K-MOT atom number on the intensity ratio $I_{\rm rep}/I_{\rm cool}$ between repumping and cooling light for three different repumping detunings $\Delta\omega_{\rm rep}^{(1)} = -3\ \Gamma$, $\Delta\omega_{\rm rep}^{(2)} = -5\ \Gamma$ and $\Delta\omega_{\rm rep}^{(3)} = -7\ \Gamma$ and a constant cooling light power of 18 mW per MOT beam. The curves have a maximum at different ratios $I_{\rm rep}/I_{\rm cool}$, the position of the maxima lying at higher ratios for lower detunings. Furthermore, the maxima have different values for the three curves. The maximum is biggest for the detuning $\Delta\omega_{\rm rep}^{(2)} = -5\ \Gamma$. The shape of the curves can be understood as follows. Each curve increases between $I_{\rm rep}/I_{\rm cool} = 0$ and the position of the maximum, because the transition probability of the repumping transition increases with increasing repumping intensity. Thus the atoms are more efficiently cooled by the cooling light, as they are more efficiently repumped into the cycling transition. However, when the intensity of the repumping light becomes too large, the curve decreases again. Then, due to the strong repumping, the atoms are exposed to the more intense near-resonant cooling light, which causes light-induced cold collisions, leading to trap loss. At the maximum, the repumping is sufficiently strong to allow for an efficient cooling, and it is sufficiently weak to preserve the atoms from cold collisions induced by the strong cooling light. The value of the curve maximum is biggest for the detuning $\Delta\omega_{\rm rep}^{(2)} = -5\ \Gamma$. It is situated at $I_{\rm rep}/I_{\rm cool} \sim 1/20$, for which, as one can see below, only ∼20% of the ^{40}K-MOT atoms occupy the cooling cycle states $F = 9/2$ or $F' = 11/2$ (see Fig. 14), the others occupying the "dark" hyperfine ground state $F = 7/2$.

For very small intensity ratios $I_{\rm rep}/I_{\rm cool} \leq 0.01$ the atom number in the ^{40}K-MOT is larger for higher repumping detunings (Fig. 13). This behavior might be a consequence of the fact that the ^{40}K-MOT is loaded from a slow atomic beam. The beam atoms, which have a negative Doppler shift of more than 5 Γ with respect to the counter-propagating MOT beams, might absorb the repumping light more likely when it has a higher detuning.

Figure 14 shows the fraction of atoms in the ^{40}K-MOT (circles) which populate the states $F = 9/2$ or $F' = 11/2$ (i.e. the cooling cycle states, see Fig. 2) as a function of the intensity ratio $I_{\rm rep}/I_{\rm cool}$ between repumping and cooling light. In the experiment, the cooling light power was fixed to 18 mW per MOT beam, and the repumping detuning was $\Delta\omega_{\rm rep} = -5\ \Gamma$. The graph was recorded as follows. The absolute population of the states $F = 9/2$ and $F' = 11/2$ was measured by simultaneously switching off both the repumping and cooling light of the ^{40}K-MOT 600 μs before taking the image (with the imaging beam being near-resonant with the $F = 9/2 \rightarrow F' = 11/2$-transition). During the 600 μs time delay, all excited atoms relax to one of the ground states. For the used detunings and intensities of the MOT-beams ∼90% of the excited atoms occupy the state $F' = 11/2$ and thus relax to the ground state $F = 9/2$, which is imaged. Therefore, the image approximately yields the sum of the populations of the states $F = 9/2$ and $F' = 11/2$. The total population of all states (i.e. the total number of trapped atoms) was measured as described in the previous paragraph.

The curve in Figure 14 is increasing with increasing ratios $I_{\rm rep}/I_{\rm cool}$ and it saturates for high ratios. For the ratio $I_{\rm rep}/I_{\rm cool} = 1/5$ about 60% of the ^{40}K-MOT atoms occupy the cooling cycle states. For this ratio the fluorescence

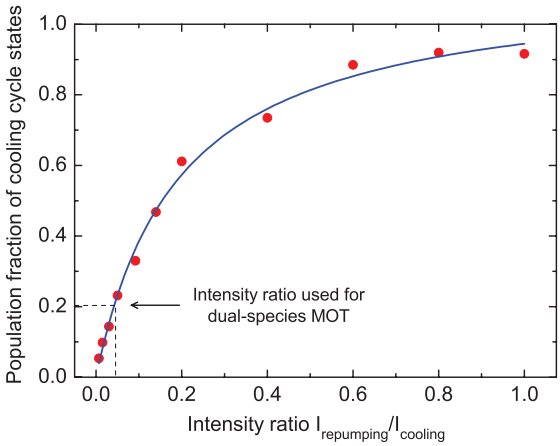

Fig. 14. (Color online) Circles: measured fraction of atoms in the ^{40}K-MOT populating the states $F = 9/2$ or $F' = 11/2$ (cooling cycle states) as a function of the intensity ratio between repumping and cooling light for the repumping detuning $\Delta\omega_{\rm rep} = -5\ \Gamma$ and a constant cooling light power of 18 mW per MOT beam (which corresponds to an intensity of $6\,I_{\rm sat}$). For the ratio which maximizes the total atom number in the ^{40}K-MOT, $I_{\rm rep}/I_{\rm cool} \sim 1/20$, only 20% of the trapped atoms occupy the cooling cycle states. Solid curve: a fit based on Einstein's rate equations.

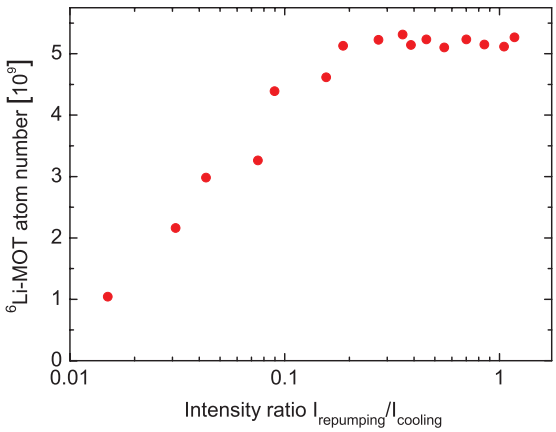

Fig. 15. (Color online) ^{6}Li-MOT atom number as a function of the intensity ratio between repumping and cooling light for a constant cooling light power of 11 mW per MOT beam (which corresponds to an intensity of 2 $I_{\rm sat}$). In comparison to ^{40}K (Fig. 13), the optimum atom number requires a larger intensity in the repumping light, which is a consequence of the unresolved excited hyperfine structure of ^{6}Li.

emitted by the ^{40}K-MOT is found to be maximum. For the ratio $I_{\rm rep}/I_{\rm cool} = 1/20$, which is used in the experiment, only ∼20% of the atoms occupy the cooling cycle states. Atom losses due to light-induced collisions are thus minimized.

The solid curve in Figure 14 shows a fit of the experimental data, based on a simple model, assuming ^{40}K to be a four-level atom (with the states $F = 9/2$, $F = 7/2$, $F' = 11/2$ and $F' = 9/2$). Einstein's rate equations yield that the curve obeys the law $P_{\rm ccs} = 1/(1 + a + b/(I_{\rm rep}/I_{\rm cool}))$, with the fitting parameters $a = -0.11$ and $b = 0.17$, which depend on the transition probabilities and the used intensities and detunings.

Figure 15 shows the dependence of the ^{6}Li-MOT atom number on the intensity ratio $I_{\rm rep}/I_{\rm cool}$ between repumping and cooling light for the repumping detuning $\Delta\omega_{\rm rep} = -3\ \Gamma$ and a constant cooling light power of 11 mW per MOT beam. In contrast to Figure 13, the curve does not have a maximum but rather increases with increasing $I_{\rm rep}/I_{\rm cool}$ and saturates. This behavior is a result of the important contribution of the repumping light to the cooling process, particular to ^{6}Li, as it has an unresolved excited state hyperfine structure.

In a dual-species MOT, inelastic collisions between atoms of the two different species can occur and represent important loss mechanisms. Previous studies have shown that the principal loss mechanisms for heteronuclear collisions in dual-species MOTs involve one ground-state and one excited atom of different species [35,36]. Such atom pairs can undergo radiative escape or fine-structure changing collisions [39]. Both these loss processes require the two atoms to approach each other sufficiently close such that a large enough interaction energy is gained to make the atoms leave the trap. The long-range behavior of the scattering potentials determines if the atoms can approach each other sufficiently. For LiK, the scattering potentials for a singly-excited heteronuclear atom pair are all attractive for the case where the K atom is excited and all repulsive for the case where the Li atom is excited [40]. As a consequence, a ground-state K atom and an excited Li atom repel each other and are prevented from undergoing inelastic collisions (optical shielding). Inelastic collisions involving singly-excited heteronuclear atom pairs thus always contain an excited K atom. In order to minimize the rate of heteronuclear collisions in the LiK-MOT, the density of excited K atoms must therefore be reduced. Furthermore, the atomic density in the trap as well as the relative speed of the colliding atoms, i.e. the temperature of the cloud, need to be minimized.

In our ^{6}Li-^{40}K dual-species MOT the following strategy is applied in order to minimize inelastic heteronuclear collisions. First the use of very low magnetic field gradients (8 G/cm), which decreases the atomic densities ($n_{\rm c}^{\rm K} \sim 3{\times}10^{10}$ atoms/cm^3 and $n_{\rm c}^{\rm Li} \sim 2{\times}10^{10}$ atoms/cm^3). Second, low intensities in the repumping light for both, ^{6}Li and ^{40}K, are used in order to decrease the number of excited atoms. Decreasing the number of excited ^{6}Li atoms here a priori serves to decrease the temperature of the ^{6}Li-cloud. Since that is much larger than the temperature of the ^{40}K-cloud, the relative speed of two colliding atoms and thus the collision rate can be efficiently decreased by minimizing the temperature of the ^{6}Li-cloud. Finally a small mutual influence of the MOTs is obtained: the atom numbers in the MOTs decrease by ∼4% in the

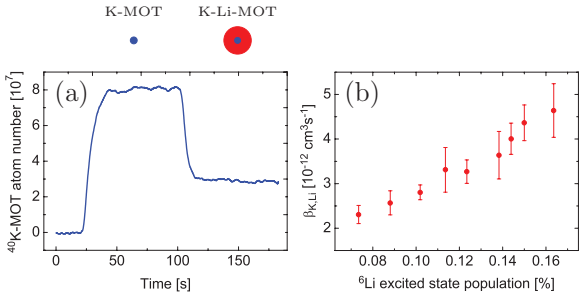

Fig. 16. (Color online) (a) Evolution of the atom number in the ^{40}K-MOT in the absence ($t < 100$ s) and presence ($t > 100$ s) of the ^{6}Li-MOT for an increased magnetic field gradient of 16 G/cm. (b) Trap loss coefficient β_{KLi} for heteronuclear collisions as a function of the relative excited state population of the trapped ^{6}Li atoms.

^{6}Li-MOT and ∼10% in the ^{40}K-MOT due to the presence of the other species.

The importance of decreasing the magnetic field gradients in order to minimize the heteronuclear collision rate in the dual-species MOT is demonstrated in Figure 16a, which depicts the effect of the ^{6}Li-MOT on the ^{40}K-MOT atom number when a two-times larger magnetic field gradient (16 G/cm) is used. At this gradient the atomic density in the ^{6}Li-MOT is by a factor of 4 larger than at the gradient used for the optimized MOT. In the experiment, the ^{40}K-MOT was intentionally reduced in size (by decreasing the 2D-MOT flux) to ensure a better inclosure in the ^{6}Li-MOT. The curve shows that ∼65% of the ^{40}K-MOT atoms leave the trap due to the enhanced heteronuclear collisions. Using a low magnetic field gradient is therefore helping significantly to decrease the heteronuclear collisions.

In the following we determine the trap loss coefficients for the (optimized) dual-species MOT in order to quantify the heteronuclear collisions. The rate equation for the atom number in a dual-species MOT (with species A and B) reads [35]

$$\frac{dN_{\mathrm{A}}}{dt} = L_{\mathrm{A}} - \gamma N_{\mathrm{A}} - \beta_{\mathrm{AA}} \int n_{\mathrm{A}}^2 dV - \beta_{\mathrm{AB}} \int n_{\mathrm{A}} n_{\mathrm{B}} dV, \quad (13)$$

where L_{A} is the loading rate, γ the trap loss rate due to collisions with background gas atoms and $n_{\mathrm{A}}, n_{\mathrm{B}}$ the local atomic densities. β_{AA} and β_{AB} denote the cold collision trap loss coefficients for homo- and heteronuclear collisions, respectively. L_{A} and γ are determined from the loading and decay curves of the single-species MOTs. The obtained values for L_{A} are given in Table 3 and γ is found to be $1/7.5$ s^{-1}. The homonuclear trap loss coefficients β_{AA} are determined from the steady state atom numbers in single-species operation using the measured density profiles. For the experimental conditions indicated in Table 3, we obtain

$$\beta_{\mathrm{LiLi}} = (8 \pm 4) \times 10^{-12}\,\mathrm{cm}^3\ \mathrm{s}^{-1}, \quad (14)$$

$$\beta_{\mathrm{KK}} = (6 \pm 3) \times 10^{-13}\,\mathrm{cm}^3\ \mathrm{s}^{-1}. \quad (15)$$

The determination of the heteronuclear trap loss coefficients β_{AB} for the optimized dual-species configuration would require the knowledge of the mutual overlap of the MOTs, which is difficult to estimate when absorption images are taken only along one direction. We therefore choose a configuration, which makes the determination of β_{AB} less dependent on assumptions about the mutual overlap (but which does not change the value of β_{AB}). We reduce the atom flux of species A, in order to decrease the spatial extension of the trapped cloud of species A and to place it in the center of the cloud of species B. A video camera which records the fluorescence of the MOTs from a different direction than that of the absorption imaging verifies that this configuration is indeed achieved. Then, in equation (13) it is $\int n_{\mathrm{A}} n_{\mathrm{B}} dV \sim n_{\mathrm{c}}^{\mathrm{B}} N_{\mathrm{A}}$. Comparing the steady-state atom numbers for the different configurations then yields

$$\beta_{\mathrm{LiK}} = (1 \pm 0.5) \times 10^{-12}\,\mathrm{cm}^3\ \mathrm{s}^{-1}, \quad (16)$$

$$\beta_{\mathrm{KLi}} = (3 \pm 1.5) \times 10^{-12}\,\mathrm{cm}^3\ \mathrm{s}^{-1}, \quad (17)$$

for the experimental conditions indicated in Table 3. Comparing all four trap loss coefficients, the dominant is β_{LiLi} (Eq. (14)) for light-induced homonuclear ^{6}Li-^{6}Li collisions. This is a consequence of the large temperature of the ^{6}Li-MOT and the unresolved hyperfine structure of ^{6}Li which prohibits the creation of a dark MOT, leading to a large excited state population. The much smaller homonuclear trap loss coefficient β_{KK} for ^{40}K (Eq. (15)) is consistent with Figure 13 which shows that, for ^{40}K, small repumping intensities are favorable. The heteronuclear trap loss coefficients $\beta_{\mathrm{LiK}}, \beta_{\mathrm{KLi}}$ (Eqs. (16) and (17)) are also much smaller than β_{LiLi}, indicating that our applied strategy for decreasing the heteronuclear collisions is good. In the Amsterdam group the heteronuclear trap loss coefficients were found by a factor of about 2 larger than ours [15]. A dark SPOT MOT has been implemented in order to reduce the excited state population of the ^{40}K atoms. In the next paragraph we show, however, that it is also important to reduce the excited state population of the ^{6}Li atoms.

Figure 16b depicts the dependence of the trap loss coefficient β_{KLi} on the relative excited state population of the ^{6}Li atoms. The graph was obtained by recording the influence of the ^{6}Li-MOT on the ^{40}K-MOT as the power of the ^{6}Li-MOT beams was varied. For each power it was verified that the ^{40}K-MOT was placed in the center of the ^{6}Li-MOT and the atomic density of the ^{6}Li-MOT was recorded. In the experiment a magnetic field gradient of 16 G/cm was used. The central atomic density of the ^{6}Li-MOT was found to be approximately constant, when the power was varied ($n_{\mathrm{c}}^{\mathrm{Li}} \sim 8 \times 10^{10}$ atoms/cm^3). The relative excited state population for a given beam power was estimated using Einstein's rate equations. In addition the variation of the excited state population was measured by recording the fluorescence emitted by the ^{6}Li-MOT and by measuring the number of captured atoms. The latter changed by a factor of 1.5 in the considered range of beam powers. The graph in Figure 16b shows that the trap loss coefficient increases by more than a factor of 2

as the relative excited state population is increased from ∼7% to ∼16%. The error bars shown in the figure refer to statistical errors. The uncertainty due to systematic errors is estimated to be 50%. The significant increase of β_{KLi} demonstrates the importance of minimizing the number of excited ^{6}Li atoms (and not only that of the excited ^{40}K atoms). One reason for this increase is the increase of temperature of the ^{6}Li-MOT, which changes from ∼1 mK to ∼1.6 mK when the beam power is increased. Another reason could be the occurence of collisions involving doubly-excited Li*K* atom pairs, the rate of which increases with the excited state populations. The scattering potentials for these collisions are known to be of a long-range, as they scale with the internuclear separation as $1/R^5$ [41], whereas they scale as $1/R^6$ for collisions involving a singly-excited heteronuclear atom pair [33].

5 Conclusions

We have produced a dual-species magneto-optical trap for fermionic ^{6}Li and ^{40}K with large atom numbers. Two strategies have been applied in order to achieve this result. First, the dual-species MOT is placed in an ultra-high vacuum environment, being continuously loaded from cold atomic beams. The atomic beams originate from separate atom sources – a Zeeman slower for ^{6}Li and a 2D-MOT for ^{40}K – which both yield a large flux of cold atoms. Second, the homo- and heteronuclear collisions have been minimized by using small magnetic field gradients and low light powers in the repumping light. The atom loss in each MOT due to the presence of the other species decreases by only 4% (^{6}Li) and 10% (^{40}K) due to the heteronuclear collisions.

We have given a detailed description of the implemented apparatus, which we hope serves as a guideline for the construction of next generation experiments with fermionic ^{6}Li and ^{40}K.

The produced dual-species MOT represents the starting point for the production of a large-atom number quantum degenerate Fermi-Fermi mixture. The atoms trapped in the dual-species MOT have already been transferred into the magnetic trap and magnetically transported to the science chamber with large optical access and low background pressure. The large depth of magnetic traps as compared to optical traps allows for a large transfer efficiency, leading to smaller losses of atoms. In the science cell, the dual-species cloud will be evaporatively cooled in a plugged magnetic trap to quantum degeneracy and then transferred into an optical trap for investigation.

The authors acknowledge support from ESF Euroquam (FerMix), SCALA, ANR FABIOLA, Région Ile de France (IFRAF), ERC Ferlodim and Institut Universitaire de France. A.R. acknowledges funding from the German Federal Ministry of Education and Research and D.R.F. from Fundação para a Ciência e Tecnologia (FCT) through grant SFRH/BD/68488/2010 and from Fundação Calouste Gulbenkian.

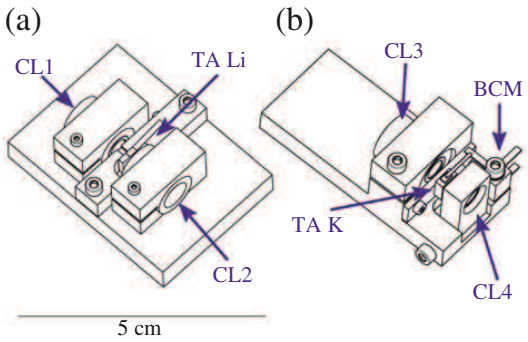

Fig. 17. (Color online) Sketch of the tapered amplifier supports for (a) Li and (b) K. In the figure, TA Li and TA K refer to the respective tapered amplifier chips, CL1, CL2, CL3 and CL4 to the (only longitudinally adjustable) collimation lens supports and BCM to the isolated mount for the blade connectors used to power the chip for K. The supports for the output collimation lenses are CL2 and CL4.

Appendix: Tapered amplifier mounts

We developed compact support designs for our tapered amplifier chips, in order to minimize the costs of the laser sources of our experimental setup. The TAs are commercial semiconductor chips which are mounted on homemade compact mechanical supports with nearly no adjustable parts. The support designs allow for an easy installation process, which does not require any gluing or the help of micrometric translation stages for the alignment of the collimation optics, as that can be accomplished by free hand. Furthermore, the design minimizes the heat capacity of the support and the produced temperature gradients, allowing for a quick temperature stabilization that makes the TAs quickly operational after switch-on. The temperature stabilization is accomplished using a Peltier element (Roithner Lasertechnik GmbH, ref. TEC1-12705T125) connected to a PID control circuit. The heat of(the chip is dissipated via an aluminum base plate which is economically cooled by air rather than running water (the base plate reaches a maximum temperature of 28 °C for diode currents of 2 A).

The commercial TA chips are sold on small heat sinks which have different dimensions for the two different wavelengths. We thus had to design slightly different supports for the Li- and K-TAs, which are both schematically shown in Figure 17.

For lithium the semiconductor chip (Toptica, ref. TA-670-0500-5) is delivered on a heat dissipation mount of type "I". It is placed between two axially aligned cylindrical lens tubes (CL1 and CL2 in Fig. 17a), each of which containing an aspheric collimation lens of focal length 4.5 mm (Thorlabs, ref. C230TME-B). The support of the tubes and the chip are precisely machined such that the chip's output beam falls on the center of the respective collimation lens (CL2 in Fig. 17a). The tubes are supported by cylindrically holed tightenable hinges in which

they can move only longitudinally, along the direction of the amplified laser beam. This restriction of the tube's motion facilitates the alignment of the collimation lenses. The support design does not allow for a transverse alignment of the collimation lenses. Since this alignment is not very critical for the performance of the TA, we found it needless to allow this degree of freedom and relied on precise machining (possible imperfections could be compensated utilizing the mechanical play of the large attachment screw holes of the commercial heat sinks of the chips). When tightened by a screw, the hinges fix the position of the tubes. Since the tightening applies a force perpendicular to the longitudinal direction, it does not move the tubes along this (critical) direction. They might only move slightly along the transverse direction, which does not affect the final performance of the TA.

For potassium, the semiconductor chip (Eagleyard, ref. EYP-TPA-0765-01500-3006-CMT03-0000) is delivered on a heat dissipation mount of type "C". Placing this mount between two hinges as for the case of lithium is less convenient since the heat dissipation mount has to be attached by a screw in the longitudinal direction which requires access from one side. Therefore one hinge is replaced by a rail which guides a parallelepipedically formed mount for the second (output) collimation lens (CL4 in Fig. 17b). The motion of this mount is also fixed by tightening a screw applying forces perpendicular to the rail direction, which does not move the collimation lens along the critical longitudinal direction. For all our TAs, the positioning of the collimation lenses never had to be adjusted again once they were aligned.

The commercial heat dissipation mount of the potassium chip is inconvenient for a simple powering of the chip. The very fragile gold wire, which has to be connected to the negative source of the current supply, has to be protected by a mechanical support before being connected to a cable. Therefore we soldered it to a blade connector that is fixed by an isolated plastic mount (BCM Fig. 17b) and which is connected to the current supply. To avoid an overheating of the chip during the soldering process we permanently cooled the gold wire by blowing cold dry air from a spray can on it.

The output beams of the TA chips are astigmatic and thus require additional collimation. The choice of the collimation optics needs to be adapted to the specifications of the subsequent optical fiber, which in our case requests a collimated circular Gaussian beam of 2.2 mm $1/e^2$-diameter for optimum coupling efficiency. The mode-matching was found optimum for a pair of lenses consisting of one spherical lens (with $f = 15$ cm for Li and $f = 4$ cm for K) and a cylindrical lens (with $f = 8$ cm for Li and $f = 2.54$ cm for K), which are placed outside the TA's housing. The cylindrical lenses are supported by rotatable mounts, in order to facilitate the mode-matching into the fibers. For all our TAs we achieve fiber-coupling efficiencies larger than 50% (Li) and 60% (K).

When injected with 20 mW, the Li-TAs yield an output power of 500 mW at 1 A driving current and the K-TAs yield an output power of 1500 mW at 2.5 A driving current. In order to increase the lifetime of the chips, we limit the driving currents to smaller values and we switch the chips on only for periods of experimentation. When switched on, the TAs quickly reach a stable functioning (usually within 10 min) due to the compactness of the mechanical support, which allows for a quick temperature stabilization.

References

1. *Proceedings of the International School of Physics Enrico Fermi on Ultracold Fermi Gases*, edited by M. Inguscio, W. Ketterle, C. Salomon (Societa Italiana di Fisica, Bologna, Italy, 2006)
2. S. Giorgini, L.P. Pitaevskii, S. Stringari, Rev. Mod. Phys. **80**, 1215 (2008)
3. R.P. Feynman, Int. J. Theor. Phys. **21**, 467 (1982)
4. A.F. Ho, M.A. Cazalilla, T. Giamarchi, Phys. Rev. A **79**, 033620 (2009)
5. D.S. Petrov, G.E. Astrakharchik, D.J. Papoular, C. Salomon, G.V. Shlyapnikov, Phys. Rev. Lett. **99**, 130407 (2007)
6. M.M. Forbes, E. Gubankova, W.V. Liu, F. Wilczek, Phys. Rev. Lett. **94**, 017001 (2005)
7. J. Levinsen, T.G. Tiecke, J.T.M. Walraven, D.S. Petrov, Phys. Rev. Lett. **103**, 153202 (2009)
8. J. Deiglmayr, A. Grochola, M. Repp, K. Mörtlbauer, C. Glück, J. Lange, O. Dulieu, R. Wester, M. Weidemüller, Phys. Rev. Lett. **101**, 133004 (2008)
9. K.-K. Ni, S. Ospelkaus, M.H.G. de Miranda, A. Péer, B. Neyenhuis, J.J. Zirbel, S. Kotochigova, P.S. Julienne, D.S. Jin, J. Ye, to be published
10. M. Aymar, O. Dulieu, J. Chem. Phys. **122**, 204302 (2005)
11. T.G. Tiecke, M.R. Goosen, A. Ludewig, S.D. Gensemer, S. Kraft, S.J.J.M.F. Kokkelmans, J.T.M. Walraven, Phys. Rev. Lett. **104**, 053202 (2010)
12. A. Ridinger, S. Chaudhuri, T. Salez, N. Bouloufa, L. Pruvost, O. Dulieu, F. Chevy, C. Salomon, to be published
13. M. Taglieber, A.-C. Voigt, F. Henkel, S. Fray, T.W. Hänsch, K. Dieckmann, Phys. Rev. A **73**, 011402 (2006)
14. F.M. Spiegelhalder, A. Trenkwalder, D. Naik, G. Kerner, E. Wille, G. Hendl, F. Schreck, R. Grimm, Phys. Rev. A **81**, 043637 (2010)
15. T. Tiecke, Ph.D. thesis, University of Amsterdam, 2009
16. M. Greiner, I. Bloch, T.W. Hänsch, T. Esslinger, Phys. Rev. A **63**, 031401 (2001)
17. U. Eismann, F. Gerbier, C. Canalias, G. Trénec, J. Vigué, F. Chevy, C. Salomon, to be published
18. K.A. Yakimovich, A.G. Mozgovoi, High Temp. **38**, 657 (2000)
19. G. Ferrari, M.-O. Mewes, F. Schreck, C. Salomon, Opt. Lett. **24**, 151 (1999)
20. M.-O. Mewes, G. Ferrari, F. Schreck, A. Sinatra, C. Salomon, Phys. Rev. A **61**, 011403 (1999)
21. Z. Hadzibabic, S. Gupta, C.A. Stan, C.H. Schunck, M.W. Zwierlein, K. Dieckmann, W. Ketterle, Phys. Rev. Lett. **91**, 160401 (2003)
22. T.G. Tiecke, S.D. Gensemer, A. Ludewig, J.T.M. Walraven, Phys. Rev. A **80**, 013409 (2009)

23. W.D. Phillips, H. Metcalf, Phys. Rev. Lett. **48**, 596 (1982)
24. H.J. Metcalf, P. van der Straten, *Laser cooling and trapping* (Springer, Berlin, 1999)
25. A. Joffe, W. Ketterle, A. Martin, D.E. Pritchard, J. Opt. Soc. Am. B **10**, 2257 (1993)
26. N.F. Ramsey, *Molecular Beams* (Oxford University Press, Oxford, 1986)
27. C.B. Alcock, V.P. Itkin, M.K. Horrigan, Can. Metall. Quart. **23**, 309 (1984)
28. K. Dieckmann, R.J.C. Spreeuw, M. Weidemüller, J.T.M. Walraven, Phys. Rev. A **58**, 3891 (1998)
29. J. Schoser, A. Batär, R. Löw, V. Schweikhard, A. Grabowski, Yu.B. Ovchinnikov, T. Pfau, Phys. Rev. A **66**, 023410 (2002)
30. J. Catani, P. Maioli, L. De Sarlo, F. Minardi, M. Inguscio, Phys. Rev. A **73**, 033415 (2006)
31. S. Chaudhuri, S. Roy, C.S. Unnikrishnan, Phys. Rev. A **74**, 023406 (2006)
32. A.M. Steane, M. Chowdhury, C.J. Foot, J. Opt. Soc. Am. B **9**, 2142 (1992)
33. A. Derevianko, W.R. Johnson, M.S. Safronova, J.F. Babb, Phys. Rev. Lett. **82**, 3589 (2002)
34. M.S. Santos, P. Nussenzveig, L.G. Marcassa, K. Helmerson, J. Flemming, S.C. Zilio, V.S. Bagnato, Phys. Rev. A **52**, R4340 (1995)
35. U. Schlöder, H. Engler, U. Schünemann, R. Grimm, M. Weidemüller, Eur. Phys. J. D **7**, 331 (1999)
36. G.D. Telles, W. Garcia, L.G. Marcassa, V.S. Bagnato, D. Ciampini, M. Fazzi, J.H. Müller, D. Wilkowski, E. Arimondo, Phys. Rev. A **63**, 033406 (2001)
37. J. Goldwin, S.B. Papp, B. DeMarco, D.S. Jin, Phys. Rev. A **65**, 021402 (2002)
38. V. Dribinski, A. Ossadtchi, V.A. Mandelshtam, H. Reisler, Rev. Sci. Instrum. **73**, 2634 (2002)
39. M. Weidemüller, C. Zimmermann, *Interactions in Ultracold Gases* (Wiley-VCH, Weinheim, 2003)
40. B. Bussery, Y. Achkar, M. Aubert-Frécon, Chem. Phys. **116**, 319 (1987)
41. M. Marinescu, H.R. Sadeghpour, Phys. Rev. A **59**, 390 (1999)

Article B:

U. Eismann, F. Gerbier, C. Canalias, A. Zukauskas, G. Trénec, J. Vigué, F. Chevy and C. Salomon, *An all-solid-state laser source at 671 nm for cold-atom experiments with lithium*, Appl. Phys. B **106**, 25-36 (2012)

Appl Phys B (2012) 106:25–36
DOI 10.1007/s00340-011-4693-y

Applied Physics B
Lasers and Optics

An all-solid-state laser source at 671 nm for cold-atom experiments with lithium

U. Eismann · F. Gerbier · C. Canalias · A. Zukauskas · G. Trénec · J. Vigué · F. Chevy · C. Salomon

Received: 8 March 2011 / Revised version: 28 June 2011 / Published online: 2 September 2011

Abstract We present an all-solid-state narrow-linewidth laser source emitting 670 mW output power at 671 nm delivered in a diffraction-limited beam. The source is based on a frequency-doubled diode-end-pumped ring laser operating on the $^4F_{3/2} \rightarrow {}^4I_{13/2}$ transition in Nd:YVO_4. By using periodically poled potassium titanyl phosphate (ppKTP) in an external buildup cavity, doubling efficiencies of up to 86% are obtained. Tunability of the source over 100 GHz is accomplished. We demonstrate the suitability of this robust frequency-stabilized light source for laser cooling of lithium atoms. Finally, a simplified design based on intracavity doubling is described and first results are presented.

1 Introduction

The lithium atomic species is of great interest for cold-atom experiments and the study of quantum degenerate gases. As a member of the alkali group, it offers strong coupling to electromagnetic fields and a simple level structure including cycling transitions, thus making it suitable for laser cooling. The significant natural abundance of fermionic (^{6}Li) as well as bosonic (^{7}Li) isotopes allows exploration of both sorts of quantum statistics. The interaction parameter at ultra-cold temperatures, the s-wave scattering length, is easily tunable for both species by applying a DC magnetic field in the vicinity of a Feshbach resonance [1]. The large width of these resonances, in addition to the light mass, adds up to the favorable properties of lithium for ultra-cold-atom experiments.

To produce large samples of quantum degenerate gases, one needs large numbers of pre-laser-cooled atoms in a magneto-optical trap (MOT). This first step is mandatory before proceeding to the evaporative cooling phase that leads to quantum degeneracy by reducing the atom number in favor of phase-space density. To optimize the MOT capture process, one usually fixes the laser intensity around a saturation intensity and uses the available output power to maximize the beam diameter. Thus, more laser power leads to a better capture efficiency and larger atom numbers. Another important requirement is the quality of the spatial mode needed to efficiently couple the laser light to single-mode (SM) optical fibers.

The wavelength of the lithium D-line resonances (670.8 nm in air) currently restricts the choice of light sources to two different kinds of lasers: dye lasers and external cavity diode lasers (ECDLs). Dye lasers typically deliver watt-level output of monochromatic light in a diffraction-limited beam [2]. The drawbacks of this technology are an important maintenance effort, high intrinsic phase noise and the requirement of an expensive pump laser. ECDLs are typically limited to 50-mW output with limited spatial mode quality; hence, further amplification by injection-locked slave lasers or tapered amplifiers is needed to run a cold-atom experiment.

It is thus desirable to develop suitable single-frequency lasers with watt-level output power. Further applications of

U. Eismann (✉) · F. Gerbier · F. Chevy · C. Salomon
Laboratoire Kastler Brussel, ENS, UPMC, CNRS UMR 8552, 24 rue Lhomond, 75231 Paris, France
e-mail: eismann@ens.fr

G. Trénec · J. Vigué
Laboratoire Collisions Agrégats Réactivité, Institut de Recherche sur les Systèmes Atomiques et Moléculaires Complexes, LCAR, Université de Toulouse, Université Paul Sabatier and CNRS UMR 5589, 31062 Toulouse, France

C. Canalias · A. Zukauskas
Department of Applied Physics, Royal Institute of Technology, AlbaNova Universitetscentrum, 10691 Stockholm, Sweden

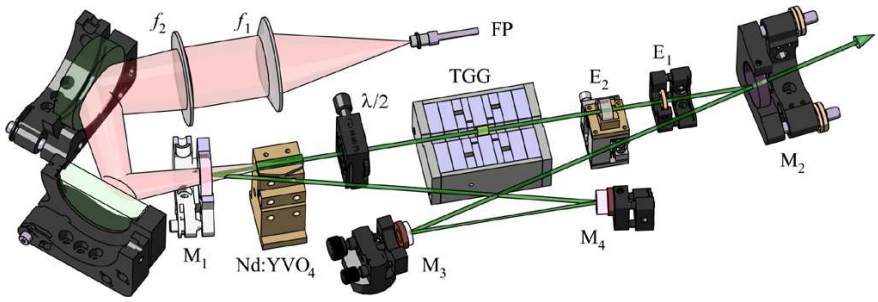

Fig. 1 The laser setup, consisting of the fiber-coupled pump source *FP*, two pump focusing lenses $f_{1,2}$, the cavity mirrors $M_{1\text{–}4}$ and the Nd:YVO$_4$ active medium. The $\lambda/2$ wave plate and the *TGG* Faraday crystal in a magnet ensemble impose unidirectional oscillation, whereas two etalons $E_{1,2}$ establish single-mode operation. The optical path of the laser beam is depicted in green. For some mechanical components, we show a sectional view to improve visibility of the beam path. The distance between M_1 and M_2 is 295 mm

such sources include atom interferometry experiments [3], pumping of Cr:LiSAF lasers [4] and lithium isotope separation [5].

Light sources emitting at 671 nm based on frequency doubling of 1342-nm Nd:YVO$_4$ or Nd:GdVO$_4$ lasers have been realized previously [6–15], reaching up to 9.5 W of cw multi-mode output [15]. A solid-state single-frequency laser source delivering 920 mW at around 657 nm has been presented in [16].

Here we report on the construction and characterization of an all-solid-state laser source with 670-mW output power in a TEM$_{00}$ mode operating at 671 nm. This is made possible by frequency doubling a home-made 1.3-W, 1342-nm Nd:YVO$_4$ single-mode ring laser in an external cavity. The advantages of our source are: watt-level output power in a single longitudinal and transverse mode with excellent beam quality, narrow linewidth (<1 MHz) and long-term frequency stabilization onto the lithium resonance lines. Furthermore, multi-mode-diode-laser pumping at 808 nm is inexpensive and only low-maintenance efforts are required for establishing reliable day-to-day operation.

The paper is organized as follows: in Sect. 2, we describe the infrared (IR) single-frequency laser design and results. Section 3 focuses on the frequency doubling of the infrared radiation, whereas Sect. 4 treats the spectroscopy and frequency-locking systems. In Sect. 5 the red laser emission is characterized in terms of relative intensity noise, linewidth and long-term stability. In Sect. 6, we describe a second setup in progress using intra-cavity doubling that has the potential to deliver similar output power at 671 nm while offering higher simplicity of the laser source design.

2 Infrared laser

2.1 Laser setup

To realize a single-longitudinal-mode (SLM) laser, it is favorable to use a design avoiding standing waves and thus the resulting spatial hole burning in the active medium [17]. Thus, we have chosen a ring cavity with proper intra-cavity etalons as frequency-selective elements.

The setup is presented in Fig. 1. The pump source is a commercial fiber-coupled Coherent FAP-400 diode stack emitting up to 42.6 W at 808 nm (90% energy width: 4 nm). Its metal housing is temperature stabilized to optimize the spectral overlap between pump emission and the gain medium absorption. The fiber output (core radius: 200 µm, numerical aperture NA = 0.22) is imaged in the gain medium using two lenses ($f_1 = 75$ mm and $f_2 = 200$ mm) to a top-hat spot of radius $w_{\text{pump}} = 530$ µm. The Nd:YVO$_4$ crystal of dimensions $3 \times 3 \times 10$ mm^3 is 0.2 at.%-doped, *a*-cut and anti-reflective (AR) coated at 808 nm and 1342 nm. It is wrapped in indium foil and fixed in a solid water-cooled copper mount to efficiently remove heat. Care needs to be taken to avoid acoustic excitations of the mount due to turbulent water flow; thus, only a small continuous flux of tap water was applied to prevent frequency fluctuations of the laser output.

The four mirrors M$_{1-4}$ (highly reflective at 1342 nm except for the output coupler M$_2$, transmitting at 808 nm) form a folded ring or bow-tie cavity. The two concave mirrors M$_3$ and M$_4$ have a radius of curvature of $R_{\text{cc}} = 100$ mm. Thermal design is crucial for the laser: even at moderate pump powers, strong thermal lensing occurs because of the large quantum defect between pump and lasing photon energies and excited-state absorption to higher levels [18–20]. Optimum spatial overlap of the pump fiber image in the laser crystal (top-hat profile of radius w_{pump}) and the laser mode ($1/e^2$ radius w_{laser}) is established by fine tuning the distance between M$_3$ and M$_4$. The choice of the mode-size ratio $\rho = w_{\text{laser}}/w_{\text{pump}} \simeq 1$ allowed for a stable TEM$_{00}$ operation at optimum output power.[1] The cavity design remains stable in the presence of a thermal focal length down

[1] Chen et al. [21] suggest a ratio $\rho = 0.8$, for which we observe reduced output power as well as higher-order transversal mode oscillation.

Table 1 Frequency scales in the setup. Typical frequencies are free spectral ranges ν_{FSR} as described in the text and FWHM for the gain profile from [19]. Reflectivities $\mathcal{R}$ are given for the output and input coupling mirrors in case of the two cavities and for the two etalon surfaces, respectively. The finesses $\mathcal{F}$ and Q-factors of the laser cavity and E_1 are calculated from the $\mathcal{R}$-values as stated, neglecting further losses. $\mathcal{F}$ and Q were measured for the doubling cavity, see Sect. 3.3

	Typ. freq.	Typ. $\mathcal{R}$	$\mathcal{F}/Q$-factor
Gain profile width	300 GHz		
Laser cavity 81 cm	360 MHz	96.5%	$110/6 \times 10^7$
Doubl. cavity 41 cm	730 MHz	93.6%	$86/3 \times 10^7$
Etalon E_1, 0.5 mm	210 GHz	3.3%	–/–
Etalon E_2, 4 mm	26 GHz	28%	2/2000

to $f_{\mathrm{th}} = 170$ mm in the Nd:YVO_4 crystal. Care was taken to design the cavity as short as possible to increase the laser's mechanical stability and the cavity free spectral range (FSR), facilitating SLM behavior.

Unidirectional oscillation is ensured by a combination of a Faraday rotator and a wave plate. The Faraday rotator is custom built by the LCAR group according to the original design presented in [22]. As a medium displaying the Faraday effect, a cylindrical AR-coated terbium gallium garnet (TGG) crystal is chosen. To minimize absorption, the length of the TGG crystal is limited to $l_{\mathrm{TGG}} = 6$ mm, and its diameter is 5 mm. The ensemble of NdFeB ring magnets delivers a magnetic field integral of $I_B = \int_0^{l_{\mathrm{TGG}}} B(z)\,\mathrm{d}z = 8$ T mm along the TGG axis. Single-pass measurements resulted in a rotation angle of $\varphi_{\mathrm{rot}} = -(9.3 \pm 0.1)^\circ$ and thus in a Verdet constant of $\mathcal{V} = \varphi_{\mathrm{rot}}/I_B = -(20.3 \pm 0.2)$ rad T^{-1} m^{-1} for the given crystal at 1342 nm. Back rotation and stable unidirectional operation at high intra-cavity powers is established by an AR-coated zero-order $\lambda/2$ wave plate, which is preferred to multi-order wave plates because of instabilities related to thermal effects [23]. The polarizing intra-cavity element is the Nd:YVO_4 crystal which provides higher gain in the c-direction as well as birefringence. The oscillation direction is chosen as indicated in Fig. 1 to spatially separate residual pump light from the output beam.

Stable SLM behavior could not be established using a single intra-cavity etalon. Thus, two infrared fused silica etalons $E_{1,2}$ of free spectral ranges $\nu_{\mathrm{FSR},1} = 210$ GHz and $\nu_{\mathrm{FSR},2} = 26$ GHz are installed, where $\nu_{\mathrm{FSR}} = c/nL_{\mathrm{rt}}$; c is the speed of light in vacuum, n the refractive index and L_{rt} the round-trip length. An overview of the typical frequency scales of the setup is given in Table 1. E_1 is non-coated, offering a modulation of the cavity transmission due to its Fresnel reflectivity of $\mathcal{R} = 3.3\%$ per surface, whereas E_2 is single-layer coated, yielding $\mathcal{R} = 28\%$.

A second role of the etalons is coarse frequency tuning of the output radiation. However, angular tuning yields walk-off losses and thus reduces the available output power. By applying the method of [24] to ring lasers, the minimum walk-off loss[2] can be estimated to be $\mathcal{L}_{\mathrm{wo}} = 0.02\%$ for E_2. It can be neglected for E_1, for which even an angular tuning of an entire free spectral range only yields $\mathcal{L}_{\mathrm{wo}} = 0.03\%$ additional loss. To avoid the higher tilt loss of E_2 ($\mathcal{L}_{\mathrm{wo}} = 2.8\%$ for angular tuning over one free spectral range of $\nu_{\mathrm{FSR}} = 26$ GHz), we chose to keep it still at the minimum angle and to change its temperature to tune the laser. For that purpose, it is enclosed in a temperature-stabilized copper mount.

Fine tuning of the laser frequency is established by mounting mirrors M_3 and M_4 on piezoelectric transducers (PZTs): a slow PZT (M_4) displaying large displacement of around 2 µm at maximum voltage of 150 V and a fast PZT (M_3) with a displacement of around ±50 nm limited by the ±15-V driver.

The laser was mounted on a 50-mm-thick breadboard. A combined aluminum–acrylic–glass housing was provided to isolate acoustic perturbations and for keeping the setup continuously under a dried air atmosphere to prevent dust and moisture from having detrimental effects on stable long-term operation.

2.2 Laser operation and characteristics

We now present a detailed description of the laser's operational characteristics. Pump light absorption in the gain medium depends on the wavelength of the radiation [25], hence on the pump diode stack temperature. Setting the chiller temperature to 24°C at maximum pump current resulted in highest output power.

By choosing a coupling mirror transmission value $\mathcal{T}_{\mathrm{oc}} = 3.5\%$, a maximum single-mode output power P_{out} of 1.3 W was obtained, see Fig. 2. The lasing threshold was found at an absorbed pump power $P_{\mathrm{abs}} = 9.8$ W. The power rises linearly above threshold with a slope efficiency of $\eta_{\mathrm{sl}} = \mathrm{d}P_{\mathrm{out}}/\mathrm{d}P_{\mathrm{abs}} = 37\%$. Between $P_{\mathrm{abs}} = 11$ W and 12 W, the output power departs from a linear behavior, and becomes unstable. We attribute this to intra-cavity-power-induced heating of etalon E_2 and the related change of its resonance frequency, thereby leaving the optimum operation range. Above $P_{\mathrm{abs}} = 12$ W, we recover the initial slope with stable operation. At P_{abs} (P_{out}) = 12.9 W (1.17 W), the slope efficiency drops to $\eta_{\mathrm{sl}} = 12\%$, indicating the presence of detrimental thermal effects. This behavior was qualitatively found before, see for instance Ref. [26]. Since no degradation of the laser parameters was observed for highest output powers, the laser was always pumped at maximum current

[2] The loss estimate of Ref. [24] yields zero for perpendicular incidence. However, one needs to account for a minimum angle on the order of the Gaussian beam divergence angle to circumvent multi-cavity behavior, causing instability of laser operation.

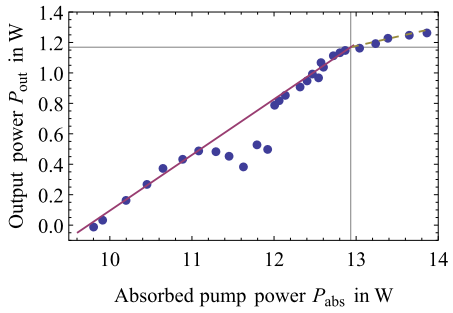

Fig. 2 Single-frequency laser output power as a function of pump current. Two regimes can be distinguished in the data (*circles*), and linear fits are performed (*solid/dashed lines*) for $P_{abs} < 12.9$ W and $P_{abs} > 12.9$ W. Points in the unstable domain near $P_{abs} = 11.5$ W were left out of the fit

for all further measurements. Removal of the etalons yields a rise in output power of ∼20%. This can be partly attributed to detuning of the laser frequency ω of ≃25 GHz from the emission peak when lasing at half the lithium resonance frequency.

The temperature derivative of the frequency of maximum etalon transmission ν_{max} yields

$$\frac{d\nu_{max}}{dT} = \frac{\nu_{max}}{\nu_{FSR}}\frac{d\nu_{FSR}}{dT} = -\nu_{max}\left(\frac{1}{n}\frac{dn}{dT} + \frac{1}{L_r}\frac{dL_r}{dT}\right), \quad (1)$$

where T is the etalon temperature. Putting in the values for IR fused silica from [27] yields $d\nu_{max}/dT = -1.42$ GHz K^{-1}. The emission wavelength was measured by single-pass frequency doubling the laser light, as described in the next section. This resulted in a second-harmonic (SH) output power in the 1-mW range, sufficient to drive a CCD-based wavelength meter (High Finesse WS-6). The measured temperature dependence of the laser emission frequency ν is $d\nu/dT = (-1.45 \pm 0.01)$ GHz K^{-1}. Tunability of ≃50 GHz is achieved, yielding ≃100 GHz of tunability for the SH output. To operate the laser at a given frequency without mode hops caused by etalon temperature drifts, the temperature of the etalon T_{set} needs to be stabilized to an interval $T_{set} \pm \delta T$, where δT can be estimated to be

$$\delta T < \frac{\nu_{FSR,\,laser}}{2|d\nu/dT|} \simeq 0.1°C. \quad (2)$$

This is accomplished using a home-made temperature controller, offering stability well below this requirement.

Continuous scanning of the laser frequency is achieved by sweeping the voltage applied to the slow PZT (M_4). For the dynamic range of 0–150 V, this results in more than three times the full mode-hop-free scan range of $\nu_{FSR,laser} = 360$ MHz. By applying simultaneous (linear) scanning of the PZT and angle tuning of etalon E_2, mode-hop-free continuous frequency tuning of the laser over 1.1 GHz could be demonstrated, with a resulting maximum output power drop of ≃10% due to etalon walk-off loss.

The beam coupled out of M_2 has a $1/e^2$ waist radius of 640 µm (820 µm) and a divergence angle of 0.8 mrad (0.9 mrad) in the horizontal (vertical) plane. The astigmatism results from the cavity design and non-isotropic thermal lensing in the Nd:YVO_4 crystal. By employing only spherical lenses, and thus imperfect mode matching, a coupling efficiency to a SM optical fiber of 75% was obtained. Stable output power and beam parameters over weeks of daily operation were demonstrated.

3 Second-harmonic generation

3.1 General considerations

Frequency-doubled light is generated using a second-order process in a nonlinear medium. In the limit of weak conversion, this yields a second-harmonic (SH) output power $P_{2\omega}$ in the form

$$P_{2\omega} = \eta P_\omega^2, \quad (3)$$

with P_ω the pump beam power of frequency ω and η the conversion efficiency. In [28], Boyd and Kleinman derived the following expression for η, assuming Gaussian beams:

$$\eta = \frac{2\omega^3 d_{ij}^2 L}{\pi\varepsilon_0 c^4 n_{\omega,i} n_{2\omega,j}} h(\alpha,\beta), \quad (4)$$

where d_{ij} is the effective nonlinear coefficient of the material with $i(j)$ the polarization of the fundamental (SH) wave, $n_{\omega(2\omega),i(j)}$ the corresponding refractive indices of the material, L the nonlinear material length, ε_0 the vacuum permittivity and c the speed of light in vacuum. The function $h(\alpha,\beta)$ is given as

$$h(\alpha,\beta) = \frac{1}{4\alpha}\left|\int_{-\alpha}^{\alpha} \frac{e^{i\beta(T)\tau}}{1+i\tau}\,d\tau\right|^2, \quad (5)$$

with the focusing parameter $\alpha = L/2z_R$, where z_R is the Gaussian beam Rayleigh length assumed here equal for both waves, yielding a smaller waist for the SH light. The phase-matching parameter

$$\beta = \frac{4\pi z_R}{\lambda}\left(n_{\omega,i}(T) - n_{2\omega,j}(T)\right) \quad (6)$$

is temperature and polarization dependent in the case of birefringent media. The derivation assumes no depletion of the fundamental wave and absence of losses. The integral in (5) needs to be calculated numerically except for limiting cases, yielding a global maximum of $h_{max}(2.84, 0.573) = 1.068$. Putting in values for the usual nonlinear media, this

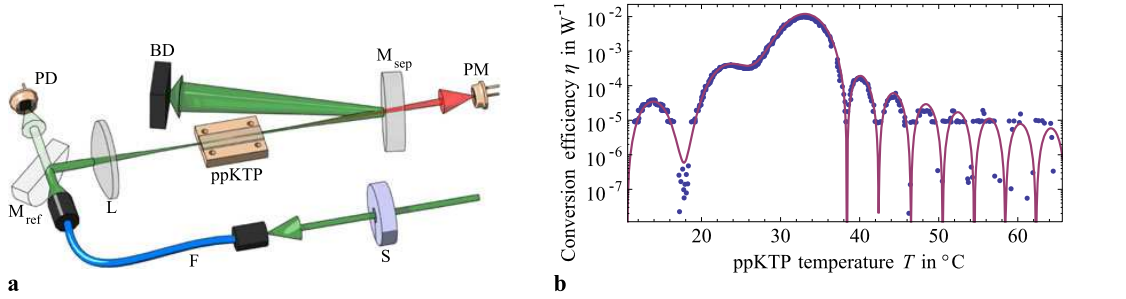

Fig. 3 (**a**) Setup of the single-pass efficiency measurements. The IR laser output (*depicted in green*) is mode cleaned by a polarization-maintaining SM fiber (*F*). The power leaking through mirror M_{ref} is referenced on a photodiode (*PD*), and the beam is then focused into the ppKTP crystal by a lens (*L*). Mirror M_{sep} separates SH (*red*) from fundamental light, which is sent into a beam dump (*BD*), whereas the converted light power is measured with a power meter (*PM*). For referencing to the dark-current values, a shutter periodically switches on and off the IR light. (**b**) Temperature-dependent single-pass doubling efficiency. Measured data (*circles*), fit to (5) (*solid line*)

results in a doubling efficiency η in the %/W range at best. Thus, for the available cw laser power, single-pass doubling is not an option and one has to resort to resonantly enhanced intra-cavity doubling.

Quasi-phase matching in periodically poled materials is favorable in the intra-cavity case because of the excellent beam quality achievable without beam walk-off [29, 30]. The accessibility of the much greater diagonal elements d_{ii} of the nonlinear tensor allows for higher single-pass efficiencies (4) while keeping the phase-matching condition of optimum β. Compared to the bulk case, the same equations (3)–(6) hold, by performing the following replacements: $\beta \to \beta - 2\pi z_{\text{R}}/\Lambda$, where Λ is the poling period and $d_{ij} \to d_{\text{eff}} = 2d_{ii}/\pi$. As a nonlinear medium, periodically poled potassium titanyl phosphate (ppKTP) was chosen because of its high transparency from 350 to 4300 nm, its high nonlinear coefficient $d_{33} = 16.9$ pm/V [31] and its high damage threshold.

3.2 Single-pass measurements

We first describe the characterization of the nonlinear crystal using a single-pass method. The completely automatized measurement setup is represented in Fig. 3. The spatial mode-cleaning fiber output power was ≃500 mW, resulting in a maximum of $P_{2\omega} \simeq 2$ mW of red light output, the two beams being separated using mirror M_{sep}. The fundamental power was monitored using a Ge photodiode (PD) exploiting the finite transmission through mirror M_{ref}. The signal was calibrated against the IR power P_ω hitting the crystal. The finite transmittance of M_{ref} at 671 nm was taken care of, and the SH power measured using a commercial power meter (Thorlabs S130A). The response of the power meter's Si photodiode at 1342 nm is negligible, and so is the corresponding transmission of M_{sep}. The shutter, driven at 1 Hz with a 50% duty cycle, allowed for the determination of dark-current offset drifts for both power measurements, which is of highest importance for low conversion efficiencies. The crystal is mounted on a transverse (xy) translation stage and temperature controlled to ∼10 mK using a Peltier element and a home-made temperature controller. A set temperature ramp was applied to the controller, scanning the full 55°C range in about 30 min. The slow ramp allowed for adiabatic behavior of the temperature measurement, permitting independent determination of the temperature of the crystal measured by a LM35 sensor attached to the crystal mount.

The ppKTP crystal used in the experiments was fabricated in-house at the Royal Institute of Technology by electric field poling at room temperature [32]. Its length is 19.2 mm, featuring an optical aperture of 6×1 mm^2. The length of the periodically poled region is 17.25 mm. The poling period was chosen to be $\Lambda = 17.61$ µm, resulting in expected plane-wave phase matching at 23.5°C using the temperature-dependent Sellmeier equations from [33, 34]. Both surfaces are AR coated at 1342 nm and 671 nm.

Experimental results are presented in Fig. 3. A weighted numerical fit to (4) well describes the measured data. The temperature dependence of the phase-matching parameter β was taken into account up to quadratic order. The full 99% width of the peak of 0.7°C allows the use of standard temperature controllers. However, the optimum phase-matching temperature of 33.2°C differs from the theoretical value. This can be explained by a small difference to the Sellmeier equations as presented in [34] and a non-perfect alignment between pump beam and crystal axis. The maximum measured single-pass efficiency of 1.13%/W represents 74% of the theoretical maximum of 1.53%/W from formula (4) with the parameters α as fitted and d_{33} for KTP from [31]. This can be explained by imperfections of the domain grating, most probably deviations from the 50% duty cycle. We thus derive an effec-

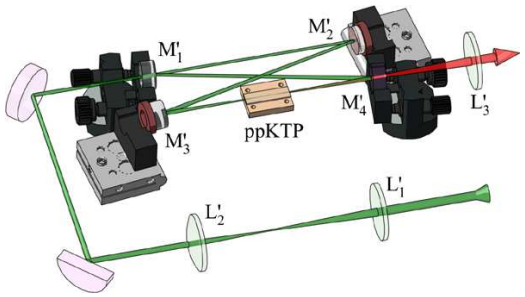

Fig. 4 The doubling cavity setup consisting of the four mirrors $M'_{1\text{–}4}$ and the *ppKTP* nonlinear crystal. The light is coupled to the cavity eigenmode using lenses $L'_{1,2}$, whereas L'_3 collimates the SH output. Some mechanical components are sectioned to improve visibility of the laser (SH) beam, depicted in *green* (*red*). The distance M'_3–M'_4 is 95 mm, the dimensions of the coupling light paths are not to scale

tive nonlinear coefficient of $d_{\text{eff}} = 9.2$ pm/V for our crystal.

3.3 Doubling cavity

The doubling cavity setup is similar to the one presented in [35] and depicted in Fig. 4. As for the laser, a four-mirror folded ring cavity is used, building up a powerful traveling fundamental wave. The pump light is coupled through the plane mirror M'_1 for which several reflectivity values $\mathcal{R}_c$ are available to account for impedance matching. All other mirrors are highly reflective at 1342 nm and transmitting at 671 nm. M'_3 and M'_4 are concave with a radius of curvature of 75 mm. M'_2 (M'_3) was glued on the same type of fast (slow) PZT as used in the laser cavity (Sect. 2.1), allowing it to act on the cavity length in the 50 nm (2 µm) range. The nonlinear crystal is inserted in the cavity's smaller waist of $w_0 \simeq 55$ µm. The weaker-than-optimal focusing leads to a slightly reduced $h(\alpha = 1.22, 0.818) = 0.865$, or a fraction $h/h_{\max} = 81\%$ of the optimum value, yielding $\eta = 0.92\%/\text{W}$. This choice represents a trade-off between maximum single-pass doubling efficiency and intensity-related detrimental effects such as nonlinear and SH-induced absorption [36] and gray tracking [37]. The cavity length was minimized and the geometry chosen to be shifted with respect to the stability range center. It also avoids frequency degeneracy of higher-order transverse cavity eigenmodes and the TEM_{00} mode. It also accounts for a circular beam in the crystal and thus for a circular SH output. Mode matching between the laser output and the cavity was accomplished using a set of spherical lenses. The crystal mount is identical to the one described in Sect. 3.2. The frequency-doubled light is transmitted through M'_4 and collimated using a $f'_3 = 150$ mm lens to a $1/e^2$ beam radius of 0.9 mm. The doubling cavity is kept in a housing equaling the laser housing in design and function.

Table 2 Passive losses in the doubling cavity measured from cavity transmission spectra at low power and conversion efficiency. $1 - \mathcal{R}_c$ is the specified coupler power transmission, $\mathcal{L}_{\text{emp}}$ are the measured empty-cavity round-trip power losses, $\mathcal{L}_{\text{tot}}$ are losses including the ppKTP crystal and $\mathcal{L}_c$ are the inferred crystal insertion losses according to $\mathcal{L}_c = 1 - (1 - \mathcal{L}_{\text{tot}})/(1 - \mathcal{L}_{\text{emp}})$

$1 - \mathcal{R}_c$	$\mathcal{L}_{\text{emp}}$	$\mathcal{L}_{\text{tot}}$	$\mathcal{L}_c$
5%	6.4%	7.1%	0.7%
10%	10.4%	11.2%	0.9%
17%	17.9%	19.0%	1.3%

For low intra-cavity powers of up to ∼500 mW and the crystal temperature tuned far from the optimum phase-matching value, nonlinear conversion can be neglected. While scanning the cavity length by ΔL, one measures a power signal leaking through M'_2, proportional to the intra-cavity power

$$P(\delta L) = \sum_{lm} \frac{P_{lm}}{1 + F \sin^2(\varphi_{lm} + \omega \Delta L / c)}, \tag{7}$$

where F is a fit parameter. P_{lm} are the contributions from the TEM_{lm} modes, displaying a constant cavity round-trip phase of φ_{lm}, and c is the speed of light in vacuum. The mode-matching efficiency is defined as $\eta_{\text{mo}} = P_{00} / \sum P_{lm}$. It was maximized to $\eta_{\text{mo}} = 92\%$. The linear cavity round-trip losses $\mathcal{L}_{\text{emp/tot}}$ can be quantified from the fit parameter F, where emp (tot) means the empty cavity (cavity including ppKTP crystal). The results are presented in Table 2. Inserting the crystal raises the losses by $\mathcal{L}_c \simeq 1\%$. This can be accounted for by residual absorption and scattering in the ppKTP crystal and imperfections of its AR coatings. Taking into account nonlinear conversion, the fundamental mode intra-cavity power $P_{00} = P_\omega$ at TEM_{00} resonance (referred to as cavity resonance) is a solution of

$$P_\omega = \frac{(1 - \mathcal{R}_c - \mathcal{L}_1)\eta_c P_p}{(1 - \sqrt{\mathcal{R}_c (1 - \mathcal{L}_{\text{pa}})(1 - \eta P_\omega)})^2}, \tag{8}$$

which can be calculated numerically, where P_p is the fundamental pump power, $\mathcal{L}_1$ is the coupling mirror (M'_1) transmission loss and $\mathcal{L}_{\text{pa}}$ is the total cavity passive loss excluding the coupler transmission. The single-pass doubling efficiency η is calculated according to (4) with d_{33} as measured in Sect. 3.2. Setting $\mathcal{L}_{\text{pa}} = \mathcal{L}_c$ and $\mathcal{L}_1 = 0$, the solution of (8) yields a maximum SH power of 710 mW at the maximum available pump power of $P_p = 860$ mW. This is accomplished for an optimized coupling mirror reflectivity of $\mathcal{R}_c = 92\%$, yielding a power conversion efficiency of $\eta_{\text{conv}} = P_{2\omega}/P_p = 84\%$.

After locking the cavity to the laser, as will be described in Sect. 4.1, the SH power $P_{2\omega}$ versus P_ω was measured for $\mathcal{R}_c = 95\%$, see Fig. 5. For low powers, the conversion shows quadratic behavior as stated in (3). A fit yields

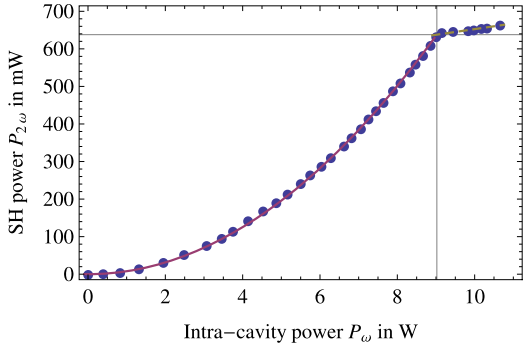

Fig. 5 Intra-cavity conversion for the cavity locked to the laser, as described in Sect. 4.1. Measured data (*circles*) versus parabolic fit (*solid line*). At $P_{2\omega} = 640$ mW, the conversion becomes less efficient (*dashed line*)

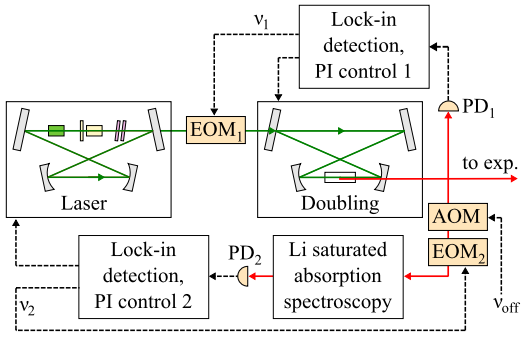

Fig. 6 Locking scheme. Straight lines depict light paths, dashed lines electronic signals. First, the doubling cavity is locked to the free-running laser using control circuit components indexed 1. A part of the SH light is used for lithium spectroscopy. In a second step, this reference serves to lock the laser frequency with respect to half of one of the lithium resonance frequencies with a tunable offset, using control circuit 2. The frequency offset is determined by the double-pass AOM driving frequency ν_{off}

a single-pass efficiency of $\eta = 0.78\%/\mathrm{W}$, slightly lower than predicted. However, starting from the threshold value P_ω ($P_{2\omega}$) = 9.0 W (640 mW), only a slow linear rise in SH power with intra-cavity power is obtained, reaching its maximum at $P_\omega(P_{2\omega}) = 10.7$ W (670 mW). We attribute this behavior to fast intensity-dependent detrimental effects. This is confirmed by the lock error signal, which becomes very noisy above threshold. In contrast to [38, 39], the cavity remains locked for all power levels. When changing the pump power, the SH output follows without observable hysteresis. Long-term degradation is not observed, indicating the absence of gray tracking. However, for further characterization the setup is operated just below threshold to avoid the related rise in intensity noise. A maximum doubling efficiency of $\eta_{\mathrm{conv}} = 86\%$ is obtained just below threshold, compatible with the theoretical predictions.

4 Lock and saturation spectroscopy

Frequency locking of the laser system to the lithium D-line transitions requires frequency-doubled light to perform spectroscopy on atomic lithium vapor. Thus, first the doubling cavity needs to be frequency locked to the free-running laser. In a second step, the laser is stabilized to half the required frequency using lithium saturated absorption phase modulation spectroscopy. The setup is presented in Fig. 6.

4.1 Cavity lock

To frequency lock the doubling cavity to the laser frequency, an error signal needs to be generated. We use a modulation technique: an electro-optical modulator (EOM$_1$ in Fig. 6) phase modulates the infrared pump light at a modulation frequency of $\nu_1 = 1$ MHz. In the doubling process, this results in a phase modulation of the frequency-doubled light, which is detected and demodulated using a home-made synchronous detection circuit. It allows us to produce an error signal with a 3-dB bandwidth of 100 kHz, which is fed into a lock circuit.

The lock circuit combines a proportional-integrating (PI) stage and splits the resulting lock signal into two frequency ranges: 0 Hz to $\nu_{3\ \mathrm{dB,slow}} = 72$ Hz for the slow PZT and 72 Hz to $\nu_{3\ \mathrm{dB,fast}} = 34$ kHz. The amplitude of the slow PZT signal is further amplified by a commercial high-voltage amplifier (Falco Systems WMA-280). The upper-frequency limits were chosen to avoid oscillation of the loop at resonances attributable to the PZTs. When scanning the laser frequency via the slow PZT (M$_4$), the ramp signal (modified by an adjustable gain) is fed forward to the lock signal, thus minimizing lock deviations and stabilizing output power. The implementation of the relocking scheme of Ref. [40] renders the doubling-cavity lock significantly more stable to external disturbances.

4.2 Saturation spectroscopy and laser lock

A small fraction of the frequency-doubled light is sent through a 200-MHz acousto-optic modulator (AOM) double-pass setup to frequency shift the light used for spectroscopy by $2\nu_{\mathrm{mod}}$. It is employed to perform saturated absorption spectroscopy in an atomic lithium vapor cell. The required vapor pressure is obtained by heating a metallic lithium sample of natural isotope composition (8% ^{6}Li, 92% ^{7}Li) to 330°C under vacuum. We use a 50-cm-long CF-40 tube with broadband AR-coated windows. The final sections of the tube are water cooled to prevent too high temperatures at the CF-40 flanges and windows. Nickel gaskets are employed because of their chemical inertness to lithium vapor. A small amount of argon

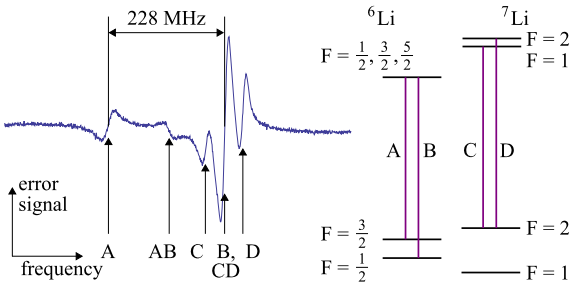

Fig. 7 (**a**) Lock-in saturated absorption spectroscopy of lithium vapor and (**b**) corresponding transitions. The transitions are $2\,^2S_{1/2} \rightarrow 2\,^2P_{3/2}$ for ^{6}Li (D2) and $2\,^2S_{1/2} \rightarrow 2\,^2P_{1/2}$ for ^{7}Li (D1). Not all levels are shown, and the hyperfine structure of the ^{6}Li excited state remains unresolved. Double indexes mark crossover lines

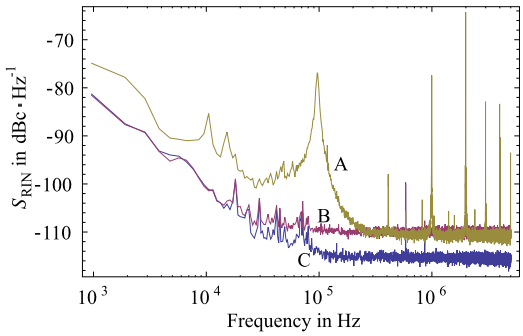

Fig. 8 The SH relative intensity noise spectrum (A), noise for an equivalent photocurrent from a non-coherent source (B) and noise of the detection circuit with no photocurrent (C)

buffer gas is used to force lithium atoms by collision to stick to the side walls before arriving at the window surfaces. The argon pressure is kept low enough to not cause significant collisional broadening of the saturated spectroscopy lines. A metallic mesh put inside the tube covers the tube walls to regain condensed lithium from the colder parts exploiting the temperature-dependent surface tension.

The spectroscopy beam $1/e^2$ radius is $\simeq$1 mm; the pump power is of the order of 10 mW, of which typically 50% is transmitted through the lithium cell on atomic resonance. The beam then passes through a neutral density filter and an EOM$_2$, which serves to phase modulate the light at $\nu_2 = 20$ MHz. A quarter-wave plate and a mirror retro-reflect the beam with a polarization rotated by 90°, thus creating the probe beam of ∼200-μW power. Around 100 μW of probe light is detected on a fast photodiode (Newport 1801). Lock-in detection using a commercial amplifier (Toptica PD110) allows us to generate a dispersive error signal. A typical example of a $\simeq$600-MHz scan over a part of the lithium lines is shown in Fig. 7. The hyperfine structure of both lithium isotopes is clearly resolved and error signals of SNR $\geq$ 100 in a 1-MHz bandwidth are detected. The saturated spectroscopy transmission signal can serve as the auto relock reference. This requires a well-pronounced peak or dip structure, as satisfied for some of the lines.

To lock the laser frequency with respect to one of the resonances, a two-way PI circuit similar to the one used for locking of the doubling cavity is employed. The AOM frequency and thus the lock offset frequency can be changed by a few MHz while the laser remains locked.

5 Laser characterization

We now present further characterizations of the light source in terms of intensity noise and linewidth. The excellent beam quality of the SH light is confirmed by a SM fiber coupling efficiency of 83%.

5.1 Relative intensity noise

The relative intensity noise spectral density $S_{\mathrm{RIN}}(\nu)$ of the SH output was measured by shining a beam of ∼120 μW on a low-noise photodiode (Newport 1801, 125-MHz bandwidth) and recording the signal using a digital oscilloscope (Pico Technology PicoScope 4424) in AC mode, yielding the relative power fluctuations $\varepsilon(t)$ after normalization, where $I(t)/\langle I\rangle_T = 1 + \varepsilon(t)$ with $I(t)$ the intensity and $\langle I\rangle_{\mathrm{T}}$ its temporal average. The definition of $S_{\mathrm{RIN}}(\nu)$ is

$$S_{\mathrm{RIN}}(\nu) = \lim_{t_{\mathrm{m}}\to\infty} \frac{1}{t_{\mathrm{m}}} \left\langle \left| \int_0^{t_{\mathrm{m}}} \varepsilon(t) \mathrm{e}^{\mathrm{i}2\pi\nu t}\, \mathrm{d}t \right|^2 \right\rangle \tag{9}$$

with the measurement time t_{m} and $\langle\cdots\rangle$ denoting temporal averaging. It was realized by employing a time-dis crete Fourier transformation method and averaging over 100 spectra.

The result is shown in Fig. 8. The broad peak at $\simeq$100 kHz can be attributed to the laser relaxation oscillations. The structure in the 10-kHz region can be attributed to the locking system. Above 300 kHz, S_{RIN} drops to the photon shot-noise level, as indicated by the spectrum of a non-coherent source producing an equivalent photocurrent (spectrum B in Fig. 8). The narrow peaks at 1 MHz and harmonics stem from the phase modulation of the pump light, see Sect. 4.1. The square root of the integral of $S_{\mathrm{RIN}}(\nu)$ from 1 kHz to 5 MHz (1 kHz to 0.9 MHz) yields a RMS relative intensity noise of 1.1×10^{-3} (0.8×10^{-3}).

5.2 Absorption spectroscopy of ultra-cold atoms

The laser setup was used as an absorption imaging light source for our lithium quantum gas experiment described elsewhere [41]. A sample of around 1.2×10^5 ^{7}Li atoms

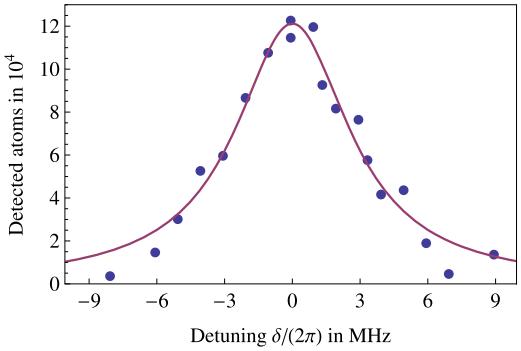

Fig. 9 In-situ absorption imaging of ultra-cold atoms in an optical dipole trap. The laser was detuned by δ from the atomic resonance using the offset lock described in Sect. 4.2, varying the detected atom number (*circles*). A Lorentzian of width $\Gamma_{\mathrm{Fit}} = 2\pi \times (6.1 \pm 0.4)$ MHz is fitted to the data (*solid line*)

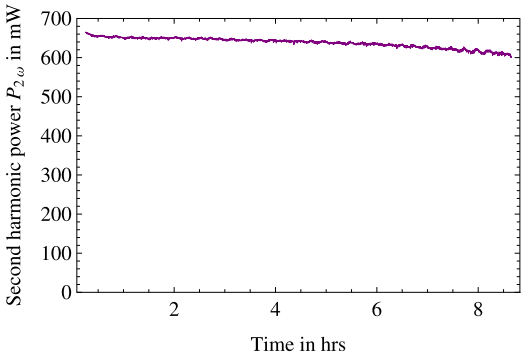

Fig. 10 Long-term stability of the SH output power, experiencing a drop of 7% over the measurement time. The system remained offset locked to the lithium resonance

above Bose–Einstein condensation threshold was prepared in an elongated optical dipole trap. Putting a 700-G magnetic offset field, the internal electronic states of the atoms are to be described in the Paschen–Back regime. The corresponding lift of degeneracy for the $F = 2 \rightarrow F' = 3$ transition frequencies results in a cycling transition, rendering this method insensitive to constant homogeneous stray fields. By applying a laser frequency detuning δ with respect to atomic resonance using the offset lock as described in Sect. 4.2, one detects a different atom number $N(\delta)$ while assuming constant trap conditions according to

$$\frac{N(\delta)}{N(0)} = \left[1 + \left(\frac{2\delta}{\Gamma}\right)^2\right]^{-1}, \tag{10}$$

where Γ is the measured linewidth of the transition and $N(0)$ the atom number detected at resonance.

The results are presented in Fig. 9. A least-squares fit according to (10) results in a linewidth of $\Gamma_{\mathrm{fit}} = 2\pi \times (6.1 \pm 0.4)$ MHz, a value compatible with the natural linewidth of $2\pi \times (5.872 \pm 0.002)$ MHz of [42]. Within our experimental resolution, we infer that the laser linewidth is much smaller than the natural linewidth of the atomic transition. Assuming a Lorentzian line shape for the laser, the linewidth can be given as 200^{+400}_{-200} kHz, compatible with zero.

5.3 Long-term stability

Figure 10 shows a long-term stability plot of the laser system under laboratory conditions. The system remained locked during the measurement time of 8.5 h. The SH output power drops by 7% and shows small modulations of a period of $\simeq$15 min. This is attributable to slight angular tilts when the cavity's slow PZT (M_4/M_3') is driven. This effect, changing the alignments, is confirmed by monitoring the laser output power, which drops by 5% in the same time interval and displays the same modulations.

6 Intra-cavity doubling

We also implemented the more direct approach of intra-cavity doubling a 1342-nm laser. This concept simplifies the optical design since only one cavity is needed. It was achieved by using a setup similar to the one presented in Fig. 1. All cavity mirrors are highly reflective at 1342 nm and mirror M_3 is also transmitting at 671 nm. A nonlinear crystal is put in the waist between mirrors M_3 and M_4.

For the Faraday rotator, we have tried various arrangements, using either gadolinium gallium garnet (GGG) or TGG as the Faraday material and we have used either a rotatory power plate (made either of TeO_2 or of crystalline quartz) or a half-wave plate to compensate the Faraday rotation. Although theory [43] favors the use of a rotatory power plate with respect to a half-wave plate, we have found that the wave plate was more convenient, with a slightly larger output power.

6.1 Infrared power

In a setup involving intra-cavity frequency doubling, it is essential to have very low parasitic losses $\mathcal{L}_{\mathrm{par}}$ [44]. We start by evaluating these losses by measuring the emitted infrared laser power as a function of the output mirror transmission $\mathcal{T}_{\mathrm{oc}}$ for a fixed absorbed pump power $P_{\mathrm{abs}} = 13$ W for which thermal effects in the Nd:YVO_4 crystal remain small. The data is presented in Fig. 11. Accurate values of the transmission coefficient of the various output mirrors have been obtained with an absolute uncertainty near 0.03% by measuring successively the direct and transmitted powers of a laser beam in an auxiliary experiment. According to [21, 45–48], the output power P_{out} is given by

$$P_{\mathrm{out}} = P_{\mathrm{sat}}\mathcal{T}_{\mathrm{oc}}\left[\frac{G_0}{\mathcal{T}_{\mathrm{oc}} + \mathcal{L}_{\mathrm{par}}} - 1\right], \tag{11}$$

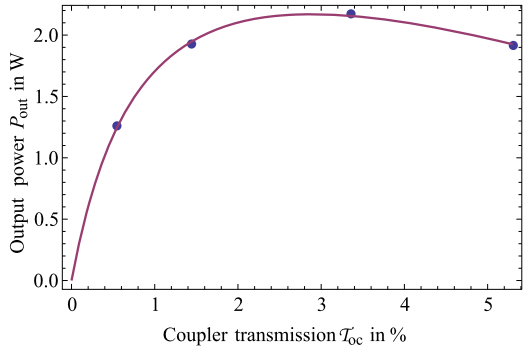

Fig. 11 Output power P_{out} of the laser emitting at 1342 nm as a function of the mirror transmission $\mathcal{T}_{oc}$. The data points are experimental while the curve is the best fit using (11)

where P_{sat} is the gain medium saturation power and G_0 the laser gain. We performed a nonlinear curve fit yielding $\mathcal{L}_{par} = (0.0101 \pm 0.0006)$, $P_{sat} = (26.3 \pm 2.0)$ W and $G_0 = (0.150 \pm 0.006)$. The measured losses $\mathcal{L}_{par}$ of ∼1% are in accordance with expectations for a cavity made of four mirrors (three high-reflection mirrors plus the output mirror), three AR-coated crystals and a Brewster plate. In Appendix, we relate the values measured for P_{sat} and G_0 to the parameters of the lasing crystal and the laser cavity. We find good agreement with literature values.

6.2 Doubling and frequency behavior

Several Nd:YVO_4 lasers emitting at 671 nm have been built based on intra-cavity frequency doubling using a LBO (lithium triborate, LiB_3O_5) crystal [6–14]. The largest achieved power was 5.5 W but none of these lasers have run in SLM operation. We have tried frequency doubling with both LBO and BIBO (bismuth triborate, BiB_3O_6) crystals installed in the small waist of the laser cavity (see Fig. 1). The BIBO crystal gave slightly more power but with a substantially more astigmatic laser mode. Therefore, we used a LBO crystal of 15-mm length and 3×3 mm^2 cross section. We apply type I SH generation, with critical phase matching at $\theta = 86.1°$ and $\phi = 0°$. The crystal is AR coated with a specified residual reflection equal to 0.15% at 1342 nm and 0.5% at 671 nm.

The nonlinear optical coefficient of LBO is $d_{eff} = 0.817$ pm V^{-1}. Using the expressions given in Ref. [49] and the SNLO software [50] to evaluate the crystal properties, we have calculated the expected optimum conversion coefficient η for this crystal.

We get $\eta = 7.3 \times 10^{-5}$ W^{-1} with an optimum waist in the crystal equal to $w_0 = 29$ µm. We use a slightly larger laser waist of ≃45 µm, for which theory predicts $\eta = 4.9 \times 10^{-5}$ W^{-1}. We have measured η by running the laser with a weakly IR-transmitting mirror M_2, with a coupling transmission value $\mathcal{T}_{oc} = (0.55 \pm 0.03)$%, and by measuring simultaneously the emitted power at both 1342 nm and 671 nm. We have found $\eta = (4.7 \pm 0.5) \times 10^{-5}$ W^{-1}, in excellent agreement with the theoretical value.

Finally, by replacing the IR-transmitting mirror M_2 by a highly reflective one, we have extracted the SH output through mirror M_3, which has a transmission near 95% at 671 nm. When the laser operates at the peak of its gain curve, corresponding to a visible emission near 671.1 nm, we get up to 1 W of SH light. At the lithium resonance wavelength 670.8 nm and with an intra-cavity 500-µm-thick etalon made of fused silica and with a reflectivity of $\mathcal{R} \simeq 30\%$, the current output power reaches ∼600 mW. Progress towards frequency stabilization as described in Sect. 4.2 is ongoing. With this simpler optical system, we expect performances comparable to those obtained with external cavity frequency doubling presented in Sect. 3.3.

7 Conclusion

We have presented a frequency-stabilized laser source to address the D-line transitions in atomic lithium. Up to 670 mW of single-mode output power has been generated, currently limited by intensity-dependent effects in the doubling crystal. Tunability, narrow-band spectral quality and stable long-term locked operation were demonstrated. This proves the suitability of the system as a laser source for experiments involving cooling and trapping of lithium species. We also presented first results of a simpler alternative setup featuring intra-cavity doubling. Higher output powers could be achieved by optimizing the doubling cavity design for less intensity in the ppKTP crystal by enlarging the waist or using less thermally sensitive doubling nonlinear materials. Further increase of the laser power at 1342 nm is feasible using a pump source at 888 nm [25], reducing the quantum defect and thus the detrimental thermal effects.

Acknowledgements We would like to thank Y. Louyer, P. Juncar and F. Balembois for their help in starting this development, J.L. Doualan, R. Moncorgé and P. Camy for a new measurement of the stimulated cross section of Nd:YVO_4, E. Mimoun for providing his design of the lock circuitry, N. Navon for his help in conducting the linewidth measurements, F. Lenhardt, P. Zimmermann and J.J. Zondy for fruitful discussions and R. Stein and A. Grier for careful reading of the manuscript. The LKB team acknowledges financial support from ERC (FerLoDim project), EuroQUAM (FerMix), IFRAF, IUF, ESF, ANR, SCALA and DARPA (OLE project) and the LCAR team acknowledges financial support from CNRS INP, BNM (grant 04-3-004), ANR (grant ANR-05-BLAN-0094) and Région Midi-Pyrénées.

Appendix: Additional material

The theoretical values of P_{sat} and G_0 are given by

$$G_0 = \eta_{\mathrm{Q}}\eta_0 \frac{\lambda_{\mathrm{p}}}{\lambda_{\mathrm{l}}} \times \frac{P_{\mathrm{abs}}}{P_{\mathrm{sat}}}, \tag{12}$$

$$P_{\mathrm{sat}} = \eta_0 I_{\mathrm{sat}} \frac{V_{\mathrm{eff}}}{L_{\mathrm{med}}}, \tag{13}$$

where η_0 is the overlap efficiency of the pump and laser cavity mode in the gain medium, η_{Q} the quantum efficiency of emission, V_{eff} the gain medium effective volume and L_{med} its length, λ_{p} and λ_{l} the pump and laser wavelengths, respectively, and P_{p} the pump laser power. In [21, 45–48] the length L_{med} is multiplied by 2 because the calculation concerns standing-wave cavities and this factor is suppressed in the case of a ring cavity. Chen et al. [47] give the general expressions of $V_{\mathrm{eff}}/L_{\mathrm{med}}$ and of η_0 as a function of the laser mode waist w_{l} and pump mode waist w_{p}.

In our experiment, the pump mode is obtained by expanding the mode emitted by a 200-µm-diameter optical fiber of NA = 0.22 by a factor of 5. After expansion, the pump mode divergence is small and it is a reasonably good approximation to assume that the pump mode waist is constant over the crystal volume. We get

$$\eta_0 = \frac{w_{\mathrm{l}}^2(w_{\mathrm{l}}^2 + 2w_{\mathrm{p}}^2)}{(w_{\mathrm{l}}^2 + w_{\mathrm{p}}^2)^2} = 0.63, \tag{14}$$

$$\frac{V_{\mathrm{eff}}}{L_{\mathrm{med}}} = \frac{\pi}{2}\left(w_{\mathrm{l}}^2 + 2w_{\mathrm{p}}^2\right) = 6.4 \times 10^{-3}\ \mathrm{cm}^2, \tag{15}$$

where we have used for the laser mode waist the value $w_{\mathrm{l}} = 400$ µm calculated at the position of the Nd:YVO_4 crystal. This calculation assumes that the thermal focal length of this crystal is 100 mm but the mode parameters are not very sensitive to this focal length, because its position is close to the large waist of the laser cavity. The pump mode waist $w_{\mathrm{p}} = 500$ µm is deduced from the fiber diameter and the expansion ratio.

By combining G_0 and P_{sat}, we get $\eta_0 = 0.50 \pm 0.06$, reasonably close to our theoretical value. To get the value of $V_{\mathrm{eff}}/L_{\mathrm{med}}$, we need to know the saturation intensity $I_{\mathrm{sat}} = h\nu_{\mathrm{l}}/\sigma\tau_{\mathrm{e}}$, where σ is the stimulated emission cross section, τ_{e} the excited-state lifetime and $\nu_{\mathrm{l}} = c/\lambda_{\mathrm{l}}$. The maximum value of σ for stimulated emission near $\lambda_{\mathrm{l}} = 1342$ nm is $\sigma = 17 \times 10^{-20}$ cm^2: this value was measured with a spectral resolution near 2.5 nm [18] and the same value has been found in an unpublished study [19]. The excited-state lifetime increases when the neodymium-ion concentration decreases [20, 51]. We have used the largest literature value $\tau_{\mathrm{e}} = 1.1 \times 10^{-4}$ s corresponding to a 0.4% Nd concentration. We thus get $I_{\mathrm{sat}} = 7.9 \pm 0.8$ kW/cm^2, with an estimated 10% error bar. The quantum yield η_{Q} depends on the neodymium-ion concentration [52] and practically $\eta_{\mathrm{Q}} = 1$ for 0.2 at.%-doped crystals. By combining our measured values of G_0 and P_{sat}, we deduce $V_{\mathrm{eff}}/L_{\mathrm{med}} = (6.6 \pm 0.9) \times 10^{-3}$ cm^2, in good agreement with (15). This gives confidence in our determination of the 1% loss of our cavity without second-harmonic generation.

References

1. C. Chin, R. Grimm, P. Julienne, E. Tiesinga, Rev. Mod. Phys. **82**, 1225 (2010)
2. J.T.F. Johnston, R.H. Brady, W. Proffitt, Appl. Opt. **21**, 2307 (1982)
3. A. Miffre, M. Jacquey, M. Büchner, G. Trénec, J. Vigué, Phys. Scr. **74**, C15 (2006)
4. S.A. Payne, L.K. Smith, R.J. Beach, B.H.T. Chai, J.H. Tassano, L.D. DeLoach, W.L. Kway, R.W. Solarz, W.F. Krupke, Appl. Opt. **33**, 5526 (1994)
5. I.E. Olivares, A.E. Duarte, E.A. Saravia, F.J. Duarte, Appl. Opt. **41**, 2973 (2002)
6. A. Agnesi, A. Guandalini, G. Reali, J. Opt. Soc. Am. B **19**, 1078 (2002)
7. A. Agnesi, A. Guandalini, G. Reali, S. Dell'Acqua, G. Piccinno, Opt. Lett. **29**, 56 (2004)
8. Y.-F. Lü, X.-H. Zhang, J. Xia, X.-D. Yin, A.-F. Zhang, L. Bao, W. Lü, Opt. Laser Technol. **42**, 522 (2010)
9. H. Ogilvy, M. Withford, P. Dekker, J. Piper, Opt. Express **11**, 2411 (2003)
10. A.-Y. Yao, W. Hou, X.-C. Lin, Y. Bi, R.-N. Li, D.-F. Cui, Z.-Y. Xu, Opt. Commun. **231**, 413 (2004)
11. A.-Y. Yao, W. Hou, Y. Bi, A.-C. Geng, X.-C. Lin, Y.-P. Kong, D.-F. Cui, L.-A. Wu, Z.-Y. Xu, Appl. Opt. **44**, 7156 (2005)
12. L. Zhang, C. Li, D. Li, P. Li, Q. Zhang, Z. Zhang, Opt. Laser Technol. **37**, 524 (2005)
13. Q. Zheng, H. Tan, L. Zhao, L. Qian, Opt. Laser Technol. **34**, 329 (2002)
14. Q. Zheng, J.-Y. Wang, L. Zhao, Opt. Laser Technol. **36**, 485 (2004)
15. F. Lenhardt, A. Nebel, R. Knappe, M. Nittmann, J. Bartschke, J.A. L'huillier, in *Conf. Lasers and Electro-Optics* (Optical Society of America, San Jose, 2010), p. CThEE5
16. R. Sarrouf, V. Sousa, T. Badr, G. Xu, J.-J. Zondy, Opt. Lett. **32**, 2732 (2007)
17. A.E. Siegman, *Lasers* (University Science Books, Mill Valley, 1986)
18. L. Fornasiero, S. Kück, T. Jensen, G. Huber, B. Chai, Appl. Phys. B, Lasers Opt. **67**, 549 (1998)
19. J. Doualan, P. Camy, R. Moncorgé, private communication (unpublished)
20. M. Okida, M. Itoh, T. Yatagai, H. Ogilvy, J. Piper, T. Omatsu, Opt. Express **13**, 4909 (2005)
21. Y.F. Chen, T.M. Huang, C.F. Kao, C.L. Wang, S.C. Wang, IEEE J. Quantum Electron. **33**, 1424 (1997)
22. G. Trénec, W. Volondat, O. Cugat, J. Vigué, Appl. Opt. **50**, 4788 (2011)
23. R. Sarrouf, T. Badr, J.J. Zondy, J. Opt. A, Pure Appl. Opt. **10**, 104011 (2008)
24. W. Leeb, Appl. Phys. A, Mater. Sci. Process. **6**, 267 (1975)
25. L. McDonagh, R. Wallenstein, R. Knappe, A. Nebel, Opt. Lett. **31**, 3297 (2006)
26. F. Song, C. Zhang, X. Ding, J. Xu, G. Zhang, M. Leigh, N. Peyghambarian, Appl. Phys. Lett. **81**, 2145 (2002)

27. D.B. Leviton, B.J. Frey, T.J. Madison, Proc. SPIE **6692**, 669204 (2007)
28. G.D. Boyd, D.A. Kleinman, J. Appl. Phys. **39**, 3597 (1968)
29. L.E. Myers, R.C. Eckardt, M.M. Fejer, R.L. Byer, W.R. Bosenberg, J.W. Pierce, J. Opt. Soc. Am. B **12**, 2102 (1995)
30. R. Boyd, *Nonlinear Optics* (Academic Press, San Diego, 2003)
31. M. Peltz, U. Bäder, A. Borsutzky, R. Wallenstein, J. Hellström, H. Karlsson, V. Pasiskevicius, F. Laurell, Appl. Phys. B, Lasers Opt. **73**, 663 (2001)
32. C. Canalias, S. Wang, V. Pasiskevicius, F. Laurell, Appl. Phys. Lett. **88**, 032905 (2006)
33. K. Fradkin, A. Arie, A. Skliar, G. Rosenman, Appl. Phys. Lett. **74**, 914 (1999)
34. S. Emanueli, A. Arie, Appl. Opt. **42**, 6661 (2003)
35. E. Mimoun, L.D. Sarlo, J.-J. Zondy, J. Dalibard, F. Gerbier, Opt. Express **16**, 18684 (2008)
36. V.A. Maslov, V.A. Mikhailov, O.P. Shaunin, I.A. Shcherbakov, Quantum Electron. **27**, 356 (1997)
37. B. Boulanger, I. Rousseau, J.P. Feve, M. Maglione, B. Menaert, G. Marnier, IEEE J. Quantum Electron. **35**, 281 (1999)
38. F. Torabi-Goudarzi, E. Riis, Opt. Commun. **227**, 389 (2003)
39. A. Arie, G. Rosenman, A. Korenfeld, A. Skliar, M. Oron, M. Katz, D. Eger, Opt. Lett. **23**, 28 (1998)
40. E. Mimoun, L. De Sarlo, J.-J. Zondy, J. Dalibard, F. Gerbier, Appl. Phys. B, Lasers Opt. **99**, 31 (2010)
41. S. Nascimbène, N. Navon, K.J. Jiang, L. Tarruell, M. Teichmann, J. McKeever, F. Chevy, C. Salomon, Phys. Rev. Lett. **103**, 170402 (2009)
42. W.I. McAlexander, E.R.I. Abraham, R.G. Hulet, Phys. Rev. A **54**, R5 (1996)
43. F. Biraben, Opt. Commun. **29**, 353 (1979)
44. R. Smith, IEEE J. Quantum Electron. **6**, 215 (1970)
45. W.W. Rigrod, J. Appl. Phys. **36**, 2487 (1965)
46. P. Laporta, M. Brussard, IEEE J. Quantum Electron. **27**, 2319 (1991)
47. Y.F. Chen, T.S. Liao, C.F. Kao, T.M. Huang, K.H. Lin, S.C. Wang, IEEE J. Quantum Electron. **32**, 2010 (1996)
48. Y.F. Chen, L.J. Lee, T.M. Huang, C.L. Wang, Opt. Commun. **163**, 198 (1999)
49. F.J. Kontur, I. Dajani, Y. Lu, R.J. Knize, Opt. Express **15**, 12882 (2007)
50. SNLO software (2011), http://www.as-photonics.com/SNLO.html
51. A.W. Tucker, M. Birnbaum, C.L. Fincher, J.W. Erler, J. Appl. Phys. **48**, 4907 (1977)
52. Y.-F. Chen, IEEE J. Quantum Electron. **35**, 234 (1999)

Bibliography

[1] F. Lenhardt, M. Nittmann, T. Bauer, J. Bartschke, and JA L'huillier. High-power 888-nm-pumped Nd:YVO_4 1342-nm oscillator operating in the TEM_{00} mode. *Applied Physics B*, 96(4):803–807, 2009. 8, 34, 94

[2] Peter Pringsheim. Zwei Bemerkungen über den Unterschied von Lumineszenz- und Temperaturstrahlung. *Zeitschrift für Physik A Hadrons and Nuclei*, 57:739–746, 1929. 10.1007/BF01340652. 11

[3] T.H. Maiman. Stimulated optical radiation in ruby. *Nature*, 187:493 – 494, 1960. 11, 15

[4] A. Ashkin. Acceleration and trapping of particles by radiation pressure. *Phys. Rev. Lett.*, 24(4):156–159, 1970. 11

[5] T.W. Hänsch and A.L. Schawlow. Cooling of gases by laser radiation. *Optics Communications*, 13(1):68 – 69, 1975. 11

[6] F. Diedrich, J. C. Bergquist, Wayne M. Itano, and D. J. Wineland. Laser Cooling to the Zero-Point Energy of Motion. *Phys. Rev. Lett.*, 62:403–406, Jan 1989. 11

[7] J. Dalibard and C. Cohen-Tannoudji. Laser cooling below the Doppler limit by polarization gradients: simple theoretical models. *J. Opt. Soc. Am. B*, 6(11):2023–2045, Nov 1989. 11

[8] C. Salomon, J. Dalibard, W. D. Phillips, A. Clairon, and S. Guellati. Laser Cooling of Cesium Atoms Below 3 μK. *EPL (Europhysics Letters)*, 12(8):683, 1990. 11

[9] W. Ketterle, D. S. Durfee, and D. M. Stamper-Kurn. Making, probing and understanding Bose-Einstein condensates. In M. Inguscio, S. Stringari, and C. Wieman, editors, *Bose-Einstein condensation in atomic gases, Proceedings of the International School of Physics Enrico Fermi, Course CXL, Varenna, 7-17 July 1998*, pages 67–176. IOS Press, Amsterdam, 1999. 11

[10] A. Einstein. Zur Quantentheorie der Strahlung. *Physikalische Gesellschaft Zürich*, 18:47–62, 1916. 15

[11] JP Gordon, HJ Zeiger, and CH Townes. Molecular Microwave Oscillator and New Hyperfine Structure in the Microwave Spectrum of NH_ {3}. *Physical Review*, 95(1):282, 1954. 15

[12] G. Basov and N.A.M. Prokhorov. Applications of molecular beams in radiospectroscopic study of rotational spectra of molecules. *Zh. Eksper. Teor. Fiz.*, 27:431, 1954. 15

[13] P. A. Franken, A. E. Hill, C. W. Peters, and G. Weinreich. Generation of Optical Harmonics. *Phys. Rev. Lett.*, 7:118–119, Aug 1961. 15

[14] J. A. Giordmaine and Robert C. Miller. Tunable Coherent Parametric Oscillation in $LiNbO_3$ at Optical Frequencies. *Phys. Rev. Lett.*, 14:973–976, Jun 1965. 15

[15] Malcolm H. Dunn and Majid Ebrahimzadeh. Parametric Generation of Tunable Light from Continuous-Wave to Femtosecond Pulses. *Science*, 286(5444):1513–1517, 1999. 16

[16] Ulrich Eismann. Aufbau einer zweidimensionalen magnetooptischen Falle als hochintensive Quelle ultrakalter Rubidiumatome. Master's thesis, Humboldt-Universität zu Berlin, 2007. 16

[17] Cheng Chin, Rudolf Grimm, Paul Julienne, and Eite Tiesinga. Feshbach resonances in ultracold gases. *Rev. Mod. Phys.*, 82(2):1225–1286, Apr 2010. 18, 99, 106

[18] O. Carnal and J. Mlynek. Young's double-slit experiment with atoms: A simple atom interferometer. *Phys. Rev. Lett.*, 66(21):2689–2692, May 1991. 18

[19] David W. Keith, Christopher R. Ekstrom, Quentin A. Turchette, and David E. Pritchard. An interferometer for atoms. *Phys. Rev. Lett.*, 66(21):2693–2696, May 1991.

[20] Ch.J. Bordé. Atomic interferometry with internal state labelling. *Physics Letters A*, 140(1-2):10 – 12, 1989.

[21] F. Riehle, Th. Kisters, A. Witte, J. Helmcke, and Ch. J. Bordé. Optical Ramsey spectroscopy in a rotating frame: Sagnac effect in a matter-wave interferometer. *Phys. Rev. Lett.*, 67(2):177–180, Jul 1991. 18

[22] J. B. Fixler, G. T. Foster, J. M. McGuirk, and M. A. Kasevich. Atom Interferometer Measurement of the Newtonian Constant of Gravity. *Science*, 315(5808):74–77, 2007. 18

[23] G. Lamporesi, A. Bertoldi, L. Cacciapuoti, M. Prevedelli, and G. M. Tino. Determination of the Newtonian Gravitational Constant Using Atom Interferometry. *Phys. Rev. Lett.*, 100(5):050801, Feb 2008. 18

[24] S. Gupta, K. Dieckmann, Z. Hadzibabic, and D. E. Pritchard. Contrast Interferometry using Bose-Einstein Condensates to Measure h/m and α. *Phys. Rev. Lett.*, 89(14):140401, Sep 2002. 18

[25] Malo Cadoret, Estefania de Mirandes, Pierre Cladé, Saïda Guellati-Khélifa, Catherine Schwob, François Nez, Lucile Julien, and François Biraben. Combination of Bloch Oscillations with a Ramsey-Bordé Interferometer: New Determination of the Fine Structure Constant. *Phys. Rev. Lett.*, 101(23):230801, Dec 2008. 18

[26] M. Kasevich and S. Chu. Measurement of the gravitational acceleration of an atom with a light-pulse atom interferometer. *Applied Physics B*, 54:321–332, 1992. 10.1007/BF00325375. 18

[27] A Peters, K Y Chung, and S Chu. High-precision gravity measurements using atom interferometry. *Metrologia*, 38(1):25, 2001. 18

[28] M. J. Snadden, J. M. McGuirk, P. Bouyer, K. G. Haritos, and M. A. Kasevich. Measurement of the Earth's Gravity Gradient with an Atom Interferometer-Based Gravity Gradiometer. *Phys. Rev. Lett.*, 81(5):971–974, Aug 1998. 18

[29] Marion Jacquey. *Expériences d interférométrie atomique avec l'atome de lithium.* PhD thesis, Université Paul Sabatier - Toulouse III, 2006. 19

[30] Christopher R. Ekstrom, Jörg Schmiedmayer, Michael S. Chapman, Troy D. Hammond, and David E. Pritchard. Measurement of the electric polarizability of sodium with an atom interferometer. *Phys. Rev. A*, 51(5):3883–3888, May 1995.

[31] Tony D. Roberts, Alexander D. Cronin, Martin V. Tiberg, and David E. Pritchard. Dispersion Compensation for Atom Interferometry. *Phys. Rev. Lett.*, 92(6):060405, Feb 2004. 19

[32] Holger Müller, Sheng-wey Chiow, Quan Long, Sven Herrmann, and Steven Chu. Atom Interferometry with up to 24-Photon-Momentum-Transfer Beam Splitters. *Phys. Rev. Lett.*, 100(18):180405, May 2008. 19

[33] A Miffre, M Jacquey, M Büchner, G Trénec, and J Vigué. Atom interferometry. *Physica Scripta*, 74(2):C15, 2006. 19

[34] A. Miffre, M. Jacquey, M. Büchner, G. Trénec, and J. Vigué. Atom interferometry measurement of the electric polarizability of lithium. *The European Physical Journal D - Atomic, Molecular, Optical and Plasma Physics*, 38:353–365, 2006. 10.1140/epjd/e2006-00015-5.

[35] R. Delhuille, C. Champenois, M. Büchner, L. Jozefowski, C. Rizzo, G. Trénec, and J. Vigué. High-contrast Mach-Zehnder lithium-atom interferometer in the Bragg regime. *Applied Physics B*, 74:489–493, 2002. 10.1007/s003400200840.

[36] M. Jacquey, A. Miffre, M. Büchner, G. Trénec, and J. Vigué. Lithium atom interferometry. *J. Phys. IV France*, 135:9–16, 2006. 19

[37] E. A. Symons. Lithium Isotope Separation: A Review of Possible Techniques. *Separation Science and Technology*, 20:633–651, 1985. 19

[38] P.A. Bokhan, V.V. Buchanov, N.V. Fateev, M.M. Kalugin, M.A. Kazaryan, A.M. Prokhorov, and D.E. Zakrevskii. *Laser isotope separation in atomic vapor*. WILEY-VCH Verlag GmbH & Co. KGaA, 2006. 19

[39] T. Arisawa, Y. Maruyama, Y. Suzuki, and K. Shiba. Lithium isotope separation by laser. *Applied Physics B*, 28:73–76, 1982. 10.1007/BF00693895. 20

[40] Ignacio E. Olivares, Andrés E. Duarte, Eduardo A. Saravia, and Francisco J. Duarte. Lithium Isotope Separation With Tunable Diode Lasers. *Appl. Opt.*, 41(15):2973–2977, May 2002.

[41] M. Saleem, S. Hussain, M.A. Zia, and M.A. Baig. An efficient pathway for Li^6 isotope enrichment. *Applied Physics B*, 87:723–726, 2007. 10.1007/s00340-007-2662-2. 20

[42] Stephen A. Payne, Larry K. Smith, Raymond J. Beach, Bruce H. T. Chai, John H. Tassano, Laura D. DeLoach, Wayne L. Kway, Richard W. Solarz, and William F. Krupke. Properties of Cr:LiSrAlF6 crystals for laser operation. *Appl. Opt.*, 33(24):5526–5536, Aug 1994. 20

[43] Jr. T. F. Johnston, R. H. Brady, and W. Proffitt. Powerful single-frequency ring dye laser spanning the visible spectrum. *Appl. Opt.*, 21(13):2307–2316, Jul 1982. 21

[44] Radiant Dyes GmbH. private communication. 2011. 21

[45] M. Gehm. Properties of Lithium. *Dep. of Physics, DUKE University http://www.phy.duke.edu/research/photon/qoptics/techdocs/pdf/PropertiesOfLi.pdf*, 2003. 21

[46] Matthias Büchner and Jacques Viqué. private communication. 2011. 21

[47] J.K. Chin. *Strongly-interacting fermions in an optical lattice*. PhD thesis, Massachusetts Institute of Technology, 2007. 21

[48] M. Praeger, V. Vuletic, T. Fischer, T.W. Hänsch, and C. Zimmermann. AÂ broad emitter diode laser system for lithium spectroscopy. *Applied Physics B*, 67:163–166, 1998. 10.1007/s003400050488. 22

[49] Gabriele Ferrari, Marc-Oliver Mewes, Florian Schreck, and Christophe Salomon. High-power multiple-frequency narrow-linewidth laser source based on a semiconductor tapered amplifier. *Opt. Lett.*, 24(3):151–153, Feb 1999. 22

[50] A. Ridinger, S. Chaudhuri, T. Salez, U. Eismann, D. Fernandes, K. Magalhães, D. Wilkowski, C. Salomon, and F. Chevy. Large atom number dual-species magneto-optical trap for fermionic ^{6}Li and ^{40}K atoms. *The European Physical Journal D - Atomic, Molecular, Optical and Plasma Physics*, 65:223–242, 2011. 10.1140/epjd/e2011-20069-4. 22, 105

[51] L. Winkelmann, O. Puncken, R. Kluzik, C. Veltkamp, P. Kwee, J. Poeld, C. Bogan, B. Willke, M. Frede, J. Neumann, P. Wessels, and D. Kracht. Injection-locked single-frequency laser with an output power of 220 W. *Applied Physics B*, 102:529–538, 2011. 10.1007/s00340-011-4411-9. 22, 94

[52] L. Cui, H. Zhang, L. Xu, J. Li, Y. Yan, P. Sha, L. Fang, H. Zhang, J. He, and J. Xin. 880 nm laser-diode end-pumped Nd:YVO_4 slab laser at 1342 nm. *Laser Physics*, 21:105–107, 2011. 10.1134/S1054660X11010075. 22

[53] Antonio Agnesi, Annalisa Guandalini, and Giancarlo Reali. Efficient 671 nm pump source by intracavity doubling of a diode-pumped Nd :YVO4 laser. *J. Opt. Soc. Am. B*, 19(5):1078–1082, May 2002. 22

[54] Antonio Agnesi, Annalisa Guandalini, Giancarlo Reali, Stefano Dell'Acqua, and Giuliano Piccinno. High-brightness 2.4-W continuous-wave Nd:GdVO4 laser at 670 nm. *Opt. Lett.*, 29(1):56–58, Jan 2004.

[55] Yan-Fei Lü, Xi-He Zhang, Jing Xia, Xiao-Dong Yin, An-Feng Zhang, Lin Bao, and Wang Lü. High-efficiency direct-pumped Nd:YVO_4-LBO laser operating at 671 nm. *Optics & Laser Technology*, 42(3):522 – 525, 2010.

[56] Hamish Ogilvy, Michael Withford, Peter Dekker, and James Piper. Efficient diode double-end-pumped Nd:YVO4 laser operating at 1342 nm. *Opt. Express*, 11(19):2411–2415, Sep 2003.

[57] Ai-Yun Yao, Wei Hou, Xue-Chun Lin, Yong Bi, Rui-Ning Li, Da-Fu Cui, and Zu-Yan Xu. High power red laser at 671 nm by intracavity-doubled Nd:YVO4 laser using LiB3O5. *Optics Communications*, 231(1-6):413 – 416, 2004.

[58] Ai-Yun Yao, Wei Hou, Yong Bi, Ai-Cong geng, Xue-Chun Lin, Yu-Peng Kong, Da-Fu Cui, Ling-An Wu, and Zu-Yan Xu. High-power cw 671 nm output by intracavity frequency doubling of a double-end-pumped Nd:YVO4 laser. *Appl. Opt.*, 44(33):7156–7160, Nov 2005.

[59] Ling Zhang, Chunyong Li, Dehua Li, Pingxue Li, Qiulin Zhang, and Zhiguo Zhang. Compact diode-pumped Nd:YVO4 intracavity-doubled red laser at 671 nm. *Optics & Laser Technology*, 37(7):524 – 526, 2005.

[60] Quan Zheng, Huiming Tan, Ling Zhao, and Longsheng Qian. Diode-pumped 671 nm laser frequency doubled by CPM LBO. *Optics & Laser Technology*, 34(4):329 – 331, 2002.

[61] Quan Zheng, Jun-Ying Wang, and Ling Zhao. 2.23 W diode-pumped Nd:YVO4/LBO Laser at 671 nm. *Optics & Laser Technology*, 36(6):485 – 487, 2004.

[62] Florian Lenhardt, Achim Nebel, Ralf Knappe, Martin Nittmann, Jürgen Bartschke, and Johannes A. L'huillier. Efficient Single-Pass Second Harmonic Generation of a Continuous Wave Nd:YVO4- Laser at 1342 nm Using MgO:PPLN. In *Conference on Lasers and Electro-Optics*, page CThEE5. Optical Society of America, 2010. 22

[63] Rodolphe Sarrouf, Virginie Sousa, Thomas Badr, Guibao Xu, and Jean-Jacques Zondy. Watt-level single-frequency tunable Nd:YLF/periodically poled KTiOPO4 red laser. *Opt. Lett.*, 32(18):2732–2734, Sep 2007. 22

[64] Hou, F.Y., Yu, L., Jia, X.J., Zheng, Y.H., Xie, C.D., and Peng, K.C. Experimental generation of optical non-classical states of light with 1.34 μm wavelength. *Eur. Phys. J. D*, 62(3):433–437, 2011. 22, 25

[65] F.A. Camargo, T. Zanon-Willette, T. Badr, N.U. Wetter, and J.J. Zondy. Tunable Single-Frequency Nd: $YVO_4BiB/_3$ O_6 Ring Laser at 671 nm. *Quantum Electronics, IEEE Journal of*, 46(5):804–809, 2010. 22

[66] CrystaLaser. Manufacturer's website, 2012. 22, 64

[67] F. Lienhart, S. Boussen, O. Carraz, N. Zahzam, Y. Bidel, and A. Bresson. Compact and robust laser system for rubidium laser cooling based on the frequency doubling of a fiber bench at 1560 nm. *Applied Physics B*, 89:177–180, 2007. 10.1007/s00340-007-2775-7. 22

[68] Thomas J. Kane and Robert L. Byer. Monolithic, unidirectional single-mode Nd:YAG ring laser. *Opt. Lett.*, 10(2):65–67, Feb 1985. 23

[69] Emmanuel Mimoun, Luigi De Sarlo, Jean-Jacques Zondy, Jean Dalibard, and Fabrice Gerbier. Sum-frequency generation of 589 nm light with near-unit efficiency. *Opt. Express*, 16(23):18684–18691, Nov 2008. 23, 68

[70] C.C. Harb, M.B. Gray, H.-A. Bachor, R. Schilling, P. Rottengatter, I. Freitag, and H. Welling. Suppression of the intensity noise in a diode-pumped neodymium:YAG nonplanar ring laser. *Quantum Electronics, IEEE Journal of*, 30(12):2907 –2913, dec 1994. 23

[71] Y. Jeong, J. Sahu, D. Payne, and J. Nilsson. Ytterbium-doped large-core fiber laser with 1.36 kW continuous-wave output power. *Opt. Express*, 12(25):6088–6092, Dec 2004. 24

[72] B. N. Samson, P. A. Tick, and N. F. Borrelli. Efficient neodymium-doped glass-ceramic fiber laser and amplifier. *Opt. Lett.*, 26(3):145–147, Feb 2001. 24

[73] M. Brierley, S. Carter, P. France, and J.E. Pedersen. Amplification in the 1300 nm telecommunications window in a Nd-doped fluoride fibre. *Electronics Letters*, 26(5):329 –330, march 1990.

[74] S. Zemon, B. Pedersen, G. Lambert, W.J. Miniscalco, B.T. Hall, R.C. Folweiler, B.A. Thompson, and L.J. Andrews. Excited-state-absorption cross sections and amplifier modeling in the 1300 nm region for Nd-doped glasses. *Photonics Technology Letters, IEEE*, 4(3):244 –247, mar 1992. 24

[75] V. K. Tikhomirov, K. Driesen, and C. Görller-Walrand. Low-energy robust host heavily doped with Dy3+ for emission at 1.3 to 1.4 μm. *physica status solidi (a)*, 204(3):839–845, 2007. 24

[76] S.F. Carter, D. Szebesta, S.T. Davey, R. Wyatt, M.C. Brierley, and P.W. France. Amplification at 1.3 μm in a Pr^{3+}-doped single-mode fluorozirconate fibre. *Electronics Letters*, 27(8):628 –629, april 1991. 24

[77] Luke R. Taylor, Yan Feng, and Domenico Bonaccini Calia. 50W CW visible laser source at 589nm obtained via frequency doubling of three coherently combined narrow-band Raman fibre amplifiers. *Opt. Express*, 18(8):8540–8555, Apr 2010. 24

[78] I.A. Bufetov and E.M. Dianov. Bi-doped fiber lasers. *Laser Physics Letters*, 6(7):487–504, 2009. 24

[79] Takenobu Suzuki and Yasutake Ohishi. Ultrabroadband near-infrared emission from Bi-doped Li_2O–Al_2O_3–SiO_2 glass. *Applied Physics Letters*, 88(19):191912, 2006.

[80] A. Chamorovskiy, J. Rautiainen, A. Rantamäki, K. M. Golant, and O. G. Okhotnikov. 1.3 μm Raman-bismuth fiber amplifier pumped by semiconductor disk laser. *Opt. Express*, 19(7):6433–6438, Mar 2011. 24

[81] S.V. Firstov, I.A. Bufetov, V.F. Khopin, A.V. Shubin, A.M. Smirnov, L.D. Iskhakova, N.N. Vechkanov, A.N. Guryanov, and E.M. Dianov. 2 W bismuth doped fiber lasers in the wavelength range 1300–1500 nm and variation of Bi-doped fiber parameters with core composition. *Laser Physics Letters*, 6(9):665–670, 2009. 24

[82] Young-Seok Seo and Yasushi Fujimoto. *Frontiers in Guided Wave Optics and Optoelectronics*. InTech, 2010. ISBN: 978-953-7619-82-4. 24

[83] J. Z. Wang, Z. Q. Luo, Z. P. Cai, M. Zhou, C. C. Ye, and H. Y. Xu. Theoretical and Experimental Optimization of O-Band Multiwavelength Mixed-Cascaded Phosphosilicate Raman Fiber Lasers. *Photonics Journal, IEEE*, 3(4):633 –643, aug. 2011. 24

[84] M.H. Dunn and M. Ebrahimzadeh. Parametric generation of tunable light from continuous-wave to femtosecond pulses. *Science*, 286(5444):1513, 1999. 24

[85] E. V. Kovalchuk, T. Schuldt, and A. Peters. Combination of a continuous-wave optical parametric oscillator and a femtosecond frequency comb for optical frequency metrology. *Opt. Lett.*, 30(23):3141–3143, Dec 2005. 25

[86] Fabrice Gerbier and Jean Dalibard. Gauge fields for ultracold atoms in optical superlattices. *New Journal of Physics*, 12(3):033007, 2010. 25

[87] Linos. *Linos Photonics OS 4500 brochure*. Photonics GmbH & Co. KG, 2011. 25

[88] Evgeny Kovalchuk. *Optical parametric oscillators for precision IR spectroscopy and metrology*. PhD thesis, Humboldt-Universität zu Berlin, 2008. 25

[89] Lockheed Martin. *Lockheed Martin Aculight Argos Model 2400 SF Series brochure*. Lockheed Martin, 2009. 25

[90] Ulrich Strössner, Jan-Peter Meyn, Richard Wallenstein, Pavel Urenski, Ady Arie, Gil Rosenman, Jürgen Mlynek, Stephan Schiller, and Achim Peters. Single-frequency continuous-wave optical parametric oscillator system with an ultrawide tuning range of 550 to 2830 nm. *J. Opt. Soc. Am. B*, 19(6):1419–1424, Jun 2002. 25

[91] Sofiane Bahbah, Fabien Bretenaker, and Cyril Drag. Single-frequency quasi-continuous red radiation generated by a green-pumped singly resonant optical parametric oscillator. *Opt. Lett.*, 31(9):1283–1285, May 2006.

[92] Dong-Hoon Lee, Seung Kwan Kim, Seung-Nam Park, Hee Su Park, Jae Yong Lee, and Sang-Kyung Choi. Continuous-wave 532 nm pumped MgO:PPLN optical parametric oscillator with external power regulation and spatial mode filtering. *Appl. Opt.*, 48(1):37–42, Jan 2009.

[93] I.-H. Bae, H. Moon, S. Zaske, C. Becher, S. Kim, S.-N. Park, and D.-H. Lee. Low-threshold singly-resonant continuous-wave optical parametric oscillator based on MgO-doped PPLN. *Applied Physics B*, 103:311–319, 2011. 10.1007/s00340-010-4297-y. 25

[94] Thu-Hien My, Cyril Drag, and Fabien Bretenaker. Single-frequency and tunable operation of a continuous intracavity-frequency-doubled singly resonant optical parametric oscillator. *Opt. Lett.*, 33(13):1455–1457, Jul 2008. 25

[95] U. Eismann, F. Gerbier, C. Canalias, A. Zukauskas, G. Trénec, J. Vigué, F. Chevy, and C. Salomon. An all-solid-state laser source at 671 nm for cold-atom experiments with lithium. *Applied Physics B*, 106:25–36, 2012. 10.1007/s00340-011-4693-y. 27, 42, 55

[96] H. E. Rast, H. H. Caspers, and S. A. Miller. Infrared Spectral Emittance and Optical Properties of Yttrium Vanadate. *Phys. Rev.*, 169(3):705–709, May 1968. 32

[97] Louis McDonagh, Richard Wallenstein, Ralf Knappe, and Achim Nebel. High-efficiency 60 W TEM00 Nd:YVO4 oscillator pumped at 888 nm. *Opt. Lett.*, 31(22):3297–3299, 2006. 32, 34, 94

[98] L. Fornasiero, S. Kück, T. Jensen, G. Huber, and B.H.T. Chai. Excited state absorption and stimulated emission of Nd3+ in crystals. Part 2: YVO4, GdVO4, and Sr5(PO4)3F. *Applied Physics B*, 67:549–553, 1998. 10.1007/s003400050543. 33, 35

[99] J.L. Doualan, P. Camy, and R. Moncorgé. Measurement of the stimulated emission cross section minus excited state absorption cross-section of Nd:YVO_4 crystal. private communication, 2008. 34, 49, 50

[100] CASIX, INC. Manufacturer's website, 2009. 34

[101] Rüdiger Paschotta. Encyclopedia of Laser Physics and Technology, 2009. 34

[102] A. W. Tucker, M. Birnbaum, C. L. Fincher, and J. W. Erler. Stimulated-emission cross section at 1064 and 1342 nm in Nd : YVO_4. *Journal of Applied Physics*, 48(12):4907–4911, 1977. 34

[103] Masahito Okida, Masahide Itoh, Toyohiko Yatagai, Hamish Ogilvy, James Piper, and Takashige Omatsu. Heat generation in Nd doped vanadate crystals with 1.34 μm laser action. *Opt. Express*, 13(13):4909–4915, Jun 2005. 34, 35, 41

[104] A. E. Siegman. *Lasers*. University Science Books, Mill Valley, California, 1986. 35, 36, 37, 45, 46

[105] G.A. Reider. Photonik: Eine Einführung in die Grundlagen. *Photonik: Eine Einführung in die Grundlagen, by Georg A. Reider. 2005 XII, 386 S. 214 Abb. 2., 3-211-21901-3. Berlin: Springer, 2005.*, 1, 2005. 35, 36

[106] P. Laporta and M. Brussard. Design criteria for mode size optimization in diode-pumped solid-state lasers. *IEEE Journal of Quantum Electronics*, 27(10):2319–2326, 1991. 38, 39

[107] Y. F. Chen, T. S. Liao, C. F. Kao, T. M. Huang, K. H. Lin, and S. C. Wang. Optimization of fiber-coupled laser-diode end-pumped lasers: influence of pump-beam quality. *IEEE Journal of Quantum Electronics*, 32(11):2010–2016, 1996.

[108] Y. F. Chen, T. M. Huang, C. F. Kao, C. L. Wang, and S. C. Wang. Optimization in scaling fiber-coupled laser-diode end-pumped lasers to higher power: influence of thermal effect. *IEEE Journal of Quantum Electronics*, 33:1424–1429, 1997. 43

[109] Y.-F. Chen. Design criteria for concentration optimization in scaling diode end-pumped lasers to high powers: influence of thermal fracture. *IEEE Journal of Quantum Electronics*, 35(2):234–239, 1999. 38, 39

[110] Sébastien Chénais, Frédéric Druon, Sébastien Forget, François Balembois, and Patrick Georges. On thermal effects in solid-state lasers: The case of ytterbium-doped materials. *Progress in Quantum Electronics*, 30(4):89 – 153, 2006. 39, 41, 62

[111] F. Lenhardt. private communication. 2009. 39, 43

[112] M. E. Innocenzi, H. T. Yura, C. L. Fincher, and R. A. Fields. Thermal modeling of continuous-wave end-pumped solid-state lasers. *Applied Physics Letters*, 56:1831–1833, May 1990. 41, 62

[113] V. Evtuhov and A. E. Siegman. A "Twisted-Mode" Technique for Obtaining Axially Uniform Energy Density in a Laser Cavity. *Appl. Opt.*, 4(1):142–143, Jan 1965. 45

[114] F. Biraben. Efficacite des systemes unidirectionnels utilisables dans les lasers en anneau. *Optics Communications*, 29(3):353 – 356, 1979. 45

[115] DC Hutchings, FAP Tooley, and DA Russell. Unidirectional operation of a ring laser using an absorbing Fabry-Pérot filter. *Optics letters*, 12:322–324, 1987.

[116] S.G. Dinev, I.G. Koprinkov, K.V. Stamenov, and K.A. Stankov. A narrowband unidirectional pulsed ring dye laser. *Optics Communications*, 35(3):403 – 406, 1980. 45

[117] Gérard Trénec, William Volondat, Orphée Cugat, and Jacques Vigué. Permanent magnets for Faraday rotators inspired by the design of the magic sphere. *Appl. Opt.*, 50(24):4788–4797, Aug 2011. 45

[118] R Sarrouf, T Badr, and J J Zondy. Intracavity second-harmonic generation of diode-pumped continuous-wave, single-frequency 1.3μm Nd:$YLiF_4$ lasers. *Journal of Optics A: Pure and Applied Optics*, 10(10):104011, 2008. 46

[119] Walter Leeb. Losses introduced by tilting intracavity etalons. *Applied Physics A: Materials Science & Processing*, 6:267–272, 1975. 10.1007/BF00883762. 48

[120] YF Chen, TM Huang, CL Wang, LJ Lee, and SC Wang. Theoretical and experimental studies of single-mode operation in diode pumped Nd: YVO4/KTP green laser: influence of KTP length. *Optics communications*, 152(4-6):319–323, 1998. 48

[121] D. B. Leviton, B. J. Frey, and T. J. Madison. Temperature-dependent refractive index of CaF2 and Infrasil 301. *Proc. SPIE 6692, 669204*, 2007. 50

[122] W.M. Haynes. *CRC handbook of chemistry and physics*. CRC Press., 2010.

[123] Paul-Edouard Dupouy, Matthias Büchner, Philippe Paquier, Gérard Trénec, and Jacques Vigué. Interferometric measurement of the temperature dependence of an index of refraction: application to fused silica. *Appl. Opt.*, 49(4):678–682, Feb 2010. 50

[124] E. Khazanov, N.F. Andreev, A. Mal'shakov, O. Palashov, A.K. Poteomkin, A. Sergeev, A.A. Shaykin, V. Zelenogorsky, I.A. Ivanov, R. Amin, et al. Compensation of thermally induced modal distortions in Faraday isolators. *Quantum Electronics, IEEE Journal of*, 40(10):1500–1510, 2004. 55

[125] Feng Song, Chaobo Zhang, Xin Ding, Jingjun Xu, Guangyin Zhang, Matthew Leigh, and Nasser Peyghambarian. Determination of thermal focal length and pumping radius in gain medium in laser-diode-pumped Nd:YVO[sub 4] lasers. *Applied Physics Letters*, 81(12):2145–2147, 2002. 55

[126] R.W. Boyd. *Nonlinear optics*. Academic Pr, 2003. 60, 61

[127] G. D. Boyd and D. A. Kleinman. Parametric Interaction of Focused Gaussian Light Beams. *Journal of Applied Physics*, 39(8):3597–3639, 1968. 60

[128] J. A. Armstrong, N. Bloembergen, J. Ducuing, and P. S. Pershan. Interactions between Light Waves in a Nonlinear Dielectric. *Phys. Rev.*, 127:1918–1939, Sep 1962. 61

[129] P. A. Franken and J. F. Ward. Optical Harmonics and Nonlinear Phenomena. *Rev. Mod. Phys.*, 35:23–39, Jan 1963. 61

[130] M. Yamada, N. Nada, M. Saitoh, and K. Watanabe. First-order quasi-phase matched LiNbO3 waveguide periodically poled by applying an external field for efficient blue second-harmonic generation. *Applied Physics Letters*, 62(5):435–436, 1993. 61

[131] L. E. Myers, R. C. Eckardt, M. M. Fejer, R. L. Byer, W. R. Bosenberg, and J. W. Pierce. Quasi-phase-matched optical parametric oscillators in bulk periodically poled LiNbO3. *J. Opt. Soc. Am. B*, 12(11):2102–2116, Nov 1995. 61

[132] M. Peltz, U. Bäder, A. Borsutzky, R. Wallenstein, J. Hellström, H. Karlsson, V. Pasiskevicius, and F. Laurell. Optical parametric oscillators for high pulse energy and high average power operation based on large aperture periodically poled KTP and RTA. *Applied Physics B*, 73:663–670, 2001. 10.1007/s003400100733. 62, 64, 67

[133] Sergey V. Tovstonog, Sunao Kurimura, and Kenji Kitamura. High power continuous-wave green light generation by quasiphase matching in Mg stoichiometric lithium tantalate. *Applied Physics Letters*, 90(5):051115, 2007. 64

[134] PZKL. *Periodisch gepolte Materialien*. PhD thesis, 2010. 64

[135] Shai Emanueli and Ady Arie. Temperature-Dependent Dispersion Equations for KTiOPO4 and KTiOAsO4. *Appl. Opt.*, 42(33):6661–6665, Nov 2003. 64, 65, 66, 67

[136] K. Fradkin, A. Arie, A. Skliar, and G. Rosenman. Tunable midinfrared source by difference frequency generation in bulk periodically poled $KTiOPO_4$. *Applied Physics Letters*, 74(7):914–916, 1999. 64, 65, 66, 67

[137] Ariel Bruner, David Eger, Moshe B. Oron, Pinhas Blau, Moti Katz, and Shlomo Ruschin. Temperature-dependent Sellmeier equation for the refractive index of stoichiometric lithium tantalate. *Opt. Lett.*, 28(3):194–196, Feb 2003. 64

[138] Junji Hirohashi. *Characterization of domain switching and optical damage properties in ferroelectrics*. PhD thesis, Department of Applied Physics, Royal Institute of Technology, Stockholm, Sweden, 2006. 64

[139] Göran Hansson, Håkan Karlsson, Shunhua Wang, and Fredrik Laurell. Transmission Measurements in KTP and Isomorphic Compounds. *Appl. Opt.*, 39(27):5058–5069, Sep 2000. 64

[140] A. Arie, G. Rosenman, A. Korenfeld, A. Skliar, M. Oron, M. Katz, and D. Eger. Efficient resonant frequency doubling of a cw Nd:YAG laser in bulk periodically poled KTiOPO4. *Opt. Lett.*, 23(1):28–30, Jan 1998. 64, 75

[141] roditi. Manufacturer's website, 2011. 64

[142] R. S. Weis and T. K. Gaylord. Lithium niobate: Summary of physical properties and crystal structure. *Applied Physics A: Materials Science & Processing*, 37(@articleashkin1970acceleration, title=Acceleration and trapping of particles by radiation pressure, author=Ashkin, A., journal=Phys. Rev. Lett., volume=24, number=4, pages=156–159, year=1970, publisher=APS):191–203, 1985. 10.1007/BF00614817. 64

[143] S. Manivannan, S. Dhanuskodi, S.K. Tiwari, and J. Philip. Laser induced surface damage, thermal transport and microhardness studies on certain organic and semiorganic nonlinear optical crystals. *Applied Physics B*, 90:489–496, 2008. 10.1007/s00340-007-2911-4. 64

[144] John D. Bierlein and Herman Vanherzeele. Potassium titanyl phosphate: properties and new applications. *J. Opt. Soc. Am. B*, 6(4):622–633, Apr 1989. 64

[145] almaz. Manufacturer's website, 2011. 64

[146] Y. Furukawa, K. Kitamura, A. Alexandrovski, R. K. Route, M. M. Fejer, and G. Foulon. Green-induced infrared absorption in MgO doped $LiNbO_3$. *Applied Physics Letters*, 78(14):1970–1972, 2001. 64

[147] C. Canalias, S. Wang, V. Pasiskevicius, and F. Laurell. Nucleation and growth of periodic domains during electric field poling in flux-grown KTiOPO[sub 4] observed by atomic force microscopy. *Applied Physics Letters*, 88(3):032905, 2006. 65

[148] Vladislav A Maslov, V A Mikhailov, O P Shaunin, and Ivan A Shcherbakov. Nonlinear absorption in KTP crystals. *Quantum Electronics*, 27(4):356, 1997. 69

[149] B. Boulanger, I. Rousseau, J. P. Feve, M. Maglione, B. Menaert, and G. Marnier. Optical studies of laser-induced gray-tracking in KTP. *IEEE Journal of Quantum Electronics*, 35(3):281–286, 1999. 69

[150] F. Torabi-Goudarzi and E. Riis. Efficient cw high-power frequency doubling in periodically poled KTP. *Optics Communications*, 227(4-6):389 – 403, 2003. 75

[151] T.W. Hansch and B. Couillaud. Laser frequency stabilization by polarization spectroscopy of a reflecting reference cavity. *Optics Communications*, 35(3):441 – 444, 1980. 79

[152] E. Mimoun, L. De Sarlo, J.-J. Zondy, J. Dalibard, and F. Gerbier. Solid-state laser system for laser cooling of sodium. *Applied Physics B*, 99:31–40, 2010. 10.1007/s00340-009-3844-x. 79, 81

[153] Gary C. Bjorklund. Frequency-modulation spectroscopy: a new method for measuring weak absorptions and dispersions. *Opt. Lett.*, 5(1):15–17, Jan 1980. 80, 87

[154] W. I. McAlexander, E. R. I. Abraham, and R. G. Hulet. Radiative lifetime of the $2P$ state of lithium. *Phys. Rev. A*, 54(1):R5–R8, Jul 1996. 84, 105, 142

[155] Armin Ridinger. How to mix repumper and principal beam without losing 50% of the total power. 2008. 86, 88

[156] Newport. *Model Series 44xx and 485x User Manual*. Newport Inc., 2011. 88

[157] Ed Miao. EOSPACE Inc. private communication, 04 2011. 88

[158] Rachel Houtz, Cheong Chan, and Holger Müller. Wideband, efficient optical serrodyne frequency shifting with a phase modulator and a nonlinear transmission Line. *Opt. Express*, 17(21):19235–19240, Oct 2009. 88

[159] D. M. S. Johnson, J. M. Hogan, S. w. Chiow, and M. A. Kasevich. Broadband optical serrodyne frequency shifting. *Opt. Lett.*, 35(5):745–747, Mar 2010. 88

[160] Sheng-wey Chiow, Sven Herrmann, Holger Müller, and Steven Chu. 6W, 1 kHz linewidth, tunable continuous-wave near-infrared laser. *Opt. Express*, 17(7):5246–5250, Mar 2009. 94

[161] L. Landau and E. Lifshitz. *Quantum Mechanics: Nonrelativistic Theory*. Butterworth-Heinemann, 1981. 99, 139, 140, 142

[162] Ugo Fano. Sullo spettro di assorbimento dei gas nobili presso il limite dello spettro d'arco. *Il Nuovo Cimento (1924-1942)*, 12:154–161, 1935. 10.1007/BF02958288. 99

[163] U. Fano. Effects of Configuration Interaction on Intensities and Phase Shifts. *Phys. Rev.*, 124:1866–1878, Dec 1961.

[164] H. Feshbach. Unified theory of nuclear reactions. *Annals of Physics*, 5(4):357–390, 1958.

[165] E. Tiesinga, B. J. Verhaar, and H. T. C. Stoof. Threshold and resonance phenomena in ultracold ground-state collisions. *Phys. Rev. A*, 47:4114–4122, May 1993. 99

[166] S. Inouye, MR Andrews, J. Stenger, H.J. Miesner, DM Stamper-Kurn, and W. Ketterle. Observation of Feshbach resonances in a Bose–Einstein condensate. *Nature*, 392(6672):151–154, 1998. 99, 100

[167] S.E. Pollack, D. Dries, and R.G. Hulet. Universality in three-and four-body bound states of ultracold atoms. *Science*, 326(5960):1683, 2009. 99

[168] F. Dalfovo, S. Giorgini, L.P. Pitaevskii, and S. Stringari. Theory of Bose-Einstein condensation in trapped gases. *Reviews of Modern Physics*, 71(3):463, 1999. 99

[169] G. Baym, J.P. Blaizot, M. Holzmann, F. Laloë, and D. Vautherin. The transition temperature of the dilute interacting Bose gas. *Phys. Rev. Lett.*, 83(9):1703–1706, 1999. 100

[170] F. Gerbier, J. H. Thywissen, S. Richard, M. Hugbart, P. Bouyer, and A. Aspect. Critical Temperature of a Trapped, Weakly Interacting Bose Gas. *Phys. Rev. Lett.*, 92:030405, Jan 2004. 100

[171] F. Gerbier, J. H. Thywissen, S. Richard, M. Hugbart, P. Bouyer, and A. Aspect. Experimental study of the thermodynamics of an interacting trapped Bose-Einstein condensed gas. *Phys. Rev. A*, 70:013607, Jul 2004.

[172] K. Xu, Y. Liu, D. E. Miller, J. K. Chin, W. Setiawan, and W. Ketterle. Observation of Strong Quantum Depletion in a Gaseous Bose-Einstein Condensate. *Phys. Rev. Lett.*, 96:180405, May 2006.

[173] Robert P. Smith, Robert L. D. Campbell, Naaman Tammuz, and Zoran Hadzibabic. Effects of Interactions on the Critical Temperature of a Trapped Bose Gas. *Phys. Rev. Lett.*, 106:250403, Jun 2011. 100

[174] N. Navon, S. Piatecki, K. Günter, B. Rem, T.C. Nguyen, F. Chevy, W. Krauth, and C. Salomon. Dynamics and Thermodynamics of the Low-Temperature Strongly Interacting Bose Gas. *Phys. Rev. Lett.*, 107(13):135301, 2011. 100, 108, 114

[175] T. D. Lee, Kerson Huang, and C. N. Yang. Eigenvalues and Eigenfunctions of a Bose System of Hard Spheres and Its Low-Temperature Properties. *Phys. Rev.*, 106:1135–1145, Jun 1957. 100

[176] D. S. Petrov, C. Salomon, and G. V. Shlyapnikov. Weakly Bound Dimers of Fermionic Atoms. *Phys. Rev. Lett.*, 93:090404, Aug 2004. 100

[177] J. Cubizolles, T. Bourdel, S. Kokkelmans, GV Shlyapnikov, and C. Salomon. Production of Long-Lived Ultracold Li_2 Molecules from a Fermi Gas. *Phys. Rev. Lett.*, 91(24):240401, 2003. 100

[178] M. Bartenstein, A. Altmeyer, S. Riedl, S. Jochim, C. Chin, J.H. Denschlag, and R. Grimm. Crossover from a molecular Bose-Einstein condensate to a degenerate Fermi gas. *Phys. Rev. Lett.*, 92(12):120401, 2004.

[179] J. Zhang, E. G. M. van Kempen, T. Bourdel, L. Khaykovich, J. Cubizolles, F. Chevy, M. Teichmann, L. Tarruell, S.J.J.M.F. Kokkelmans, and C. Salomon. Expansion of a lithium gas in the BEC–BCS crossover. In *Proceedings of the XIX International Conference on Atomic Physics, ICAP 2004, AIP Conference Proceedings 770*, pages 228–237, 2005. 100

[180] CA Regal, M. Greiner, and DS Jin. Lifetime of Molecule-Atom Mixtures near a Feshbach Resonance in ^{40}K. *Phys. Rev. Lett.*, 92(8):83201, 2004. 100

[181] S. Cowell, H. Heiselberg, IE Mazets, J. Morales, VR Pandharipande, and CJ Pethick. Cold Bose gases with large scattering lengths. *Phys. Rev. Lett.*, 88(21):210403, 2002. 100

[182] J.L. Song and F. Zhou. Ground State Properties of Cold Bosonic Atoms At Large Scattering Lengths. *Phys. Rev. Lett.*, 103(2):25302, 2009.

[183] Y.L. Lee and Y.W. Lee. Universality and stability for a dilute Bose gas with a Feshbach resonance. *Physical Review A*, 81(6):063613, 2010. 100

[184] C. C. Bradley, C. A. Sackett, J. J. Tollett, and R. G. Hulet. Evidence of Bose-Einstein Condensation in an Atomic Gas with Attractive Interactions. *Phys. Rev. Lett.*, 75:1687–1690, Aug 1995. 100

[185] C. C. Bradley, C. A. Sackett, J. J. Tollett, and R. G. Hulet. Erratum: Evidence of Bose-Einstein Condensation in an Atomic Gas with Attractive Interactions. *Phys. Rev. Lett.*, 79:1170–1170, Aug 1997.

[186] C. C. Bradley, C. A. Sackett, and R. G. Hulet. Bose-Einstein Condensation of Lithium: Observation of Limited Condensate Number. *Phys. Rev. Lett.*, 78:985–989, Feb 1997.

[187] SL Cornish, NR Claussen, JL Roberts, EA Cornell, and CE Wieman. Stableˆ{85} Rb Bose-Einstein Condensates with Widely Tunable Interactions. *Phys. Rev. Lett.*, 85(9):1795–1798, 2000. 100

[188] PO Fedichev, MW Reynolds, and GV Shlyapnikov. Three-body recombination of ultracold atoms to a weakly bound s level. *Phys. Rev. Lett.*, 77(14):2921–2924, 1996. 100

[189] Eric Braaten and H.-W. Hammer. Three-Body Recombination into Deep Bound States in a Bose Gas with Large Scattering Length. *Phys. Rev. Lett.*, 87:160407, Oct 2001. 100

[190] J. Stenger, S. Inouye, M. R. Andrews, H.-J. Miesner, D. M. Stamper-Kurn, and W. Ketterle. Strongly Enhanced Inelastic Collisions in a Bose-Einstein Condensate near Feshbach Resonances. *Phys. Rev. Lett.*, 82:2422–2425, Mar 1999. 100

[191] J. L. Roberts, N. R. Claussen, S. L. Cornish, and C. E. Wieman. Magnetic Field Dependence of Ultracold Inelastic Collisions near a Feshbach Resonance. *Phys. Rev. Lett.*, 85:728–731, Jul 2000.

[192] T. Weber, J. Herbig, M. Mark, H.C. Nägerl, and R. Grimm. Three-body recombination at large scattering lengths in an ultracold atomic gas. *Phys. Rev. Lett.*, 91(12):123201, 2003. 100, 120, 121

[193] BD Esry, C.H. Greene, and J.P. Burke Jr. Recombination of three atoms in the ultracold limit. *Phys. Rev. Lett.*, 83(9):1751–1754, 1999. 101

[194] LM Delves. Tertiary and general-order collisions. *Nuclear Physics*, 9(3):391–399, 1959.

[195] LM Delves. Tertiary and general-order collisions (II). *Nuclear Physics*, 20:275–308, 1960. 101

[196] W. Li and T.L. Ho. Bose Gases Near Unitarity. *Arxiv preprint arXiv:1201.1958*, 2012. 101, 127, 135

[197] V. Efimov. Energy levels arising from resonant two-body forces in a three-body system. *Physics Letters B*, 33(8):563–564, 1970. 101

[198] V. Efimov. Energy levels arising from resonant two-body forces in a three-body system. *Physics Letters B*, 33(8):563–564, 1970.

[199] V. Efimov. Weakly-bound states of three resonantly-interacting particles. *Sov. J. Nucl. Phys*, 12:589, 1971. 101

[200] C.H. Greene, BD Esry, and H. Suno. A revised formula for 3-body recombination that cannot exceed the unitarity limit. *Nuclear Physics A*, 737:119–124, 2004. 101, 125

[201] J.P. D'Incao, H. Suno, and B.D. Esry. Limits on universality in ultracold three-boson recombination. *Phys. Rev. Lett.*, 93(12):123201, 2004. 101, 125, 126, 134

[202] T. Kraemer, M. Mark, P. Waldburger, JG Danzl, C. Chin, B. Engeser, AD Lange, K. Pilch, A. Jaakkola, H.C. Nägerl, et al. Evidence for Efimov quantum states in an ultracold gas of caesium atoms. *Nature*, 440(7082):315–318, 2006. 101

[203] M. Zaccanti, B. Deissler, C. D'Errico, M. Fattori, M. Jona-Lasinio, S. Müller, G. Roati, M. Inguscio, and G. Modugno. Observation of an Efimov spectrum in an atomic system. *Nature Physics*, 5(8):586–591, 2009. 101

[204] S.E. Pollack, D. Dries, M. Junker, YP Chen, TA Corcovilos, and RG Hulet. Extreme Tunability of Interactions in a ^{7}Li Bose-Einstein Condensate. *Phys. Rev. Lett.*, 102(9):90402, 2009. 102, 106

[205] N. Gross, Z. Shotan, S. Kokkelmans, and L. Khaykovich. Observation of Universality in Ultracold^{7} Li Three-Body Recombination. *Phys. Rev. Lett.*, 103(16):163202, 2009. 102

[206] T. Lompe, T.B. Ottenstein, F. Serwane, A.N. Wenz, G. Zürn, and S. Jochim. Radio-frequency association of Efimov trimers. *Science*, 330(6006):940, 2010. 102

[207] T. Lompe, TB Ottenstein, F. Serwane, K. Viering, AN Wenz, G. Zürn, and S. Jochim. Atom-dimer scattering in a three-component Fermi gas. *Phys. Rev. Lett.*, 105(10):103201, 2010.

[208] S. Nakajima, M. Horikoshi, T. Mukaiyama, P. Naidon, and M. Ueda. Nonuniversal Efimov Atom-Dimer Resonances in a Three-Component Mixture of ^{6}Li. *Phys. Rev. Lett.*, 105(2):23201, 2010. 102

[209] F. Ferlaino, S. Knoop, M. Berninger, W. Harm, J. P. D'Incao, H.-C. Nägerl, and R. Grimm. Evidence for Universal Four-Body States Tied to an Efimov Trimer. *Phys. Rev. Lett.*, 102:140401, Apr 2009. 102

[210] F. Ferlaino and R. Grimm. Forty years of Efimov physics: How a bizarre prediction turned into a hot topic. *Physics*, 3:9, 2010. 102

[211] Gabriele Ferrari. *Simultaneous trapping of the bosonic and fermionic isotopes of lithium, theoretical study of the collisional relaxation in a degenerate Fermi gas.* PhD thesis, Université Pierre et Marie Curie -Paris VI, 2000. 103

[212] Florian Schreck. *Mixtures of ultracold gases: Fermi sea and Bose-Einstein condensate of Lithium isotopes*. PhD thesis, Université Pierre et Marie Curie -Paris VI, 2002. 109

[213] Thomas Bourdel. *Strongly interacting Fermi Gas: From molecular condensate to Cooper pairs*. PhD thesis, Université Pierre et Marie Curie -Paris VI, 2004.

[214] Julien Cubizolles. *Degenerate fermions and bosons in the vicinity of a Feshbach resonance : Production of molecules and matter-wave solitons*. PhD thesis, Université Pierre et Marie Curie -Paris VI, 2004.

[215] Martin Teichmann. *Ultracold Lithium-6 Atoms in the BEC-BCS Crossover: Experiments and the Construction of a New Apparatus*. PhD thesis, Université Pierre et Marie Curie -Paris VI, 2007. 104

[216] Leticia Tarruell. *Superfluidité dans un gaz de fermions ultrafroids*. PhD thesis, Université Pierre et Marie Curie -Paris VI, 2008.

[217] S. Nascimbène, N. Navon, KJ Jiang, F. Chevy, and C. Salomon. Exploring the thermodynamics of a universal Fermi gas. *Nature*, 463(7284):1057–1060, 2010. 103, 128

[218] Nir Navon. *Thermodynamics of ultracold Bose and Fermi gases*. PhD thesis, Université Pierre et Marie Curie -Paris VI, 2011. 103, 106, 107, 114, 115

[219] M.E. Gehm. *Preparation of an optically-trapped degenerate Fermi gas of 6Li: Finding the route to degeneracy*. PhD thesis, PhD thesis, Duke University, 2003. 104

[220] TG Tiecke, SD Gensemer, A. Ludewig, and JTM Walraven. High-flux two-dimensional magneto-optical-trap source for cold lithium atoms. *Phys. Rev. A*, 80(1):013409, 2009. 104

[221] G. Breit and I. I. Rabi. Measurement of Nuclear Spin. *Phys. Rev.*, 38:2082–2083, Dec 1931. 105

[222] E. Arimondo, M. Inguscio, and P. Violino. Experimental determinations of the hyperfine structure in the alkali atoms. *Rev. Mod. Phys.*, 49:31–76, 1977. 106

[223] K.E. Strecker, G.B. Partridge, A.G. Truscott, and R.G. Hulet. Formation and propagation of matter-wave soliton trains. *Nature*, 417(6885):150–153, 2002. 106

[224] L. Khaykovich, F. Schreck, G. Ferrari, T. Bourdel, J. Cubizolles, LD Carr, Y. Castin, and C. Salomon. Formation of a matter-wave bright soliton. *Science*, 296(5571):1290, 2002. 106

[225] N. Gross, Z. Shotan, S. Kokkelmans, and L. Khaykovich. Nuclear-spin-independent short-range three-body physics in ultracold atoms. *Phys. Rev. Lett.*, 105(10):103203, 2010. 106

[226] Noam Gross and Lev Khaykovich. All-optical production of ^{7}Li Bose-Einstein condensation using Feshbach resonances. *Phys. Rev. A*, 77:023604, Feb 2008. 106

[227] Claude Cohen-Tannoudji. Piégage non dissipatif d'atomes neutres. In *Cours au Collège de France*, 1996. 109

[228] Steffen P. Rath, Tarik Yefsah, Kenneth J. Günter, Marc Cheneau, Rémi Desbuquois, Markus Holzmann, Werner Krauth, and Jean Dalibard. Equilibrium state of a trapped two-dimensional Bose gas. *Phys. Rev. A*, 82:013609, Jul 2010. 114

[229] BD Esry, C.H. Greene, and H. Suno. Threshold laws for three-body recombination. *Physical Review A*, 65(1):010705, 2001. 126

[230] E. Braaten, H.W. Hammer, D. Kang, and L. Platter. Three-body recombination of identical bosons with a large positive scattering length at nonzero temperature. *Physical Review A*, 78(4):043605, 2008. 126, 134, 143

[231] O. Machtey, Z. Shotan, N. Gross, and L. Khaykovich. Association of Efimov trimers from three-atoms continuum. *Arxiv preprint arXiv:1201.2396*, 2012. 126

[232] H. Suno, BD Esry, C.H. Greene, and J.P. Burke Jr. Three-body recombination of cold helium atoms. *Physical Review A*, 65(4):042725, 2002. 127

[233] T.L. Ho and Q. Zhou. Obtaining the phase diagram and thermodynamic quantities of bulk systems from the densities of trapped gases. *Nature Physics*, 6(2):131–134, 2009. 128

[234] Chi-Ho Cheng and Sung-Kit Yip. Trapped resonant fermions above the superfluid transition temperature. *Phys. Rev. B*, 75:014526, Jan 2007.

[235] Yong-il Shin. Determination of the equation of state of a polarized Fermi gas at unitarity. *Phys. Rev. A*, 77:041603, Apr 2008. 128

[236] C. F. Ockeloen, A. F. Tauschinsky, R. J. C. Spreeuw, and S. Whitlock. Detection of small atom numbers through image processing. *Phys. Rev. A*, 82:061606, Dec 2010. 129

[237] Félix Werner. private communication. 2011. 129, 130, 134, 135, 145

[238] Tilman Zibold, Eike Nicklas, Christian Gross, and Markus K. Oberthaler. Classical Bifurcation at the Transition from Rabi to Josephson Dynamics. *Phys. Rev. Lett.*, 105:204101, Nov 2010. 134

[239] J. Williams, R. Walser, J. Cooper, E. Cornell, and M. Holland. Nonlinear Josephson-type oscillations of a driven, two-component Bose-Einstein condensate. *Phys. Rev. A*, 59:R31–R34, Jan 1999. 134

[240] M. Iskin. Dimer-atom scattering between two identical fermions and a third particle. *Phys. Rev. A*, 81:043634, Apr 2010. 135, 137

[241] K. Helfrich, H.-W. Hammer, and D. S. Petrov. Three-body problem in heteronuclear mixtures with resonant interspecies interaction. *Phys. Rev. A*, 81:042715, Apr 2010. 135, 137

[242] Klaus Mølmer. Bose Condensates and Fermi Gases at Zero Temperature. *Phys. Rev. Lett.*, 80:1804–1807, Mar 1998. 137

[243] Robert Roth. Structure and stability of trapped atomic boson-fermion mixtures. *Phys. Rev. A*, 66:013614, Jul 2002.

[244] M. Lewenstein, L. Santos, M. A. Baranov, and H. Fehrmann. Atomic Bose-Fermi Mixtures in an Optical Lattice. *Phys. Rev. Lett.*, 92:050401, Feb 2004. 137

[245] R. P. Feynman. Slow Electrons in a Polar Crystal. *Phys. Rev.*, 97:660–665, Feb 1955. 137

[246] E. G. M. v. Kempen, B. Marcelis, and S. J. J. M. F. Kokkelmans. Formation of fermionic molecules via interisotope Feshbach resonances. *Phys. Rev. A*, 70:050701, Nov 2004.

[247] Cheng-Hsun Wu, Ibon Santiago, Jee Woo Park, Peyman Ahmadi, and Martin W. Zwierlein. Strongly interacting isotopic Bose-Fermi mixture immersed in a Fermi sea. *Phys. Rev. A*, 84:011601, Jul 2011. 137

[248] NP Mehta, S.T. Rittenhouse, JP D'Incao, J. Von Stecher, and C.H. Greene. General theoretical description of N-body recombination. *Phys. Rev. Lett.*, 103(15):153201, 2009. 139, 141

[249] Seth T. Rittenhouse. *Control and dynamics of few-body systems at ultracold temperatures*. PhD thesis, University of Colorado, 2009. 139, 141

[250] J. Avery. *Hyperspherical Harmonics: Applications in Quantum Theory*, volume 5. Springer, 1989. 140, 141

[251] Frédéric Chevy. Notes on the 3-body problem. 2011. 142

[252] H. Suno, BD Esry, and C.H. Greene. Recombination of three ultracold fermionic atoms. *Phys. Rev. Lett.*, 90(5):53202, 2003. 143